Ultraviolet Photofragmentation Spectroscopy of Metal Dication Sandwich Complexes in the Gas Phase Combined with DFT/TDDFT Calculations

Ma Lifu, MSc.

Thesis submitted to the University of Nottingham for the degree of Doctor of Philosophy

July 2013

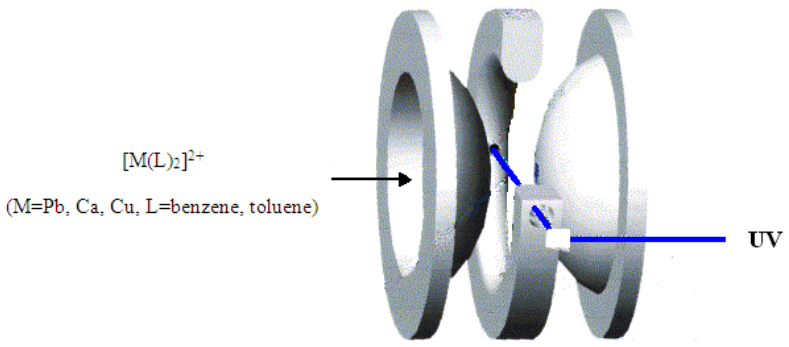

Abstract

Metal dication-ligand sandwich complexes have attracted intense attention recently for their widely use in catalysis, biochemistry and material science. The experimental techniques developed by our group have allowed forming, confining, cooling and investigating a wide range of metal dication complexes in the gas phase. In this thesis, the ultraviolet photofragmentation studies of Pb(II), Cu(II) and Ca(II) sandwich complexes with aromatic ligands are performed using a hybrid quadrupole ion trap instrument, followed by DFT/TDDFT calculations. The experimental results indicate that the complexes are capable of yielding structured, sometimes conformation resolved, UV spectra. The spectra of metal dication-benzene complexes exhibit features in the wavelength range 220-270 nm and a big raise as the wavelength decreases. The lead dication-bis(toluene) complex spectrum shows some well-resolved features arising from different conformers. The theory suggests that all of these complexes have excitations including significant contributions from the metal-based orbital. The adiabatic TDDFT methodology is able to give reasonable agreement between the calculated excitations and the experimental spectra for the close-shell complexes. But for some open-shell complexes, the calculated excitations are spin contaminated, which need to be discarded or corrected in the future. The degree of spin contamination for selected excitations is qualified by calculating the $<\hat{S}^2>$ values. For lead and calcium open-shell complexes, most of the excitations that can match the experimental features can be trusted. However, for the copper open-shell complex, only three states are ~90% doublet in their character which are responsible for some excitations that can match the spectra. Challenges such as developing the theory to describe the open-shell system and refining the experimental techniques to improve the resolution of the spectra, still remain.

Acknowledgements

I would like to thank Prof. Anthony J. Stace for kindly offering me the opportunity to join his legendary research group, for his consistent patient and sound guidance on my work, for leading me to the amazing chemical physics world.

I thank Dr. Wu Guohua for his state-of-art designing and many years of efforts on constructing the experimental apparatus that I have been used in my Ph.D period and many useful suggestions when the machine went wrong. His training leads me to establish a solid fundamental on vacuum technology, laser technology and mass spectrometry technology, which are the most important transferable skills for my future career.

I thank Dr. Adrian Boatwright for his help on laser aligning and training on using Nd:YAG pump laser and Sarah tuneable double frequency dye laser.

I thank Dr. Hazel Cox for her detailed training on DFT/TDDFT calculations, usage of computational chemistry software, and data analyzing, consistent help on fixing the high performance computer problems.

I would like to thank my senior student Dr. Hamish Stewart for designing the computer programme for recording the mass spectra, for his kind help on paper writing, poster generating, presentation rehearsing, and many helpful suggestions on my experiments, Dr. Adrian Gardner for his help on the laser aligning and many useful suggestions on my work, Dr. Do Hainam for proof reading of my thesis and kind help on my calculations.

I would like to thank all of the technicians in the workshop in school of chemistry, the technician Mr. Neil Barns, the electrician Mr. James Warren, Mr. David Litchfield and Mr. Kevin Hind, the vacuum technician Mr. John Whalley, IT technician Mr. Peter Morgan-Tansley and Mr. Patrick Hutchinson. I cannot finish this experiment without their help.

I would like to thank technicians outside the university, Dr Ben Agate from Photonics for his help on laser fixing and aligning, Mr. Kevin Kuchta and Mr. Tom O'Hara from Extrel for their help on maintenance of the quadrupole mass spectrometer.

I would like to thank my parents for their constant encouragement and support.

I also thank the university of Nottingham and school of chemistry for their financial support.

Contents

Chapter 1 General Introduction

In this thesis, ultraviolet photofragmentation spectroscopy of a series of metal dication-ligand sandwich complexes have been recorded in the gas phase using a hybrid quadrupole (Paul) ion trap device that originates from a Finnegan ITMS system. The experimental spectra are recorded to bench-mark the theory. This chapter aims to establish background, to elucidate motivation of this research, to explain theory that has been applied, to introduce developments of experimental techniques that make significant contributions to this research.

1.1 Molecular clusters

Clusters consisting of finite numbers (2 to 1000) of atoms or molecules are easily formed in the gas phase with new experimental technologies.[1] They have fascinating properties in their own right and they also serve as models for bulk systems in a wide variety of contexts.[1] In reality, there are few opportunities to realize this objective because the scale over which many physical properties operate can far exceed the equivalent size of cluster that can be manipulated and studied in a systematic fashion.[2] In some respects, the realization of bulk behaviour in clusters is probably not the most important goal because many aspects of nanotechnology rest on the identification and characterization of any unique properties finite-sized particles may possess.[2] Bridging the gap between single atoms or molecules and the condensed phase is the most frequently quoted statement in cluster science nowadays.[3] Cluster science emerged from the confluence of molecular spectroscopy, molecular beam techniques, and low-temperature matrix spectroscopy on the ‘chemistry’ side and solid state electronics, magnetic, and surface science on the ‘physics’ side.

There is considerable interest in studies of gas phase clusters for many reasons. First, as nanoparticles they constitute intermediates between molecules, with clearly defined energy states (electronic, vibrational, etc.) and condensed matter where these states

form continua or bands. The high ratio of surface atoms to bulk atoms means that there are many analogies between the chemistry and physics of clusters and of solid surfaces. Clusters are also of interest in their own science, in this intermediate size regime, finite size effects can lead to electronic, magnetic and other properties that are quite different from those of molecules or condensed matter. Normally, cluster experiments can be demonstrated as three main stages; cluster preparation, cluster investigation and cluster detection.

1.1.1 Clusters preparation

The first stage of cluster experiments is preparation of clusters. Clusters are generated in a cluster source, following processes of vaporization, nucleation, growth and coalescence. Clusters can grow by addition of more atoms or molecules to the initially formed nucleus. On the other hand, they can also shrink by evaporation or fragmentation. Clusters produced with distributions in size that are dependent on the source are seen in nature. For this experiment, a supersonic expansion source is applied.

Supersonic expansion can generate continuous, intense cluster beams with narrow velocity distributions. Due to a high stagnation pressure and relative small diameter of the nozzle, the particle mean free path is much smaller than the nozzle diameter. Many collisions occur during the expansion and these cool the vapour down to supersaturation.[4] During the cooling procedure, mean velocities and kinetic energies of the clusters increase but random thermal motions are reduced, which means that the velocities of the clusters relative to each other are very low, corresponding to low temperatures. The collisions cause energy redistribution, converting internal vibrational and rotational energy to kinetic energy. Comparing to conventional effusive equivalent, the resultant molecular beam possess a higher velocity and a narrower distribution of velocity. Further cooling can be achieved by the evaporation

of atoms from clusters and very low temperatures can be generated. There are three factors affecting the cluster number and size; stagnation pressure, temperature and the nozzle aperture cross-section. The number and average size of clusters both increase with increasing pressure and nozzle aperture cross-section, while they decrease with increasing temperature.

In a supersonic expansion experiment, collisions during expansion can cool down the vapour to produce the condensed clusters. If local thermal energy of beam is less than binding energy of a dimer, then a three-atom collision can lead to formation of a dimeric nucleus, while the third atom takes away the excess energy as kinetic energy as detailed in equation 1.1.

$$A + A + A(KE_1) \rightarrow A_2 + A(KE_2 > KE_1) \quad \text{(eq.1.1)}$$

Further aggregation is started from the dimer. The initially formed cluster nucleus acts as a seed for further cluster growth. Early growth occurs by aggregation of molecules one at a time. Subsequently, collisions between smaller clusters can lead to further coalescence and the formation of larger cluster as equation 1.2.

$$A_N + A_M \rightarrow A_{N+M} \quad \text{(eq.1.2)}$$

During the aggregation procedure, the clusters are hot so there is competition between growth and decay. There are three mechanisms by which the clusters can be cooled down. First, collisions with other molecules can remove the excess energy as kinetic energy. Second, clusters can lower their internal energies by evaporation. Last, clusters can emit radiation thereby lowering their internal energy.

Apart from supersonic expansion, there are some other sources that need to be mentioned. For instance, Knudsen cell or effusive sources are subsonic continuous sources. They form clusters by heating a solid or liquid in an oven with a small aperture, thereby generating a low vapour pressure. The resolution of effusive sources

is not as good as supersonic expansion sources, as broad energy distributions are obtained. Laser vaporization source is a pulsed source which combines laser ablation with a supersonic expansion. Vapour is produced by laser vaporization and is introduced into a pulse of cold helium which can cool the vapour down to form cluster. The ion sputtering source can produce clusters by bombarding a target with high energy inert gas ions. The clusters are hot and can be cooled by evaporation so that the abundance spectra reflect the thermodynamic stabilities of the clusters via their binding energies. A gas aggregation or smoke source produces continuous cluster beams of low-boiling metals. The metal vapour is generated by evaporation or sputtering and quenched by inert cooling gas (He or Ar), where the vapour becomes supersaturated and clusters aggregate. This mechanism of cluster formation is analogous to cloud and smoke formation. Cluster beam intensities are much lower than supersonic sources, however very large clusters (>20000 atoms) can be formed. Electrospray sources are used to form clusters from liquids and solutions. The operation principle and several typical application examples of this kind of source will be introduced in the following section.

1.1.2 Ionization and fragmentation

In many gas phase cluster investigations, clusters need to be separated according to their mass and charge ratio before detection. In order to do this, it is necessary to ionize the clusters so that mass selection can be achieved. Cluster cations can be formed by electron impact or photoionization of corresponding neutral clusters. Electron impact ionization creates cluster ions by knocking electrons off neutral clusters by a focussed thermal electron beam. Electron impact ionization is always accompanied by cluster fragmentation because of excess energy arising from the ionization process.

Photoionization can create cationic clusters without fragmentation using a near-threshold frequency light source, where the laser frequency is tuned until the photons have just enough energy to ionize the clusters but not sufficient to break cluster bonds. The reason that photoionization can do this is because the photon frequencies can be tuned across a wide range. In this type of experiment, the appearance potential of cluster ion and ionization energy of the corresponding neutral cluster can be determined.

1.1.3 Mass selection and detection

As mass spectrometry techniques have been highly developed nowadays, there are many instruments can be used to select and detect cluster ions. One way to select mass of cluster ions is by deflecting charged clusters depending on their mass/charge ratio and their velocities using homogeneous electric or magnetic field sectors. Our group developed a double sector instrument (Vacuum Generators ZAB-E reverse geometry high resolution double focussing mass spectrometer),[3, 5] and with this device, cluster ions are accelerated to the same kinetic energy and deflected by a magnetic sector field so that only one mass, with the correct momentum can exit the magnetic sector. The cations then pass through an electric sector field with an energy dispersion adjusted to compensate for that of the magnetic sector. [3, 5]

The quadrupole mass filter is another widely used mass-selecting device for gaseous cluster ions investigation. Resolving powers of 10^3 and masses up to 9000 mass unit (amu) can be achieved by quadrupole mass spectrometer. Since this thesis is based on experiments operated using a quadrupole ion trap mass spectrometer, more details will be provided in the following experimental chapter.

Time-of-Flight mass spectrometer is also widely used and a very important experimental device. In the TOF mass spectrometer, cluster ions are accelerated by a succession of homogeneous electric fields into a field-free flight tube, finally

impacting on an ion detector. The mass/charge ratio of the ions is determined from the measured time-of-flight. [6] The mass resolution of this spectrometer can be improved by using a reflectron. Since fast ions take longer to reverse their direction than slower ions, the time spread of ions is reduced and all ions with same mass/charge ratio but with different initial velocities arrive at the detector almost simultaneously. When an electric field of an ion source is responsible for the extraction of ions into a flight tube, delayed extraction can also improve the mass resolution. Since the thickness of the ion packets arriving at a detector is important to mass resolution, delayed extraction is a compensation for the initial momentum of ions, which can provide same arrival times at the detector for ions with the same mass/charge ratio but with different initial velocities. In its way, the delayed extraction acts as a one-dimensional time-of-flight focusing element. [7] This technique can be applied on Resonance Enhanced Multi-Photon Ionization (REMPI), Electron Impact ionization (EI) and Matrix-Assisted Laser Desorption/Ionization (MALDI) experiments.

1.2 Typical experimental techniques for gas-phase preparation of metal ion-ligand complexes clusters

Interactions between metal ions and solvent molecules play a paramount role in biology, organic and inorganic chemistry, and science of materials.[8] To understand metal ion-molecule interactions, many metal ion-ligand complexes have been formed and investigated in the condensed phase either in solution or in the form of a matrix.[9] However, the presence of a counterion or a solvent molecule restricts the degree to which accurate correlations can be made between electron configuration and spectral bands.[5c] Inhomogeneous broadening and the perturbation of spectra are common problems in the condensed phase studies.[10] Therefore, gas-phase study which can isolate species independent of both solvent and counterion becomes a reasonable option.

For the past few years, there are many experiments that have been conducted to investigate multiply charged metal ion-ligand complexes in the gas phase.[2] These experiments have covered a wide range of complexes containing first-row transition metals in charge states commonly observed in condensed phase chemistry such as Mn(II)[5b], Co(II)[11], Fe(II)[12], Ni(II)[12a], and Cu(II)[13]. Laser ablation, electrospray and pick-up technique are the most widely used technologies.

1.2.1 Laser vaporization or ablation source

Laser vaporization has been used to produce gaseous molecular species which are non-volatile or generally decompose upon heating.[14] Many different kinds of vaporization methods have been widely used combined with a supersonic expansion, such as laser desorption[15], supercritical fluids[16], fast atom bombardment[17]. In spectroscopic studies, laser desorption has been used as a neutral species source and is usually separated from an ionization process such as REMPI and electron impact (EI). The experimental apparatus normally included two vacuum chambers, one source chamber and one spectrometer chamber. In the source chamber, the cluster ion source normally has a Smalley vaporization source with a rotating and translating target metal rod, and the laser pulse introduced to vaporize the target to form metal clusters. Metal clusters would be entrained with the desired ligand/carrier gas mixture to form a beam of neutral metal-ligand complexes which can be ionized and mass selected. The other chamber normally housed a mass spectrometer and ion detection devices to give the mass spectra and spectroscopy.

Recently, many experimental results using laser vaporization have been reported. Duncan [18] used a pulsed laser vaporization source to prepare a variety of gas-phase metal ion-benzene complexes. The molecules were cooled through seeded supersonic expansion and investigated by laser photodissociation in a reflectron time-of-flight mass spectrometer. Wright and co-workers [19] used laser ablation technique to

generate metal atoms from the surface of a solid Au rod within a liquid-nitrogen-cooled polyetherketone laser vaporization (LaVa) cluster source. The Au-Ar clusters are formed by free jet expansion subsequently, ionized by REMPI methodology and extracted into a time-of-flight tube. Mackenzie and co-workers [20] also used this technique to produce VO clusters. The REMPI spectra of VO were recorded using a homebuilt Wiley-Mclaren time-of-flight mass spectrometer with laser ablation source.

1.2.2 Electrospray ionization source

Electrospray ionization-mass spectrometry (ESI-MS) has been used in a wide variety of fields to examine the formation, stoichiometry and speciation of complexes involving metal and organic ligands.[21] ESI-MS can provide a gentle transition from solution to gas phase that maintains solution phase speciation to a large extent which makes this method interesting for metal complex investigation. By this technology, the metal-ligand complexes are normally pre-made in the solvent and the mixed solutions are electrosprayed into ion droplets through a nozzle charged by high voltage. Then the small charged liquid ion droplets can be broke down and desolvated by a flow of carrying gas while passing through a heated capillary followed by mass selecting and ion detection. However, perturbations to the solution chemistry during the ionization process and ions undergoing gas-phase reactions prior to reaching the detector could have some side-effects during the experiment.

Numerous groups have combined this technique with other mass-selecting and ion detecting techniques to achieve a wide range of excellent measurements. For example, Kim and co-workers [22] used ESI cluster source to generate neutral tyrosine molecular clusters and record the photodepletion spectrum of gaseous protonated ions with a quadrupole ion trap reflectron time-of-flight mass spectrometer (QIT-reTOFMS). They also recorded ultraviolet photodepletion spectroscopy of alkaline earth metal [23] and alkali metal [24] complexes cations baring a dibenzo-18-crown-6-ether ligand. At

longer wavelengths, Williams and co-workers have successfully used a combination of electrospray and multi-photon IR excitation to record spectra from a range of doubly charged metal ion/water complexes,[25] and tuneable infrared radiation has also been used to investigate the structures of complexes formed between alkaline earth ions and small molecules of biological significance.[26]

1.2.3 The pick-up technique

The pick-up technique is developed by our group to form multiply charged metal ion-ligand complexes. [5b, c, 13a, 27] Metal vapour is generated by heating up an effusion cell loaded with the desired metal chips which sits in an oven. When argon/ligand clusters formed by supersonic expansion pass through the oven chamber, the metal atom will be picked up and metal complexes clusters will be formed. The metals which are suitable for this method need to have the capability to provide sufficient vapour pressures at temperature less than 1800 ^{o}C.

Walker used this method to form Mg(II), Cu (II), Ag(II), and Au(II) in the gas phase, respectively.[27c, 28] Puskar produced Al(III), Ag(II), Cu(II) cations by pick-up technique in the gas phase and studied the stability of complexes formed through experiments and theories (*ab initio* and DFT).[5c, 29] Duncombe formed Zn(II), Mn(II), Pb(II), and Cu(II) cation with a wide range of ligands using this technique.[5a, b, 30] Chen produced gas phase $[Zn(H_2O)_N]^{2+}$ complexes with pick-up technique to investigate the enhanced acidity of Zn^{2+} in the presence of small numbers of water molecules.[31] Sn(II) and Pb(II) with water complexes were produced by pick-up technique as well to study the acidities of these gaseous metal complexes using combined experimental and theoretical methodology.[32]

The most important advantage of the pick-up technique when compared with electrospray and laser ablation is the very diverse range of ligands that can be studied. In some instances, only the pick-up method has thus far provided access to certain

complexes that have played a pivotal role in solution-phase transition metal chemistry, such as $[Cu(NH_3)_n]^{2+}$.[2] But this technique has its own limitations, such as poor performance when organic ligands with low evaporation pressures involved, such as porphyrin.

1.3 Experimental techniques for gas-phase spectroscopic investigation of metal dication-ligand complexes clusters

1.3.1 Significance of the gas-phase spectroscopic study

Many experimental techniques have been developed for the gas-phase investigation of metal ion-ligand complexes. Thermodynamic measurements[33], collision induced fragmentation studies or unimolecular decay[34], and electronic or vibrational spectroscopy are typical examples that attract the most attention.[35] The ability to generate ionic complexes with sufficient signal strength for quantitative study offers an opportunity to perform spectroscopic measurements.[36] The significance of UV spectroscopic measurements of metal dication-ligand complexes is two-fold. First, there is a need to bench-mark theoretical methods. The involvement of a metal ion in chemistry requires an understanding of electronic energy levels. Second, in the development of spectroscopic markers where the influence an ion has on electronic transitions in a ligand needs to be understood if improvements are to be made in sensitivity and specificity.[37]

1.3.2 Experimental challenges in the spectroscopic investigation of doubly charged species

To date, even with experimental techniques that make it possible to prepare and study complexes containing a wide range of multiply charged metal ions in the gas phase,[35] most of experiments in this nature still concentrate on singly charged ions.[38] In contrast, the most common charge state found for metal ions in nature is +2.[9] There

are very compelling reasons for developing new experiments that are focusing on metal ions in oxidation states that are more characteristic of those found in chemistry and biochemistry. However, some experimental problems still need to be overcome. For instance, the traditional single collision approach does not work for preparation of some multiple charged metal ion-ligand complexes in the gas phase. [33, 39] A collision between a doubly charged metal ion and a ligand molecule could lead immediately to charge transfer from the metal ion to the solvent molecule forming two singly charged species instead of a doubly charged species. The second ionisation energy of a metal is normally much higher than the first ionisation energy of a typical ligand such as water (12.6 eV), pyridine (9.25eV) and benzene (9.2 eV). Therefore, experimental techniques that can generate metal dications which are already encapsulated in a stable solvent environment when they enter the gas phase have to be developed.

1.3.3 Photofragmentation and depletion studies

In general, the spectroscopic measurements follow a common pattern. Ions of a particular m/z ratio are selected and photoexcited with tuneable laser radiation. The absorption of a photon on the part of a complex leads to dissociation and the resultant phtofragmentation signal is monitored as a function of laser wavelength to provide a spectrum. Given that the ion signal strengths of doubly charged species that can be achieved using currently available techniques are far too low (10^7 ions/s, ion current of ~10^{-12} A) for any form of direct absorption spectroscopy, the most effective ways of accessing spectroscopic transitions are probably via either photofragmentation or through monitoring signal depletion.[38] The method of UV photofragmentation spectroscopy has the advantage of sensitivity in that an ion signal can be recorded against zero background, but the signal can also be very weak.[36] Depletion measurements have the advantage that they reflect the sum of all photofragmentation channels, which is the most effective method of measuring an absorption spectrum when there are two or more competing photofragmentation pathways. But they also

have the disadvantage that spectra are derived from the difference of two large numbers. Both approaches have been used successfully.[5c]

1.3.4 Recent advances in the spectroscopic studies of metal dication-ligand complexes

Recently, there are some significant success in recording the electronic spectra from transition metal complexes using both photofragmentation and signal depletion in the gas phase. Posey and co-workers firstly reported electron-transfer spectra that recorded from low-spin iron (II) complexes.[40] The experimental spectra recorded exhibit metal-to-ligand charge transfer (MLCT) electronic transitions at visible wavelengths. Puskar [29a] reported a UV photofragmentation study of doubly charged transition metal complexes $[Cu(pyridine)_n]^{2+}$ and $[Ag(pyridine)_n]^{2+}$, and for the first time presented evidence of ligand-to-metal charge transfer (LMCT) electronic transitions in their spectra. The ligand field spectroscopy at visible wavelengths for the same complexes has also been reported.[29b] Metz and co-workers [41] studied Co(II) and Ni(II) complexes using an ion trap. Signal accumulation within the ion trap is one way to overcome the problem of low ion number density. The photofragement spectroscopy exhibited features very similar to those seen in the aqueous phase. Most recently, Wu and Stewart reported a series of UV photofragment spectroscopy for Zn(II)[42], Mn(II)[43] and doubly charged Group Two metal[10] complexes in the gas phase combined with theoretical calculations. For some of them, it has been possible to resolve individual electronic transitions.

1.4 Quadrupole ion trap (QIT)

Apart from the experimental techniques above, a three-dimensional radio-frequency (RF) quadrupole ion trap (QIT) has been used in this experiment. The QIT can raise the number of ions available for photoexcitation by accumulating and holding the mass-selected ions for a period of time in the presence of a cold helium buffer gas.

The confining capacity arises from the formation of a trapping potential well when appropriate potentials are applied to the electrodes of the ion trap.[44] Capability of bringing down the internal energies of the trapped ions makes the QIT an important development in how well individual electronic states can be resolved. The QIT also offers an equivalent level of sensitivity in that it can be operated in a mode whereby both the precursor and fragments can be monitored simultaneously. Given importance of this device, a general introduction of its history, principle and application will be given in this section.

1.4.1 History and developments of QIT

The QIT has been used as a mass spectrometer or as an ion storage source employed in conjunction with an external mass analyzer for over 50 years.[44] There are enormous amount of development has been made in particular its use for studying the spectroscopy of trapped ions. The milestones in development of the QIT may be divided into three distinct periods, as suggested in Table 1.1.

Table 1.1 Milestones in the development of QIT[45]

Year	Milestone
Mass-selective detection	
1953	First disclosure (Paul and Steinwedel)
1959	Storage of microparticles (Wuerker, Shelton and Langmuir)
1959	Use as a mass spectrometer (Fischer)
1962	Storage of ions for RF spectroscopy (Dehmelt and Major)
Mass-selective storage	
1968	Use as a mass spectrometer (Dawson and Whetten)
1972	Characterization of the trap, chemical ionization (CI), ion kinetics, etc. (Todd et al.)
1976	Collisional focusing of ions (Bonner, March and Durup)
1978	Selective ion reactor (Fulford and March)
1979	Resonant ejection of ions (Armitage, Fulford, Hoa, Hughes, March, Bonner and Wong)
1980	Use as GC detector (Armitage and March)
1982	Multiphoton dissociation of ions (Hughes, March and Young)
Mass-selective Ejection	
1984	Disclosure of ion trap detector(ITD) (Stafford, Kelley, Syka, Reynolds and Todd)

1985	Ion trap mass spectrometer (ITMS) (Kelley, Stafford, Syka, Reynolds, Louris and Todd)
1987	MS/MS, CI, photo dissociation, injection of ions, mass-range extension, etc. Fourier transform quadrupole ion trap (Syka and Fies)
1989	Extension of mass/charge range via resonant ejection (Kaiser, Louris, Amy and Cooks)
1990	High-resolution mode of operation (Schwartz, Syka and Louris)
1994/1998	Linear ion traps (schwartz, Senko, Syka, Hager)

As one can notice in Table 1.1, the first method employed for the detection of ions was based on the principle of mass-selective detection, in which the presence of ions in the trap was recorded through sensing the motion of the ions by means of circuitry connected between the end-cap electrodes. Paul[46], Fischer[47], Rettinghaus[48], Burnham[49], Syka[50] and Cooks[51] have made some leading achievements in this area. Subsequently, mass-selective storage was developed which generally fell into two parallel branches. Firstly, some spectroscopists considered QIT as a device enabling a wide range of gas-phase spectroscopic experiments to be performed with simple atomic and molecular ions.[52] On the other hand, QIT was used as a mass analyzer, based on the realization by Dawson and Whetten[53] that ions could be ejected efficiently from the trap through holes in one of the end-cap electrodes onto the dynode of an electron multiplier or into a channeltron and thus be detected externally, thereby avoiding many of the difficulties associated with mass-selective detection. The idea of detecting ions by ejecting them from the QIT can be considered as a watershed in the development of the device, and within a short space of time various other groups reported further developments and refinements of this method.[54]

1.4.2 Theory of QIT

The basic theory of operation of quadrupole devices was enunciated almost 100 years before the QIT was invented by Paul and Steinwedel.[55] The theory is based on the behaviour of a single ion in an infinite, ideal quadrupole field in the total absence of any background gas. The QIT consists of three shaped electrodes that are shown in open array in Figure 1.1.

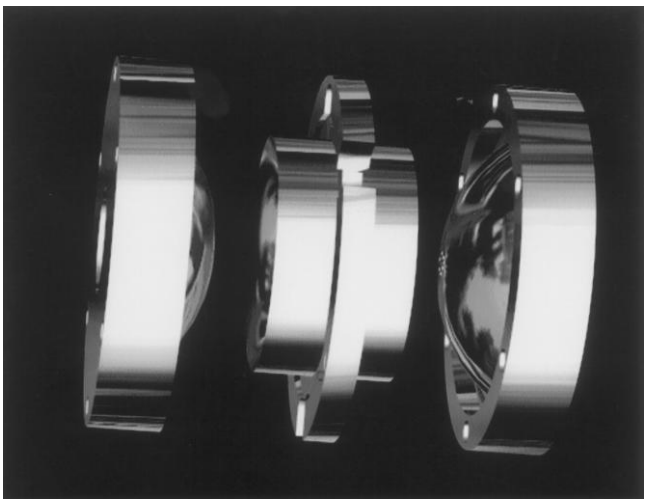

Figure 1.1 Three electrodes of QIT shown in open array.[56]

Two of the three electrodes are virtually identical and, while having hyperbolical geometry, resemble small inverted saucers; these saucers are the so-called end-cap electrodes and each has one or more holes in the center. One end-cap electrode contains the 'entrance' aperture through which electrons and/or ions can be gated periodically while the other is the 'exit' electrode through which ions pass to a detector. The third ring electrode has an internal hyperbolical surface. In a quadrupolar device described with reference to rectangular coordinates, the potential $\Phi_{x,\,y,\,z}$ at any given point within the device can be expressed in its most general form as equation 1.3.

$$\Phi_{x,y,z} = A(\lambda x^2 + \sigma y^2 + \gamma z^2) + C \quad \text{(eq. 1.3)}$$

Where A is a term independent of x, y and z that includes the electric potential applied between the electrodes of opposing polarity, C is a fixed potential applied effectively to all the electrodes so as to 'float' the device. Both of A and C may be an RF potential either alone or in combination with a DC potential. In an electric field, it is essential that the Laplace condition, which is the second differential of the potential at a point, be equal to zero, be satisfied as equation 1.4.

$$\nabla^2\Phi_{x,y,z} = \frac{\partial^2\Phi}{\partial x^2} + \frac{\partial^2\Phi}{\partial y^2} + \frac{\partial^2\Phi}{\partial z^2} = 0$$

$$2\lambda A + 2\sigma A + 2\gamma A = 0 \quad \text{(eq. 1.4)}$$

For the cylindrically symmetric three-dimensional QIT, an infinite number of combinations of λ, σ and γ exist which satisfy the equation above, however, the simplest that have generally been chosen in practice are, λ=σ=1, γ=-2. So the equation 1.3 can be written as

$$\Phi_{x,y,z} = A(x^2 + y^2 - 2z^2) + C \quad \text{(eq. 1.5)}$$

If we consider r_0 as the radius of the ring electrode in the central horizontal plane and $2z_0$ as the separation of the two end-cap electrodes measured along the axis of the ion trap (as Figure 1.2), the equation 1.5 can be convert into cylindrical polar coordinates employing the standard transformations x=rcosθ, y=rsinθ, z=r, as equation 1.6.

$$\Phi_{r,z} = A(r^2 - 2z^2) + C \text{ (eq. 1.6)}$$

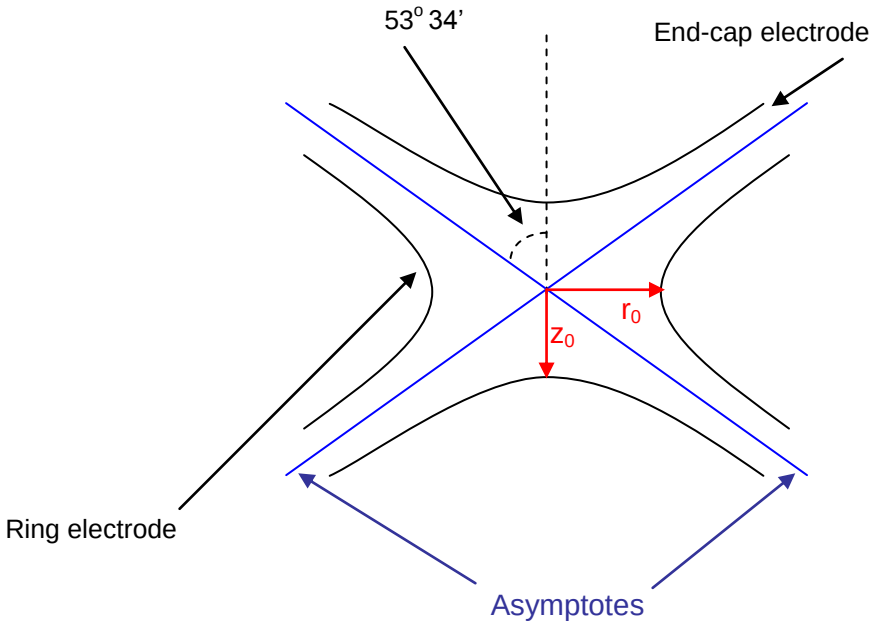

Figure 1.2 Schematic diagrams showing the cross-section of an ion trap showing the dimensions r_0 and z_0.

The quadrupolar potential Φ_0 is defined in terms of the difference between the potentials applied to the ring and the pair of end-cap electrodes,

$$\Phi_{\text{ring}} = A(r_0^2) + C$$

$$\Phi_{\text{endcaps}} = A(-2z_0^2) + C$$

$$\Phi_0 = A(r_0^2 + 2z_0^2)$$

$$A = \frac{\Phi_0}{r_0^2 + 2z_0^2}$$

$$\Phi_{r,z} = \frac{\Phi_0(r^2 - 2z^2)}{r_0^2 + 2z_0^2} + C$$

In the QIT, the end-cap electrodes are normally held at ground potential while RF potential and any DC voltage are applied to the ring electrode only. Thus

$$\Phi_{0,z_0} = \Phi_{\text{endcaps}} = \frac{\Phi_0(0 - 2z_0^2)}{r_0^2 + 2z_0^2} + C = 0$$

$$C = \frac{2\Phi_0 z_0^2}{r_0^2 + 2z_0^2}$$

Hence

$$\Phi_{r,z} = \frac{\Phi_0(r^2 - 2z^2)}{r_0^2 + 2z_0^2} + \frac{2\Phi_0 z_0^2}{r_0^2 + 2z_0^2} \quad \text{(eq. 1.7)}$$

If we define the value of Φ_0 in terms of the real system potentials applied to the ring electrode as $\Phi_0 = (U + V\cos\Omega t)$, then the equation 1.7 can be re-written as

$$\Phi_{r,z} = \frac{(U + V\cos\Omega t)(r^2 - 2z^2)}{r_0^2 + 2z_0^2} + \frac{2(U + V\cos\Omega t)z_0^2}{r_0^2 + 2z_0^2} \quad \text{(eq. 1.8)}$$

As a result of electric field at the point (r, 0), the force acting on an ion at this point, F_z should be

$$F_z = -e\left(\frac{d\Phi}{dz}\right)_r = e\frac{4\Phi_0 z}{r_0^2 + 2z_0^2} = ma = m\left(\frac{d^2z}{dt^2}\right)$$

Therefore from the equation 1.8, we have

$$\frac{d^2z}{dt^2} = \left(\frac{4eU}{m(r_0^2+2z_0^2)} + \frac{4eV\cos\Omega t}{m(r_0^2+2z_0^2)}\right)z \quad \text{(eq. 1.9)}$$

The commonly accepted form of the Mathieu equation is

$$\frac{d^2u}{d\xi^2} + (a_u - 2q_u\cos 2\xi)u = 0$$

Where u is a displacement, ξ is a dimensionless parameter equal to $\Omega t/2$ such that ξ must be a frequency as t is time, and a_u and q_u are additional dimensionless stability parameters which, in the present context of quadrupole devices, are in fact trapping parameters. It can be shown by substituting $\xi = \Omega t/2$ and using operator notation to find

$$\frac{d}{dt} = \frac{d\xi}{dt}\frac{d}{d\xi} = \frac{\Omega}{2}\frac{d}{d\xi}$$

$$\frac{d^2}{dt^2} = \frac{d\xi}{dt}\frac{d}{d\xi}\left(\frac{d}{dt}\right) = \frac{\Omega^2}{4}\frac{d^2}{d\xi^2}$$

$$\frac{d^2u}{dt^2} = \frac{\Omega^2}{4}\frac{d^2u}{d\xi^2}$$

So that using the transformations above, and replacing u by z, we can re-write the equation 1.9 as

$$\left(\frac{4eU}{m(r_0^2+2z_0^2)} + \frac{4eV\cos\Omega t}{m(r_0^2+2z_0^2)}\right)z = -\left(\frac{\Omega^2}{4}a_z - 2\times\frac{\Omega^2}{4}q_z\cos\Omega t\right)z$$

Where one deduces the relationships

$$a_z = -\frac{16eU}{m(r_0^2 + 2z_0^2)\Omega^2}$$

$$q_z = \frac{8eV}{m(r_0^2 + 2z_0^2)\Omega^2}$$

When this derivation is repeated for the radial component of motion at a fixed value of z, one can find out that $a_z = -2a_r$ and $q_z = -2q_r$ arising from the values $\lambda=\sigma=1$, $\gamma=2$ inserted into the equation 1.5 when it is applied to the QIT. Historically, the relationship between the dimensions r_0 and z_0 has been selected as a requirement for forming the ideal quadrupolar potential distribution as follow.[57]

$$r_0^2 = 2z_0^2$$

The stability diagram for QIT is a diagram that demonstrates whether an ion can be stored within the QIT or is ejected from the QIT and either lost or detected externally using trapping parameters. There are two types of solutions to the Mathieu equation which are periodic but unstable and periodic and stable. The former type, which is also called Mathieu functions of integral order, forms the boundaries of unstable regions on the stability diagram. The boundaries correspond to those values of the new trapping parameter β_z that are integers. The boundaries represent, in practical terms, the point at which the trajectory of an ion becomes unbounded. The later type of solutions determines the motion of ions in an ion trap. The stability regions corresponding to stable solutions of the Mathieu equation in the z and r direction are shaded in Figure 1.3(a) and Figure 1.3(b), respectively.

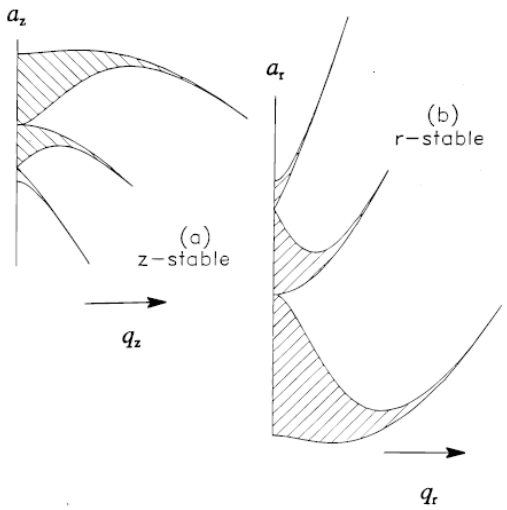

Figure 1.3 Graphical representation of three Mathieu stability regions: (a) z stable, (b) r stable. [44]

Ions can be stored in the QIT provided that their trajectories are stable in the r and z directions simultaneously. Region A and B in Figure 1.4 are referred to as stability regions. Region A is of the greatest importance at this time and is shown in greater

detail in Figure 1.4. In Figure 1.5, the β_z=1 stability boundary intersects with the q_z axis at q_z=0.908. This point is that of the ion of lowest mass/charge ratio (low-mass cutoff, LMCO) that can be stored in the ion trap for given values of r_0, z_0, V and Ω.

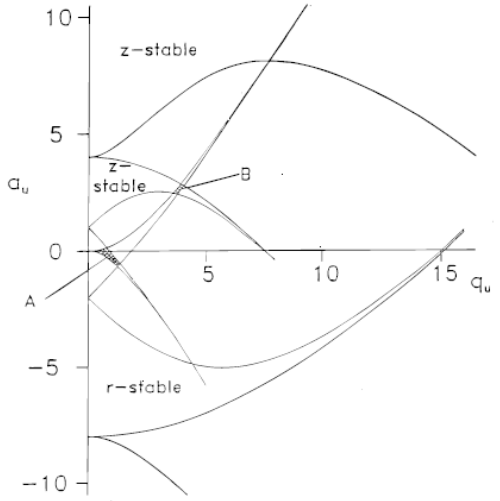

Figure 1.4 Mathieu stability diagram in (a_z, q_z) space for QIT in both r and z directions. While the axes are labelled a_u and q_u, the diagrammatic representation shown here shows the ordinate and abscissa scales in units of a_z and q_z, respectively.[44]

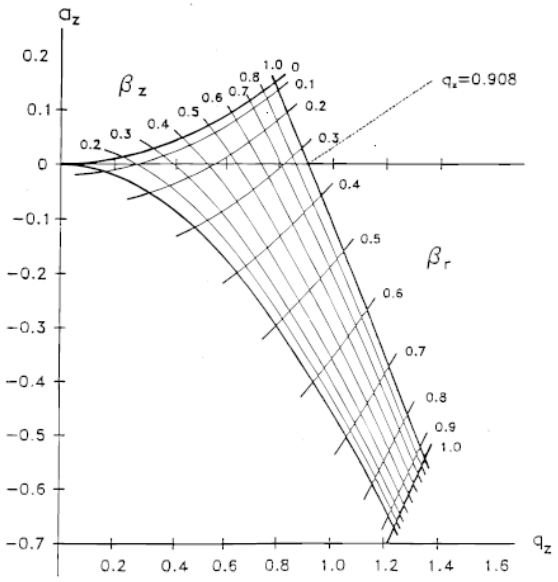

Figure 1.5 Stability diagram in (a_z, q_z) space for region A. [44]

A three dimensional representation of an ion trajectory in the QIT is shown in Figure 1.6. The trajectory has general appearance of a Lissajous curve.[58]

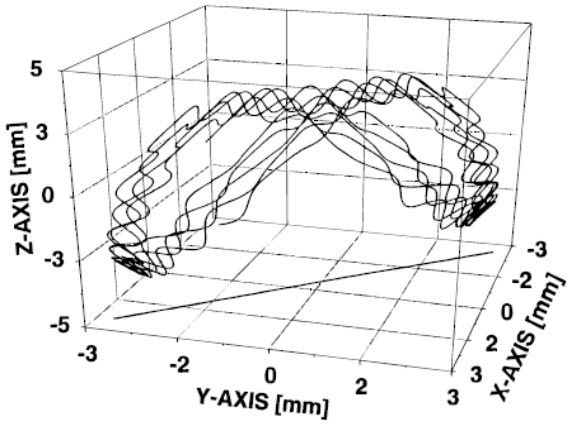

Figure 1.6 trajectory of a trapped ion of m/z 105. [58]

The sensitivity of QIT mass spectrometer is determined directly by the fraction of the ions formed from a given quantity of sample and which, after analysis, reaches the detector. A corresponding parameter is the rate of ion loss during the period between creation and detection. Ion loss may occur though a number of different processes. Firstly, the ions can be lost while they are formed in unstable trajectories which include two types. One is intrinsically unstable trajectories which are unbounded outside the stability boundary; the other is quasi-unstable trajectories which are theoretically capable of being trapped, however the limit of excursion of the ion exceeds the internal dimension of the device. Secondly, the occurrence of ion/neutral molecule collisions and ion/ion interaction processes may lead to the charged species developing unstable orbits such as damping, elastic scattering, inelastic scattering, charge transfer and ion/molecule reactions. Thirdly, nonlinear resonances could cause ion loss because of deliberate or unintentional imperfections in the quadrupole field. Last, self-emptying, which is very difficult to characterize, could be another reason leading to ion loss. For the QIT mass spectrometer used for the work contained in this

thesis, some previous research about trapping efficiency has been conducted.[59] The quantitative analysis of operating parameters which influence trapping process within the experiment such as ion current, accumulating time, multiplier gain, amount of buffer gas and effects of water residue were used to certify that this QIT mass spectrometer had ability to yield quantitative photodissociation signals.

1.5 Structural information yielded by UV photofragmentation spectroscopy of metal dication-ligand complexes

Investigation of the electronic spectroscopy of doubly charged metal ion-ligand complexes in the gas phase could reveal structural information on these complexes without the influence from the solvent environment usually associated with condensed phase studies. To understand these structural information, there are two theoretical approximations need to be mentioned, crystal field (CF) and ligand field (LF) theories.

1.5.1 Ligand field theory

The basic notion of a ligand field was first developed by Bethe in 1929.[60] In more general model of a metal ion-ligand complex, the electrons of the central ion are subject to a potential, not necessarily of simple electrostatic origin, from the ligand atoms. The term ligand field theory has been employed to cover all aspects of the manner in which an ion or atom is influenced by its nearest neighbours. Physical properties which reflect changes in ligand environment can be sorted to three categories, thermodynamic, spectral and magnetic properties. Spectral properties of metal ion-ligand systems which include electronic transitions between ground states and excited states can be manifested by recording the UV spectra. Spectra of coordination compounds can be classified into two bands, ligand field (LF) band and charge transfer (CT) band. LF spectra are concerned with transitions between different types of d orbitals resulting from the application of ligand field. CT spectra are focusing on transitions between levels which correspond to different electron

distributions amongst the metal and the ligand atoms in the ground and the excited states, such as charge transfer from central metal ion to the ligand (MLCT) or vice versa. In ligand field theory, it is difficult to distinguish sharply between LF and CT spectra, however, the mixing of ligand and central ion orbitals in LFT do provide a facile mechanism for transitions of charge transfer type. Most of the results of LFT depend only on the approximate symmetry of the ligand distribution around the central metal ion such as octahedral, tetrahedral, rather than on the details of their locations.

1.5.2 Crystal field theory

The electrostatic crystal field theory is approached from the point of view of electron configurations in a complex ion and saw that it was the same as a theory in which a metal ion is placed in an electrostatic field due to its ligands, the latter being assumed fixed and unpolarizable.[61] The potential developed near an ion which was part of a lattice, and that such a lattice could occur only in a crystal, led to the term crystal field theory being coined to cover the subject.[62] This theory assumes that the properties of metal-ligand complexes can be calculated satisfactorily by supposing it to be an aggregate of non-interacting metal ions arranged in an unpolarizable and perfectly insulating medium. Ligand field theory, then, contains crystal field theory as a special case.[62]

Practically, the electrons of the bonding shell of metal ion and ligand atoms cannot be entirely associated either with metal ion or with ligand nuclei. If electrons of a free ion remain completely attached to that ion while a set of ligand atoms are brought up to the equilibrium distance, one has obviously the CFT model. On the other hand, electrons of free ion mix with electrons of ligand atoms during the assembly, which gives the whole system a completely covalent account of the bonding. Both of the two possibilities above are special cases of the molecular orbital treatment. However,

by means of this treatment, all intermediate degrees of electron sharing can be described. CFT model is for the extreme in which there is no mixing of central metal ion and ligand electrons, and LFT is for all non-zero degrees of mixing.

1.5.3 Charge transfer electronic transitions

The assignment of the UV spectra can be simplified by sorting electronic transitions into classes according to localization of the shift in charge density. If the metal complex can be simply considered as a single metal center surrounding by a shell of multiple ligands, the localization of charge density shifting during certain electronic transitions can only have following four possibilities.

1.5.3.1 Ligand to metal charge transfer transitions

A ligand to metal charge transfer (LMCT) transition is an electronic transition in a metal complex that corresponds to excitation populating an electronic state in which considerable electron transfer from a ligand to a metal centre has occurred. The metal charge is expected to be reduced in this case and the charge difference between metal and ligand will decrease. An example of ligand to metal charge transfer transition in an octahedral complex is detailed in Figure 1.7.

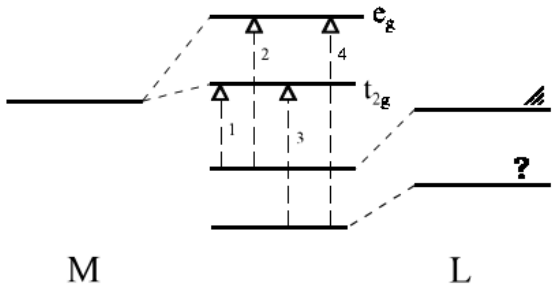

Figure 1.7 Ligand to metal charge transfer in an octahedral complex

Mason[63] reported an electronic absorption and magnetic circular dichroism (MCD) spectra of a series of Au halide complexes in acetonitrile solution. A numbers of

intense bands in the vis-UV region that are assigned to LMCT from occupied halide-based orbitals to the lowest energy σ* orbital, which is primarily $5d_{x^2-y^2}$ localized on gold can be found in the spectra. A detailed model for LMCT in planar complexes of D_{4h} and D_{2h} symmetries was also presented for the first time. The LMCT absorption bands in the red/near-IR region of Ru(III) and Os(III) bpy complexes had been recorded by Kalyanasundaram.[64] The intensity of the LMCT band increases with increasing effective donor strength of the substituted bpy ligand. The LMCT transitions in $[Cu(pyridine)_n]^{2+}$ and $[Ag(pyridine)_n]^{2+}$ are identified in previous research by our group.[29a] The excitation energy of LMCT transitions are not only dependent on geometry of the complex[65] but also on the metal centre itself. For example, the excitation energies for triggering the LMCT transitions in metal ion-ligand complexes that bear the same ligand decrease while the oxidizing power of metal is increasing.[66]

1.5.3.2 Metal to ligand charge transfer transitions

A metal to ligand charge transfer (MLCT) transition is an electronic transition of a metal-complex in which considerable electron transfer from the metal to a ligand has occurred. Consequently, what is expected to happen here is that the ligand is reduced by possessing a low lying empty orbital, such as the π* orbital in pyridine and benzene, while the metal is oxidized and generates more easily oxidized metal ions, for example Pb^{2+}.[9] Posey [12b, 67] firstly reported the spectra of $[Fe(bpy)_3]^{2+}$ and $[Fe(terpy)_2]^{2+}$, which exhibit a MLCT transition at visible wavelengths. By the aid of the electrospray technique, the evolution of spectral features can be studied as a function of numbers of solvent molecules.

1.5.3.3 Intervalence (metal centered) transitions

The metal centred transitions normally occur between metal atom orbitals such as d-s and d-d transitions. If d-d transitions happen within the ligand field, they should be

assigned to LF transitions. It also needs to be noted that the d orbital related transitions do not only depend on ligand shell, but also have a strong relationship with metal ligand bonding.[68] In principle, for a centre symmetric species, the LF in form of d-d transitions are forbidden according to Laporte selection rule ($\Delta l \neq 0$)[9, 69], which means that in the absence of contributing factors, such as intensity stealing or vibronic coupling[9], it can be expected that extinction coefficients associated with ligand field transitions will be three or four orders of magnitude lower than those typically seen in other areas of gas phase ion spectroscopy. However, when the inversion centre of the complex is removed by some interactions such as losing a ligand molecule by photofragmenting, the forbidden transition will be observable. Vibronic coupling may also cause distortion leading to unsymmetrical configuration that may allow the forbidden transition to occur. The resultant degeneracy of d orbitals depends on both the symmetry and the strength of the ligand field. Thus, structural information of metal ions in different ligand environments and influence of ligands on the electronic structure of the transition metal itself can be investigated by probing the d-d transitions.

1.5.3.4 Intraligand (Ligand-ligand) charge transfer transitions

Ligand-ligand charge transfer transitions are electronic transitions involving ligand molecules themselves such as n-π* or π-π* transitions. They depend on the perturbation of the molecular orbital which are usually presented in the spectra of their complexes. Coordination of an organic ligand to a metal centre can result in large perturbations of its electronic structure, especially for those states directly involved in bonding. Compared with the spectra of pure ligand molecule, the ligand-ligand charge transfer transitions can be easily assigned because the metal centre usually does not have significant involvement. Many organic molecules have well-known n-π* or π- π* transitions in the UV region. Both benzene and toluene have π-

π* transitions around 260 nm, while the pyridine n-π* transition occurs at ~287 nm and a higher energy π- π* transition occurs at ~260 nm in the gas phase. [70]

1.6 Overview of chapters

Besides the background theory and principles that have been elucidated in this chapter, the second chapter will detail the experimental apparatus and techniques, and summarize the conditions such as temperature in the oven and pressure of carrying gas for all of the experiments in this thesis. Chapter three introduces background of the theory that has been applied to perform the calculations. The UV photofragmentation spectroscopy of $[Pb(benzene)_2]^{2+}$, $[Pb(toluene)_2]^{2+}$, $[Cu(benzene)_2]^{2+}$ and $[Ca(benzene)_2]^{2+}$, which are followed by the DFT/TDDFT calculations are reported in Chapter four to seven, respectively. Finally, chapter eight presents overall conclusions and perspective for the future research.

Chapter 2 Experimental section

The experiment apparatus was constructed by Stace and Wu by 2006.[71] Generally, it can be divided into two systems, a laser system and a cluster ion investigation system. Target ions are produced, trapped and investigated by the combination of these two systems. The laser system consists of a Nd:YAD laser (Surelite, Contimuum) and a pulsed tuneable dye laser (Sirah Cobra Stretch). The ion investigation system is constructed from three main sections, cluster formation section, pick-up section and ion trap mass spectrometer section. For data processing, the main experimental apparatus is followed by a data recording section which is composed of two channeltron detectors, an analogue amplifier, a Lecroy LT347M oscilloscope, a Leroy 9310 digital oscilloscope and a computer programme designed by Labview 7 software package (National Instruments) to collect the experimental data. Final UV spectra are generated by Origin. To design this apparatus which can produce and hold the selected ions for around 1 second, experimental techniques such as high vacuum technique, pick-up technique, supersonic expansion, electron impact ionization and photofragmentation mass spectrometry are involved. This chapter gives a general introduction to the experimental apparatus.

2.1 Cluster Formation

Clusters are generated by a gas mixture of carrier gas (Argon) and the ligands undergoing supersonic expansion in the collimation chamber (Figure 2.1). The carrier gas is passed through a reservoir where desired solvents (benzene, toluene) are held (The benzene and toluene need to be cooled by ice due to their vaporization pressure). The seeded gas was fed into a stagnation vessel suspended by a stainless steel rod within a source chamber. Supersonic expansion of the mixture occurred though a nozzle with 50 μm diameter sitting on the front plate of the stagnation vessel. The centre of the resultant molecular beam passed about two centimetres into the

collimation chamber through the orifice of a fluted nickel skimmer with 1 mm diameter. Although the skimmer was locked on the bulkhead, alignment of the molecular beam with the skimmer was possible due to a manipulator on the stagnation vessel mount, allowing control over the nozzle position within the chamber. The expansion chamber and collimation chambers were pumped by a 8000 L/s diffusion pump backed by a mechanical booster plus a 40 L/s rotary pump and a 2000 L/s diffusion pump backed by a 80 L/s rotary pump, respectively. The pressure within the chambers was monitored by a combination of pirani and penning gauges. The operating pressure is around 10^{-4} mbar in expansion chamber, and 10^{-6} mbar for collimation chamber. The high vacuum in both chambers can reduce scattering of the molecular beam before it is transferred into the pick-up chamber.

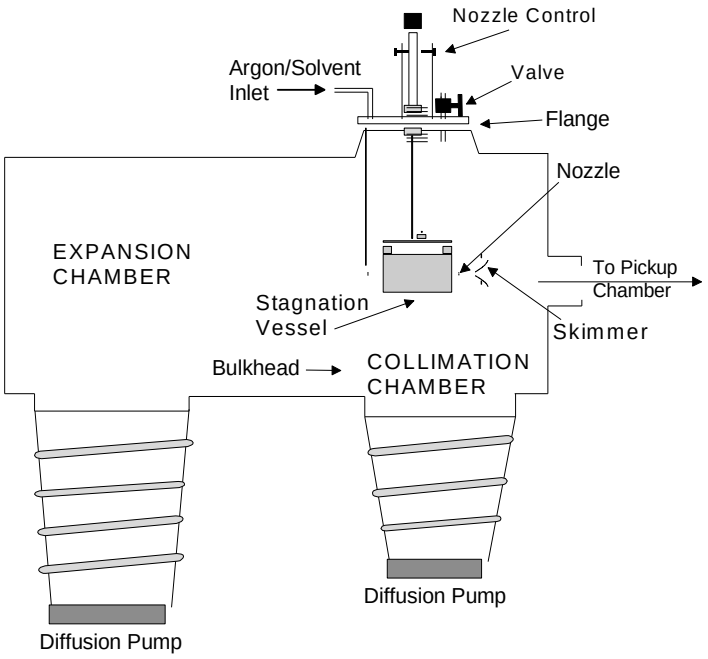

Figure 2.1 Schematic of Cluster Generation Chamber.

2.2 Pick-up Process

The argon/ligand cluster beam passed through an oven chamber containing metal vapour at a partial pressure of 10^{-2} – 10^{-1} mbar, which was generated by a Knudsen effusion cell. From Figure 2.2, it can be noticed that the neutral metal-ligand

complexes were produced from the collision of mixed argon/ligand clusters and metal atoms (Pb, Cu, Ca) in the oven chamber, and the vaporization of argon atoms to stabilize the neutral metal-ligand complex, whereby a pick-up process. The excess amount of argon, ligand and metal vapour were pumped away by two rotary pump backed turbo-molecular pumps to minimize the scattering of the molecular beam. The operating pressure in the oven chamber was kept in the region of 10^{-6} mbar. The pick-up technique is applicable to almost all of the metals capable of generating sufficient vapour pressure at temperatures below 1800 ^{o}C. Using the pick-up technique, we have generated multiply charged complexes from a wide range of metals, including Cu[5c], Ag[27b, 72], Mn[5b, 30a, 43], Zn[31, 42], Pb[5a, 5e, 73], Al[5f] and the alkaline earth metals Mg , Ca and Sr[10].

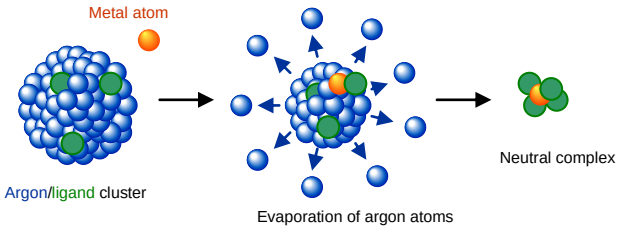

Figure 2.2 the pick-up process

In this thesis, the metal elements Pb, Cu and Ca were investigated. The desired metal pieces were held in a pyrolitic boron nitride (PBN) crucible, which was sitting in the Knudsen effusion cell and heated to an appropriate temperature. Although signal intensity increased while the heating temperature was increasing, the metal would become more consumable and possibly could not survive a period of reasonable experimenting time. Plus, an extremely high temperature could produce unnecessary metal vapour load to scatter the molecular beam, resulting to a reduction of signal intensity. Therefore, achieving a balance between getting acceptable signal strength for mass spectra generation and lifetime of the metal is desirable. The temperatures

used and ion signal strengths obtained for all of the experiments are summarized in Table 2.1.

Table 2.1 Experimental temperature of desired metal element

Metal element	Temperatures(^{o}C)	Vapour pressure(mbar) [a]	Signal intensity [b]
Lead	890	2×10^{-1}	~500PA at 207 amu
Copper	1350	5.32×10^{-2}	~6000 PA at 63 amu
Calcium	600	1.33×10^{-2}	~8000PA at 40 amu

[a] reading of vapour pressure of desired metal is taken from an online database[74]

[b] 120 psi argon was used as carrying gas to investigate the signal intensity in the spectra scan.

2.3 Electron impact (EI) ionizer and quadrupole deflector

For the purpose of mass selecting and ion trapping, the neutral complexes need to be ionized beforehand. In this experiment, a molecular beam ionizer (ABB Extrel, Pittsburgh, PA, USA) is applied to achieve this target. In the EI ion source, electrons are produced through thermionic emission by heating a wire filament that has electric current running through it. The electrons generated are accelerated to 100 eV and then concentrated into a beam by being attracted to an anode. The cluster beam which contains the neutral metal-ligand complex is introduced to the ion source in a perpendicular direction to the electron beam. Collisions between electrons and neutral complexes result in the ionization of the sample. Under these conditions, a quasi-plasma is produced in the ionization region and ion space charge appears to dominate over electron space charge, with the former playing a major role in determining extraction efficiency and final ion signal intensity. A schematic diagram of our electron impact ionizer is shown in Figure 2.3.

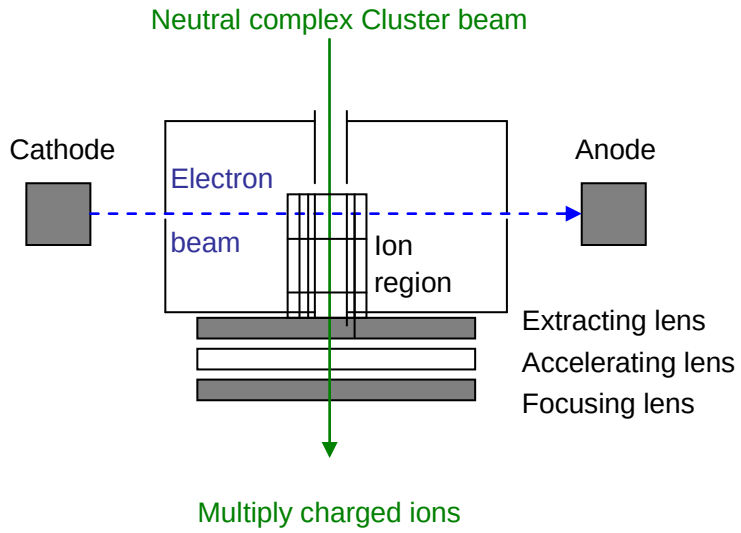

Figure 2.3 A schematic diagram of an electron impact ioniser.

The EI ionization is often followed by fragmentation which is dependent upon many qualities, such as primary structure, electron energy and ion source temperature. The ionization efficiency is highly affected by the electron impact energy. By reducing the EI energy, one can expect to reduce the amount of fragmentation and observe molecular peaks in low eV spectra; however, the total number density of ions formed is not sufficient to generate a mass spectrum with a good resolution. In this case, the density of doubly charged ions is always a challenge, so the electron impact energy needs to be balanced between the total ion number density and mass resolution of spectra. With the correct ion source conditions, it is observed that singly- and doubly-charged complexes can have similar ion signal intensities.

A quadrupole deflector is a device that can separate ions with pre-set kinetic energy from other species such as photons, metastable species, particulates and molecular beam gases which were not ionized. It can be used as system design component, energy filter and noise reduction device. In this experiment, the quadrupole deflector is used as a way to introduce the molecular beam into the quadrupole mass filter and

quadrupole ion guide. The deflector consists of four electrodes through which the ion beam passes, as shown in Figure 2.4. A positive voltage is applied to one pair of opposite electrodes, and a negative voltage is applied to the other pair. In this way, only the ions with desired mass/charge ratios are bent by 90^{o}, and therefore only this group of ions are allowed through. The EI ionizer is mounted directly onto the first quadrupole deflector, where the voltages that each part needs to be applied are as follow: Ion region, negative voltage, -0.1 to -20 V DC; Inner Poles, negative voltage, -50 to -250 V DC; Outer Poles, positive voltage, 5 to 100 V DC. All of these voltages are provided by an Extrel 150-QC quadruple Power Supply module and can be optimized by tuning the related parameters in a Merlin Automation tune file.

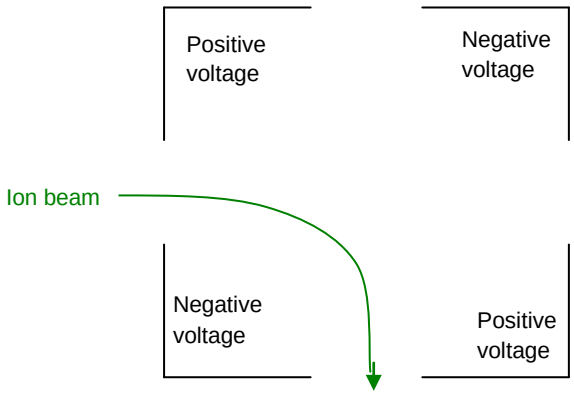

Figure 2.4 A schematic diagram of the cross-section of a quadrupole energy deflector.

2.4 Quadrupole mass filter (QMF) and beam focusing

After ionization, the ion beam is bent into a QMF by the first quadrupole deflector. A QMF is used to prevent all ions except those with a specific mass/charge ratio from passing through. A linear QMF ideally consists of four parallel rods which are shown in Figure 2.5. The pre- and post-filters and Entrance/Exit lenses for focusing of the ion beam can be also found in the diagram.

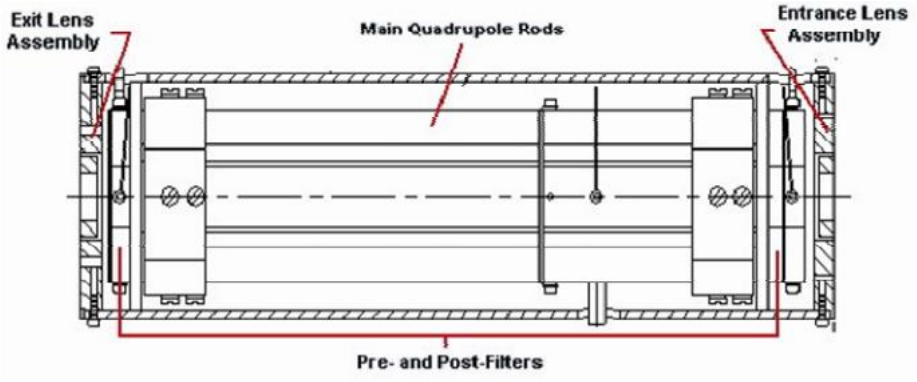

Figure 2.5 Tri-filter quadrupole mass filter details

The basic theory of operation of the QMF was developed by Paul and Steinwedel.[75]

In practice, $\Phi_0 = 2(U + V\cos\Omega t)$, where V is the zero-to-peak amplitude of a RF potential oscillating with angular frequency Ω and +U is a DC voltage applied to the x pair of electrodes while a DC voltage of -U volts is applied to the y pair of electrodes, therefore,

$$\frac{d^2x}{dt^2} = -\left(\frac{2eU}{mr_0^2} + \frac{2eV\cos\Omega t}{mr_0^2}\right)x \quad (2.1)$$

It has been generally acknowledged that the commonly accepted form of the Mathieu Equation is

$$\frac{d^2u}{d\xi^2} + (a_u - 2q_u\cos 2\xi)u = 0$$

Where u is a displacement, ξ is a dimensionless parameter equal to Ωt/2 such that ξ must be a frequency as t is time, and a_u and q_u are additional dimensionless stability parameters which, in the present context of quadrupole devices, are in fact 'trapping' parameters. The Mathieu equation can be written by substituting ξ= Ωt/2 in form of

$$\frac{d^2u}{dt^2} = -\left(\frac{\Omega^2}{4}a_u - 2\times\frac{\Omega^2}{4}q_u\cos\Omega t\right)u \quad (2.2)$$

If we compare the left hand sides of equation 2.1 and 2.2, recalling that u represents the displacement x, to obtain

$$-\left(\frac{2eU}{mr_0^2}+\frac{2eV\cos\Omega t}{mr_0^2}\right)x=-\left(\frac{\Omega^2}{4}a_u-2\times\frac{\Omega^2}{4}q_u\cos\Omega\mathrm{t}\right)x$$

$$a_x=\frac{8eU}{mr_0^2\Omega^2}$$

$$q_x=\frac{-4eV}{mr_0^2\Omega^2}$$

From a solution of the Mathieu equation, it can be found that a_u and q_u are functions of mass/charge ratio and the magnitude of either the DC voltage or the RF voltage applied to the QMS. Therefore the ion trajectory stability in a quadrupole electric field can be defined. A diagram that represents ion trajectory stability regions can be constructed by the overlap regions of x and y stable boundaries, which is detailed in Figure 2.6. In this figure, if we focus on the stability region that been enlarged, one can notice that only the upper part of the diagram is shaded because the stability region is symmetric about the q_u axis. For an ion to have a stable trajectory in a quadrupole rod array, its coordinates in both x and y directions must lie within the diamond-shaped region shown in Figure 2.6.

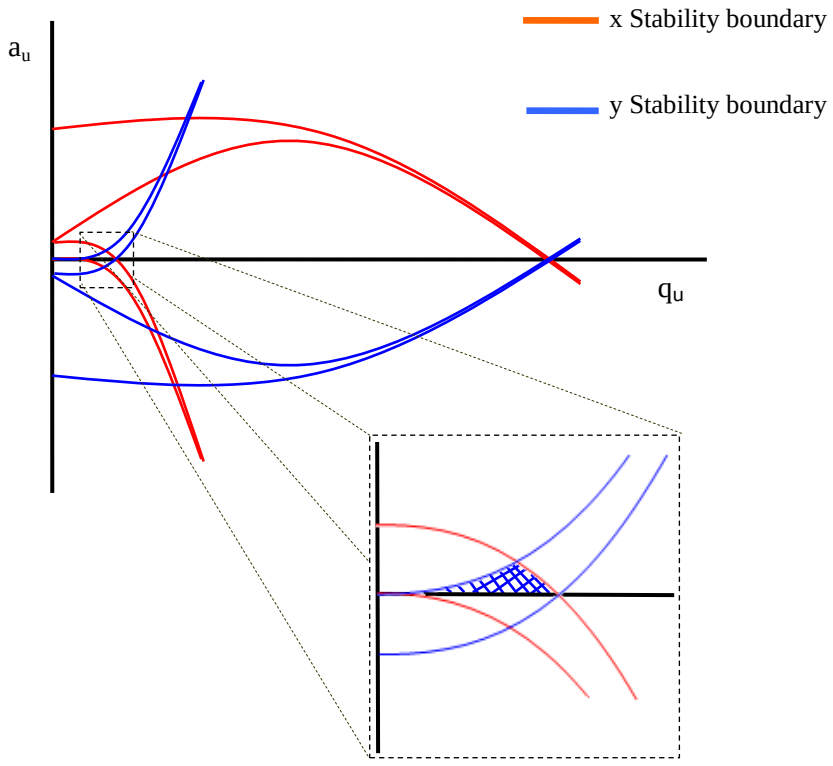

Figure 2.6 Drawing of Stability Boundaries for x and y Axes Emphasising First Stable Region.

Alternately, the upper part of the stability diagram shown in Figure 2.6 can be displayed in U, V space as shown in Figure 2.7. In the U, V space, a stability diagram for ions with mass/charge ratio m1, m2 and m3 are shown in this figure, where m1<m2<m3 in mass/charge ratio. The straight angle line in Figure 2.7 is a scan line. When U and V are increased at a constant ratio, the scan line passes close to the apex for each ion in order of increasing mass/charge ratio. In practice, relatively few ions will be transmitted when the scan line is close to the apex but the mass resolution will be high in that few. As the slope of the scan line is reduced, ion signal intensity increases but at the sacrifice of mass resolution.

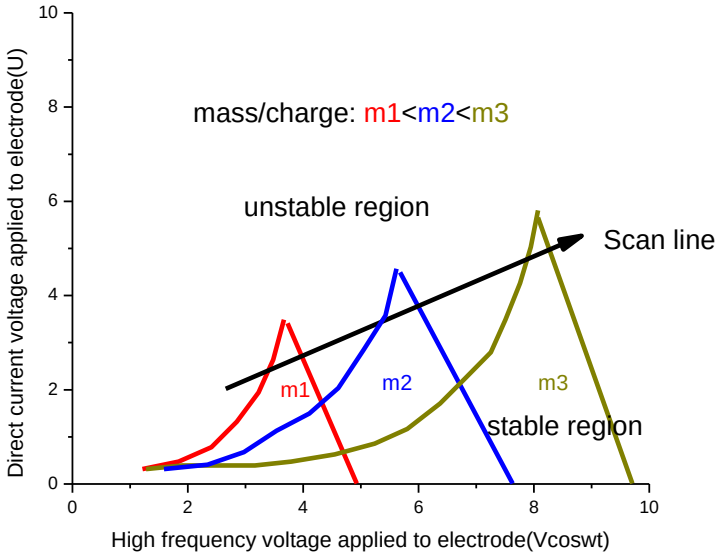

Figure 2.7 Stable region for ions displayed in U, V space

A QMS can be operated either in the spectra scanning mode, or in the secondary ion monitoring (SIM) mode. In the spectra scanning mode, the voltages are swept at a constant DC/RF ratio, whereby the mass/charge ratios of ions that have stable trajectories are changed uniformly, and a mass spectrum of the sample can be obtained. In the SIM mode, the voltages are set to constant values so that only ions of a pre-selected mass/charge ratio can pass through. In this way, the quadrupole acts as a filter.

Potentials on the various electrodes were set and regularly tuned using the Merlin software package to provide optimal ion signal, which could be measured by connecting the ion trap's channeltron detector to the Extrel controls. The mass spectrometer was also used to scan through the mass spectrum immediately before an experiment, accomplished by sweeping the U and V potentials at a constant ratio with time, to find the exact position of the metal complex peak on a mass scan.

Subsequently, the mass selected ions will be bent 90 degree towards a quadrupole ion guide by a second quadrupole deflector, which is mounted on the other end of the

quadrupole filter. The vacuum flange from the opposite direction provides the mounting structure for the multiplier system and contains the electrical feedthroughs necessary to power the detecting device. There is a second channeltron ion detector facing to the direction that the ion beam is travelling. This detector can detect the mass selected ion when the second quadrupole deflector sets to bend the ion beam towards it. This ion detector is very useful when the alignment of the quadrupole mass filter, ion source and the two-quadrupole deflectors need to be adjusted. More details about the principle of this detector are provided in data recording section. The quadrupole ion guide shares the same design as the quadrupole mass filter except the DC voltage is missing for this device. Einzel lens stacks for focusing and collimating ions and Entrance/Exit lenses providing a Pole Bias voltage are also associated with this quadrupole device. The voltages applied on the lenses are provided by an Extrel 150-QC power supply and controlled by the related parameters in Merlin tune file.

2.5 Quadrupole ion trap (QIT)

Next, the mass-selected metal dication-ligand complexes are ejected into a liquid nitrogen cooled, helium buffered Quadrupole Ion Trap (QIT, Finnigan ITMS system, San Jose, CA, USA). In this experiment, the QIT is used as both an ion storage device and a mass spectrometer. Ions are trapped for 1.2 seconds and exposed to seven pulses of UV laser radiation, then ejected effectively towards a channeltron detector by ramping up the RF voltage on the ring electrode. Heavy ions with large mass charge ratios possess a lower value for q_z than light ions. Ramping up the RF voltage V increases the value of q_z, ejecting lighter ions first and then heavier ions as their q_z values pass above the threshold for a stable trajectory in the z dimension (q_{eject}), and so the ions leave through holes in the end cap electrodes. Combining this action with a detector allows the ion trap to function as a mass spectrometer.

The quadrupole chamber was kept at ~2×10^{-8} mbar by a 18L rotary pump (Edwards, England) backed diffusion pump ('Diffstak' 160/700, Edwards, England) and two 12L rotary pump backed turbo molecular pumps (TURBOVAC 361, Oerlikon Leybold Vacuum, Germany). There was a reservoir holding 2.5 litres of liquid nitrogen sitting on the top of the chamber. The reservoir is connecting to a copper cooling jacket surrounding the second end cap electrode of the QIT with two sealed stainless steel pipes. Liquid nitrogen can flow into the sealed reservoir-cooling jacket system and is refilled once every 1 hour to keep the ion trap cold (approximately 150K) during the trapping process. The QIT was composed of three electrodes which are two end cap electrodes sandwiching one ring electrode. There was a 5 mm radius hole straight through both sides of ring electrode so to allow the laser beam come through. A photograph of the QIT section is given in Figure 2.8.

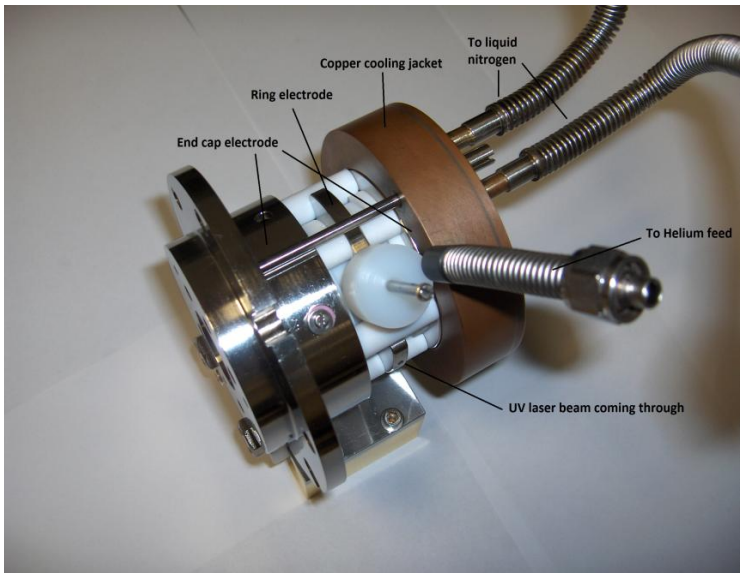

Figure 2.8 Photograph of QIT section including cooling jacket, stainless steel pipes to helium cylinder and liquid nitrogen reservoir

The potentials applied to the end-cap electrodes are grounded, and an oscillating RF potential of about 1.1 MHz is applied to the ring electrode. This results in a quadrupole field or saddle-shaped potential energy surface within the trap, which is constantly flipping as the sign of the voltage changes. The result of this is that an ion

in the trap is contained in a pseudo potential energy well, and continuously orbits the centre of the trap. This can be considered by representing an ion in the trap as a ball on the potential energy surface, as shown in Figure 2.9. At the maximum positive ring electrode potential, the ion is focussed radically (pushed away from the ring electrode) but defocused axially (pulled towards the end-cap electrodes). At the maximum negative potential, the opposite is true. Therefore the ball is always rolling downhill, but confined within a small volume. There is a high frequency wobble superimposed on the figure-of-eight due to undulations of the potential energy surface.[44] However, seeing as the entire width of this orbit in the ion trap is likely to be less than 1 mm, the ions will always be within a small area at the centre of the trap, and so the exact trajectories of the ions are not important.

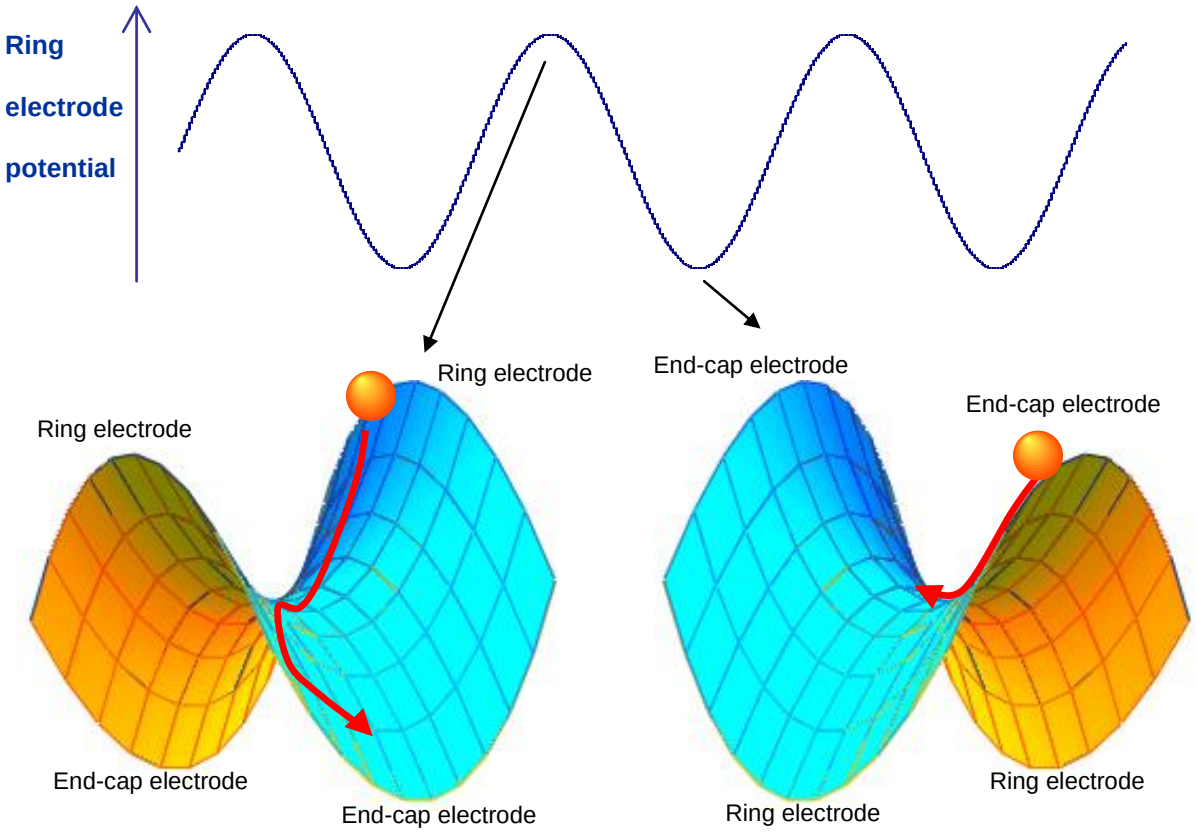

Focussed radically, defocused axially

Defocused radically, focussed axially

Figure 2.9 Representation of an ion (shown as a ball) on the potential energy surface within the ion trap as the voltage between the ring electrode and end-cap electrodes oscillates.

The ion trap are operated typically at 10^{-6} mbar, using high purity helium as a buffer gas, which can improve sensitivity and mass resolution by quenching the kinetic energy of ions and directing their movement to the center of the ion trap. The second benefit of buffer gas is that the helium atoms become cold due to collisions with the liquid nitrogen cooled walls of the end cap electrodes, and these atoms can remove heat from the relatively hot ions. This process of collision cooling brings down the internal energy of the ions and reduces its effect on spectral resolution.

2.6 Detection

Electronics for quadrupole ion trap are controlled by an ITMS software package installed on an Intel 486 computer. Timings for the gate electrodes that allow the molecular beam to access the trap and the optical shutter that opens to allow the laser beam into the trap are controlled by a DG535 pulse generator, which is triggered by an external TTL pulse from ITMS. The whole scan function was set up to work over a 1200 ms cycle during which ions were collected, exposed to laser radiation, and ejected for detection. Throughout the cycle the ion trap's end cap electrodes are at ground potential. During the collection of ions, the gate electrodes were held grounded for 300 ms to allow ions into the trap. They were then closed for the rest of the cycle by application of 900 ms, 50V potential. After collection, the RF current on ring electrodes was ramped for 50 ms to expel ions with a low mass/charge ratio and then dropped back to storage levels for 700 ms, during which time the optical shutter was opened and seven pulses of laser radiation allowed to enter the trap. After the laser irradiation, the RF potential was ramped for 150 ms again to expel all ions including the precursor ions and any photo fragmentations from the trap to the channeltron detector. The resultant timing schedule is detailed in Figure 2.10.

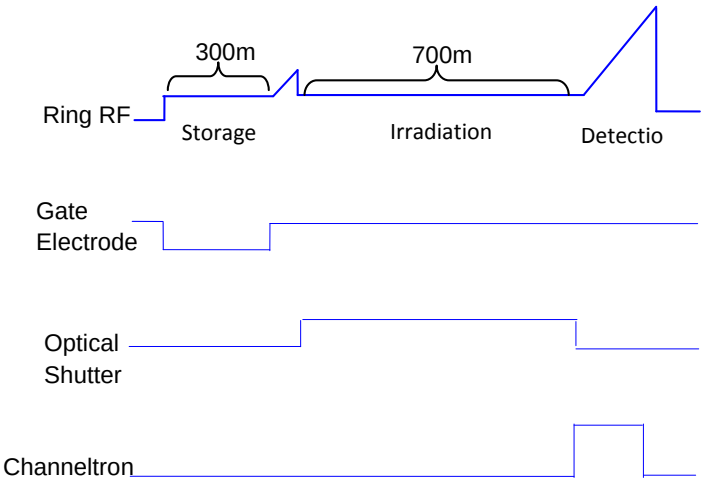

Figure 2.10 Timings during the 1200ms trapping cycle, showing variation in RF magnitude, and the activation of the gate, shutter and detector over that period.

The detection of fragments in this experiment was made by a channel electron multiplier located downstream from the exit of the end cap electrode (Figure 2.11).

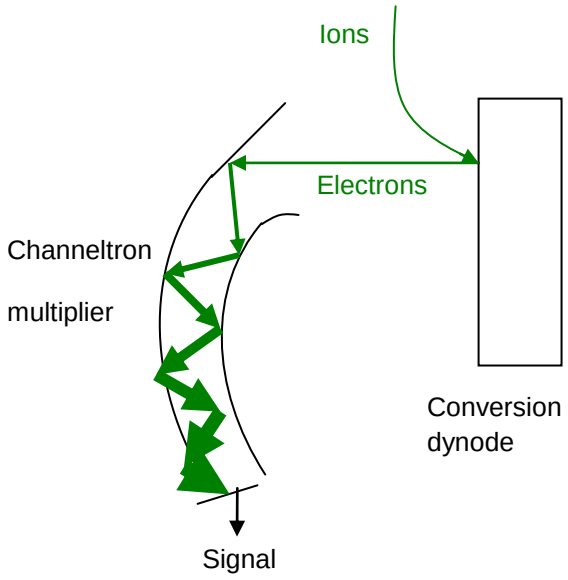

Figure 2.11 Diagram of a conversion dynode multiplier.

An electron multiplier consists of a dynode, which when struck by an ion, photon or electron of sufficient energy, emits secondary electrons. An applied voltage attracts

these secondary electrons towards the next stage of the device, which can be either a second dynode or a different area of the same dynode. As they strike this area, more electrons are emitted. This process continues, and is known as an avalanche effect.[76] Each stage is held at a more positive voltage than the previous stage, so that electrons from each stage are attracted to the next. In this way one electron striking the input results in the production of a pulse of a large number of electrons at the output.[77]

A Channeltron multiplier does not have separate dynodes, but instead consists of a hollow tube, the interior of which is the surface that emits secondary electrons. The tube is slightly curved, so that an electron emitted at one point along the tube will have a low probability of reaching the exit without striking the interior again. The curvature also prevents ionic feedback, which occurs when a secondary ion emitted near the end of the tube passes backwards through the tube, striking the surface at the beginning as if it is a new ion.

The channel multiplier itself was preceded by a conversion dynode, which is applied a -4.7 kV potential so that the ejected ions are accelerated towards it. When an ion impacts with the surface of the conversion dynode, secondary electrons are produced, which are attracted towards the channeltron, the top end of the channeltron is fluted to promote access for electrons, and is held at -2kV whilst the other end holds an anode at ground potential. Electrons from the conversion dynode are accelerated from the dynode to the relatively less negatively charged funnel, and they are then accelerated down the tube towards the end. Due to the curve of the tube the electrons are likely to strike the charged inner surface walls of the multiplier with enough energy to release secondary electrons, which are themselves accelerated down the tube and gain enough energy that collisions with the walls releases even more electrons.[78] The electron multiplication that results from this is shown in Figure 2.11.

2.7 Laser system

For photon radiation induced fragmentation of trapped species, a laser source is needed. To meet the needs of generating UV spectra, the laser radiation was provided by an Nd-YAG pumped pulsed dye laser.

In general, a laser consists of a gain medium in order to amplify a light beam and an optical resonator in order to reflect the amplified beam back into the gain medium, thus amplifying it further. The action of the gain medium results from the stimulated emission of light with a specific wavelength from species in excited energy states. Stimulated emission occurs when a species is forced to emit light by an approaching photon. The emitted light is of the same wavelength as the incident beam, and is emitted in the same direction. The phases of the incident light and emitted light are synchronised. This process can be considered to be the opposite of absorption, whereby a species in its ground state absorbs an approaching photon, transferring it to an excited state. In order for the intensity of a beam passing through the gain medium to be increased, more stimulated emission must occur than absorption. Therefore conditions must be created such that there are more species in the excited state than in the ground state. This is known as a population inversion.[79] Particular methods to induce and maintain the population inversion vary between different laser systems. For example, gas lasers such as CO_2 lasers and He/Ne lasers use electrical pumping whereby a potential is applied which generates free electrons in the gas mixture that move as an electrical current. Under the applied potential these electrons are accelerated and collide with gas molecules, exciting them, and then spontaneous emission can occur from which laser action follows.[80] Alternatively, population inversion can be achieved by light from flash lamps, the efficiency of which is often improved by focusing the light produced in on the gain medium by ellipsoidal mirrors. The Nd-YAG laser is a form of solid state laser that uses Nd^{3+} held within an

yttrium-argon-garnet crystal as a gain medium, which is commonly pumped by the former for pulsed operation, and the latter for continuous wave operation. [80]

The optical resonator typically consists of an arrangement of two highly reflecting mirrors at either end of a cavity. One mirror must be only partially reflecting, or contain small holes, so that the amplified beam can emerge.[81] A diagram of this set-up is shown in figure 2.12.[80]

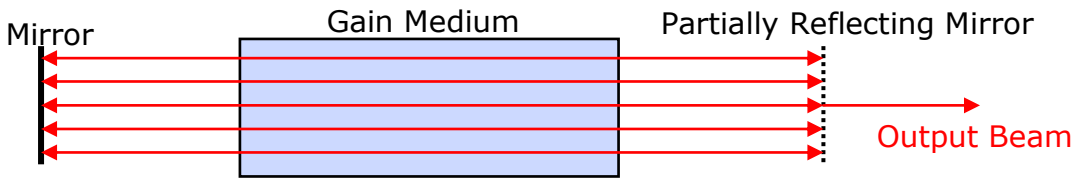

Figure 2.12 Simple Diagram of Laser Operation[80]

The gain medium of the dye laser is built up with an aromatic compound methanol solution, pumped by the frequency tripled 355 nm output of an Nd-YAG laser. To cover the entire desired spectral region (435-565 nm), several different dyes must be used in sequence, which are coumarin 153 (540A), coumarin 307 (503), coumarin 102 (480, shown in Figure 2.13), coumarin 47 (460), coumarin 2 (450) and coumarin 120 (440). The tuning curves of these laser dyes are listed in Figure 2.13. According to the diagram, efficiency of the laser dyes varied as a function as wavelength. During operation dye laser was continuously scanned through a desired spectral region. Each specific laser dye was applied in the laser wavelength range where the gain medium could provide efficiency higher than 15%. When the efficiency dropped lower than this level, the laser dye would be changed by the next one in the diagram to maintain a consistent level of efficiency. The chief advantage is that in solution the dye molecule's energy levels are broadened so that they have built wide absorption and emission bands, enabling the laser system to be tuned through a region rather than over narrow lines such as those found with gas lasers. [80]

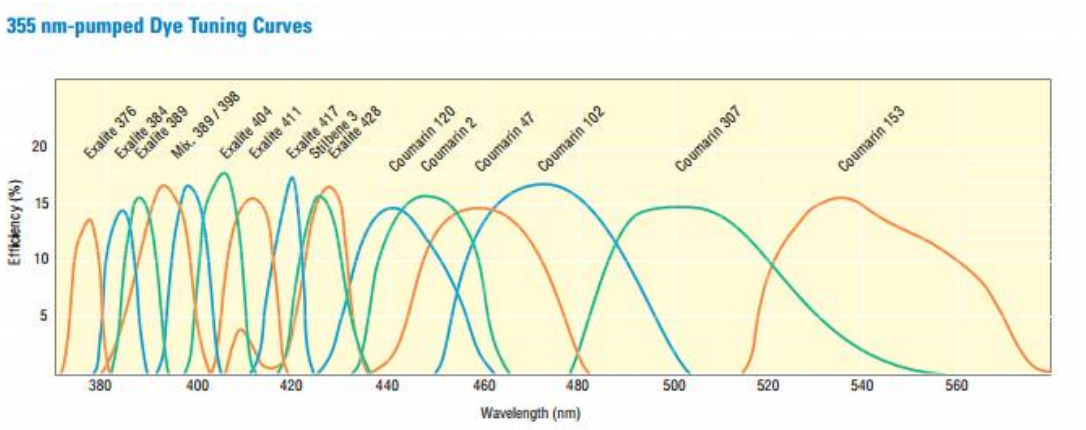

Figure 2.13 Diagram of tuning curves for 355 nm-pumped laser dyes

The dye laser is controlled by a Sirah Cobra Stretch software package. A diagram including key features of its operation is shown in Figure 2.14. Pumped by the Nd-YAG, the excited dye molecules spontaneously emit a range of photon wavelengths. The light of the desired wavelength is reversed by a diffraction grating linked to a moveable mirror and sent back through the cell for amplification. The wavelength of the output laser beam can be tuned by moving the mirror. The beam is reversed back through the 20mm cell for further amplification, and then it passes through an additional 40mm dye cell which serves as an additional amplifier stage. Both the expansion of the beam before entering the amplifier and the length of the amplifier cell can maximise the interaction of the light with the dye and make the output greater.

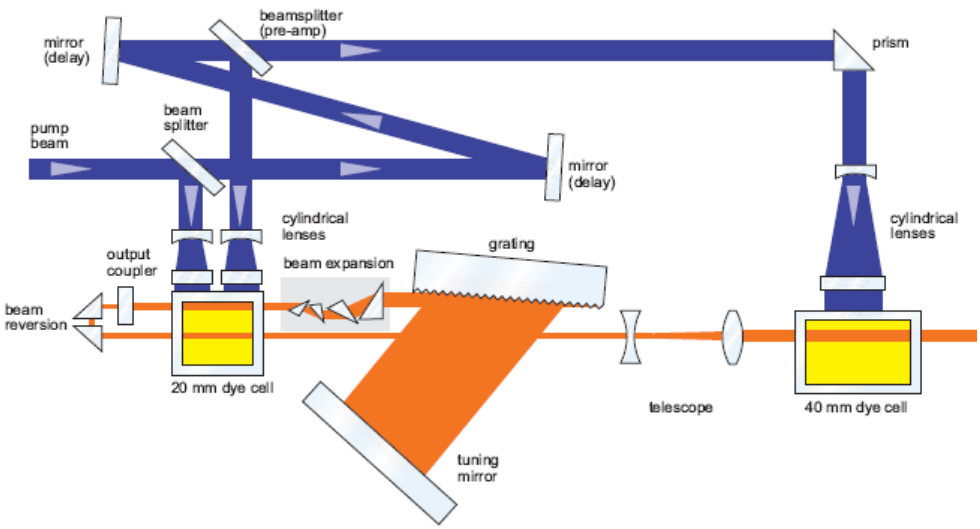

Figure 2.14 Diagram showing the key features of the dye laser's operation. The blue lines represent the 355nm pump beam and the red lines are the dye laser beam [82]

Usually, one experiment covers 10 nm of photon wavelength and then the scanning table of laser scan will be re-tuned to maintain acceptable laser power. The software will drive the motor under the BPO crystals in frequency conversion unit (FCU) to achieve an optimized UV laser intensity. Thereby, the scanning table for another 10 nm will be set up based on these optimized points. Normally, around 150 data points are needed for one scanning table. The length of each scan step was set to 0.0008 nm per second by the software to achieve a ~3.5 hr (12500 seconds) of total experiment time for a 10 nm scan.

2.8 Data Recording and Processing

As previously described, a channeltron detector was used to record the ion signal. Before every single scan, the detector was connected to a preamplifier (PMT-5R, ADVANCED RESEARCH, USA) which was connected to a computer. The signal intensity was optimized by tuning the parameters in the Merlin tuning file. During the scans, the channeltron detector was disconnected from the preamplifier and connected to amplifier of the Finnigan ITMS electronic unit. Mass spectra samples were generated at the end of every scan function and transferred to a 486 computer which

was connected to the unit. The gap between graphic data obtained from the ion trap directly and the data required to process the UV spectra by the graphic software can be bridged by connecting a testing point of the Finnigan ITMS electronic unit to a Lecroy LT347M oscilloscope. The ion signal from the multiplier of the ITMS can be transferred to the oscilloscope and processed to give exactly the same image as the mass spectra recorded by the 486 computer. This graph will be then transferred to another computer by GPIB port and recorded by a Labview data acquisition and processing programme. The software could read the graph and record ion signal intensity attributed to different peaks in separate channels. Data recorded from these channels could be used to calculate the general photofragment intensity and normalized fragmentation intensity. Photofragment intensity was calculated by adding data collected from all the fragment channels and then dividing by the total ion signal intensity (parent ions + fragments) as shown by the following equation.

$$General\ photofragments\ intensity = \frac{\sum photofragment\ intensities}{\sum photofragment\ intensities + \sum parent\ ion\ intensities} \quad (2.6)$$

The photofragment intensity was then normalized to the averaged laser power of individual scan function cycles recorded by the Leroy 9310 digital oscilloscope as shown by the following equation.

$$Normalized\ photofragment\ intensity = \frac{general\ photofragments\ intensity}{Averaged\ laser\ power} \quad (2.7)$$

Both of the oscilloscopes were controlled by the Labview programme which would then reset every 200 scan functions (240 s) to make every photofragment mass spectrum based on an average of 200 mass spectra samples. To collaborate with the Labview programme, the RF voltage applied on ring electrode of the ion trap was controlled by an ITMS scan function, which could ensure that every mass spectra sample would be generated in exactly 1200 ms. The whole programmed procedural is detailed in the following schematic diagram.

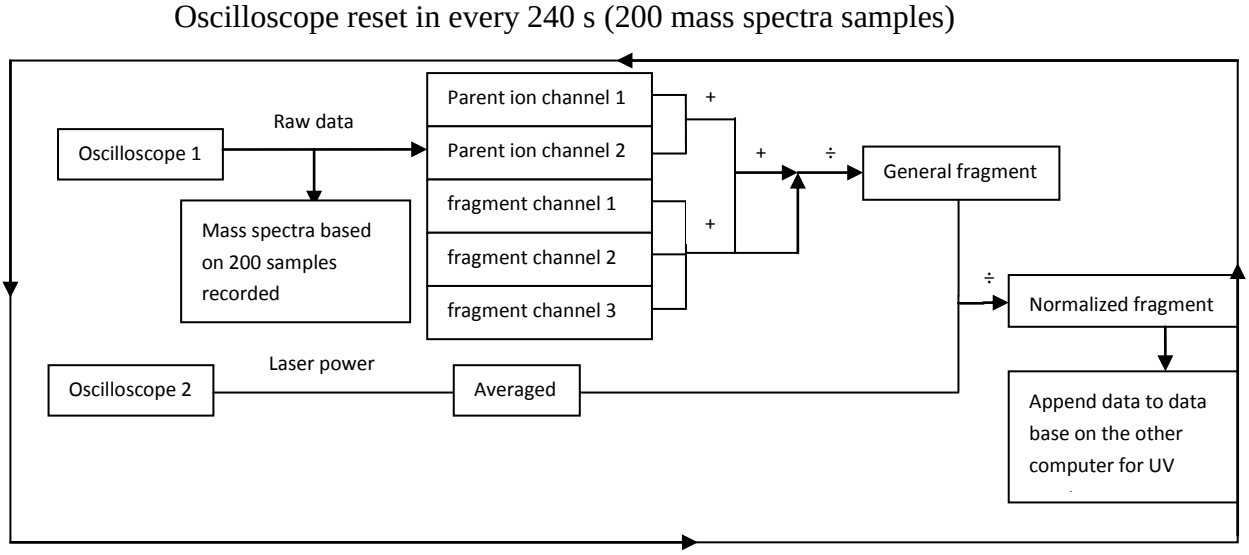

Figure 2.15 Schematic diagram of data collecting programme designed by Labview

A range of 130 nm (436 – 563 nm) in wavelength, as well as ~10500 cm^{-1} (~35300-~45800 cm^{-1} in wave numbers) has been covered in one experiment. Each experiment was cut into thirteen individual scans to allow for change of laser dye during the scans to maintain an acceptable laser power, each one covering 10 nm. Around 52 mass spectra will be recorded by the Labview for a 10 nm scan. The peak height of the averaged laser power trace was used as a measure of the laser power, as were the heights of the peaks on the mass spectra used as measures of the parent ions and identifiable fragments; in both cases a baseline correction to the peak heights was applied. The intensities of precursors and photofragments peaks on the mass spectra were monitored simultaneously to calculate a photofragment yield, normalized by laser power and signal intensity of the trapped ion, and plotted against photon energy. Then, thirteen patterns of these UV spectra were combined and fitted together by averaging in regions of overlap between adjacent scans to construct a complete UV photofragmentation spectroscopy. For the part of generating a UV photofragmentation spectrum that had to be done manually, Origin was used to fill in the photon energy

axis, which to do accurately require the laser scan to be synchronised with the oscilloscope's data acquisition cycle.

2.9 Experiment Overview

The apparatus was constructed for preparing and detecting laser-induced fragments to form a series of mass spectroscopy and obtain the UV action spectra finally. The overview of this process is as follows. The carrier gas (Argon at 120 psi) comes through a stainless steel reservoir containing the liquid solvent (benzene or toluene). The mixture is directed to the stagnation vessel and undergoes supersonic expansion through a continuous nozzle generating molecular clusters beam. The cluster beam passes into the oven chamber, where a proportion of the clusters collide with vaporised metal (Pb, Cu and Ca) atoms generated by a high temperature effusive cell. The neutral complexes clusters obtained are then ionized by electron impact, deflected by two quadrupole deflectors and mass selected by a quadrupole mass filter. Then ions with the desired mass/charge ratio are injected by ion guides into a liquid nitrogen cooled helium gas buffered quadrupole ion trap. Inside the ion trap, they will be exposed over 700 ms to seven pulses of UV radiation from an Nd-YAG pumped, frequency doubled, and tuneable dye laser. All the precursors and fragments generated are ejected effectively by the end of the scan function and detected by a channeltron detector for mass analysis. There are two oscilloscopes recording mass spectra and laser power simultaneously, and normalised photofragmentation data is automatically produced by a Labview programme. A schematic diagram and a photograph of this experimental apparatus are detailed in Figure 2.16.

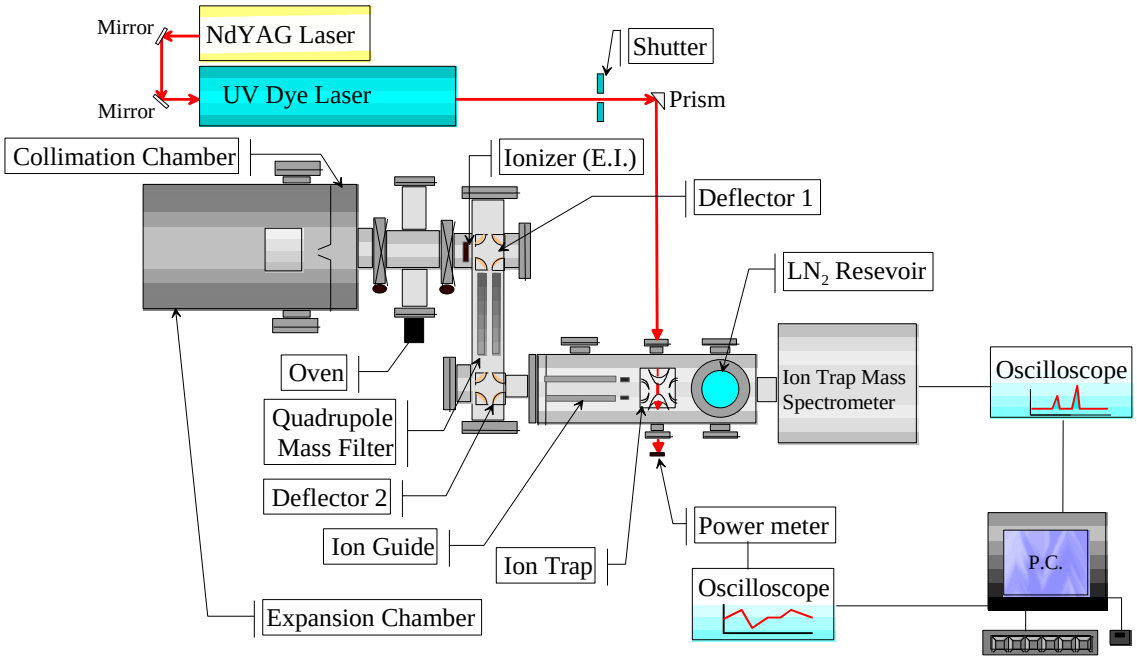

Figure 2.16(a) A schematic diagram of the experimental apparatus.

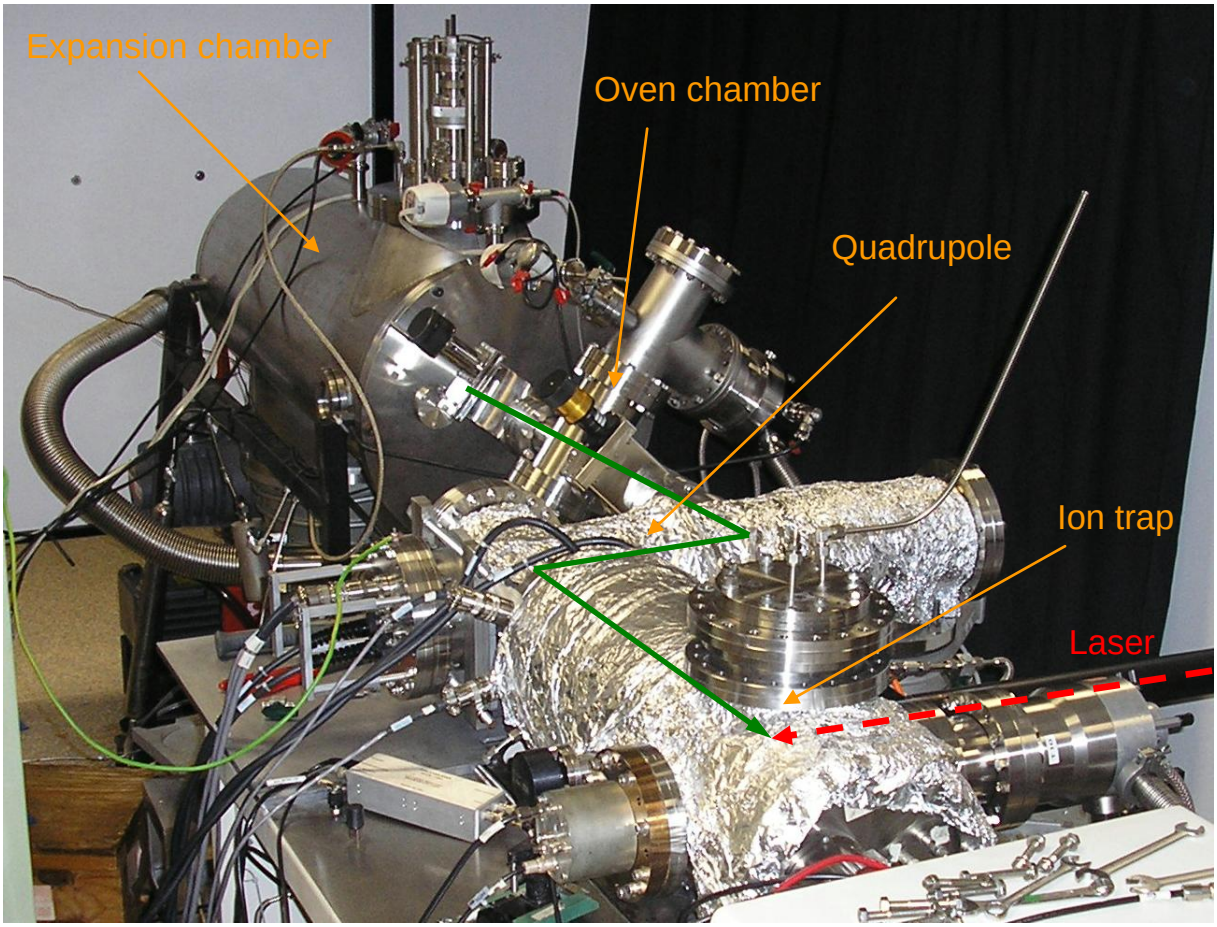

Figure 2.16(b) A photograph showing the main components of the apparatus in the laboratory.

The green line shows the path of the clusters, then complexes.

Chapter 3 Theoretical Section

3.1 General introduction to density functional theory (DFT)

Computational chemistry is an important subfield of chemistry which focuses on construction, transformation and properties of molecules based on fundamental laws of physics.[83] Many molecular properties can be calculated from theory, including stable geometries of molecules and their relative energies, dipole moment, polarizability and NMR coupling constants, and time dependence properties. It is well acknowledged that the Schrodinger's equation can only be solved exactly for two-particle systems. Computational chemistry provides tools to approximate the solutions of this equation with some desired degree of accuracy.

The classic way to solve the Schrodinger's equation is to neglect the coupling between the nuclei and electronic motion (Born-Oppenheimer approximation) and to take all interactions between the particles into account in an average fashion (independent-particle models) which is known as Hartree-Fock (HF) theory. In the HF model, the electrons are described by their own orbital, and the overall wave function can be obtained by arranging these orbital in a Slater determinant. Starting from HF model, more additional determinants can be added thereby generating models that can be made to converge towards the exact solution of Schrodinger's equation systematically (Full Configuration Interaction). On the other hand, more approximations can be applied to generate semi-empirical methods to improve the efficiency and accuracy of *ab initio* HF calculations by fitting related parameters to experimental data. Many different approximate methods exist for solving the Schrodinger's equation, and which one to use for a specific problem is usually chosen by comparing the performance against known experimental data. The experimental data thus guides the selection of the computational model, rather than directly entering into the computational procedure. Density Functional Theory (DFT) is a very important semi-empirical method. In orbital free DFT, the energy functional can be

divided into three parts, kinetic energy T[ρ], attraction between the nuclei and electrons $E_{ne}[\rho]$, and electron-electron repulsion $E_{ee}[\rho]$. The nuclear-nuclear repulsion can be considered as constant here under the Born-Oppenheimer approximation. Furthermore, the $E_{ee}[\rho]$ can be divided into Coulomb part J[ρ] and exchange part K[ρ], which includes correlation energy in all the terms. So the energy functional can be written in form of equation 3.1.

$$E_{TF}[\rho]=T_{TF}[\rho]+E_{ne}[\rho]+J[\rho] \text{ (eq. 3.1)}$$

Equation 3.1 is also known as Thomas-Fermi (TF) model[84], while inclusion of the $K_D[\rho]$ exchange part constitutes the Thomas-Fermi-Dirac (TFD) model[85]. The accuracy of both are limited because of the errors in the expression for the kinetic energy, exchange energy and complete neglect of electron correlation energy.[86]

DFT is a methodology improved based on HF theory and TF model, where the many-body effect of electron correlation is modelled by a function of the electron density. Also, it can be considered as an independent-particle model which is analogous to HF. Comparing to the HF theory, DFT can provide a better accuracy. However, there is no systematic way to improve the results towards an exact solution. The main idea of DFT is to solve Schrodinger's equation by building up connections between electron density and energy instead of calculating the overall wave function. To achieve this target, the ground state electronic energy is determined completely by a function of electron density ρ[r]. For instance, the kinetic energy is calculated from an auxiliary set of orbitals used for representing the electron density. The exchange-correlation energy, which is a small part of the total energy, is represented by some approximations. The accuracy of DFT calculations can be improved by selecting proper exchange-correlation functional for different systems, adding terms depending on the derivative of electron density to the kinetic and exchange functional, and

mixing a percentage of HF exchange into the functional. The following section will provide more details about fundamental and practical application of DFT.

3.2 Hohenberg-Kohn theorem

DFT is made possible by the existence of two lemma of Hohenberg-Kohn (H-K) theorems proven by Hohenberg and Kohn in 1964.[87] In the first lemma, the ground state electron density uniquely determines the nuclear potential, Hamiltonian operator and ground state energy. An H-K functional can be defined as a universal functional of the density as equation 3.2.

$$F[\rho(\mathbf{r})]=T[\rho(\mathbf{r})]+U[\rho(\mathbf{r})] \quad \text{(eq. 3.2)}$$

Where *T* is the kinetic energy operator, U is the interaction energy operator.

In the second lemma, if one *N* electron system trapped in a potential V_{ext}(r), its density functional can be written in form of equation 3.3.

$$E_{(V,\,N)}[\,\rho(\mathbf{r})]=F[\rho(\mathbf{r})]+\int v(\boldsymbol{r})\rho(\boldsymbol{r})d\boldsymbol{r} = (\psi|H|\psi) \quad \text{(eq. 3.3)}$$

Since ρ(**r**) determines both *N* and *V*(**r**), it gives the full *H* and N for the electronic system. Hence ρ(**r**) determines implicitly all properties derivable from *H* through the solution of the time-independent or time-dependent Schrodinger's equation. The ground state energy of a nondegenerate electronic system is defined by its ground state electron density. For a degenerate ground state, ρ(**r**) is any one of the ground state densities. The proof of this lemma can be found from a list of DFT papers and books.[83, 88]

For the first time, the H-K theorem claims that for a fixed ground state, there is a one-to-one correspondence between the electron density and the overall energy, and Hamiltonian operator, and nuclear potential, and thereby also the overall wave function. It is well known that an electronic wave function for an N electron system

contains 4N variables; three spatial and one spin coordinate for each electron. The complexity of a wave function increases significantly with the number of electrons. Unlike the wave function approach, the electron density is the square of the wave function, integrated over N-1 electron coordinates, and each spin density only depends on three spatial coordinates, independent of the number of electrons. While the number of electrons increases, the electron density has the same number of variables, independent of the system size. However, it has also been proven that different density yields different ground state energy, which means the exact functional connecting electron density with the energy is still unknown. The goal of DFT methods is to design these functionals to connect the electron density with the energy.

3.3 Kohn-Sham formulation

The main elements of DFT are energy, electron density and functional. If we put all of these important terms together in one equation, the Kohn-Sham (K-S) equation will be generated (equation 3.4). This equation is defined by the movement of non-interactive particles in an effective local external potential (Kohn-Sham potential), and named after Walter Kohn and Sham Lu Jeu who introduced it for the first time in 1965. [88b]

$$\rho(\mathbf{r}) = \sum_i^N |\varphi_i(\mathbf{r})|^2 \qquad \text{(eq. 3.4)}$$

In K-S theory, except for kinetic energy ($T_s[\rho]$), interaction of electron distribution to nuclear framework ($E_{ne}[\rho]$) and classical Coulomb energy between electrons ($J[\rho]$), there is another part E_{xc} called exchange-correlation energy which includes the interaction correction to $T[\rho]$, the correction to $E_{ee}[\rho]$ for the fact that real electrons do not interact with themselves, the exchange energy due to the indistinguishability of electrons exchanging their space and spin variables, and the correlation energy due to the fact that the many-electron spin densities are not uncorrelated products of spin-orbital densities. E_{xc} is written as a functional, called the DFT functional. As what has

been mentioned in H-K section, the density functional exists but a closed-form expression for the exact spin-density functional does not, and there is no systematic route to improving an approximate functional. However, since DFT has been used for many years, many useful approximations have been devised and further improved.

3.4 Basis sets

An unknown molecular orbital (MO), which is also a solution of Schrodinger's equation, can be considered as a function in the infinite coordinate system spanned by a complete basis set. Obviously, expanding the unknown MO wave function to a set of known functions is not an approximation if the basis set is complete. However, a complete basis set is impossible for actual calculations because the number of functions is infinite. So, an approximation that only components of the MO along coordinate axes corresponding to the selected basis functions can be represented is applied. An approximate comparison between the two types of basis functions, Slater Type Orbitals (STO) and Gaussian Type Orbitals (GTO), revealed that one STO can be modelled by a linear combination of three GTOs while the accuracy is roughly same. The expansion of the MO leads to integrals of quantum mechanical operators over basis functions.

The basis set that is sufficient to represent all electrons with the smallest number of functions can be a called minimum basis set. Based on this, the number of functions can be doubled to form a double zeta (DZ) basis set. By doubling the number of functions, the DZ basis set can have a better capability to describe the wave function while electron distribution is different in different directions. In principle, the number of functions can be tripled and quadrupled for the same reason to form triple zeta (TZ) and quadruple zeta (QZ) basis set. To improve the description of chemical bond in the molecule, polarization functions are introduced when we consider the higher angular momentum functionals. For example, adding a single set of polarization functions to the DZ basis set can form a double zeta plus polarization (DZP) basis set. If two sets

of polarization functions are added to a TZ basis set, a Triple Zeta plus double polarization (TZ2P) basis set is obtained. The choice of the number of functions depends on consideration of the property of interest and the computational cost.

Contract GTO to be more representative of radial part of orbital, it is quite efficient to contract the basis functions by making the variational coefficients in front of the inner basis functions constant. By doing so, number of basis functions to be handled by the variational procedure can be reduced significantly. The full set of basis functions is named primitive GTOs (PGTOs) whereas the basis functions after the explicit treatment are called contracted GTOs (CGTOs). There are many different contracted basis sets available. For example, 6-311++G(d, p) is a triple split valence basis, where the core orbitals are a contraction of six PGTOs and the valence split into three functions, represented by three, one and one PGTOs, respectively. Two sets of diffuse functions, which are one d functions to heavy atom and one diffuse sp function to hydrogen, are added.

For a system that involves a heavy atom from lower part of the periodic table, which has plenty of chemically non-important core electrons, it is also very important to model the core electrons by a suitable function. The function modelling the core electrons is called an Effective Core Potential (ECP) or pseudo potential (PP). For transition metal ion Cu^{2+}, the valence shell is constituted by 3s, 3p and 3d orbitals. An all-electron based calculation will provide a reasonable geometry, however, the energetics are not always satisfactory. The ECP can achieve a better accuracy for heavy atoms by only taking account electrons outside the big core with desired size. The ECP can be varied for different DFT functionals. However, the difference is relatively small. Thus, in this thesis, we use the same PP to optimize different functionals without any re-optimization.

3.5 DFT Functional

The spin-polarized Kohn-Sham formalism and the spin-density functional are usually called Kohn-Sham theory. The density functional is usually written as the sum of an 'exchange' part and a 'correlation' part.

Initially, the most basic kind of approximation is the local spin density approximation (LSDA) which depends only on spin densities, such as Vosko-Wilk-Nusair (VWN)[89], Perdew-Zunger (PZ81)[90] and Perdew-Wang (PW92)[91]. The exchange part of this set of functional is derived from the exact exchange energy of a uniform electron gas (UEG) system, which is a system with a constant electron density neutralized by a constant background positive charge. The correlation energy of the UEG system can be calculated and fitted in many different ways. [92] Due to LSDAs' ability to express the exact correlation energy of UEG system, they are often used as an explicit component to construct higher level of approximations for more sophisticated and realistic systems.

Next, by taking account gradients of local densities at the same coordinates into the exchange-correlation energy, a group of higher level approximation called generalized gradient approximations (GGA) was generated. The GGA functional can combine exchange part and correlation part from one source or different sources. For example, the BP86 functional combines Becke's 1988 exchange functional (B)[93] and Perdew's 1986 correlation functional (P86)[94]. The BLYP functional is constructed by combination of B exchange and Lee-Yang-Parr correlation functionals (LYP)[95]. BP86 and BLYP combine B exchange functional with a different correlation functional. Otherwise, PW91 functional combines Perdew-Wang 1991 exchange functional (PW91)[96] and PW91 correlation functional, which makes the exchange and correlation part coming from the same source. Furthermore, a group of developed GGA functional as known as meta-GGA functional has been introduced which is

taking account the second derivative of electron density (the Laplacian). This set of functional depends on the local densities, the gradient and the Laplacian of the local densities which is more accurate than GGA. Some examples of meta-GGA functional are Becke95 (B95)[97] for correlation and TPSS[98] for exchange and correlation.

Thirdly, by adding Hartree-Fock exchange to meta-GGA yields hybrid meta-GGA functional or hybrid functional. In this case, if an electron interacts with its own charge density, it could make an error in LSDA and GGA exchange functionals due to the increasing energy of localized states and produce excessively delocalized charge distributions.[99] This delocalization is associated with the dominance of kinetic energy terms and the localization is associated with the dominance by screened Coulomb potentials which depends on electron correlation very much because the correlation minimizes the interatomic repulsion of electrons near the same center. To decrease or eliminate the self-exchange, the partial or full Hartree-Fock exchange energy is introduced. To eliminate the self-correlation and decrease the sensitivity to the percentage of this Hartree-Fock exchange[100], the Hartree-Fock kinetic energy density is included.[100-101] Therefore, the resulting hybrid functionals can reduce inaccuracies of the LSDA and GGA functionals in certain level while their computational advantages still remain. By far, the hybrid functionals are more preferable than LSDAs and GGAs in organic chemistry field because they can predict energy more accurately. The way to generate a hybrid functional is replacing a percentage of local density functional exchange (X) by Hartree-Fock exchange. For example, PBE1PBE (also called PBE0 in this thesis, with X=25) is generated by 1996 pure functional of Perdew, Burke and Ernzerhof (PBE)[102], as made into a hybrid by Adamo[103] with 25% exchange and 75% correlation weighting. The digit '1' in the name of the functional means one parameter X Instead, the B3LYP functional has three parameters (X=20 and two other parameters), which is generated by LYP functional as non-local correlation and VWN for local correlation. Since LYP

contains both local and non-local terms and its local term is essentially equivalent to VWN, the VWN is used to provide the excess local correlation required.

Finally, there are some other functionals which have not been applied widely to transition metal systems. In this category, Range-separated functionals are very promising. This set of functionals involves separating the electron-electron interaction into a short-range and a long-range part, and treating the contribution of one part of the exchange energy by Hartree-Fock method and the other part by a local exchange functional. Depending on the point in space, the local hybrid functional can be a mixture of a percentage of Hartree-Fock exchange and a percentage of density functional exchange. The percentage can depend on any local function of the point in space. One example of this kind of functionals, CAM-B3LYP, has been involved in this thesis for TDDFT calculations of transition metal complexes. This functional is derived by Handy and co-workers' long range corrected version of B3LYP using the Coulomb-attenuating method.[104]

3.6 Ground state geometry optimization and vibrational frequency calculation

To locate the stable geometry of a molecule, a desired stationary point which occupies the lowest energy in its region of potential energy surface (PES) is required. A PES indicates the relationship between the energy of a molecule and its geometry. In other words, geometry optimization is the process of starting with an input structure and finding a stationary point on the PES. For a three-dimension transition metal ion-ligand model, it can be done using Cartesian coordinates x, y, z. Each of the atoms has an x, y and z coordinate which is giving 3n geometric parameters n equals number of atoms) to construct the 3n dimensional PES. For each geometric parameter, the first derivatives and the second derivatives of energy need to be calculated, respectively. All of these calculated derivatives can be manipulated as matrices. The first derivative matrix is for the input structure and the second derivative matrix is for the force constant (which is also called Hessian). The Hessian is very important because it is

not only for geometry optimization but also for characterization of nature of the stationary points (minima, transition states or nth order saddle point).

Most optimization methods determine the nearest stationary point, but a multi-dimensional function may contain many different stationary points. A stationary point has the first derivative equals zero and a second derivative either positive in all directions (minimum) or negative in one direction and positive in other directions (transition state or 1st order saddle point). Therefore, it is necessary to check that a stationary point is a minimum or a saddle point by calculating its vibrational frequency. The vibrational frequency equals square root of a force constant (which is one of the eigenvalues of the Hessian), and the square root of a negative number is an imaginary number. Therefore, for a minimum, all force constants are positive and all calculated vibration frequencies are real, while a transition state (saddle point) has n negative force constants and n imaginary vibration. An nth-order saddle point has n negative force constants and so n imaginary frequencies. In this thesis, geometry optimizations are followed by vibrational frequency calculations to find out how many imaginary modes are present. Results of these calculations can be found from the following chapters.

3.7 Time dependent density functional theory (TDDFT)

Base on the H-K theorem and K-S formulation, Runge and Gross introduced an DFT method for time-dependent systems which was called Time Dependent DFT (TDDFT).[105] Runge-Gross (RG) theorem provides the possibility to investigate properties and dynamics of many-body systems in time-dependent potentials, such as electric or magnetic fields. The TDDFT can be used as a powerful tool to study features like excitation energies, to predict frequency-dependent response properties or to reproduce experimental spectra. This method can capture the essentially dynamical nature of an excitation process, during a transition between the ground states and excited states. Periodic charge-density fluctuations are included, which are

accompanied by dynamical many-body effects and mixing of K-S eigenstates. This leads to the corrections of static K-S eigenvalue spectrum towards true spectrum. It can be used for large systems (up to thousand atoms), and is more efficient and accurate than *ab initio* methods for some systems.

The main idea of TDDFT is to determine a fictitious non-interacting system that has the same density as the physical interacting system of interest. According to RG theorem, for a fixed initial state, there is a unique mapping between the time dependent external potential and the time dependent electron density of the system. In another word, for the same initial state, two different time dependent external potentials cannot produce the same time dependent density because the time dependant density is a unique functional of the time dependent external potential. Energy of a time dependent interacting system can be also written as function as time dependent electron density in the form of K-S formulation, which is also called time dependent Kohn-Sham system. The most common application of TDDFT is to calculate the energies of excited states of isolated systems. Such calculations are based on the linear response TDDFT that was introduced by Gross and Kohn later on. [106] With this theory, the linear response of electron density to the external potential can be used to define excited states energies. Given the relative small external perturbation is not enough to destroy the ground state structure of the system, the variation of the system will depend only on the ground state wave function so that all of DFT properties can be applied. In this thesis, the excitation energies and oscillator strengths are calculated using TDDFT based on all optimized structures for the doubly charged metal-ligand complexes. More details can be found in the following chapters.

3.8 Natural Transition Orbital

As discussed described, the end result of TDDFT calculations is excitation energy and a set of coefficients describing the contribution that each particle-hole pair makes to

the excited state. However, there are some other properties that may be derived such as definition of electron population around nuclei. The population analysis based on electron density is very important because it will directly determine the nature of electronic transitions derived from the photo excitation process. For the purpose of characterizing the type of electronic transitions, the Natural Transition Orbitals (NTOs) are generated from a given transition density, which are the result of unitary transformations of the original canonical molecular orbitals. By applying separate unitary transformations to the occupied and the virtual orbitals, a maximal correspondence between the excited particle and the empty hole can be obtained.[107]

For instance, an overview of NTO application on a TDDFT calculation of $[Pb(benzene)_2]^{2+}$ is detailed as follow. In the set of results using CAM-B3LYP as the functional, 6-311++G(d, p)[SDD] as the basis set, based on the BVP86 optimized geometry (using the same basis set) of C_{2v} conformer, excited state 7 was most intense in excitation energy. Therefore, a unitary transformation of this excited state was obtained by NTO analysis and summarized in Table 3.1.

Table 3.1 NTO analysis for excited state7 in TDDFT of $[Pb(benzene)_2]^{2+}$ using CAM-B3LYP, 6-311++G(d, p)[SDD] as basis set, for C_{2v} conformer BVP86 geometry.

Involved orbital	OE	Unitary transformation
Alpha occ 42	0.450	C13-p=0.12 C3-p=0.12 C14-p=0.12 C5-p=0.12 C17-p=0.12 C2-p=0.12 C15-p=0.12 C1-p=0.12
Alpha occ 43	0.521	C19-p=0.16 C11-p=0.16 C12-p=0.16 C7-p=0.16
Alpha vir 44	0.521	Pb22-p=0.95
Alpha vir 45	0.450	Pb22-p=0.95

From Table 3.1, it can be noticed that NTO 43 and NTO 44 are the dominant orbitals for the ground to the seventh excited state electronic transition, being 'electron' and 'hole', respectively. NTO 43 has a 16% contribution from p orbital in carbon atom 19, 11, 12 and 7, respectively. NTO 44 has a 95% contribution from p orbital in Pb atom 22. Based on this NTO analysis, the charge transfer transition from NTO 43 to NTO

44 can be assigned to ligand-to-metal charge transfer (LMCT, π→6p) electronic transition, which can be confirmed by the image of involved orbitals in Figure 3.1.

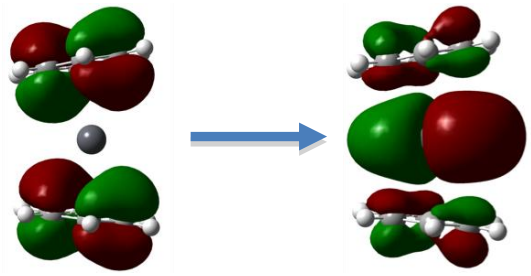

NTO 43(HOMO) NTO 44(LUMO)

Figure 3.1 Image of HOMO and LUMO orbitals for excited state7 in TDDFT of $[Pb(benzene)_2]^{2+}$ using CAM-B3LYP, 6-311++G(d, p)[SDD] as basis set, for C_{2v} conformer BVP86 geometry.

3.9 Summary of computational details

Thus far, one could have a general impression of DFT as the main computational tool in this thesis. For the matter of computing time and theoretical accuracy, a basis set 6-311++G(d,p) has been chosen for all of the atoms except copper and lead atom, which are using SDD instead as their basis set. For C_2 conformer of $[Pb(benzene)_2]^{2+}$, BVP86 and TPSSh were used as functional to obtain the optimized geometry, and CAM-B3LYP, PBE0 and TPSSh were used as functional to calculate the excitation energies and oscillator strength. For C_{2v} conformer of $[Pb(benzene)_2]^{2+}$, besides all of above functionals, PBE0 was added to optimize the structure to approach a more stable geometry with lower energy. The DFT and TDDFT calculations on transient intermediates $[Pb(benzene)]^{+/2+}$ are performed using the same basis sets, with chosen functionals to make a good complement to the complex calculations. For $[Pb(toluene)_2]^{2+}$, BVP86, PBE0 and TPSSh were used to optimize geometries of all conformers, followed by TDDFT calculations using CAM-B3LYP, PBE0 and TPSSh for each optimized structure. The optimized geometry and time-dependant properties of intermediates $[Pb(toluene)]^{+/2+}$ were calculated using the selected functionals as

similar as lead benzene case. For $[Cu(benzene)_2]^{2+}$ complex, the same set of functionals were applied to optimize the geometries. TDDFT calculations were performed using CAM-B3LYP, PBE0 and TPSSh functional for all of these optimized structures, respectively. For $[Ca(benzene)_2]^{2+}$ and $[Ca(benzene)(H_2O)_n]^{2+}$ (n=2 and 4) complex, BVP86, PBE0 and TPSSh were used to optimize the structures. TDDFT calculations were performed based on all of optimized structures using CAM-B3LYP, PBE0 and TPSSh functional. A 6-311++G(d,p) basis set was used for all atoms in this case. All of the computational methodologies are summarized in Table 3.2. More details about the theoretical results will be reported in the following chapters.

Table 3.2 summary of involved computational details for all doubly charged transition metal ion-ligand complexes

Complex	Symmetry	Ground state DFT		Excited state TDDFT	
		Basis sets	Functional	Basis sets	Functional
$[Pb(benzene)_2]^{2+}$	C_2	6-311++G**/SDD	BVP86 TPSSh	6-311++G**/SDD	CAM-B3LYP PBE0 TPSSh[a]
	C_{2v}		BVP86 PBE0 TPSSh		
$[Pb(benzene)]^+$	C_s	6-311++G**/SDD	BVP86 TPSSh	6-311++G**/SDD	CAM-B3LYP TPSSh
$[Pb(benzene)]^{2+}$	C_{6v}				
$[Pb(toluene)_2]^{2+}$	C_{2v}: Eclipsed/Cis	6-311++G**/SDD	BVP86 PBE0 TPSSh	6-311++G**/SDD	CAM-B3LYP PBE0 TPSSh[a]
	C_2: Staggered/Cis				
	C_2: Staggered/Trans				
$[Pb(toluene)]^+$	C_1	6-311++G**/SDD	BVP86 TPSSh	6-311++G**/SDD	CAM-B3LYP TPSSh
$[Pb(toluene)]^{2+}$	C_1				
$[Cu(benzene)_2]^{2+}$	C_2:Staggered	6-311++G**/SDD	BVP86	6-311++G**/SDD	CAM-B3LYP PBE0 TPSSh
	C_{2v}-bent		BVP86		
	C_2:Eclipsed		PBE0 TPSSh[b]		
$[Cu(benzene)]^+$	C_{6v}	6-311++G**/SDD	BVP86 PBE0 TPSSh	6-311++G**/SDD	PBE0
$[Cu(benzene)]^{2+}$	C_s	6-311++G**/SDD	BVP86 PBE0 TPSSh	6-311++G**/SDD	PBE0
$[Ca(benzene)_2]^{2+}$	C_2	6-311++G**	BVP86 PBE0 TPSSh	6-311++G**	CAM-B3LYP PBE0 TPSSh
	C_{2v}				
$[Ca(benzene)]^+$	C_s				
$[Ca(benzene)]^{2+}$	C_{6v}				
$[Ca(benzene)(H_2O)_4]^{2+}$	C_2				
$[Ca(benzene)(H_2O)_2]^{2+}$	C_1				

[a] The TDDFT results were selected depending on fitness with experimental spectra reported in the related chapters.

[b] The C_{2v} structure optimized by BVP86 was different from the other two, which were optimized by PBE0 and TPSSh. More details are reported in the related chapter.

Chapter 4 Ultraviolet photofragmentation spectroscopy of lead dication-bis(benzene) sandwich complex in the gas phase combined with DFT/TDDFT calculations

4.1 Introduction

Lead is the heaviest element in group IV and has the highest atomic number of all of the stable elements. The element has two common oxidation states, Pb(II) (electronic structure: [Xe] $4f^{14}$ $5d^{10}$ $6s^2$) and Pb(IV) (electronic structure: [Xe] $4f^{14}$ $5d^{10}$). The former dominates the inorganic chemistry of lead while organic lead chemistry is dominated by the latter.[108] Lead is also a ubiquitous environmental contaminant which can cause many poisoning diseases from inhalation of inorganic lead (II), ingestion of Pb(II) paint (PbO) and Pb(II) leached water or exposure to contaminated soil.[109] For detecting and sequestering lead poisoning in the environment, investigation on the Pb(II) complexes has attracted a wide-spread attention.[110] In this category, sandwich shape aromatic structures received far more attention than the others for two reasons. First, many of them have been identified as key intermediates in heterogeneous catalysis. Second, the active LMCT transitions in the UV can provide important signatures for the Pb(II) in order to develop more effective sequestering agents.[111]

To date, for generation of metal-ion ligand complexes in the gas phase there are three main techniques have been used, which are electrospray, laser vaporization and the pick-up technique. Some experimental studies using the electrospray ionization mass spectrometry (ESI-MS) technique involved lead complexes baring a wide range of ligands have been successfully conducted. Cai [112] and co-workers recorded the UV-vis spectra, infrared and Raman spectra of β-halogen or alkyl octasubstituted phthalocyanine lead complexes. Cuenot [113] and co-workers synthesized and

spectroscopily characterized a series of Lead(II) complexes chelated by octadentate carbamoyl-armed macrocycles. The laser vaporization technique has also been used to form metal ion-ligand complexes to investigate their photodissociation process, electronic properties or reaction mechanism. For instance, Yang and co-workers investigated the spectroscopy of a wide range of metal-ligand complexes such as gadolinium with benzene[114] and group 6 metal with bis(toluene)[111]. Kaya and co-workers made use of an experiment setup which combines a laser-vaporization source and a time-of-flight mass spectrometer to record mass spectra of metal-benzene complexes $[M_n(benzene)_m(M=Sc-Cu)]$ in order to investigate the electronic properties.[115] Tang and co-workers used a high-resolution reflectron time-of-flight mass spectrometer with laser vaporization source to study the mechanisms of lead clusters with benzene from their mass spectra.[116] In terms of pick-up technology, Stace and co-workers recorded the state-resolved UV photofragmentation spectra of $[Zn(pyridine)_4]^{2+}$, $[Mn(pyridine)_4]^{2+}$ and group two metal with pyridine and picoline complexes in favor of pick-up technology with a cold ion trap mass spectrometer. The experimental data has been combined with theoretical calculation results for an assignment of the observed transitions. [10, 42-43]

Apart from the experiments, there are some theoretical studies of Pb(II) complexes for the purposes of tracking changes that occur in metal ion coordinating with different environments and identifying suitable sequestering agents. For example, Cornard and coworkers have reported the results of a series of TDDFT calculations on the electronic spectra of numerous Pb(II) chelated complexes involving aromatic molecules.[117] Both Pb(II)-caffeate and Pb(II)-quercetin complexes showed evidence of spectral features that could be attributed to ligand-metal-charge transfer transitions. Jarzecki has presented the results of a detailed TDDFT study of electronic excitations in lead-poisoned model proteins. The calculations identified the presence of a number of ligand-to-metal charge transfer transitions at between 200 and 230 nm.[118] Zhang

and co-workers have used TDDFT to calculate electronic absorption and circular dichroism spectra of Pb(II)/phthalocyanine complexes over a wavelength range that overlaps with the work presented here.[119]

In this chapter, benzene is chosen as appropriate ligands to form metal dication-ligand sandwich complex with lead, because benzene can form strongly bound sandwich structures with the metal and is a simple aromatic molecule that can be considered as a good start. The UV photofragmentation spectroscopy of doubly charged sandwich shape lead-bis(benzene) complex has been recorded in the gas phase and combined with the theoretical data for assignment of the main features that appear in the UV spectra to all dominant electronic transitions in the range of photon energy.

4.2 Photofragment mass spectra of $[Pb(benzene)_2]^{2+}$

A detailed description of the apparatus has been given in chapter 2. The signal that should correspond to $[Pb(benzene)_2]^{2+}$ is at 181.5 amu, which could usually be improved by fine tuning of the ion optics to the peak at 181.5 amu with the RF of the ion trap switched off. With the RF switched on the 1200 ms cycle of trapping, excitation and ejection was initiated and an example of typical photofragment mass spectra of $[Pb(benzene)_2]^{2+}$ is detailed in Figure 4.1. The mass spectra provide three clearly distinguishable peaks on a m/z scale that has been calibrated using the known masses of cluster ions. It can be found that there are two parent ion peaks which are identified as $[Pb(benzene)_2]^{2+}$ and $[Pb(benzene)_2H_2O]^{2+}$ and one fragment peak corresponding to $benzene^{+}$. The parent ion, $[Pb(benzene)_2]^{2+}$, can be found to pick up one or two water molecule from the background in the mass spectra. In previous studies of the spectra of $[ML_4]^{2+}$ complexes,[10, 42-43] (M = Zn, Mn, Mg, Ca, Sr; L = pyridine and picoline), the precursor ions were also observed to pick up water molecules. However, calculations showed that their presence had very little influence on the recorded UV spectra.[10] In addition, the degree of water attachment was found

to decline as the ion trap cooled and any background water was removed via cryopumping.

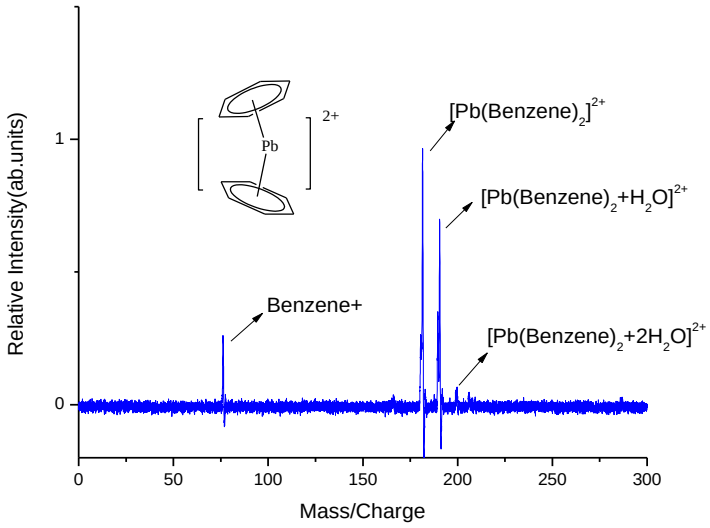

Figure 4.1 Photofragment Mass spectrum of $[Pb(benzene)_2]^{2+}$ recorded by ion trap mass spectrometer under laser irradiation at an average photon energy of 45355 cm^{-1}. The chemical structure of $[Pb(benzene)_2]^{2+}$ is presented on the top of the spectrum.

4.3 Ultraviolet photofragment Spectroscopy of $[Pb(benzene)_2]^{2+}$

The UV photofragmentation spectrum of $[Pb(benzene)_2]^{2+}$ is shown in Figure 4.2. From Figure 4.2, it can be seen that the spectrum consists of three main features: two well-resolved peaks at 39800 cm^{-1} and 42000 cm^{-1}, and a broad feature which extends beyond the upper limit of the photon energy range available from the laser ~ 45500 cm^{-1}.

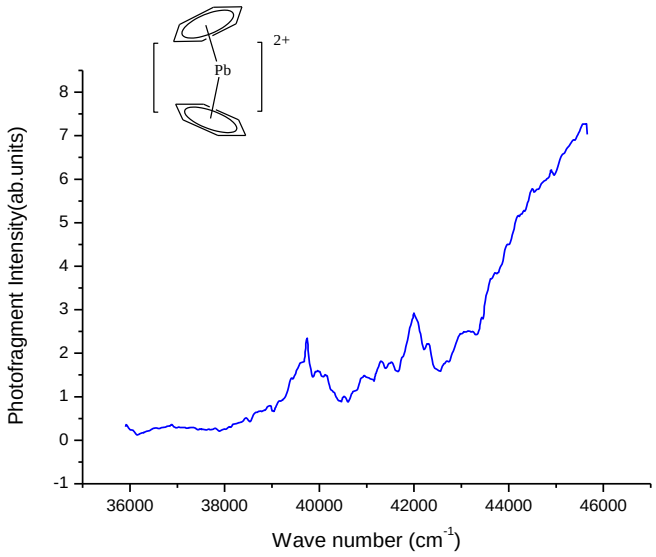

Figure 4.2 UV photofragment spectroscopy of $[Pb(benzene)_2]^{2+}$ recorded by the ion trap mass spectrometer. The chemical structure of $[Pb(benzene)_2]^{2+}$ is presented on the top of the spectrum.

4.4 Methodology of theoretical calculations

The structures and binding energies of $[Pb(benzene)_2]^{2+}$ and $[Pb(benzene)]^{+/2+}$ were calculated using density functional theory as implemented in Gaussian09. Geometry optimization and frequency analysis were performed using the local density approximation (LDA) together with the gradient-corrected exchange of Becke [120] and the correlation correction of Perdew [94, 121] (BVP86), and minima were verified by the absence of imaginary vibrational modes. These calculations were compared with results calculated using the meta-hybrid functional of Tao, Perdew, Staroverov and Scuseria (TPSSh) [122] and the Adamo hybrid functional of Perdew, Burke and Ernzerhof (PBE1PBE, known as PBE0 in the literature).[123] A 6-311++G(d,p) basis set was used for all atoms except Pb for which the standard SDD relativistic pseudopotential, ECP78MWB, was used.[124]

Excitation energies and oscillator strengths were calculated using time dependent density functional theory (TDDFT) for the optimized structures calculated using each

of the methodologies above (viz. BVP86, TPSSh and PBE0). The SCF step of TDDFT was performed using the long-range corrected hybrid exchange-correlation functional CAM-B3LYP (Coulomb-Attenuating Method B3LYP), [125] PBE0 and TPSSh. The dominant transitions predicted by TDDFT were analyzed by calculating the natural transition orbitals (NTOs)[126] for the purposes of identifying the contribution each orbital makes to an electronic transition. The results obtained were qualitatively similar and so only the CAM-B3LYP excitation at the BVP86 geometry is presented as this methodology provided the best overall agreement with experiment.

4.5 Calculated Structures and binding energy of $[Pb(benzene)_2]^{2+}$

All of the $[Pb(benzene)_2]^{2+}$ conformers were optimized as parallel geometries initially which were D_{6d} and D_{6h} symmetries respectively. However, these geometries had been found as stationary states and characterized by a large imaginary mode. To get rid of the imaginary mode, the D_{6d} and D_{6h} structures were distorted resulting in the bent hemi-directed analogues with symmetries C_2 (staggered) and C_{2v} (eclipsed), respectively. The rings of the sandwich complexes are not parallel anymore. Instead, they had a centroid-Pb-centroid angle of ~ 162° rather than 180°. The Pb-ligand bonds were usually found to be directed throughout only part of the coordination sphere for Pb(II) complexes,[109, 127] so it is possible that the calculated bent structures are a manifestation of this effect. The hemi-directed nature of Pb(II) complexes has been attributed to the "inert pair effect" ascribed to a relativistic effect causing the Pb(II) $6s^2$ orbital to contract. [127] The $[Pb(benzene)]^{2+}$ is essentially η^6 as expected, whereas the $[Pb(benzene)]^{+}$ is closer to η^1 with approximate C_s symmetry.

Table 4.1 provides the calculated binding energies with respect to complete neutral loss, defined as $[Pb(benzene)_2]^{2+} \rightarrow Pb^{2+}$ + 2benzene, charge transfer, defined as $[Pb(benzene)_2]^{2+} \rightarrow [Pb(benzene)]^{+}$ + $benzene^{+}$, and the incremental neutral loss,

defined as $[Pb(benzene)_2]^{2+} \rightarrow [Pb(benzene)]^{2+}$ + benzene. It is clear from this data that the staggered and eclipsed conformers for $[Pb(benzene)_2]^{2+}$ complex are extremely close in energy (within a $kJmol^{-1}$) and so all of the conformers are accessible in the ion trap.

Table 4.1 Binding energies for the $[Pb(benzene)_2]^{2+}$ complex with respect to various loss products and calculated using both BVP86/6-311++G(d,p)[SDD] and TPSSh/6-311++G(d,p)[SDD]

Reaction	$[Pb(Bz)_2]^{2+}$	Energy / $kJmol^{-1}$	
		BVP86	TPSSh
$[Pb(Bz)_2]^{2+} \rightarrow Pb^{2+} + 2\ (Bz)$	$^1A_1$ (C_{2v}: Eclipsed)	645.0	638.2
	^1A (C_2: Staggered)	644.8	638.2
$[Pb(Bz)_2]^{2+} \rightarrow [Pb(Bz)]^{+} + (Bz)^{+}$	$^1A_1$ (C_{2v}: Eclipsed)	24.2	22.5
	^1A (C_2: Staggered)	24.1	22.4
$[Pb(Bz)_2]^{2+} \rightarrow [Pb(Bz)]^{2+} + (Bz)$	$^1A_1$ (C_{2v}: Eclipsed)	191.6	192.4
	^1A (C_2: Staggered)	191.5	192.3

4.6 TDDFT Excited States Calculation of $[Pb(benzene)_2]^{2+}$

The excitation energies and oscillator strengths for both the C_2 (staggered) and C_{2v} (eclipsed) structures of the $[Pb(benzene)_2]^{2+}$ complex using CAM-B3LYP functional based on BVP86 and TPSSh optimized geometries are plotted as stick spectra overlaid with the experimental UV spectra in Figure 4.3 and Figure 4.5. The assignment of dominant transition and nature of these electronic transitions are listed in Table 4.2 and Table 4.3. From Figure 4.3, no transitions were predicted to occur below 37000 cm^{-1} and both structures, gave just one very strong (oscillator strength, f = 0.9) ligand-to-metal charge transfer (LMCT) electronic transition at 43243 cm^{-1} and 43276 cm^{-1}, respectively (see Table 4.2), with a number of much weaker transitions (f < 0.002) in the experimental range. Figure 4.4 provides the NTO orbitals involved in the two configurations that give rise to the transition at 43276 cm^{-1}, and are representative of the other LMCT transitions that are calculated to be present. The same transitions using the TPSSh geometry with TD-CAM-B3LYP reside at ~44000

cm^{-1} (Figure 4.5). From the results it can be seen that the dominant calculated transitions coincides reasonably well with the large experimental feature at ~45500 cm^{-1}. However, the calculations fail to match the two relatively small features observed at 39800 and 42000 cm^{-1} in the spectra.

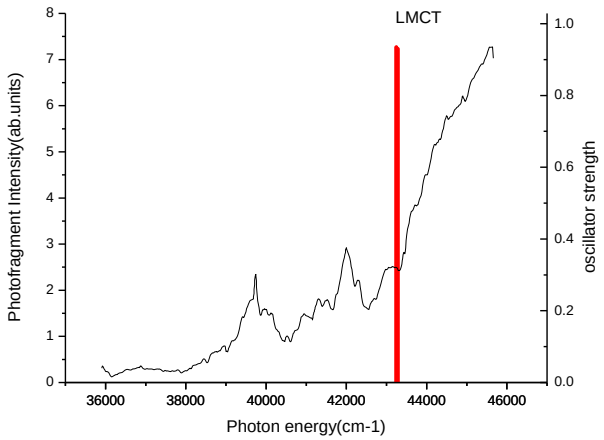

Figure 4.3 UV photofragmentation spectroscopy of $[Pb(benzene)_2]^{2+}$ overlaid with the electronic excitation energies calculated using TDDFT (CAM-B3LYP/6-311++G(d,p)[SDD] at BVP86 geometry). The calculated transitions are shown as vertical lines and are for two conformers (C_2 and C_{2v}) of $[Pb(benzene)_2]^{2+}$; on the scale of the plot the individual transitions are not resolved.

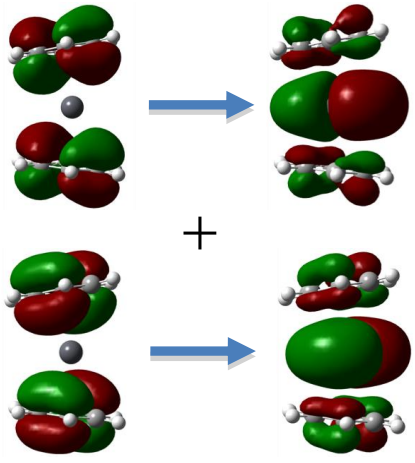

Figure 4.4 Configurations involved in the dominant electronic excitation of C_{2v} $[Pb(benzene)_2]^{2+}$ at 43276 cm^{-1}. This Ligand-to-Metal ($\pi \rightarrow$ 6p) Charge Transfer (LMCT) transition is

representative of other LMCT transitions. The lead atom is depicted at the centre of the structure as a grey sphere.

Table 4.2 Summary of the observed peak positions and the calculated TDDFT (CAM-B3LYP/6-311++G(d,p)[SDD] at BVP86 geometry) electronic transitions and oscillator strengths (f ≥ 0.01 in the experimental range 35000-45000 cm^{-1}) for $[Pb(benzene)_2]^{2+}$. The weight and character of the dominant configurations, and the % Pb character are also provided.

Peak position/cm^{-1}					
Observed	Structure	Calculated	f	NTO description	Assignment
~45500	C_2	43243	0.936	LMCT (51%) +LMCT (46%)	LMCT $\pi \rightarrow$ 6p (> 95% Pb)
~45500	C_{2v}	43276	0.932	LMCT (52%) +LMCT (45%)	LMCT $\pi \rightarrow$ 6p (> 95% Pb)

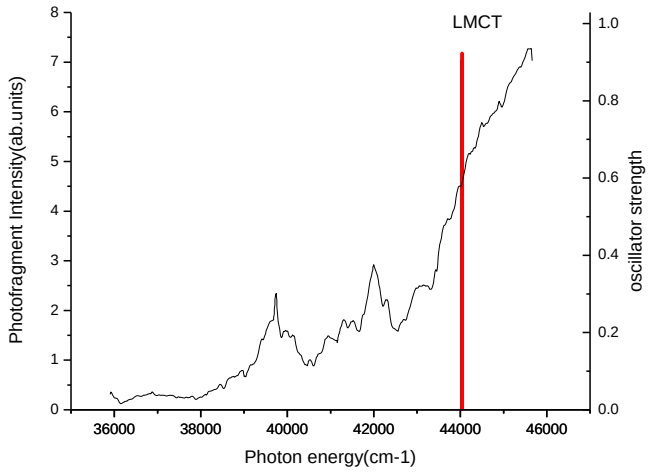

Figure 4.5 UV photofragmentation spectroscopy of $[Pb(benzene)_2]^{2+}$ overlaid with electronic excitation energies calculated using TDDFT (CAM-B3LYP/6-311++G(d,p)[SDD] at TPSSh geometry). The calculated transitions are shown as vertical lines and are for two conformers (C_2 and C_{2v}) of $[Pb(benzene)_2]^{2+}$; on the scale of the plot the individual transitions are not resolved.

Table 4.3 Summary of the observed peak positions and the calculated TDDFT (CAM-B3LYP/6-311++G(d,p)[SDD] at TPSSh geometry) electronic transitions and oscillator strengths (f ≥ 0.01 in the experimental range 35000-45000 cm^{-1}) for $[Pb(benzene)_2]^{2+}$. The weight and character of the dominant configurations, and the % Pb character are also provided.

Peak position/cm^{-1}					
Observed	Structure	Calculated	f	NTO description	Assignment
~45500	C_2	44031	0.9039	LMCT (54%)+ LMCT (42%)	LMCT $\pi \rightarrow$ 6p (94% Pb)
~45500	C_{2v}	44043	0.9234	LMCT (53%) +LMCT (44%)	LMCT $\pi \rightarrow$ 6p (95% Pb)

To investigate further the origin(s) of these additional features, calculated excitation energies and oscillator strengths for the $[Pb(benzene)]^+$ fragment, based on BVP86 and TPSSh geometries are plotted as stick spectra on the experimental photofragment spectra in Figure 4.6 and Figure 4.7, tabulated in Table 4.4 and Table 4.5. From both of them, there are four calculated transitions in the experimental range (with f ≥ 0.01), and they are a good match with features that have been recorded in the experimental spectrum. Furthermore, three of the excitations are LMCT. This level of agreement suggests that the $benzene^+$ photofragment could come from the photodissociation of $[Pb(benzene)]^+$, which in turn is a product of the photofragmentation of $[Pb(benzene)_2]^{2+}$. However, it should be noted that the electronic transitions calculated for $[Pb(benzene)]^+$ have associated with them a significant degree of spin contamination.

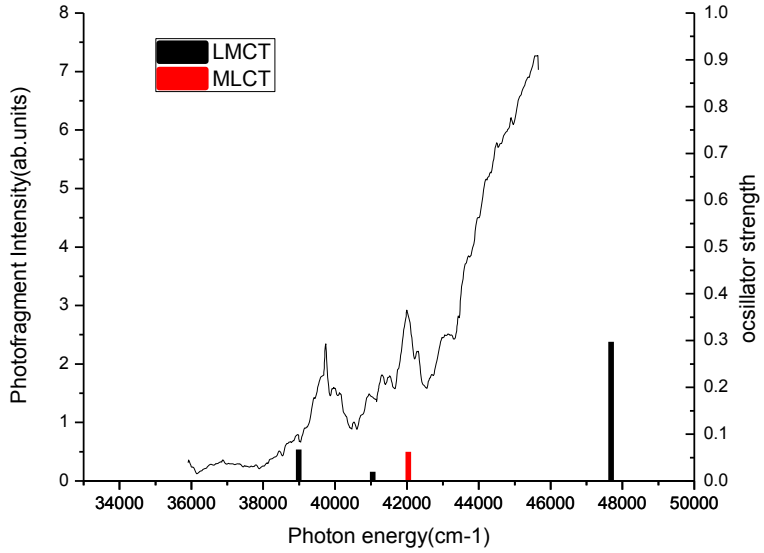

Figure 4.6 UV photofragmentation spectroscopy of $[Pb(benzene)_2]^{2+}$ overlaid with the electronic excitation energies calculated for $[Pb(benzene)]^+$ using TDDFT (CAM-B3LYP/6-311++G(d,p)[SDD] at BVP86 geometry). The calculated results are shown as vertical lines.

Table 4.4 Summary of the observed peak positions and the calculated TDDFT (CAM-B3LYP/6-311++G(d,p)[SDD] at BVP86 geometry) electronic transitions and oscillator strengths ($f \geq 0.01$ in the experimental range 35,000 – 45,000 cm^{-1}) for $[Pb(benzene)]^+$. The weight and character of the dominant configuration for each spin and the % Pb character are also given along with the total spin operator values $<\hat{S}^2>$, which should be 0.75 in the absence of contamination.

Peak position/cm^{-1}					
Observed	Calculated	f	$<\hat{S}^2>$	NTO description	Assignment
39800	38990	0.0672	0.995	α-LMCT (49%) β-LMCT (110 %)	LMCT π → 6p (> 80% Pb)
-	41050	0.0196	1.892	α-LMCT (69%) β-LMCT (89 %)	LMCT π → 6p (> 64% Pb)
42000	42038	0.0623	0.771	α-MLCT (196%) β-MLMLCT (1.7 %)	MLCT 6p (94% Pb)→ σ* + s (12% Pb)
~45500	47680	0.2974	0.758	α-LMCT (78%) β-LMCT (85 %)	LMCT π → 6p (> 66% Pb)

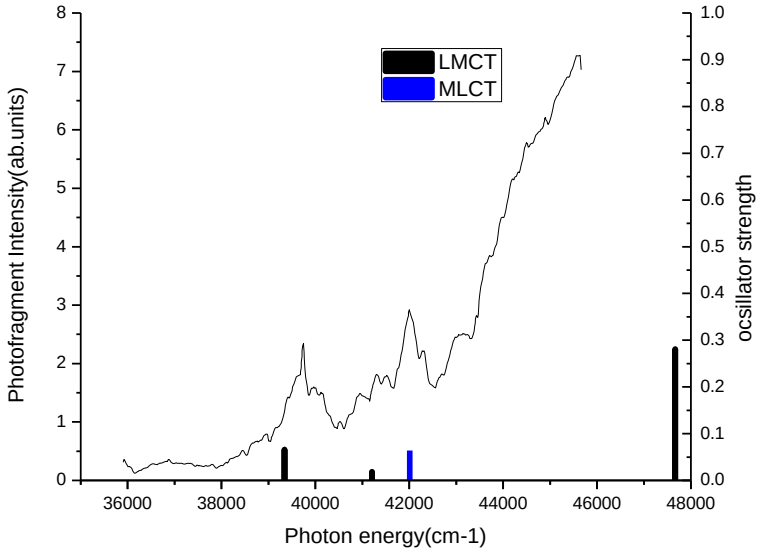

Figure 4.7 UV photofragmentation spectroscopy of $[Pb(benzene)_2]^{2+}$ overlaid with the electronic excitation energies calculated for $[Pb(benzene)]^+$ using TDDFT (CAM-B3LYP/6-311++G(d,p)[SDD] at TPSSh geometry). The calculated results are shown as vertical lines.

Table 4.5 Summary of the observed peak positions and the calculated TDDFT (CAM-B3LYP/6-311++G(d,p)[SDD] at TPSSh geometry) electronic transitions and oscillator strengths ($f \geq 0.01$ in the experimental range 35,000 – 45,000 cm^{-1}) for $[Pb(benzene)]^+$. The weight and character of the dominant configuration for each spin and the % Pb character are also given along with the total spin operator values, $\langle \hat{S}^2 \rangle$, which should be 0.75 in the absence of contamination.

Peak position/cm^{-1}					
Observed	Calculated	f	$\langle \hat{S}^2 \rangle$	NTO description	Assignment
39800	39342	0.0663	1.012	α-LMCT (46%) β-LMCT (113 %)	LMCT π → 6p (> 82% Pb)
-	41206	0.0184	1.952	α-LMCT (72%) β-LMCT (83 %)	LMCT π → 6p (> 60% Pb)
42000	42011	0.064	0.778	α-MLCT (196%) β-MLMLCT (1.7 %)	MLCT 6p (94% Pb)→ σ* + s (12% Pb)
~45500	47664	0.2813	0.759	α-LMCT (78%) β-LMCT (84 %)	LMCT π → 6p (> 70% Pb)

On the other hand, the calculated excitation energies and oscillator strengths for the $[Pb(benzene)]^{2+}$ fragment generated based on BVP86 and TPSSh geometries are also plotted overlaid with the experimental spectra in Figure 4.10 and Figure 4.11, tabulated in Table 4.6 and Table 4.7. There is no electronic transition can be found in the experimental range and the only dominant transition close to the experimental range appears around ~51000 cm^{-1}.

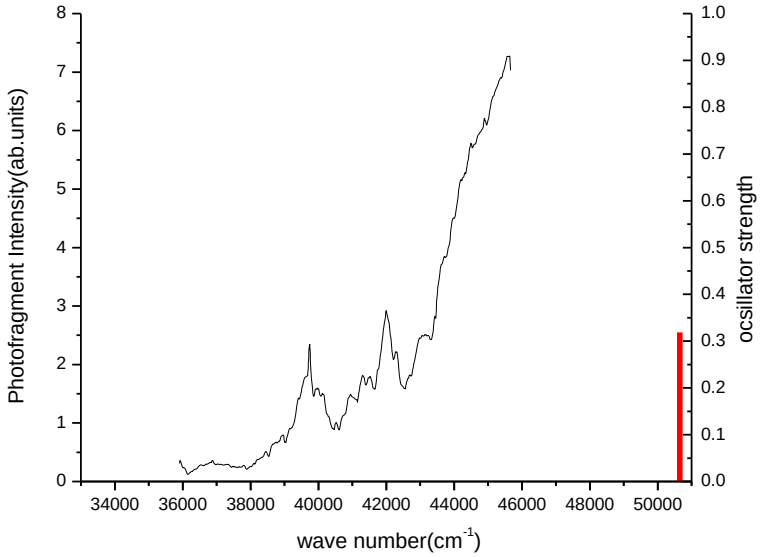

Figure 4.10 UV photofragmentation spectroscopy of $[Pb(benzene)_2]^{2+}$ overlaid with the electronic excitation energies calculated for $[Pb(benzene)]^{2+}$ using TDDFT (CAM-B3LYP/6-311++G(d,p)[SDD] at BVP86 geometry). The calculated results are shown as vertical lines.

Table 4.6 Summary of the observed peak positions and the calculated TDDFT (CAM-B3LYP/6-311++G(d,p)[SDD] at BVP86 geometry) electronic transitions and oscillator strengths (f ≥ 0.01 in the experimental range 35000-45000 cm^{-1}) for $[Pb(benzene)]^{2+}$. The weight and character of the dominant configurations, and the % Pb character are also provided.

Peak position/cm^{-1}			
Calculated	f	Assignment	orbitals
50656	0.319	(LM)MCT (46%) (LM)MCT (46%)	LMCT π +6p (10%) $\rightarrow$ 6p (93% Pb)

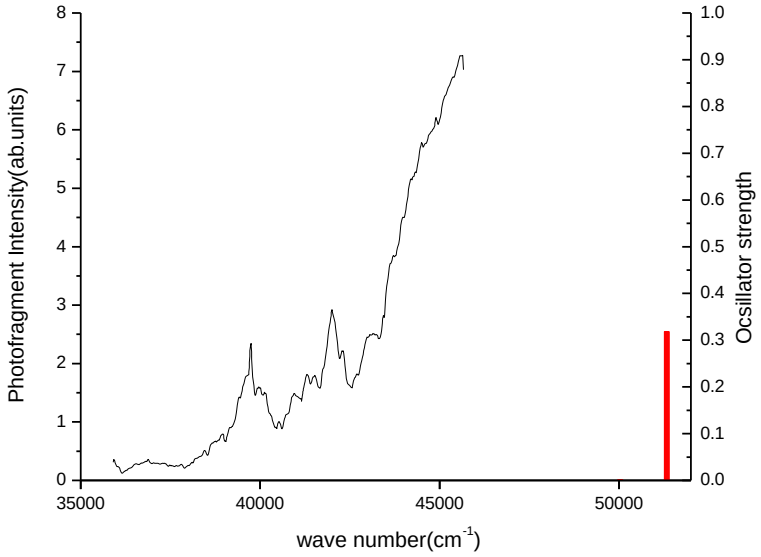

Figure 4.11 UV photofragmentation spectroscopy of $[Pb(benzene)_2]^{2+}$ overlaid with the electronic excitation energies calculated for $[Pb(benzene)]^{2+}$ using TDDFT (CAM-B3LYP/6-311++G(d,p)[SDD] at TPSSh geometry). The calculated results are shown as vertical lines.

Table 4.7 Summary of the observed peak positions and the calculated TDDFT (CAM-B3LYP/6-311++G(d,p)[SDD] at TPSSh geometry) electronic transitions and oscillator strengths (f ≥ 0.01 in the experimental range 35000-45000 cm^{-1}) for $[Pb(benzene)]^{2+}$. The weight and character of the dominant configurations, and the % Pb character are also provided.

Peak position/cm^{-1}			
Calculated	Oscillator Strength, *f*	NTO description	Assignment
51324	0.3184	(LM)MCT (46%) (LM)MCT (46%)	LMCT π +6p (10%) $\rightarrow$ 6p (93% Pb)

From what has been discussed above, it can be found that the excitations in $[Pb(benzene)_2]^{2+}$ calculated by TDDFT-CAM-B3LYP/6-311++G(d,p)[SDD] match the large feature in the experimental spectra. However, they cannot be afford to match all of the features in the UV spectra without the aid of calculated excitations in the $[Pb(benzene)]^{+}$. Thus, in order to achieve a good agreement of the theoretical data and the experimental spectrum, the two sets of calculation data has been put together in

one image overlaid with the experimental spectra. The TDDFT-CAM-B3LYP/6-311++G(d,p)[SDD] data based on BVP86 optimized geometry of $[Pb(benzene)_2]^{2+}$ and $[Pb(benzene)]^{+}$ has been selected as an example and showed in Figure 4.12.

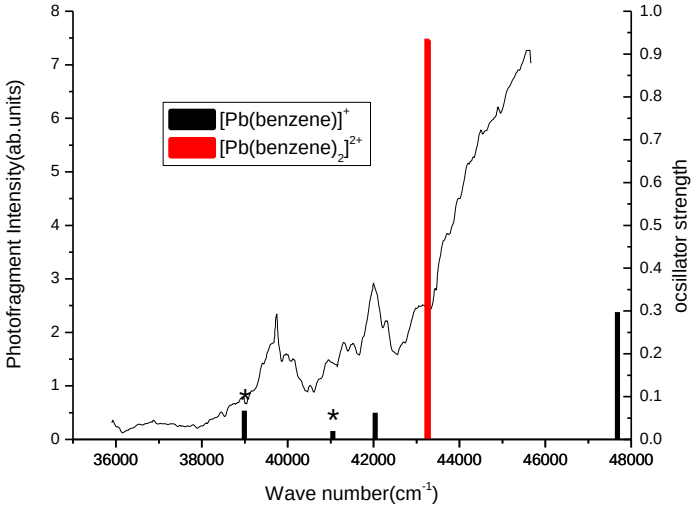

Figure 4.12 Experimental spectrum overlaid with both the dication $[Pb(benzene)_2]^{2+}$ and the mono-cation $[Pb(benzene)]^{+}$ TDDFT-CAM-B3LYP data based on BVP86 geometry. The calculated transitions are in different colours so it's clear which peaks are from the dication and which are from the monocation. The electronic transitions are labeled with asterisk (*) if they are significantly spin contaminated.

The excitation energy and oscillator strength of most intense electronic transitions for two conformers of $[Pb(benzene)_2]^{2+}$ optimized by BVP86, PBE0 and TPSSh functional, calculated on the CAM-B3LYP, PBE0 and TPSSh/6-311++G(d,p)[SDD] level are detailed in Table 4.8. From this table, one can notice that the excitation data, and assignment for the most dominant electronic transition obtained with different methodologies are consistent, except for some shift in excitation energies and oscillator strengths. The nature of the electronic transition does not change throughout different functional, but there is some slight difference on the contribution from their frontier orbital as expected.

Table 4.8 Comparison of the dominant transition for the two conformers of $[Pb(benzene)_2]^{2+}$. The notation TD-functional1/functional2 is used to indicate the functional used in the TD calculation and the geometry optimization, respectively. The 6-311++G(d,p) basis set with SDD on Pb was used in all cases.

Method	C_2 (staggered)			
	E / cm^{-1}	f	NTO description	Assignment
TD-CAM-B3LYP/BVP86	43243	0.94	LMCT (51%) +LMCT (46%)	LMCT $\pi \rightarrow$ 6p (> 95% Pb)
TD-CAM-B3LYP/TPSSh	44031	0.90	LMCT (54%)+ LMCT (42%)	LMCT $\pi \rightarrow$ 6p (94% Pb)
TD-PBE0/BVP86	41004	0.84	LMCT (51%)+ LMCT (46%)	LMCT $\pi \rightarrow$ 6p (95% Pb)
TD-PBE0/TPSSh	38548	0.67	LMCT (52%)+ LMCT (42%)	LMCT $\pi \rightarrow$ 6p (91% Pb)
TD-TPSSh/BVP86	39606	0.79	LMCT (50%)+ LMCT (45%)	LMCT $\pi \rightarrow$ 6p (95% Pb)
TD-TPSSh/TPSSh	40381	0.76	LMCT (54%)+ LMCT (42%)	LMCT $\pi \rightarrow$ 6p (93% Pb)
	C_{2v} (eclipsed)			
TD-CAM-B3LYP/BVP86	43276	0.93	LMCT (52%) +LMCT (45%)	LMCT $\pi \rightarrow$ 6p (> 95% Pb)
TD-CAM-B3LYP/TPSSh	44023	0.90	LMCT (53%) +LMCT (44%)	LMCT $\pi \rightarrow$ 6p (95% Pb)
TD-CAM-B3LYP/PBE0	44526	0.90	LMCT (55%) +LMCT (41%)	LMCT $\pi \rightarrow$ 6p (94% Pb)
TD-PBE0/BVP86	41027	0.84	LMCT (52%) +LMCT (45%)	LMCT $\pi \rightarrow$ 6p (94% Pb)
TD-PBE0/TPSSh	38543	0.67	LMCT (52%) +LMCT (42%)	LMCT $\pi \rightarrow$ 6p (91% Pb)
TD-PBE0/PBE0	39023	0.66	LMCT (53%) +LMCT (41%)	LMCT $\pi \rightarrow$ 6p (90% Pb)
TD-TPSSh/BVP86	39678	0.80	LMCT (48%) +LMCT (47%)	LMCT $\pi \rightarrow$ 6p (96% Pb)
TD-TPSSh/TPSSh	40370	0.76	LMCT (54%) +LMCT (42%)	LMCT $\pi \rightarrow$ 6p (93% Pb)
TD-TPSSh/PBE0	40869	0.75	LMCT (55%) +LMCT (41%)	LMCT $\pi \rightarrow$ 6p (93% Pb)

4.7 Photofragmentation mechanism

The calculations above have identified contributions to the UV photofragmentation spectra of $[Pb(benzene)_2]^{2+}$ that could arise from singly and doubly charged lead-

containing ions. Taking this observation together with the fact that the photofragment mass spectra display just a single non-metallic fragment, two possible mechanisms that are capable of generating the product ions of interest are:

$$[Pb(benzene)_2]^{2+} + h\gamma \rightarrow [Pb(benzene)]^{+} + benzene^{+}$$

$$[Pb(benzene)]^{+} + h\gamma \rightarrow Pb + benzene^{+} \qquad (1)$$

$$[Pb(benzene)_2]^{2+} + h\gamma \rightarrow [Pb(benzene)]^{2+} + benzene$$

$$[Pb(benzene)]^{2+} \rightarrow Pb^{+} + benzene^{+} \qquad (2)$$

Each mechanism presents a problem in that $C_6H_6^+$ is the only photofragment to be observed. Thus, with mechanism (1) the second step might be expected to yield Pb^+ rather than $C_6H_6^+$ because lead has a lower first ionization energy (IE(Pb) = 7.42 eV and IE(Bz) = 9.24 eV). Likewise, mechanism (2) should yield Pb^+, which is not the case. Mechanism (1) could make sense if $Pb(benzene)^+$ fragmented from an electronic excited state that correlated with $C_6H_6^+$ as a reaction fragment. A charge transfer step of this nature has been observed following the photoexcitation of singly charged $[Pb(benzene)]^+$ and $[Pb(benzene)_2]^+$ complexes at visible wavelengths.[128] Additional contributions to the photofragment spectrum could also come from $[Pb(benzene)]^+$ should it remain in the trap during each cycle. An earlier study of the formation and fragmentation of Pb^{2+} complexes failed to observe $[Pb(benzene)]^{2+}$[5e], which would suggest that the dimer complex is unstable and that second step in mechanism (2) should be spontaneous following the loss of neutral benzene from $[Pb(benzene)_2]^{2+}$. That being the case, then Pb^+ should be observed in the trap; however, charge transfer followed by Coulomb explosion will release up to 1.8 eV of kinetic energy. The corresponding momentum of Pb^+ could be sufficiently high that the very light helium containment gas is unable to quench and confine the ion to the trap. Previous experiments have shown the trapping efficiency for metal complexes to be extremely

sensitive to ion kinetic energy.[59] As discussed earlier, one reason why heavy singly charged fragments from Coulomb explosion are not be observed in the mass spectra is that they acquire sufficient momentum that they cannot be contained in the trap by collisions with the very much lighter helium gas. Since Coulomb explosion occurs on a ~ 10^{-13} s timescale, as $[Pb(benzene)]^+$ passes through the trap it will remain susceptible to photofragmentation from the residual photons in each 5 ns laser pulse. The spectral features attributed to $[Pb(benzene)]^+$ were found to be strongly dependent on laser power.

Either mechanism will only work if Coulomb fission imparts sufficient momentum to the metal-containing fragment that it cannot be contained within the trap. Mechanism 2 provides the most obvious route to the appearance of $benzene^+$ as the principal photofragment. However, the match between calculated and experimental spectra provides evidence for the presence of $[Pb(benzene)]^+$ ions at some point in the photoexcitation cycle. Then mechanism 1 in association with a charge transfer transition in the second step must also make a contribution.

4.8 Spin contamination in open-shell excited states

Adiabatic TDDFT is a single excitation theory and neglects additional roots stemming from the interaction between single and double excitations.[129] Spin contamination is the extent to which the calculated $<\hat{S}^2>$ value differs from the expected eigenvalue of the same operator. Spin contamination in open-shell excited states results from the absence of double- or higher-excitations needed to correctly describe spin-permuted configurations.[130]

The types of excitation arising from a doublet ground state, such as that of $[Pb(benzene)]^+$, can be categorised into 3 types (see Figure 4.8). Type I and Type II involve the singly-occupied molecular orbital (SOMO) and can represent proper spectroscopic states as they are clearly doublets and well described by a single

excitation theory. However, the Type III excitations give states, as single determinants, which are not in themselves eigenfunctions of the spin operator $\langle \hat{S}^2 \rangle$. They are part of the manifold of configurations associated with 'three electrons in three orbitals'.

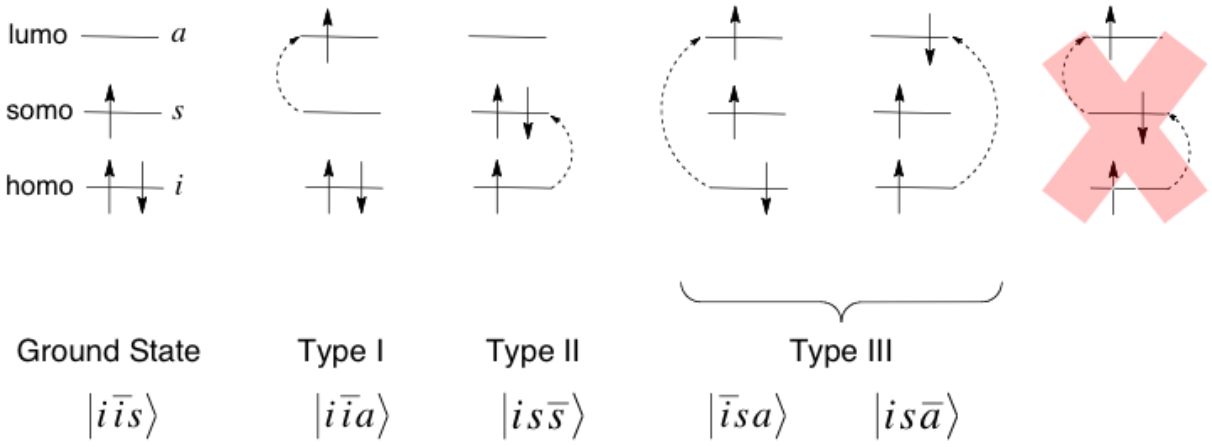

Figure 4.8 The types of excitation arising from a doublet ground state. Where i represents a doubly occupied orbital, s represents the singly occupied orbital, and α represents an unoccupied orbital. The presence or absence of a bar over i, s or α indicates a beta or alpha spin electron, respectively.[131]

To describe the states arising from Type III excitations (i.e., $|\bar{i}sa\rangle$ and $|is\bar{a}\rangle$), spin-adapted linear combinations are required. The linear combinations of the M_S = +1/2 configuration state functions arising from 'three electrons in three orbitals' (shown in Figure 4.8) are constructed using the S_3 symmetry group which is isomorphic to C_{3v}. From the three determinants, a quartet (S=3/2) and two doublets (S=1/2) each with M_S = +1/2 arise,

$$\psi_Q = \frac{1}{\sqrt{3}}\left(|\bar{i}sa\rangle + |is\bar{a}\rangle + |i\bar{s}a\rangle\right)$$

$$\psi_{D_1} = \frac{1}{\sqrt{2}}\left(|\bar{i}sa\rangle - |is\bar{a}\rangle\right)$$

$$\psi_{D_2} = \frac{1}{\sqrt{6}}\left(|\bar{i}sa\rangle + |is\bar{a}\rangle - 2|i\bar{s}a\rangle\right)$$

Since ordinary TDDFT cannot flip spins only singlet-coupled and triplet-coupled excitations may occur,[130] i.e.,

$$\frac{1}{\sqrt{2}}\left(\left|\bar{i}sa\right\rangle \pm \left|is\bar{a}\right\rangle\right)$$

Therefore, only doublet 1 has a clear physical interpretation as a true eigenfunction of the spin operator, and may have nonzero oscillator strength. As the coupling in doublet 2 involves the spin-flip configuration $\left|i\bar{s}a\right\rangle$ which is nominally a spin-flip or double excitation, only the unphysical triplet-coupled excited state will be found and must be either discarded or the effects of the missing configuration must be included. Ipatov and co-workers[130] have recently provided a formula for determining excited state spin contamination in spin unrestricted TDDFT calculations and this has been implemented in Gaussian 09. For a doublet system, the $<\hat{S}^2>$ value should be 0.75. Clearly several of the values presented above (Table 4.4 and Table 4.5) are severely spin contaminated and should ideally be discarded. Assuming that the quartet state ($<\hat{S}^2>$ = 3.75) constitutes the primary source of contamination in the cations, i.e.,

$$|Pb(benzene)^{+}\rangle = C_D|doublet\rangle + C_Q|quartet\rangle$$

$$\left\langle \hat{S}^2_{calc} \right\rangle = 0.75|C_D|^2 + 3.75\left|C_Q\right|^2$$

The percentage doublet character in the Kohn-Sham wave function for each of the open shell excited states are calculated and listed in Table 4.9. The excitations at 42038 and 47680 cm^{-1} are >99% doublet in character and so it is safe to classify these states as primarily doublet in character. However, the excitation at 41050 cm^{-1} is severely spin contaminated with $\Delta\hat{S}^2\approx1$ which corresponds to states which are too spin contaminated to be considered further as it is ill-defined (i.e., not singlet- or triplet-coupled TDDFT excitations, the latter would result in $\Delta\hat{S}^2\approx2$) and unphysical. It should be discarded. The validity of the excitation at 38990 cm^{-1} with $\Delta\hat{S}^2\approx0.25$ is questionable. Assuming that all spin contamination comes from the next highest

allowed spin component, the excited states are around 90% doublet in character, and so an excitation in this region is likely.

Table 4.9 The excited state spin contamination in each of the [Pb(benzene)]$^+$ excited states calculated by TDDFT-CAM-B3LYP/6-311++G(d,p)[SDD] for BVP86 geometry, assuming that all spin contamination comes from the next highest allowed spin component. The significantly spin contaminated entry is in bold.

E(cm^{-1})	$<\hat{S}^2>$	$\Delta<\hat{S}^2>$	Doublet character(%)	Spin contamination (%)
38990	1.00	0.25	91.8	8.2
41050	**1.89**	**1.14**	**61.9**	**38.1**
42038	0.77	0.02	99.3	0.7
47680	0.76	0.01	99.7	0.3

To further analyse this problem, the TDDFT electronic excitation energies of [Pb(benzene)]$^+$ (Figure 4.9) are presented below along with the nature of the orbitals involved in the most dominant transitions. Herein, we have assumed same orbitals with different spins (SODS), however, the calculations were performed using different orbitals for different spins (DODS).

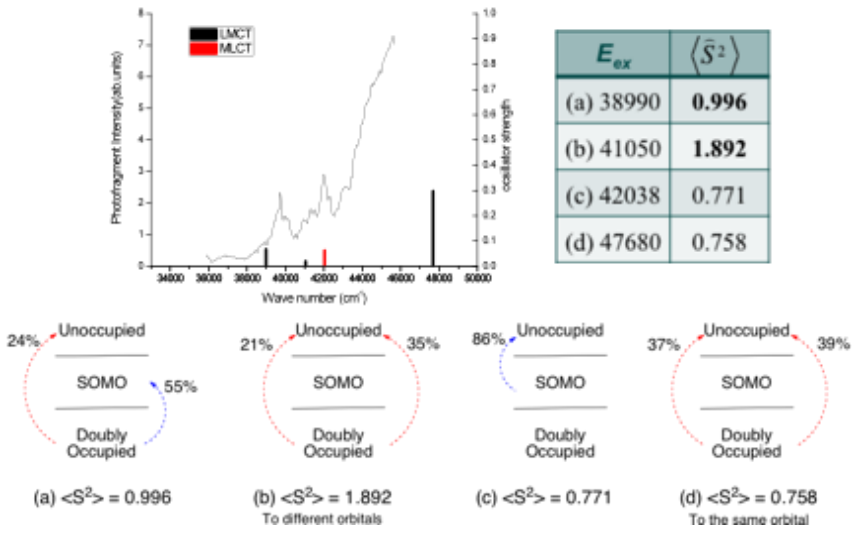

Figure 4.9 Analysis of the TDDFT (CAM-B3LYP/6-311++G(d,p)[SDD] based on BVP86 geometry) excitations arising from the [Pb(benzene)]$^+$ complex. The percentage is calculated by taking the square of the coefficient of the transition. The analysis is rather a rough guide than a definite

interpretation because the calculations are performed using DODS (different orbitals for different spin), whereas we assume the same orbital for different spins (e.g., 23A(alpha)=23B(beta)) while the calculations do not impose this. [131]

It is clear from this analysis that excitation (c) at 42038 cm^{-1} is reliable; it is a Type I excitation. Excitation (a) at 38990 cm^{-1} is predominantly type II but with some unphysical type III, which is reflected in the deviations of $<\hat{S}^2>$ from the true value of 0.75. Excitation (b) is clearly an unphysical triplet-coupled excitation and should be discarded. Excitation (d) is not significantly spin contaminated and can be assumed to arise from the physical singlet-coupled excitation (doublet 1 above). This is particularly interesting, as it demonstrates the vital need for computational quantum chemistry programs to implement the calculation of the $<\hat{S}^2>$ value of excited states, as a simple analysis of the orbitals involved is insufficient to distinguish between the unphysical and physical Type III excitations of (b) and (d).

4.9 Conclusions

The gas phase UV spectra of the dication sandwich complexes, $[Pb(benzene)_2]^{2+}$ has been recorded from ions that have been held and cooled in an ion trap. The TDDFT calculations have revealed that the dication is most likely responsible for the largest experimental feature at ~ 45500 cm^{-1}. This is a $\pi \rightarrow$ Pb (6p) LMCT transition. To account for the smaller features the spectra of $[Pb(benzene)]^+$ must be considered. It is shown that the calculated energy difference between the $[Pb(benzene)_2]^{2+}$ and its charge transfer asymptote is very small, < 25 $kJmol^{-1}$, and thus it is likely that a $[Pb(benzene)]^+$ transient intermediate is present. The TDDFT excitations of $[Pb(benzene)]^+$ are in excellent agreement with the experimental features, however, it must be noted that these states are severely spin contaminated.

In summary, this combined theory and experimental investigation has successfully accounted for the electronic spectra of Pb(II)-bis(benzene) sandwich complex.

However, it is also clear from the theory, that the product of photoexcitation $[Pb(benzene)]^+$, must also be considered to fully evaluate the spectra. The success of TDDFT both in terms of the transition energies and the relative oscillator strengths that mirror the experimental photofragment yields beautifully, further demonstrates the unprecedented success of this method. However, for open-shell complexes further work is imperative to understand why the adiabatic TDDFT method, a single excitation theory, can provide quantitative agreement to experiment with spin-contaminated states caused by double excitation character.

Chapter 5 Conformation resolved ultraviolet photofragmentation spectroscopy of dication lead-bis(toluene) sandwich complex combined with DFT/TDDFT calculations

5.1 Introduction

In the previous chapter, the significance of gas phase investigation of lead dication sandwich complex has been enunciated. The gas-phase UV photofragment spectroscopy of $[Pb(benzene)_2]^{2+}$ has been reported and assigned successfully by the TDDFT calculations. However, one may notice that the only feature in the UV spectra that can be assigned by the TDDFT data extends beyond the upper limit of laser wavelength that was applied in the experiment. Therefore, a perfect match between the calculated LMCT transitions in the $[Pb(benzene)_2]^{2+}$ and the feature in its spectra can be only presumed rather than actually seen while part of the feature is missing.

To further confirm the photodissociation behavior of lead dication sandwich complexes within the ion trap and to further bench mark the theory that is modeling electronic excitations in this species, recording the spectra of a different but comparable analogous lead complex will be very helpful. It is apparent that a better assignment can be expected when the lead dication complex is bearing a ligand that can bring down the photon energy required to access the LMCT transitions. In this case, adding an electron donating group such as a methyl group to the benzene ring will obviously lead to higher electronegativity of the ligand and lower the energy gap between the acceptor (metal ion) and donor (ligand).[132] Since the energy of charge transfer band is very sensitive to the difference of ligand and metal ion, the photon energy required to access the charge transfer transition would be lower, whereby the feature arising from these transitions should red-shift in wavelength in the electronic spectra.[133] On the other hand, the closed shell lead dication species has been found to

produce simple spectra in the former chapter. To retain this metal center and change the ligand could offer an opportunity to explore the possibility of developing the spectroscopic mark for this metal ion.[10] According to the vapor pressure and complexation of toluene, a sufficient number density for spectroscopic measurement can be expected while the experiment is operating under the same condition as the lead benzene case.

The UV spectra of benzene and toluene in the liquid phase have been shown in Figure 5.1.[134] It can be noticed that the toluene has a group of subtle absorption in the range of 240-265 nm and a resolved peak at around 268nm, while benzene is having large absorptions at around 178 nm. It indicates that the lead toluene complex spectra will be more complicated than its benzene analogue.

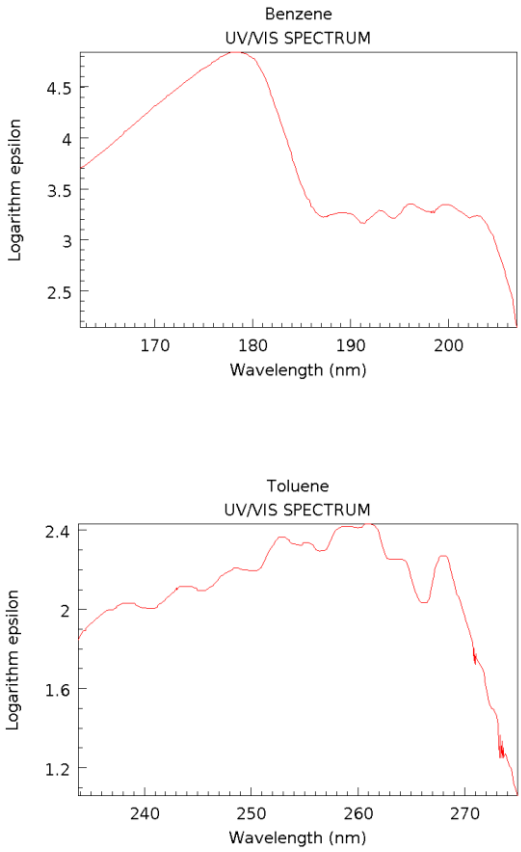

Figure 5.1 UV spectra of benzene and toluene in the liquid phase[134]

In general, the gas-phase spectroscopic measurement of $[Pb(toluene)_2]^{2+}$ is a reasonable extension of this line of research. Plus, by adding a methyl group to the benzene ring, toluene introduces the possibility for generating more conformers and makes the resultant spectra a good comparison with the lead benzene data. In this chapter, the UV photofragmentation spectroscopy of doubly charged lead-bis(toluene) sandwich complex has been recorded in the gas phase and combined with the DFT/TDDFT calculations for an assignment of the main features that appear in the UV spectra to all dominant electronic transitions in the range of photon energy.

5.2 Ultraviolet photofragment mass spectra of $[Pb(toluene)_2]^{2+}$

A detailed description of the experimental apparatus has been given in chapter 2. The data produced over every 200 ion trap cycles was averaged and recorded as a mass spectrum. The m/z scale was calibrated by the positions of the parent and major fragment peak. A typical example of the $[Pb(toluene)_2]^{2+}$ photofragment mass spectra is reported in Figure 5.2. It is a simple spectrum with three peaks clearly distinguishable from a low and consistent baseline. The example in Figure 5.2 shows two parent ion which are $[Pb(toluene)_2]^{2+}$ and $[Pb(toluene)_2H_2O]^{2+}$ and one fragment peak corresponding to the $toluene^+$ ion. As in the lead benzene case, this pattern indicated that the parent ion $[Pb(toluene)_2]^{2+}$ can pick up a water molecule from the background within the trap. The $[Pb(toluene)_2H_2O)]^{2+}$ peak was also seen in the warm trap (room temperature), however, the presence was minimal after cooling.

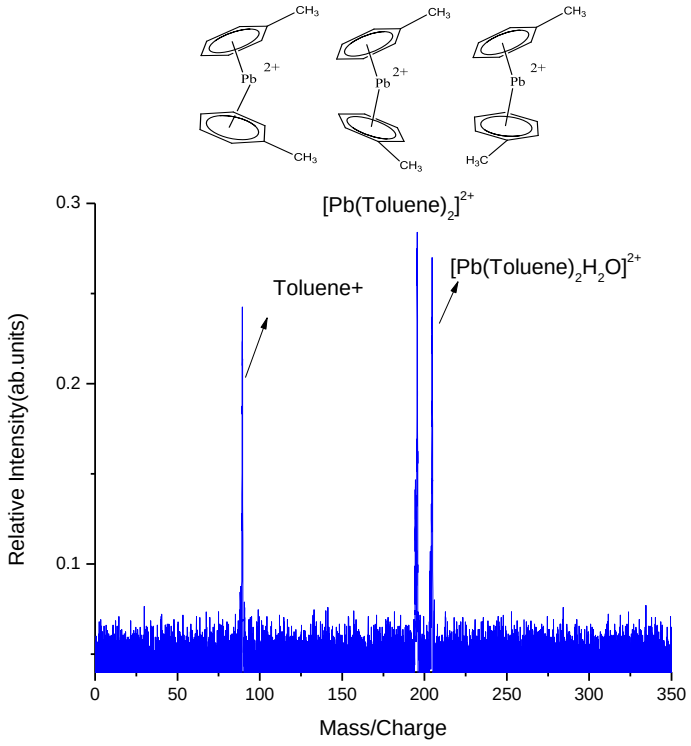

Figure 5.2 Photofragment mass spectrum of $[Pb(toluene)_2]^{2+}$ recorded by the ion trap mass spectrometer under laser radiation at an average photon energy of 41111 cm^{-1}. Possible structures that $[Pb(toluene)_2]^{2+}$ could adopt in the trap have been drawn on top of the spectra.

5.3 Ultraviolet photofragment Spectroscopy of $[Pb(toluene)_2]^{2+}$

Experimental UV photofragmentation spectra for $[Pb(toluene)_2]^{2+}$ is presented in Figure 5.3, and for the purposes of comparing the data, $[Pb(benzene)_2]^{2+}$ and $[Pb(toluene)_2]^{2+}$ spectra are presented together in Figure 5.4. For each scan the photofragment yield of the mass spectra were plotted against their respective photon energies and normalised by the laser power and parent ion signal intensity tendency.

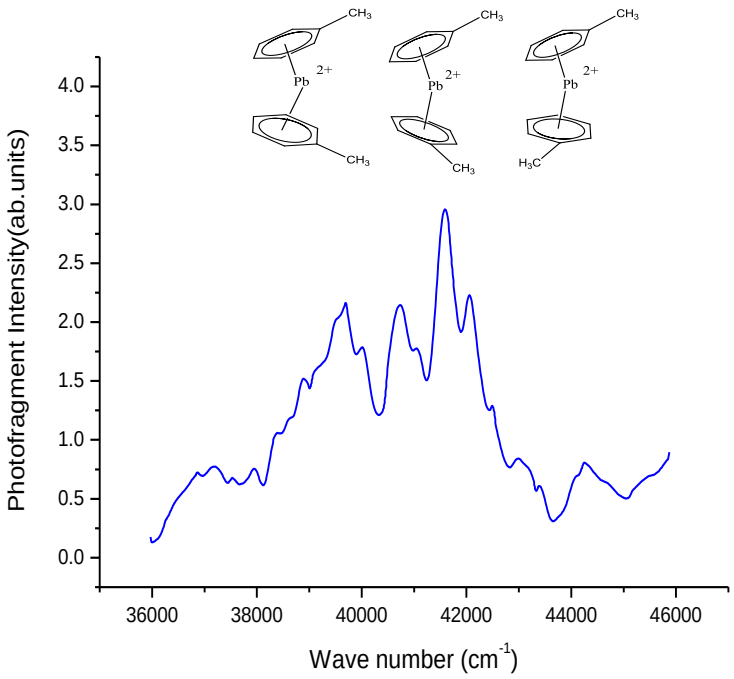

Figure 5.3 UV Photofragmentation spectroscopy of $[Pb(toluene)_2]^{2+}$. Possible structures that $[Pb(toluene)_2]^{2+}$ could adopt in the trap have been drawn on top of the spectra.

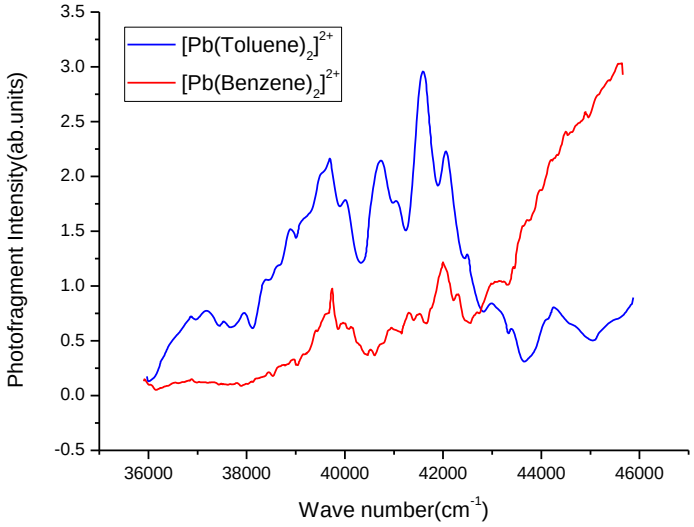

Figure 5.4 Comparison of UV Photofragmentation spectroscopy of $[Pb(benzene)_2]^{2+}$ and $[Pb(toluene)_2]^{2+}$

From Figure 5.3, it can be found that there are a number of resolved features in a spectrum that is very different from the recorded for $[Pb(benzene)_2]^{2+}$ spectrum. The spectrum consists of five main features at around 37000, 39700, 40700, 41600 and 44300 cm^{-1}. There is also a well-resolved peak at around 42000 cm^{-1} which sits close to the dominant peak at around 41600 cm^{-1}. From Figure 5.4, it can be observed that the two spectra share two features around 39800 and 42000 cm^{-1}. The UV spectra of $[Pb(benzene)_2]^{2+}$ has a significant broad feature beyond 45500 cm^{-1}, instead of a relative small feature around 44300 cm^{-1} in $[Pb(toluene)_2]^{2+}$ case.

5.4 Methodology of theoretical calculations

The structure and binding energy of $[Pb(toluene)_2]^{2+}$ and $[Pb(toluene)]^{+/2+}$ were calculated using density functional theory (DFT) as implemented in Gaussian09. Geometry optimization and frequency analysis were performed using the local density approximation (LDA) together with the gradient-corrected exchange of Becke [120] and the correlation correction of Perdew [94, 121] (BVP86), and minima were verified by the absence of imaginary vibrational modes. These calculations were compared with results calculated using the meta-hybrid functional of Tao, Perdew, Staroverov and Scuseria (TPSSh) [122] and the Adamo hybrid functional of Perdew, Burke and Ernzerhof (PBE1PBE, known as PBE0 in the literature).[123] A 6-311++G(d,p) basis set was used for all atoms except Pb for which the standard SDD relativistic pseudopotential, ECP78MWB, was used.[124] All energies presented are zero point energy corrected at 298 K.

Excitation energies and oscillator strengths were calculated using TDDFT for the optimized structures calculated using each of the methodologies above (viz. BVP86, TPSSh and PBE0). The TDDFT calculations were performed using the long-range corrected hybrid exchange-correlation functional CAM-B3LYP (Coulomb-Attenuating Method B3LYP), [125] PBE0 and TPSSh. The dominant transitions

predicted by TDDFT were analyzed by calculating the natural transition orbitals (NTOs)[126] for the purposes of identifying the contribution each orbital makes to an electronic transition. The results obtained were qualitatively similar so only the CAM-B3LYP excitations at the BVP86 and TPSSh geometry are presented as this methodology provided the best overall agreement with experiment.

5.5 Calculated Structures and binding energy of $[Pb(toluene)_2]^{2+}$

As similar as $[Pb(benzene)_2]^{2+}$, the $[Pb(toluene)_2]^{2+}$ complex has bent structures with either staggered rings (C_2 symmetry) or eclipsed rings (C_{2v} symmetry). However, due to the methyl group, this gives rise to an additional staggered conformation depending on the relative orientation of the methyl groups (i.e., cis or trans). The 3 minima identified will be referred to as: (i) eclipsed-cis, (ii) staggered-cis and (iii) staggered-trans. The eclipsed-cis structure calculated using the hybrid functionals TPSSh and PBE0 has a small imaginary mode (3i cm^{-1}). Distorting along this mode resulted in the staggered-cis conformation. However, for BPV86 the C_{2v} eclipsed-cis structure was a true minimum. The TPSSh energy in Table 5.1 is calculated using the symmetry-constrained C_{2v} structure. For a particular functional, the geometries of all 3 toluene structures were extremely similar, i.e., the metal-centroid distance and centroid-metal-centroid bond angle were within a tenth of a pm and within 1 degree, respectively. However, comparing functionals for each structure, the hybrid functionals (TPSSh and PBE0) both has a slightly shorter Pb-centroid distance (3 pm) than that of the BPV86 and a slightly wider bend angle (4°). The $[Pb(toluene)]^{2+}$ is closer to η^1 with approximate C_s symmetry (i.e., the shortest Pb-C distance involves the para-carbon of toluene). The $[Pb(toluene)]^{+}$ is also η^1 but in this case the Pb ion sits over the meta-carbon.

The calculated binding energies for three optimized geometry using BVP86 and TPSSh are detailed in table 5.1. The binding energy with respect to the complete

neutral loss, charge transfer and the incremental neutral loss are defined as equation 5.1-5.3, respectively. From table 5.1, it can be found that the calculated binding energy of all conformers for $[Pb(toluene)_2]^{2+}$ complex are very close (within a $kJmol^{-1}$) and the charge transfer binding energy is reported as the lowest value throughout all of the possible routes. The Pb(II)-toluene bond is slightly stronger than the Pb(II)-benzene bond, but in both cases, the charge transfer energy asymptote is very similar in energy to that of the $[Pb(benzene)_2]^{2+}$ complex.

$$\text{Binding Energy} = DFT([Pb(toluene)_2]^{2+}) - 2 \times DFT(toluene) - DFT(Pb^{2+}) \quad \text{(eq. 5.1)}$$

$$= DFT([Pb(toluene)_2]^{2+}) - DFT(toluene^{+}) - DFT([Pb(toluene)]^{+}) \quad \text{(eq. 5.2)}$$

$$= DFT([Pb(toluene)_2]^{2+}) - DFT(toluene) - DFT([Pb(toluene)]^{2+}) \quad \text{(eq. 5.3)}$$

Table 5.1 Binding energies for the three conformers of $[Pb(toluene)_2]^{2+}$ with respect to various loss products and calculated using both BVP86/6-311++G(d,p)[SDD] and TPSSh/6-311++G(d,p)[SDD] .

Reaction	$[Pb(tol)_2]^{2+}$	Energy / $kJmol^{-1}$	
		BVP86	TPSSh
$[Pb(tol)_2]^{2+} \rightarrow Pb^{2+} + 2\ (tol)$	C_{2v}: Eclipsed/Cis	692.1	682.7
	C_2: Staggered/Cis	692.0	682.6
	C_2: Staggered/Trans	692.0	682.7
$[Pb(tol)_2]^{2+} \rightarrow [Pb(tol)]^{+} + (tol)^{+}$	C_{2v}: Eclipsed/Cis	8.8	9.8
	C_2: Staggered/Cis	8.7	9.7
	C_2: Staggered/Trans	8.7	9.7
$[Pb(tol)_2]^{2+} \rightarrow [Pb(tol)]^{2+} + (tol)$	C_{2v}: Eclipsed/Cis	197.5	198.1
	C_2: Staggered/Cis	197.4	198.0
	C_2: Staggered/Trans	197.4	198.1

5.6 TDDFT Excited States Calculation of $[Pb(toluene)_2]^{2+}$

The calculated excitation energies and oscillator strengths for the three structures of $[Pb(toluene)_2]^{2+}$ based on BVP86 and TPSSh geometry are plotted as stick spectra on the experimental photofragment spectra in Figure 5.5 and Figure 5.7, respectively. The observed and calculated electronic transitions and their assignments are

summarized in Table 5.2 and 5.3. From Figure 5.5, together the three optimized structures yield seven dominant ($f > 0.05$) LMCT transitions (see entries in bold in Table 5.2). The positions of the calculated transitions can be matched to the two main features at 39700 and 41600 cm^{-1} and the third shoulder/peak at 42000 cm^{-1} in the UV spectrum. The calculation also predicts weaker transitions that can account for the additional features in the spectrum at approximately 37000 and 44300 cm^{-1} but fails to account adequately for the peak at 40700 cm^{-1}. Altogether, calculations provide thirteen electronic transitions ($f \geq 0.01$) arising from the three structures. Ten can be assigned predominantly to LMCT transitions, with those predicted to be at 39016 and 39663 cm^{-1} matching the substantial peak occurring at ~ 39700 cm^{-1}, and intense LMCT transitions predicted at 41844 and 41955 cm^{-1} showing excellent agreement with the large features at 41600 cm^{-1} and 42000 cm^{-1} in the experimental spectrum. Figure 5.6 provides the NTO orbitals involved in the two configurations that give rise to the transition in eclipsed-cis conformer at 41955 cm^{-1}, and are representative of other LMCT transitions that are calculated to be present. A cluster of excitations involving configuration mixing of LMCT and ligand-based electronic transitions from 44095 to 44708 cm^{-1} is in good agreement with the relatively small feature observed at 44300 cm^{-1}.

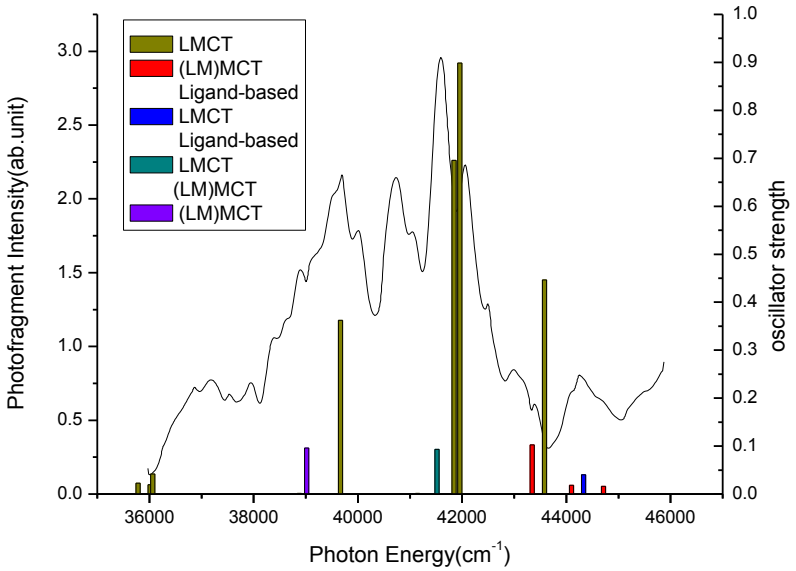

Figure 5.5 UV photofragmentation spectroscopy of $[Pb(toluene)_2]^{2+}$ overlaid with the electronic excitation energies and oscillator strengths calculated using TDDFT (CAM-B3LYP/6-311++G(d,p)[SDD] at BVP86 geometry). The calculated transitions are shown as vertical lines and are for three conformers (eclipsed-cis, staggered-cis and staggered-trans) of $[Pb(toluene)_2]^{2+}$.

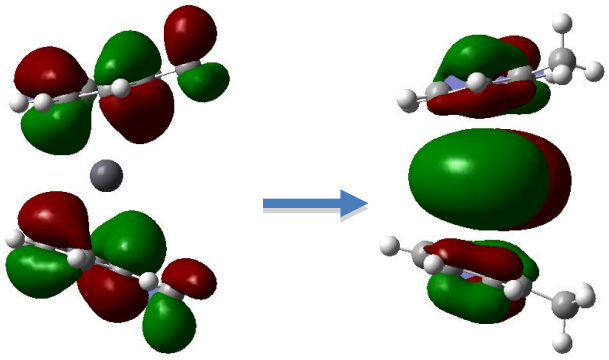

Figure 5.6 Configurations involved in the dominant electronic excitation for C_{2v}:Eclipsed_Cis conformer of $[Pb(toluene)_2]^{2+}$ at 41955 cm^{-1}. This LMCT ($\pi \rightarrow 6p$) electronic transition is representative of other LMCT transitions. The lead atom is depicted at the centre of the structure as a grey sphere.

Table 5.2 Summary of the observed peak positions and the calculated TDDFT (CAM-B3LYP/6-311++G(d,p)[SDD] at BVP86 geometry) electronic transitions and oscillator strengths (f ≥ 0.01 in the experimental range 35000-45000 cm^{-1}) for $[Pb(toluene)_2]^{2+}$. The weight and character of the two most dominant configurations and % Pb character are also provided. Dominant transitions, theory and experiment, are shown in bold.

Peak positions / cm^{-1}		*f*	NTO description	Assignment
Observed	Calculated			
-	35778[a]	0.023	LMCT(64%) +LMCT (35%)	LMCT $\pi \rightarrow$ 6p (> 88% Pb)
36873	36012[b]	0.020	LMCT(63%) +LMCT (36%)	LMCT $\pi \rightarrow$ 6p (> 88% Pb)
37000	36062[c]	0.042	LMCT(70%) +LMCT (29%)	LMCT $\pi \rightarrow$ 6p (> 88% Pb)
39700	**39016 [b]**	**0.096**	**(LM)MCT (90%)**	**(LM)MCT π+6p (11%) $\rightarrow$ 6p (92 % Pb)**
	39663 [a]	**0.363**	**LMCT 51%) +LMCT (47%)**	**LMCT $\pi \rightarrow$ 6p (> 86% Pb)**
40700	**41516 [a]**	**0.094**	**LMCT (62%) +(LM)MCT (37%)**	**LMCT $\pi \rightarrow$ 6p (92 % Pb) (LM)MCT π+6p (12%) $\rightarrow$ 6p (92 % Pb)**
41600	**41844 [b]**	**0.696**	**LMCT (63%) +LMCT (34%)**	**LMCT $\pi \rightarrow$ 6p (> 90 % Pb)**
42000	**41955 [c]**	**0.899**	**LMCT(69%) +LMCT (28%)**	**LMCT $\pi \rightarrow$ 6p (> 90 % Pb)**
43000	**43342 [b]**	**0.103**	**(LM)MCT (56%) 10%Pb$\rightarrow$78%Pb + Ligand-based electronic transition (19%)**	**(LM)MCT π+6p (10%) $\rightarrow$ 6p (78 % Pb) Ligand-based electronic transition $\pi \rightarrow \pi^*$**
	43576 [a]	**0.447**	**LMCT(72%) +LMCT (23%)**	**LMCT $\pi \rightarrow$ 6p (> 78 % Pb)**
44300	44095 [a]	0.018	L(LM)CT (36%) + Ligand-based electronic transition (36%)	L(LM)CT $\pi \rightarrow \pi^*$ +6p (13 % Pb) Ligand-based electronic transition $\pi \rightarrow \pi^*$

	44328 [b]	0.040	LMCT (46%) 86%Pb + Ligand-based electronic transition (25%)	LMCT $\pi \rightarrow$ 6p (86 % Pb) Ligand-based electronic transition $\pi \rightarrow \pi^*$
	44708 [c]	0.017	(LM)MCT (40%) + Ligand-based electronic transition (30%)	(LM)MCT π+6p(12 %) $\rightarrow$ 6p (86 % Pb) Ligand-based electronic transition $\pi \rightarrow \pi^*$

[a] (Stag-trans) [b] (Stag-cis) [c] (Eclips-cis)

From Figure 5.7, there are twelve electronic transitions ($f \geq 0.01$) arising from all three structures altogether and seven of them are dominant ($f > 0.05$) LMCT transitions (see entries in bold in Table 5.3). The positions of these transitions have a good agreement with the experimental spectra with a ~800 cm^{-1} blue shift. In all of the twelve calculated transitions, ten of them can be assigned to LMCT transitions. Two LMCT transitions at 39821 and 40574 cm^{-1} can be matched to the dominant feature at around ~39700 and ~40700 cm^{-1} in the UV spectra, respectively. A cluster of LMCT transitions at 42417, 42578 and 42631 cm^{-1} can be matched to the large feature at around ~42000 cm^{-1} with a ~500 cm^{-1} shift towards low energy. The two LMCT transitions at 44341 and 44601 cm^{-1} together with a weak mixing ((LM)MCT) and ligand-based electronic transition at 45197 cm^{-1} and a mixing (L(LM)CT) and ((LM)MCT) transition at 43952 cm^{-1} are in a good agreement with the relative small feature at around ~44300 cm^{-1}. Overall, comparing the two set of data, excited state calculation based on BVP86 geometry fits the UV spectra better than TPSSh geometry.

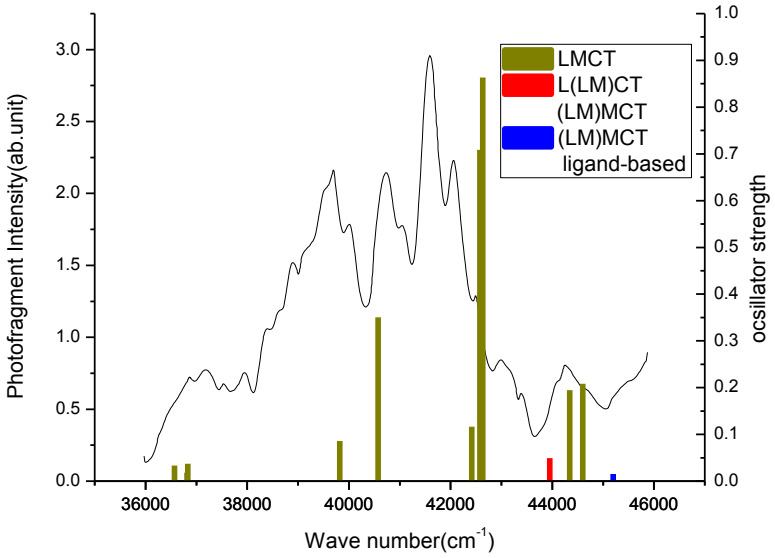

Figure 5.7 UV photofragmentation spectroscopy of $[Pb(toluene)_2]^{2+}$ overlaid with the electronic excitation energies and oscillator strengths calculated using TDDFT (CAM-B3LYP/6-311++G(d,p)[SDD] at TPSSh geometry). The calculated transitions are shown as vertical lines and are for three conformers (eclipsed-cis, staggered-cis and staggered-trans) of $[Pb(toluene)_2]^{2+}$.

Table 5.3 Summary of the observed peak positions and the calculated TDDFT (CAM-B3LYP/6-311++G(d,p)[SDD] at TPSSh geometry) electronic transitions and oscillator strengths ($f \geq 0.01$ in the experimental range 35000-45000 cm^{-1}) for $[Pb(toluene)_2]^{2+}$. The weight and character of the two most dominant configurations and % Pb character are also provided. Dominant transitions, theory and experiment, are shown in bold.

Peak positions / cm^{-1}		*f*	NTO description	Assignment
Observed	Calculated			
37000	36568[a]	0.0334	LMCT(67%) +LMCT (32%)	LMCT $\pi \rightarrow$ 6p (> 89% Pb)
	36814[b]	0.0178	LMCT(63%) LMCT(36%)	LMCT $\pi \rightarrow$ 6p (> 89% Pb)
	36833[c]	0.037	LMCT(70%) LMCT(30%)	LMCT $\pi \rightarrow$ 6p (> 89% Pb)
39700	**39821[b]**	**0.0859**	**LMCT(91%)** **LMCT(80%)**	**LMCT** **$\pi \rightarrow$ 6p (> 87% Pb)**

40700	**40574[a]**	**0.3503**	**LMCT(53%) LMCT(45%)**	**LMCT π → 6p (> 86% Pb)**
42000	**42417[a]**	**0.1162**	**LMCT(63%) LMCT(35%)**	**LMCT π → 6p (92% Pb)**
	42578[b]	**0.7086**	**LMCT(65%) LMCT(32%)**	**LMCT π → 6p (>91% Pb)**
	42631[c]	**0.8632**	**LMCT(68%) LMCT(28%)**	**LMCT π → 6p (>91% Pb)**
44300	43952[b]	0.0491	L(LM)CT(36%) (LM)MCT(28%)	L(LM)CT π → π+6p (13 % Pb) (LM)MCT π+6p(10%) → π+6p (54 % Pb)
	44341[a]	**0.1949**	**LMCT(45%) L(ML)CT(28%)**	**LMCT π → 6p (>19% Pb)**
	44601[a]	**0.2083**	**LMCT(45%) LMCT(24%)**	**LMCT π → 6p (>24% Pb)**
	45197[c]	0.0151	(LM)MCT(59%) Ligand-based electronic transition (20%)	(LM)MCT π+6p(12%) → 6p (91 % Pb) Ligand-based electronic transition π → π*

[a] (Stag-trans) [b] (Stag-cis) [c] (Eclips-cis)

As with $[Pb(benzene)_2]^{2+}$, the dominant photofragment observed following the excitation of $[Pb(toluene)_2]^{2+}$ is a molecule ion, in this case toluene$^+$. Therefore, steps were taken to see if the photofragmentation of the intermediate $[Pb(toluene)]^+$ contributed to the spectrum given in the UV spectra section. TDDFT calculations of $[Pb(toluene)]^+$ were undertaken on the same level of theory and these results are given in Figure 5.8 and Figure 5.9. The observed feature positions and calculated electronic transitions and their assignments are summarized in Table 5.4 and Table 5.5. From Figure 5.8, there are six dominant transitions ($f \geq 0.01$) calculated to reside within the energy range of the experimental spectrum. Five can be assigned predominantly to LMCT, and the strongest transition is a metal-to-ligand charge transfer (MLCT) transition at 41111 cm^{-1}, which is in good agreement with a feature observed at approximately 40700 cm^{-1}; the latter could not be matched with any transitions calculated for $[Pb(toluene)_2]^{2+}$ based on the same geometry.

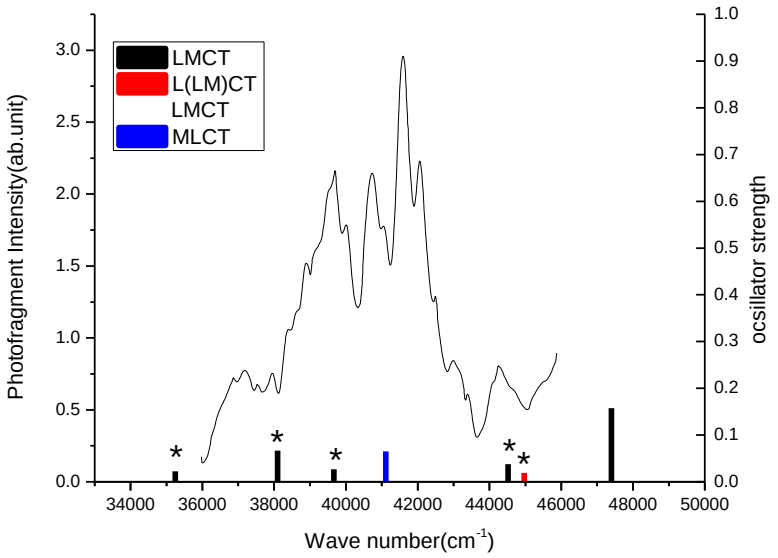

Figure 5.8 UV photofragmentation spectroscopy of $[Pb(toluene)_2]^{2+}$ overlaid with the electronic excitation energies and oscillator strengths for $[Pb(toluene)]^+$ calculated using TDDFT (CAM-B3LYP/6-311++G(d,p)[SDD] at BVP86 geometry). The calculated transitions are shown as vertical lines. The electronic transitions are labeled with asterisk (*) if they are significantly spin contaminated.

Table 5.4 Summary of the observed peak positions and the calculated TDDFT (CAM-B3LYP/6-311++G(d,p)[SDD] at BVP86 geometry) electronic transitions and oscillator strengths ($f \geq 0.01$ in the experimental range 35,000 – 45,000 cm^{-1}) for $[Pb(toluene)]^+$. The weight and character of the dominant configuration for each spin and the % Pb character are also given along with the total spin operator values, $\langle \hat{S}^2 \rangle$, which should be 0.75 in the absence of contamination.

Peak Positions / cm^{-1}		Oscillator strength	$\langle \hat{S}^2 \rangle$	NTO Description	Assignment
Observed	Calculated				
-	35244	0.022	1.03	α-LMCT (94 %) β-LMCT (79 %)	LMCT $\pi \rightarrow 6p$ (> 57% Pb)
37000	38098	0.066	1.04	α-LMCT (45 %) β-LMCT (109 %)	LMCT $\pi \rightarrow 6p$ (> 70% Pb)

39700	39663	0.027	1.69	α-LMCT (68 %) β-LMCT (115 %)	LMCT $\pi \rightarrow$ 6p (> 63% Pb)
40700 41600	41111	0.065	0.77	α-MLCT (196 %)	MLCT 6p (93% Pb)$\rightarrow \sigma^*$ + s (13% Pb)
44300	44517	0.038	1.31	α-LMCT (62%) β-LMCT (66 %)	LMCT $\pi \rightarrow$ 6p (> 73% Pb)
	44966	0.019	2.14	α-L(LM)CT (36%) β-LMCT (106 %)	L(LM)CT $\pi \rightarrow \pi^*$ + 6p (25 % Pb) LMCT $\pi \rightarrow$ 6p (63 % Pb)
-	47397	0.157	0.77	α-LMCT (72%) β-LMCT (82 %)	LMCT $\pi \rightarrow$ 6p (> 61% Pb)

From Figure 5.9, there are seven dominant transitions ($f \geq 0.01$) calculated in the experimental energy range. Five of them can be assigned to LMCT transitions. The MLCT transition at 41045 cm^{-1} is in a good agreement with the large feature at around 40700 cm^{-1} as well. Again, it would appear that the dominant photofragment can be accounted for by assuming the presence of a transient intermediate in the form of $[Pb(toluene)]^+$, which the trap is unable to capture, the photodissociation of which contributes to the observed spectrum; but it should be noted that several of the other electronic transitions calculated for $[Pb(toluene)]^+$ have associated with them a significant degree of spin contamination and hence there is uncertainty over their validity.

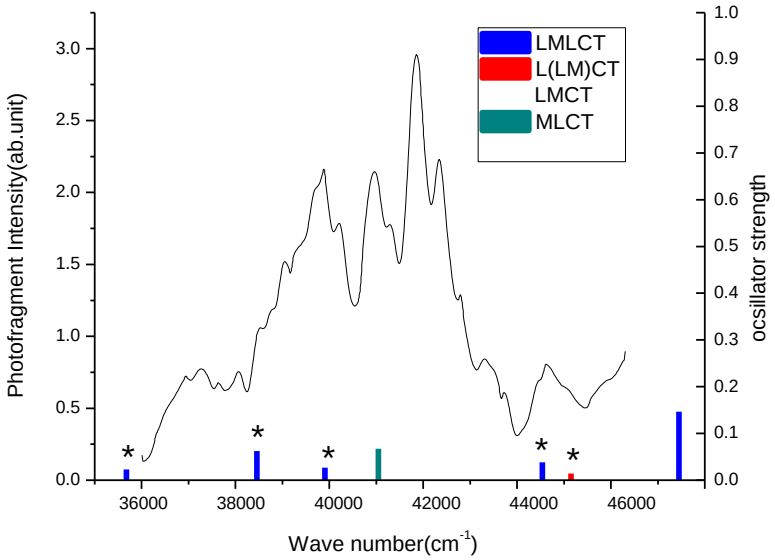

Figure 5.9 UV photofragmentation spectroscopy of $[Pb(toluene)_2]^{2+}$ overlaid with the electronic excitation energies and oscillator strengths for $[Pb(toluene)]^+$ calculated using TDDFT (CAM-B3LYP/6-311++G(d,p)[SDD] at TPSSh geometry). The calculated transitions are shown as vertical lines. The electronic transitions are labeled with asterisk (*) if they are significantly spin contaminated.

Table 5.5 Summary of the observed peak positions and the calculated TDDFT (CAM-B3LYP/6-311++G(d,p)[SDD] at TPSSh geometry) electronic transitions and oscillator strengths ($f \geq 0.01$ in the experimental range 35,000 – 45,000 cm^{-1}) for $[Pb(toluene)]^+$. The weight and character of the dominant configuration for each spin and the % Pb character are also given along with the total spin operator values, $\langle \hat{S}^2 \rangle$, which should be 0.75 in the absence of contamination.

Peak Positions / cm^{-1}		Oscillator strength	$\langle \hat{S}^2 \rangle$	NTO Description	Assignment
Observed	Calculated				
-	35673	0.0228	0.945	α-LMCT (106%) β-LMCT (84%)	LMCT $\pi \rightarrow$ 6p (> 66% Pb)
37000	38455	0.0621	1.063	α-LMCT (43 %) β-LMCT (112 %)	LMCT $\pi \rightarrow$ 6p (> 69% Pb)

39700	39904	0.027	1.773	α-LMCT (69 %) β-LMCT (111 %)	LMCT π → 6p (> 64% Pb)
40700 41600	41045	0.0674	0.781	α-MLCT (193 %) β-LMCT (4%)	MLCT 6p (93% Pb)→ σ* + s (14% Pb)
44300	44537	0.0383	1.187	α-LMCT (74%) β-LMCT (69 %)	LMCT π → 6p (> 80% Pb)
	45146	0.0143	2.297	α-L(LM)CT (41%) β-LMCT (107 %)	L(LM)CT π → π* + 6p (36 % Pb) LMCT π → 6p (60 % Pb)
-	**47451**	**0.1468**	**0.765**	**α-LMCT (72%) β-LMCT (82 %)**	**LMCT π → 6p (> 66% Pb)**

On the other hand, the calculated excitation energies and oscillator strengths for the $[Pb(toluene)]^{2+}$ fragment based on BVP86 and TPSSh geometries are also plotted as stick spectra overlaid with the experimental UV spectra in Figure 5.10 and Figure 5.11, tabulated in Table 5.6 and Table 5.7. There is only one electronic transition which is not very significant (f = 0.03) can be found in the experimental range for both of them. It can be seen that the calculated excitation fits to the feature at around 39700 cm^{-1} in the experimental spectra. However, this feature has already been found to match to the (LM)MCT electronic transition in staggered-cis conformer of $[Pb(toluene)_2]^{2+}$ at 39016 cm^{-1}, with a much higher oscillator strength (f = 0.096). It indicates that the $toluene^+$ photofragment could come from photodissociation of $[Pb(toluene)]^{2+}$, but the contribution from $[Pb(toluene)]^{2+}$ is much less than the $[Pb(toluene)_2]^{2+}$.

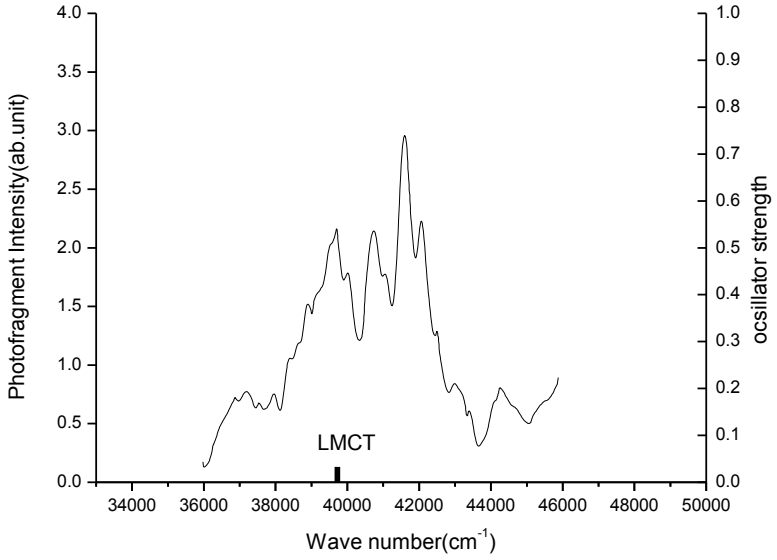

Figure 5.10 UV photofragmentation spectroscopy of $[Pb(toluene)_2]^{2+}$ overlaid with the electronic excitation energies calculated for $[Pb(toluene)]^{2+}$ using TDDFT (CAM-B3LYP/6-311++G(d,p)[SDD] at BVP86 geometry). The calculated results are shown as vertical lines.

Table 5.6 Summary of the observed peak positions and the calculated TDDFT (CAM-B3LYP/6-311++G(d,p)[SDD] at BVP86 geometry) electronic transitions and oscillator strengths ($f \geq 0.01$ in the experimental range 35000-45000 cm^{-1}) for $[Pb(toluene)]^{2+}$. The weight and character of the dominant configurations, and the % Pb character are also provided.

Peak position/cm^{-1}			
Calculated	f	Assignment	orbitals
39722	0.0328	(LM)MCT (75%) (LM)MCT (24%)	LMCT π +6p (10%) $\rightarrow$ 6p (86% Pb)

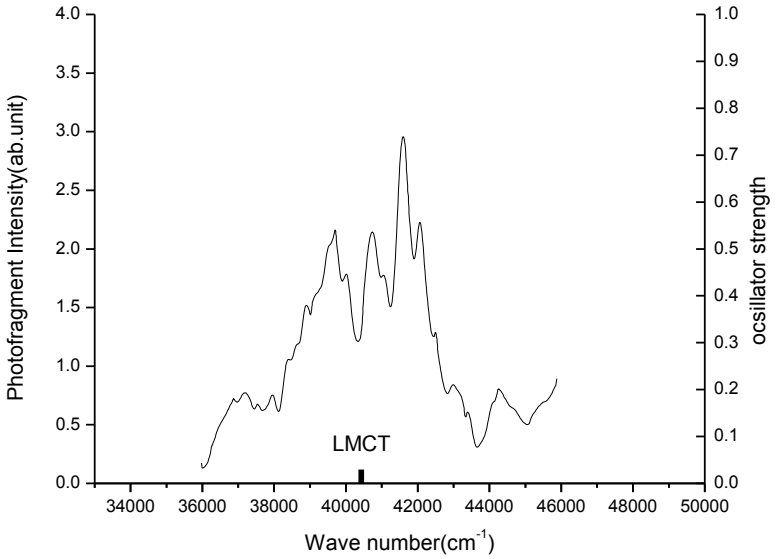

Figure 5.11 UV photofragmentation spectroscopy of $[Pb(toluene)_2]^{2+}$ overlaid with the electronic excitation energies calculated for $[Pb(toluene)]^{2+}$ using TDDFT (CAM-B3LYP/6-311++G(d,p)[SDD] at TPSSh geometry). The calculated results are shown as vertical lines.

Table 5.7 Summary of the observed peak positions and the calculated TDDFT (CAM-B3LYP/6-311++G(d,p)[SDD] at TPSSh geometry) electronic transitions and oscillator strengths ($f \geq 0.01$ in the experimental range 35000-45000 cm^{-1}) for $[Pb(toluene)]^{2+}$. The weight and character of the dominant configurations, and the % Pb character are also provided.

Peak position/cm^{-1}			
Calculated	Oscillator Strength, *f*	NTO description	Assignment
40429	0.0296	(LM)MCT (75%) (LM)MCT (25%)	LMCT π +6p (10%) $\rightarrow$ 6p (86% Pb)

To achieve a better agreement of TDDFT calculation and experimental spectra, the TDDFT-CAM-B3LYP/6-311++G(d,p)[SDD] data of $[Pb(toluene)_2]^{2+}$ and $[Pb(toluene)]^{+}$ based on BVP86 geometry are plotted together with the UV spectra in Figure 5.12. From Figure 5.12, one can noticed that the newly built UV spectra can be matched to the excitations calculated by TDDFT-CAM-B3LYP/6-311++G(d,p)[SDD]

very well. The theoretical data also suggests that the calculated electronic transitions can be assigned to resolved features arising from different conformers in the spectra.

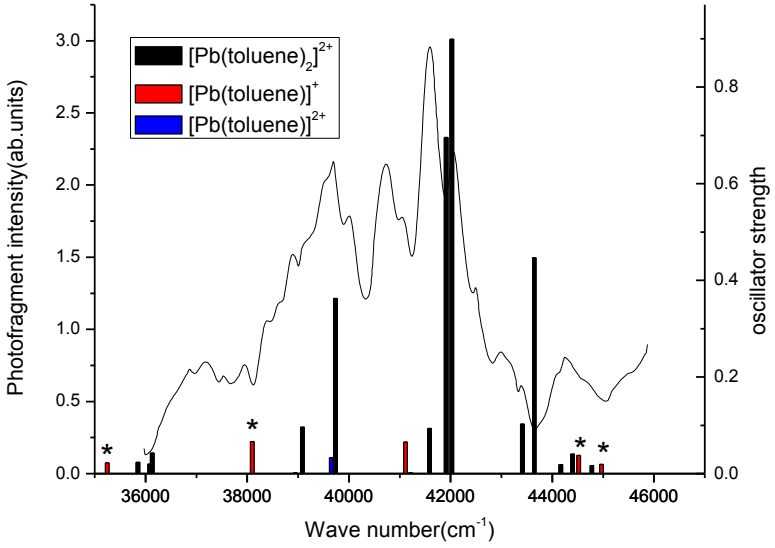

Figure 5.12 Experimental spectrum overlaid with the excitations in both the dication $[Pb(toluene)_2]^{2+}$ and the mono-cation $[Pb(toluene)]^{+}$ calculated by TDDFT-CAM-B3LYP/6-311++G(d,p)[SDD] at BVP86 geometry. The calculated excitations are in different colours so it's clear which peaks are from the dication and which are from the monocation. The excitations are labeled with asterisk (*) if they are spin contaminated.

The excited energies and oscillator strengths of most intense electronic transitions for three conformers of $[Pb(toluene)_2]^{2+}$ optimized by BVP86, PBE0 and TPSSh functional, calculated by CAM-B3LYP, PBE0 and TPSSh functional are detailed in Table 5.8. This set of data shows that the excitation energies are more sensitive to the functional used in the SCF part of the TDDFT calculation than they are to the functional used to determine the ground state geometry. It also shows that there is qualitative agreement on the trends in the excitation energies and oscillator strengths for the various conformers.

Table 5.8 Comparison of the dominant transition for each of the three distinct conformers of $[Pb(toluene)_2]^{2+}$. The notation TD-functional1/functional2 is used to indicate the functional used in the TD calculation and the geometry optimization, respectively. The 6-311++G(d,p) basis set with SDD on Pb was used in all cases.

Method	Eclip-Cis		Stag-Cis		Stag-Trans	
	E / cm^{-1}	f	E / cm^{-1}	f	E / cm^{-1}	f
TD- CAM-B3LYP/BVP86	41955	0.90	41845	0.70	43575	0.45
TD- CAM-B3LYP/TPSSh	42631	0.86	42578	0.71	40574	0.35
TD- CAM-B3LYP/PBE0	43017	0.69	43015	0.71	40986	0.35
TD-TPSSh/BVP86	38022	0.71	37906	0.58	39606	0.39
TD-TPSSh/TPSSh	38710	0.69	38643	0.59	40489	0.33
TD-PBE0/BVP86	39516	0.78	39400	0.63	41207	0.40
TD-PBE0/PBE0	40619	0.74	40573	0.63	42662	0.31

5.7 Spin contamination in open-shell excited states

For a doublet system, the $<\hat{S}^2>$ value should be 0.75. Clearly several of the values presented in this chapter (in Table 5.4 and Table 5.5) are severely spin contaminated and should ideally be discarded. Following Ipatov and Casida's formula[130], and assuming that the quartet state ($<\hat{S}^2>$ = 3.75) constitutes the primary source of contamination in the cations, i.e.,

$$|Pb(toluene)^+\rangle = C_D|doublet\rangle + C_Q|quartet\rangle$$

$$\langle \hat{S}^2_{calc} \rangle = 0.75|C_D|^2 + 3.75\left|C_Q\right|^2$$

The percentage doublet character in the Kohn-Sham wave function for each of the open shell excited states are calculated and listed in Table 5.9. The excitations at 41111 and 47397 cm^{-1} are >99% doublet in character and so it is safe to classify these states as primarily doublet in character. However, the excitations at 39663, 44517 and 44966 cm^{-1} are severely spin contaminated with $\Delta\hat{S}^2 \approx 1$ which corresponds to states which are significantly spin contaminated. They should be discarded. The validity of

the excitations at 35244 and 38098 cm^{-1} with $\Delta\hat{S}^2 \approx 0.3$ is questionable. Assuming that all spin contamination comes from the next highest allowed spin component, the excited states are around 90% doublet in character, and so an excitation in this region is likely.

Table 5.9 The excited state spin contamination in each of the $[Pb(toluene)]^+$ excited states calculated by TDDFT-CAM-B3LYP/6-311++G(d,p)[SDD] for BVP86 geometry, assuming that all spin contamination comes from the next highest allowed spin component. The significantly spin contaminated entry is in bold.[131]

$E(cm^{-1})$	$\langle\hat{S}^2\rangle$	$\Delta\langle\hat{S}^2\rangle$	Doublet character (%)	Spin contamination (%)
35244	1.03	0.28	90.7	9.3
38098	1.04	0.29	90.3	9.7
39663	**1.69**	**0.94**	**68.7**	**31.3**
41111	0.77	0.02	99.3	0.7
44517	**1.31**	**0.56**	**81.3**	**18.7**
44966	**2.14**	**1.39**	**53.7**	**46.3**
47397	0.77	0.02	99.3	0.7

The types of excitation arising from a doublet ground state of $[Pb(toluene)]^+$ can be categorised into 3 types (see chapter 4, Figure 4.8). To further analyse this problem, the electronic excitation energies of $[Pb(toluene)]^+$ calculated by TDDFT (CAM-B3LYP/6-311++G(d,p)[SDD] for BVP86 geometry) are presented in Figure 5.13, along with the nature of the orbitals involved in the dominant transitions. Again, we have assumed same orbitals with different spins (SODS), whereas the calculations were performed using different orbitals for different spins (DODS).

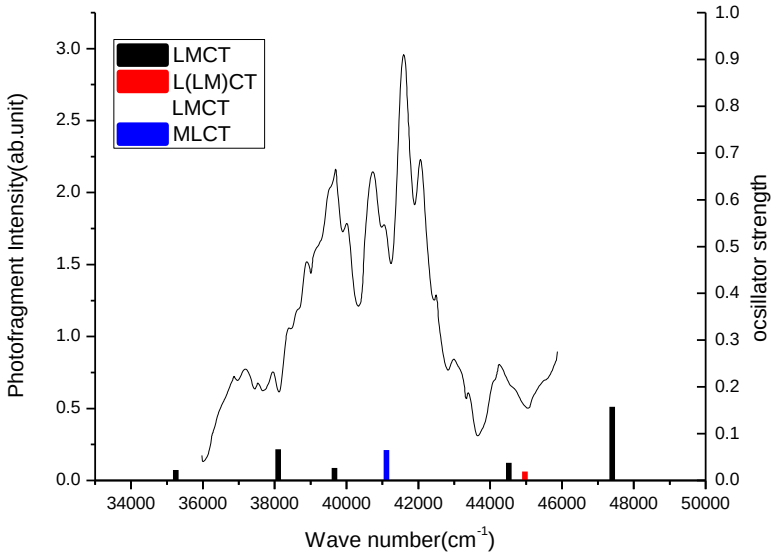

E_{ex}	$<\hat{S}^2>$
(a)35244	1.03
(b)38098	1.04
(c)39663	1.69
(d)41111	0.77
(e)44517	1.31
(f)44966	2.14
(g)47397	0.77

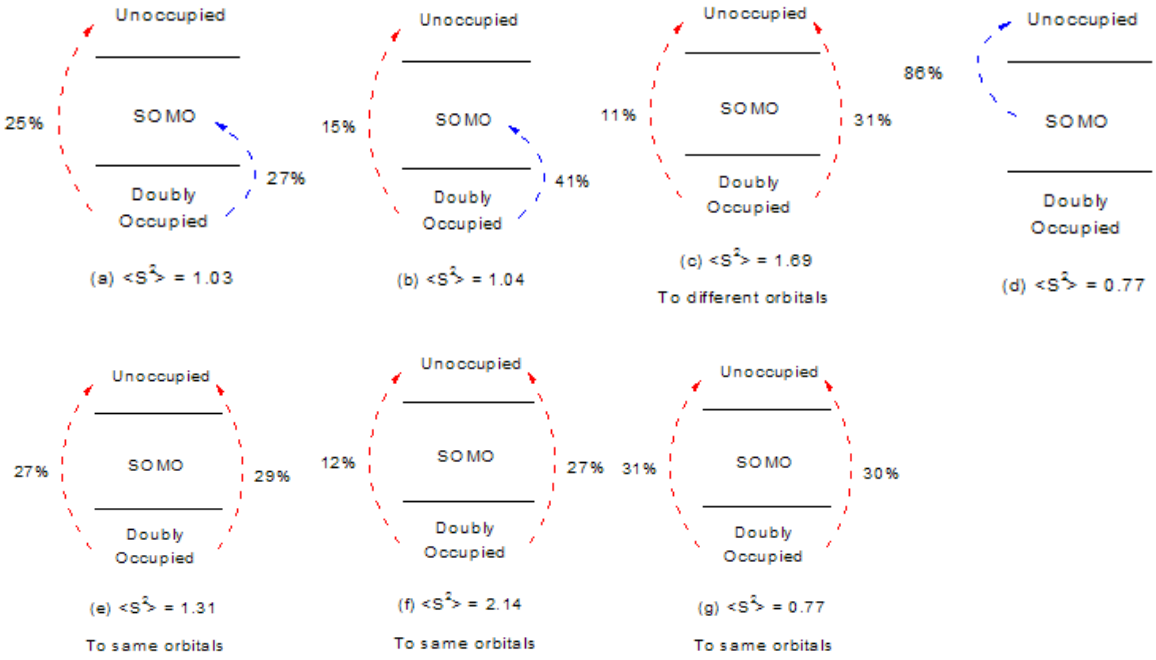

Figure 5.13 Analysis of the TDDFT excitations arising from the $[Pb(toluene)]^+$ complex. [131]

It can be found from this analysis that excitation (d) at 41111 cm^{-1} is reliable which is a Type I excitation. Excitation (a) and (b) are partly type II with some unphysical type III, which is reflected in the deviations of $<\hat{S}^2>$ from the true value of 0.75. Excitation (c), (e) and (f) are clearly an unphysical triplet-coupled excitation and should be

discarded. Excitation (g) is not significantly spin contaminated and can be assumed to arise from the physical singlet-coupled excitation. Again, this observation indicates that the simple involved orbital analysis is failed to distinguish between the unphysical excitations (c), (e), (f) and physical Type III excitation (g). The calculations of spin operator $\hat{S}^2$ values need to be concerned. Overall, the (c), (e), (f) excitations in $[Pb(toluene)]^+$ are severely spin contaminated and need to be discarded. However, the MLCT transition (d) at 41111 cm^{-1}, which is a close match to the unassigned experimental feature, is not spin contaminated.

5.8 **Conclusions**

The gas-phase UV spectra of the dication sandwich complex $[Pb(toluene)_2]^{2+}$ combined with DFT/TDDFT calculations of itself and $[Pb(toluene)]^{+/2+}$ have been detailed in this chapter. The $[Pb(toluene)_2]^{2+}$ complex has a rich spectrum and the TDDFT results indicate that three distinct conformers each contribute to its spectrum. All of the dominant spectral features arising from this dication can be attributed to $\pi \rightarrow 6p$ LMCT transitions. However, as the spectra shifts towards the UV, configuration mixing involving $\pi \rightarrow \pi^*$ Ligand-based electronic transitions occur. It is shown that the calculated energy difference between the $[Pb(toluene)_2]^{2+}$ and its charge transfer asymptote is very small, < 10 $kJmol^{-1}$, and thus it is likely that a $[Pb(toluene)]^+$ transient intermediate is present. To fully assign the spectra, the spectra arising from the charge transfer product $[Pb(toluene)]^+$ has also been considered. Here, the transition responsible for the one unaccounted experimental peak at 40,700 cm^{-1} can be attributed to MLCT. This state is not significantly spin contaminated, unlike other excitations in the experimental range.

Overall, this combined theory and experimental investigation has successfully assign the electronic spectra of Pb(II)-bis(toluene) sandwich complex. In particular, the theory suggests that the experiment is able to resolve distinct features arising from the

various conformers. It is also confirmed by the theory that the calculated MLCT transition in $[Pb(toluene)]^{+}$ complement the assignment of $[Pb(toluene)_2]^{2+}$ calculations without significant spin contaminations. The final fully evaluated spectrum can be considered as a valuable comparison to the lead benzene experiment, by which setting a typical example of developing bench mark for the theory in a systematic fashion.

Chapter 6 Ultraviolet photofragmentation spectroscopy of dication copper bis(benzene) sandwich complex combined with DFT/TDDFT calculations

6.1 Introduction

Transition metal ion-benzene complexes are currently receiving much attention because of their particular contribution to catalysis and biological chemistry, [135] and numerous condensed phase studies have been undertaken of the structure and reactivity of metal ion-bis(benzene) complexes[136]. Complementing this extensive catalogue of work is the more limited study of metal ion-benzene complexes that can be prepared as stable species in the gas phase.[16, 18a, b, 18e, 137] The advantages to come from such experiments are that they can be performed on extremely small samples and they avoid any perturbations that may come from solvent molecules and/or counter ions. These latter considerations are of particular significance when it comes to recording spectra. To date most experiments on metal ion-benzene complexes have been undertaken on singly charged species, which are comparatively easy to prepare and avoid any problems that may arise from charge transfer since very few metals have ionization energies that are higher than that of benzene. If valid comparisons are to be made with their condensed phase analogues, then it is important to develop experimental methods that are capable of preparing metal-benzene complexes where the metal occupies its more common charge state, i.e. Fe(II), Cu(II), Ni(II) etc. In recent years suitable techniques have appeared and a wide range of complexes containing first row transition metals in charge states commonly observed in condensed phase chemistry have been prepared, and these include Mn(II)[5b], Co(II)[11], Fe(II)[12a, 40b], and Cu(II)[5c, 13, 27d, 28-29, 30b, 138]. These experiments are frequently done in association with ligands that occupy pivotal positions in traditional transition metal chemistry, such as H_2O, NH_3, pyridine and bipyridine.

To date, a number of research groups have made important contributions to spectroscopic studies of gas-phase transition metals complexed with benzene. Duncan and co-workers have applied the IR-REMPI technique to investigate a range of spectroscopic and chemical properties. [18a, b, 18e, 137a, b] Freiser and co-workers have investigated photodissociation mechanisms of ions Fe^+, Co^+ and Ni^+ in association with benzene and as a function of the radiation wavelength.[137d] Yang have recorded PFI (pulsed-field-ionization) spectroscopy of group 6 metal (Cr, Mo, W) ion-bis(benzene) sandwich complexes using the pulsed-field ionization zero-electron kinetic energy (PFI-ZEKE) technique.[137e] Rodgers have employed CID measurements to reveal the influence of the d orbital occupation on the nature and strength of copper cation-π interactions[137f], and Armentrout and co-workers have investigated the binding energy of first-row transition metal ions (Ti^+-Cu^+) and bis(benzene) using collision-induced-dissociation.[137g]

In addition to this experimental progress, considerable effort has been devoted to calculating bonding energies and exploring the nature of the bond between transition metal ions and benzene molecules. Bauschlicher and co-workers have reported theoretical binding energies for all first-row and selected second-row transition metal ions with benzene for the first time.[139] Numerous DFT studies on cationic, neutral, and anionic 3d transition metal ion-benzene half-sandwich and sandwich complexes have been reported[140], as have the results of calculations on Yttrium and Gadolinium bis(benzene) sandwich complexes[141]. Of the benzene complexes with first-row transition metals, the bis(benzene) complex with Cu (II) is of particular interest because of its d^9 electronic configuration, which provides the potential for structural distortion. Many of the issues surrounding the structure and deformation of Cu(II) complexes in general have been discussed in detail by Deeth.[142] As an extension to the work on benzene complexes, Fan and co-workers have proposed a novel class of complex where a copper dimmer is sandwiched between benzene molecules.[143]

Recently, our work on metal dication d^9 complexes has combined experiment and theory in order to better understand the origins of electronic transitions that have been observed at visible wavelengths in gas phase complexes of Cu(II) and Ag(II) with a variety of ligands.[5c, 29b, 72] Although intended as studies of ligand field transitions, it was concluded from either recorded absorption cross-section data or ion fragmentation patterns, that most of these experiments have in fact involved charge transfer transitions. In this chapter, the doubly charged copper ion-bis (benzene) sandwich complex are prepared in the gas phase using the pick-up technique, and investigated using a hybrid quadrupole ion trap instrument. This study represents the first investigation where the spectroscopy of a transition metal sandwich complex has been recorded for a metal in its most common charge state. The experimental UV spectra are compared with the results of DFT and TDDFT calculations to assign dominant electronic transitions appearing in the wave-number range 36000-46000 cm^{-1}.

6.2 UV photofragment mass spectra of $[Cu(benzene)_2]^{2+}$

Initially, a mass spectrum of $[Cu(benzene)_2]^{2+}$ was recorded in the absence of laser radiation for reference purposes and this is reported in Figure 6.1. The parent ion $[Cu(benzene)_2]^{2+}$ appears at 109.5 amu. There are three other peaks that can be observed at 95.6, 81.5, and 67.8 amu respectively. Subsequently, trapped ions were exposed to laser radiation and UV photofragment mass spectra were generated. A typical example of a photofragment mass spectrum that is recorded with a photon energy of 39500 cm^{-1} is reported in Figure 6.2. In response to laser radiation, these particular ions exhibited a similar variation in intensity to the precursor ion, $[^{63}Cu(benzene)_2]^{2+}$, therefore, they were included in with the latter for the purposes of determining the relative intensities of fragment ions. Tentative assignments for two of the ions are Cu^+H_2O (80.6 amu) and Cu^+O_2 (95 amu); the ion at m/e 67 was the least sensitive to laser radiation, and could be derived from a precursor that is coincident in

mass with $[^{63}Cu(benzene)_2]^{2+}$. A double peak and a relative small photofragment peak appear at 39-40 amu and 52.8 amu, respectively. It is highly possible that these peaks correspond to $C_3H_3^+$, $C_3H_4^+$ and $C_4H_4^+$, which are fragment ions that have been seen following the photoexcitation of benzene.[144] The fracture fragment intensity is calculated by sum of the intensities of the peaks at 39-40 amu and 52.8 amu over itself plus intensities of the parent ions (the peaks at 109.5 amu, 95.6, 81.5, and 67.8 amu). Then the fracture fragment intensity was normalised by the laser power to get the normalized fragment intensity.

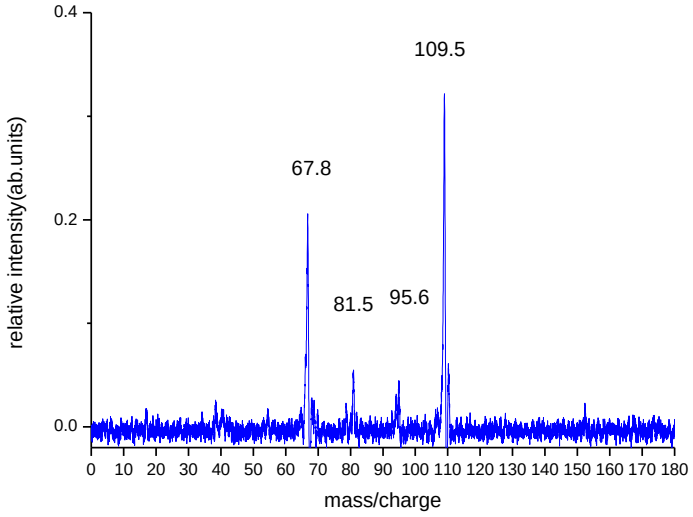

Figure 6.1 Original mass spectrum of $[Cu(benzene)_2]^{2+}$.

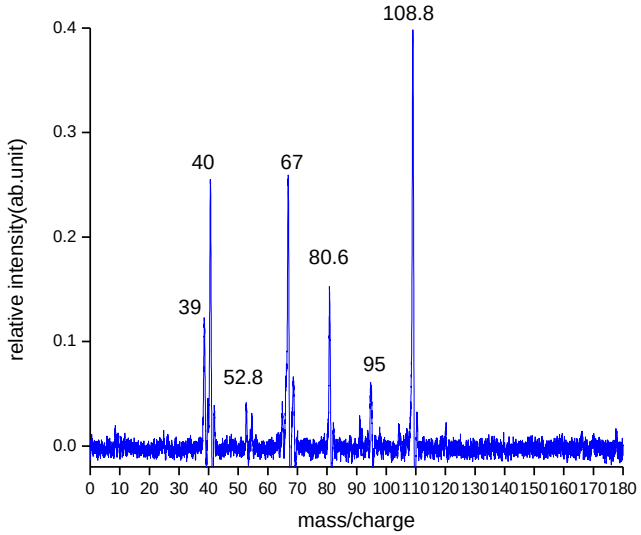

Figure 6.2 A typical example of a photofragment mass spectrum of $[Cu(benzene)_2]^{2+}$ wave number=39500 cm^{-1}.

Examples taken from every individual scan which covers 10 nm in laser wavelength have been selected and plotted together in Figure 6.3. From Figure 6.3(a), it can be noticed that the peaks at 109.5, 95.6, 81.5, and 67.8 amu appeared before the laser was introduced. Peaks at around 39-40 and 52.8 amu appeared with the presence of laser radiation, and their intensities varied significantly while the laser was scanning. From Figure 6.3(b), an overlap of ten mass spectra of $[Cu(benzene)_2]^{2+}$ essentially reflects the photodissociation behaviour of the trapped ions and their response to laser radiation in each of the scans.

a

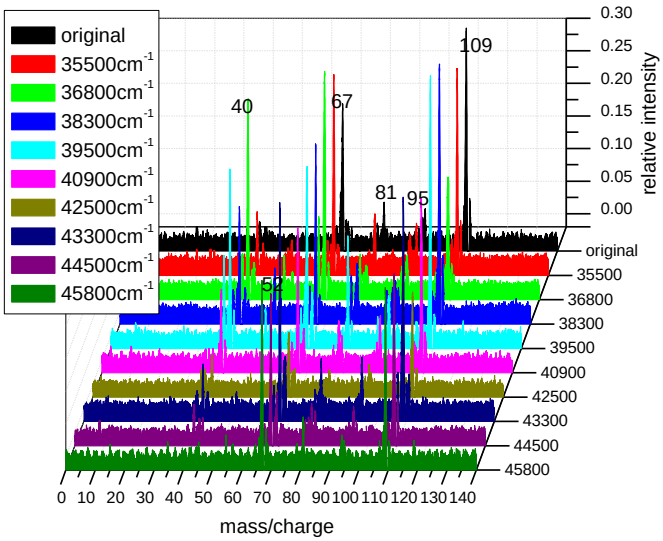

b

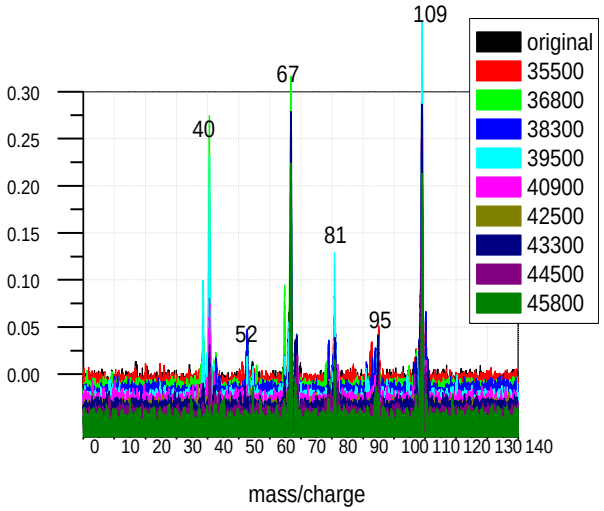

Figure 6.3 Three-dimensional photofragment mass spectrum of $[Cu(benzene)_2]^{2+}$ intensity *vs* m/e *vs* wave number (a) comparison of ten mass spectra examples (b) the overlap of ten mass spectra.

6.3 UV photofragmentation spectroscopy of $[Cu(benzene)_2]^{2+}$

From the photofragment yields a UV photofragment spectrum of $[Cu(benzene)_2]^2$ has been constructed by plotting the normalized ion intensity against photon wavenumber and these result are given in Figure 6.4. The spectrum can be seen to consist of two

principal features: a moderately intense region centred at ~ 38,000 cm^{-1} and a more intense feature that starts to rise at ~ 43,500 cm^{-1} and extends beyond the upper limit of the laser.

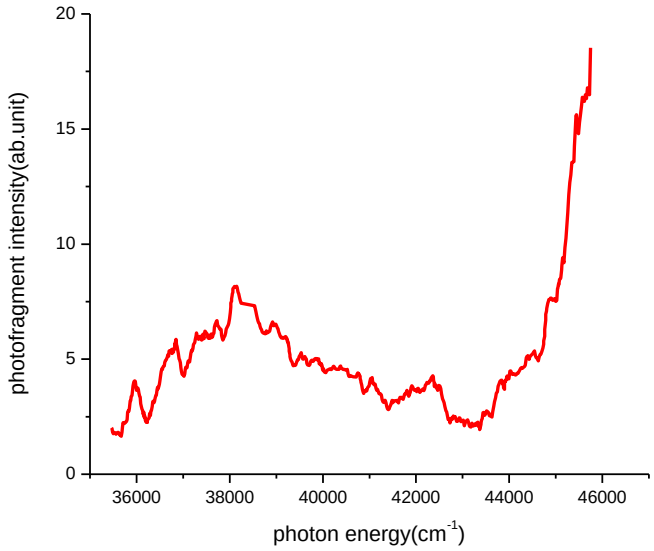

Figure 6.4 UV photofragmentation spectroscopy of $[Cu(benzene)_2]^{2+}$

6.4 Methodology of theoretical calculations

The structure and binding energies of the complexes $[Cu(benzene)_2]^{2+}$ and $[Cu(benzene)]^{+/2+}$ were calculated using DFT as implemented in Gaussian09. Geometry optimization and frequency analysis were performed using BVP86[94, 121], TPSSh[122] and PBE0[123]. Structural minima were verified by the absence of imaginary vibrational modes. A 6-311++G(d, p) basis set was used for all atoms except Cu^{2+}, for which the standard SDD pseudo potential was used;[124] this will referred to as 6-311++G(d,p)[SDD] throughout the text. All energies presented were zero point energy corrected.

Excitation energies and oscillator strengths were calculated using TDDFT with the optimized structures calculated using each of the methodologies outlined above (viz.,

BVP86, TPSSh, and PBE0). The SCF step of TDDFT was performed using CAM-B3LYP[125], PBE0 and TPSSh. The dominant transitions predicted by TDDFT were analyzed by calculating the natural transition orbitals (NTOs)[126] in order to identify the contribution each orbital makes to the electronic transition.

6.5 Calculated Structures and binding energies of $[Cu(benzene)_2]^{2+}$

DFT calculations predict three structures for the $[Cu(benzene)_2]^{2+}$ complex, and these are shown in Figure 6.5. All three functionals predict an approximately parallel sandwich complex with slipped rings, confirmed as minima by the absence of imaginary vibrational modes. However, for the hybrid (PBE0) functional and the meta-hybrid (TPSSh) functional this structure had an eclipsed C_2 configuration, whereas for the non-hybrid functional (BVP86) only the staggered C_2 configuration was found. In both cases (staggered and eclipsed) the structure has the metal localized over a η^3 site on each benzene ring instead of the more usual η^6, as for example in ferrocene. This type of distortion has been seen previously in calculations on $[Cu(benzene)_2]^+$ and $[Ni(benzene)_2]^+$ [137b, 145] and has been attributed to a pseudo Jahn-Teller distortion. [142e, 142g, 146] Such a distortion is thought to arise from a mixing of the σ_u ligand-based HOMO with the π_g orbitals of the metal, resulting in new covalency which stabilizes this configuration.[147] The third structure shown in Figure 6.5 was obtained using BVP86 only. It consists of a C_{2v} bent eclipsed geometry. A similar configuration has been identified in the optimized geometry of a copper-bis(phenalenyl) complex,[148] where a molecular geometry with higher symmetry has been destabilized by a combination of Jahn-Teller distortion and the participation of d orbitals in σ bonding.

To fully evaluate the spectra, calculations on $[Cu(benzene)]^{+/2+}$ were also performed at the same level of theory. $[Cu(benzene)]^+$ has η^6 coordination with C_{6v} symmetry, whilst $[Cu(benzene)]^{2+}$ has reduced symmetry due to the benzene ring having two

carbon atoms distorted slightly towards the metal. A similar distortion was observed following calculations on $[Ni(benzene)]^+$ and other mono-cation-benzene complexes and the results presented here agree with the suggestion that more strongly bound complexes favour a distorted structure.[148]

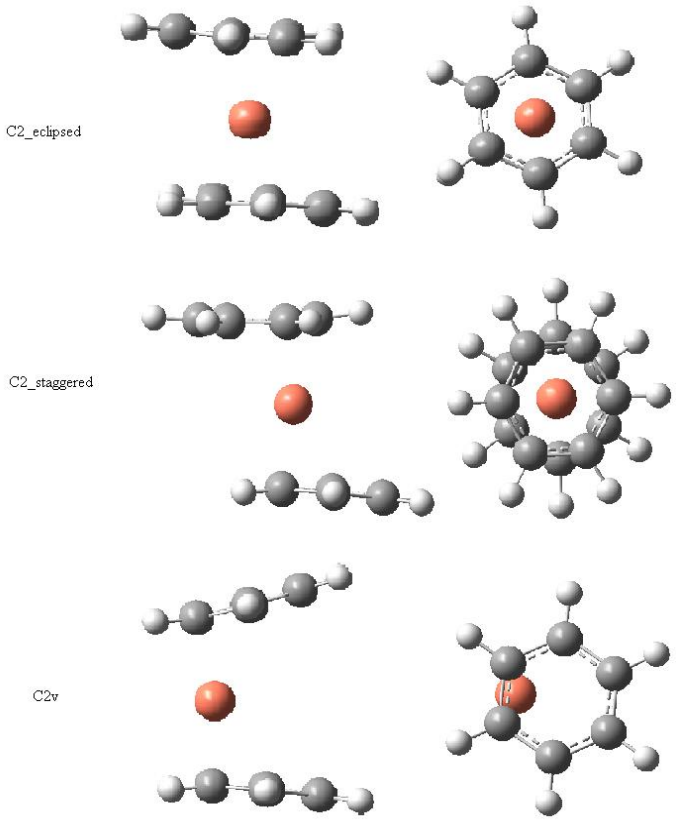

Figure 6.5 optimized structures of $[Cu(benzene)_2]^{2+}$ by DFT on BVP86, PBE0 and TPSSh/6-311++G(d, p)[SDD] level, respectively.

Binding energies of the dication complexes relative to complete neutral loss: $[Cu(benzene)_2]^{2+} \rightarrow Cu^{2+}$ + 2benzene, charge transfer: $[Cu(benzene)_2]^{2+} \rightarrow [Cu(benzene)]^+ + benzene^+$, and incremental neutral loss: $[Cu(benzene)_2]^{2+} \rightarrow [Cu(benzene)]^{2+}$ + benzene are given in Table 6.1. It can be seen that the lowest energy asymptote corresponds to charge transfer but this binding energy is still substantial (> 100 $kJmol^{-1}$) compared to the energy of $[Pb(benzene)_2]^{2+} \rightarrow [Pb(benzene)]^+ + benzene^+$, which was less than 25 $kJmol^{-1}$. There is very good

agreement between the calculated energies of the C_2_eclipsed structures by the two hybrid functionals; the largest error arising due to errors in the bare dication. It is clear from Table 1 that the binding energies for the different conformers are quite close; for example, for the charge transfer reaction the energies using the different conformer differ by less than 26 $kJmol^{-1}$ and for the incremental loss by less than 20 $kJmol^{-1}$. When compared with the energy available at the point of formation, the comparatively small differences shown in Table 6.1 mean that all conformers must be considered in the TDDFT calculations in order to fully assign the spectra as all may be accessible experimentally.

Table 6.1 Binding energy ($kJmol^{-1}$) for the $[Cu(benzene)_2]^{2+}$ complex with respect to various loss products calculated. The BVP86 C_2 structure is staggered and the PBE0 and TPSSh C_2 structures are eclipsed.

Reaction	Binding Energy / $kJmol^{-1}$			
	Geometry	BVP86	PBE0	TPSSh
$[Cu(benzene)_2]^{2+} \rightarrow Cu^{2+}$ + 2benzene	C_2	1238	1182	1214
	C_{2v}	1228		
$Cu(benzene)_2]^{2+} \rightarrow [Cu(benzene)]^{+}$ + benzene^{+}	C_2	115	141	133
	C_{2v}	124		
$[Cu(benzene)_2]^{2+} \rightarrow [Cu(benzene)]^{2+}$ + benzene	C_2	339	349	348
	C_{2v}	330		

6.6 TDDFT Excited States Calculation of $[Cu(benzene)_2]^{2+}$

Excitation energies and oscillator strengths of all optimized structures for C_{2v}, C_2_staggered and C_2_eclipsed conformers of the $[Cu(benzene)_2]^{2+}$ complex that are calculated on the CAM-B3LYP, PBE0 and TPSSh/6-311++G(d,p)[SDD] level of theory are plotted as stick spectra alongside the complete experimental UV photofragment spectrum in Figures 6.6-6.8. Assignments for dominant electronic transitions ($f \geq 0.01$) and NTO contributions from those frontier orbitals involved in the transitions are summarized in Table 6.2-6.4.

From Figure 6.6(a), no electronic transition with high oscillator strength ($f \geq 0.01$) can be found below 38000 cm^{-1}. There are some electronic transitions calculated based on the C_2_staggered conformer which cannot be assigned to any feature in the spectra. In Figure 6.6(b) and Table 6.2, the two dominant metal-based electronic transitions at 39398 and 39844 cm^{-1} can be matched to the feature at around 38200 cm^{-1}. They arise from charge transfer between 3d+3s and 4p orbitals of the copper ion with a high metal character. This electron re-distribution in Cu^{2+} could be contributed from a charge transfer due to electronic relaxation.[36] The Metal-Ligand-to-Ligand Charge Transfer (MLLCT) transition at 46884 cm^{-1} and the LMCT transition at 46888 cm^{-1} fit to the large increase in intensity starting from 43500 cm^{-1} and extending beyond the upper limit of the photon energy. The 3s, 3d, and 3p orbitals of copper ion are involved. The ligand-based electronic transitions also have good agreement with the two features that have been mentioned above except the two transitions at 40987 cm^{-1} and 42761 cm^{-1}, which cannot be assigned to any experimental feature. Both of them arise from the C_2_staggered structure of $[Cu(benezene)_2]^{2+}$. Both of the C_2_eclipsed conformers show metal-based electronic transition at around 39500 cm^{-1} and MLLCT transition at around 46900 cm^{-1} which could be assigned to the two features in the spectra with a ~1000 cm^{-1} shift towards the low energy end, whereas the C_{2v} conformer provides ligand-based electronic transitions and LMCT transitions in the same region with the higher oscillator strengths. If all of the calculated transitions shift to low energy end by ~1500 cm^{-1}, the calculated results will show a good agreement with the experimental data. It also needs to be noted that all of the calculated excitations are significantly spin contaminated.

a

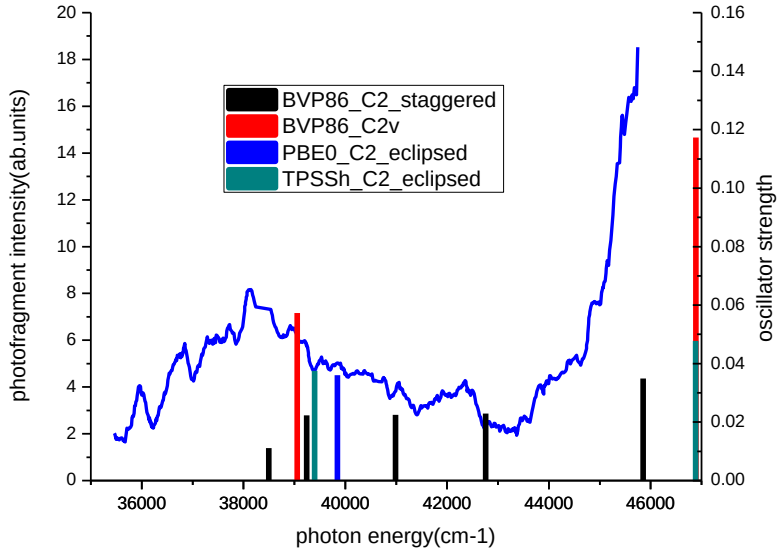

b

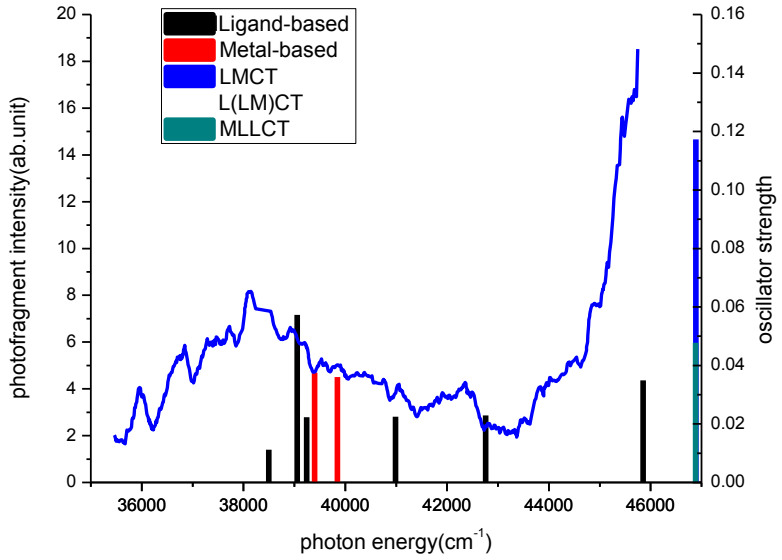

Figure 6.6 UV photofragmentation spectroscopy of $[Cu(benzene)_2]^{2+}$ overlaid by tabulated TDDFT calculated excitation energies and oscillator strengths using CAM-B3LYP functional, 6-311++G(d,p)/SDD as basis sets, a) Calculated transitions for all optimized structures of C_2 and C_{2v} $[Cu(benzene)_2]^{2+}$ conformers using BVP86, PBE0 and TPSSh, respectively; b) The transitions are sorted in their nature.

Table 6.2 Summary of observed and calculated TDDFT electronic transitions and oscillator strengths ($f \geq 0.01$ in the experimental range 35,000 – 45,000 cm^{-1}) of $[Cu(benzene)_2]^{2+}$ using CAM-B3LYP, along with the $\langle \hat{S}^2 \rangle$ value which should be 0.75 in the absence of spin contamination. The weight and character of the dominant configuration for each spin, and the % Cu character, is also provided.

Peak positions / cm^{-1}		f	$\langle \hat{S}^2 \rangle$	NTO description*	Assignment*
Observed	Calculated				
38200	38496[a]	0.0112	2.672	α- Ligand-based electronic transition (125%) β- Ligand-based electronic transition (65 %)	Ligand-based electronic transition $\pi \rightarrow \pi^*$
	39053[b]	0.0573	1.325	α- Ligand-based electronic transition (159%) β- Ligand-based electronic transition (47%)	Ligand-based electronic transition $\pi \rightarrow \pi^*$
	39240[a]	0.0223	2.117	α- Ligand-based electronic transition (81%) β- Ligand-based electronic transition (49 %)	Ligand-based electronic transition $\pi \rightarrow \pi^*$
	39398[d]	0.0375	1.967	α- Metal-based electronic transition (30%) β- Metal-based electronic transition (62 %)	Metal-based electronic transition (13% Cu) 3d+ (>12% Cu) 3s+$\pi \rightarrow$ 4p (>26% Cu)+π^*

	39844[c]	0.036	1.961	α- Metal-based electronic transition (36%) β- Metal-based electronic transition (78 %)	Metal-based electronic transition (11% Cu) 3s + (>13% Cu) 3d+ π→ 4p (>27% Cu)+π*
-	40987[a]	0.0225	1.751	α- Ligand-based electronic transition (133%) β-(LM)LCT (48 %)	Ligand-based electronic transition π → π* (LM)LCT 3p (11% Cu)+π→π*
-	42761[a]	0.0229	1.054	α- Ligand-based electronic transition (43%) β-L(LM)CT (79 %)	Ligand-based electronic transition π→π* L(LM)CT π → 3d (31% Cu)+π
~45700	45852[a]	0.0349	1.212	α- Ligand-based electronic transition (18%) β-(LM)LCT (97 %)	Ligand-based electronic transition π→π* (LM)LCT (11% Cu) 3p+π → π*
	46884[d]	0.0478	1.315	α-MLLCT (22%) β-MLLCT (175 %)	MLLCT (18% Cu) 3d (12% Cu) 3s+(13% Cu) 3p +π → π*
	46888[b]	0.1173	1.038	α-LMCT (114%) β-L(LM)CT (45 %)	LMCT π → 4s (14% Cu) L(LM)CT π → 4p (36% Cu)+π*

[a] BVP86_C_2_staggered, [b] BVP86_C_{2v} [c] PBE0_C_2_eclipsed [d] TPSSh_C_2_eclipsed

* Only the most dominant transition is shown for each spin; weight is given in parenthesis. Assume, arbitrarily, that less than 60% metal character is more appropriately classed as an ML orbital rather than an M orbital.

From Figure 6.7(a), it can be seen that all of the calculated excitations coming from the three geometries fall into two groups under the two broad structures at ~38200 and

~45700 cm^{-1} that are seen in the experimental spectrum. Overall, the agreement between the locations of calculated transitions and the broad experimental features is excellent. The TDDFT-PBE0 result based on the C_{2v} structure provides two electronic transitions at 37820, and 45356 cm^{-1} which can be matched to two features at around 38200 and 45700 cm^{-1} in the UV spectrum very well. C_2_staggered conformer gives the most electronic transitions again, with a better agreement with the UV spectrum in this case.

From Figure 6.7(b) and Table 6.3, the excitations are labelled according to contributions that been identified from frontier orbitals involved in the movement of electron population. Three ligand-based excitations at 37614, 37820, and 38264 cm^{-1} and two metal-based excitations at 38187 and 38646 cm^{-1} can be matched to the feature at around 38200 cm^{-1}. A separate group of MLLCT and LMCT transitions in the range 44000-46000 cm^{-1} can be assigned to the broad feature which starts at ~44500 cm^{-1}. Comparing Figure 6.7(a) and Table 6.3, it can be seen that the metal-based electronic transitions belong to the C_2_eclipsed conformers, the LMCT transitions arise from the C_{2v}_eclipsed conformer, and ligand-based and MLLCT transitions arise from all three conformers.

Comparing with the TDDFT-CAM-B3LYP data, the metal-based excitations and the MLLCT transitions in C_2_eclipsed conformers, together with the LLCT and LMCT transitions in C_{2v} conformer are shifted towards low energy end by ~1500 cm^{-1}, by which provides a perfect match to the features at around 38200 and 45700 cm^{-1}. Even the cluster of MLLCT and ligand-based excitations in C_2_staggered conformer which cannot be assigned in TDDFT-CAM-B3LYP case fit to the spectrum better in this case. However, it should be noted that almost all of these transitions are significantly spin contaminated.

a

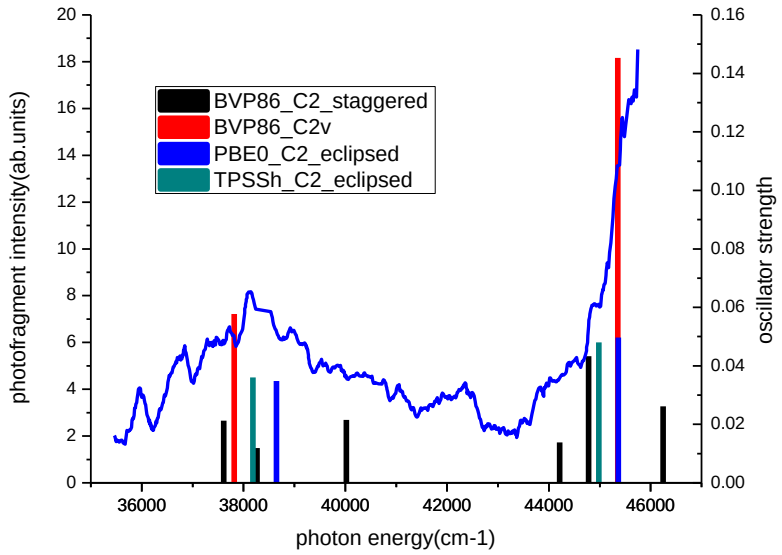

b

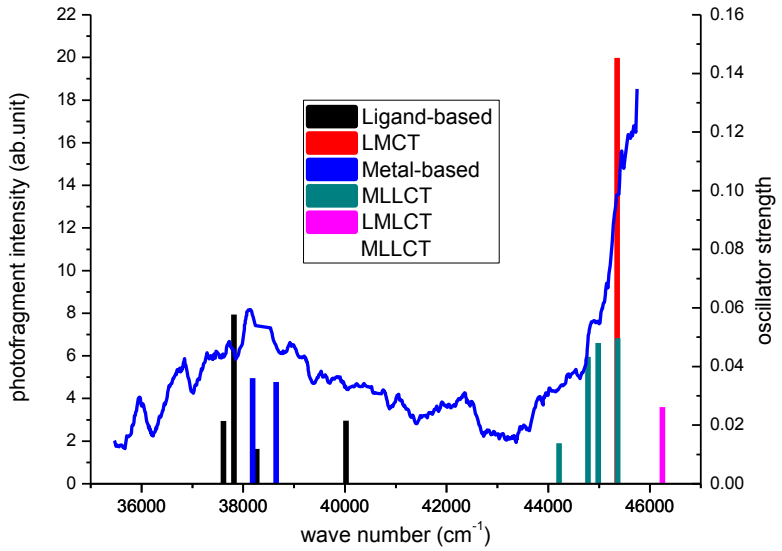

Figure 6.7 UV photofragment spectrum of $[Cu(benzene)_2]^{2+}$ overlaid by tabulated TD-DFT using PBE0 functional, 6-311++G(d,p)/SDD as basis sets, a) Calculated transitions for all optimized structures of C_2 and C_{2v} $[Cu(benzene)_2]^{2+}$ conformers using BVP86, PBE0 and TPSSh, respectively; b) The transitions are sorted by their nature.

Table 6.3 Summary of observed and calculated TDDFT electronic transitions and oscillator strengths ($f \geq 0.01$ in the experimental range 35,000 – 45,000 cm^{-1}) of $[Cu(benzene)_2]^{2+}$ using PBE0, along with the $<\hat{S}^2>$ value which should be 0.75 in the absence of spin contamination. The weight and character of the dominant configuration for each spin, and the % Cu character, is also provided.

Peak positions / cm^{-1}		f	$<\hat{S}^2>$	NTO description*	Assignment*
Observed	Calculated				
38200	37614[a]	0.0214	2.530	α- Ligand-based electronic transition (89%) β- Ligand-based electronic transition (68 %)	Ligand-based electronic transition $\pi \rightarrow \pi^*$
	37820[b]	0.0577	1.027	α- Ligand-based electronic transition (180%) β- Ligand-based electronic transition (3%)	Ligand-based electronic transition $\pi \rightarrow \pi^*$
	38187[d]	0.036	1.814	α- Metal-based electronic transition (34%) β- Metal-based electronic transition (74 %)	Metal-based electronic transition (>11% Cu) 3d+(>13% Cu) 3s+$\pi \rightarrow$ 4p (>29% Cu)+π^*
	38264[a]	0.0119	2.155	α- Ligand-based electronic transition (65%) β- Ligand-based electronic transition (40 %)	Ligand-based electronic transition $\pi \rightarrow \pi^*$

	38646[c]	0.0347	1.806	α- Metal-based electronic transition (41%) β- Metal-based electronic transition (93 %)	Metal-based electronic transition (12% Cu) 3s + (11% Cu) 3d+π → 4p(30% Cu)+π*
-	40022[a]	0.0215	1.725	α- Ligand-based electronic transition (124%) β-(LM)LCT (54 %)	Ligand-based electronic transition π → π* (LM)LCT (12% Cu) 3p+π→π*
~45700	44213[a]	0.0138	1.185	α-MLLCT (32%) β-MLLCT (85 %)	MLLCT (12% Cu) 3p + (14% Cu) 3d + (10% Cu) 3s + π → π*
	44779[a]	0.0433	1.243	α-MLLCT (26%) β-MLLCT (85 %)	MLLCT (12% Cu) 3d + (11% Cu) 3p + π → π*
	44984[d]	0.048	1.071	α-MLLCT (37%) β-MLLCT (131 %)	MLLCT (18% Cu) 3d + (13% Cu) 3s+(12% Cu) 3p+π → π*
	45356[b]	0.1453	1.725	α-LMCT (16%) β-LMCT (30 %)	LMCT π → 4s (>22% Cu)
	45364[c]	0.0497	1.082	α-MLLCT (43%) β-MLLCT (149 %)	MLLCT (13% Cu) 3p+(18% Cu) 3d+(12% Cu) 3s+π → π*
	46245[a]	0.0262	1.725	α-LMLCT (172%) β-MLLCT (8%)	LMLCT π→3s(14% Cu)+π* MLLCT π+(18% Cu)3d→π*

[a] BVP86_C_2_staggered, [b] BVP86_C_{2v}, [c] PBE0_C_2_eclipsed, [d] TPSSh_C_2_eclipsed

* Only the most dominant transition is shown for each spin; weight is given in parenthesis. Assume, arbitrarily, that less than 60% metal character is more appropriately classed as an ML orbital rather than an M orbital.

From Figure 6.8, it can be noticed that the TDDFT-TPSSh data is much more complicated than the TDDFT-CAM-B3LYP and TDDFT-PBE0 data. Electronic

transitions of all natures obtained for all conformers appear in the lower range of photon energy. From the assignments of electronic transitions in Table 6.4, all of the transitions are metal related except one, the ligand-based excitation at 36146 cm^{-1}. It can be noticed that the large feature at 45700 cm^{-1} matches the LMLCT in C_{2v} conformer, the mixing MLLCT and metal-based electronic transitions and the pure metal-based electronic transitions in C_2 conformers in the range of 41800-46800 cm^{-1} with a ~2000 cm^{-1} shift towards low energy. Due to this shift, there are more electronic transitions appearing in this region which cannot be found in TDDFT-CAM-B3LYP and TDDFT-PBE0 data. They can be sorted into mixing MLLCT and metal-based electronic transitions, metal-based and LMLCT transitions. The mixing MLLCT and metal-based electronic transitions, LMLCT and ligand-based excitations in the range of 36000-37000 cm^{-1} can be matched to the feature at 38200 cm^{-1} with a ~2000 cm^{-1} shift towards high energy. Again, all of the calculated transitions have significant spin contaminations.

a

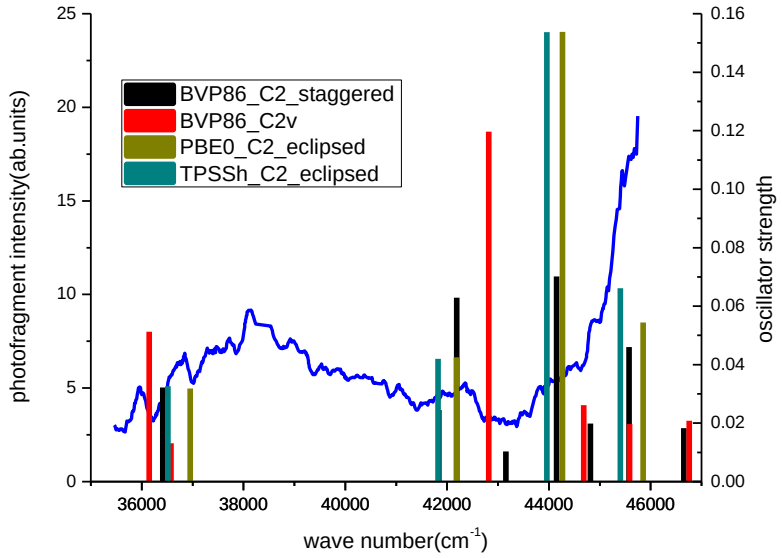

b

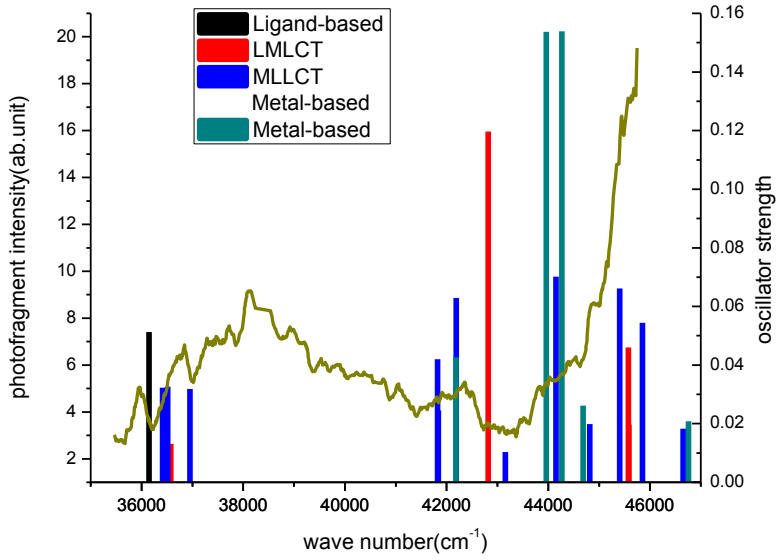

Figure 6.8 UV photofragment spectrum of $[Cu(benzene)_2]^{2+}$ overlaid by tabulated TD-DFT using TPSSh functional, 6-311++G(d,p)/SDD as basis sets, a) Calculated transitions for all optimized structures of C_2 and C_{2v} $[Cu(benzene)_2]^{2+}$ conformers using BVP86, PBE0 and TPSSh, respectively; b) Transitions are sorted by nature.

Table 6.4 Summary of observed and calculated TDDFT electronic transitions and oscillator strengths ($f \geq 0.01$ in the experimental range 35,000 – 45,000 cm^{-1}) of $[Cu(benzene)_2]^{2+}$ using TPSSh, along with the $\langle \hat{S}^2 \rangle$ value which should be 0.75 in the absence of spin contamination. The weight and character of the dominant configuration for each spin, and the % Cu character, is also provided.

Peak positions / cm^{-1}		f	$\langle \hat{S}^2 \rangle$	NTO description*	Assignment*
Observed	Calculated				
38200	36146[b]	0.0513	0.890	α- Ligand-based electronic transition (148%) β- Ligand-based electronic transition (2 %)	Ligand-based electronic transition $\pi \rightarrow \pi^*$
	36413[a]	0.0323	2.137	α-MLLCT (63%) β- Metal-based electronic transition (65 %)	MLLCT (13% Cu)3d+π→π* Metal-based electronic transition (15% Cu)3d+π→ 4p(11% Cu)+π*
	36513[d]	0.0326	1.603	α-MLCT (36%) β- Metal-based electronic transition (84%)	MLCT (39% Cu)3d→π* Metal-based electronic transition (20% Cu)3d (13% Cu)3s+π →4p(28% Cu)+π*
	36576[b]	0.0131	2.645	α-LMLCT (16%) β-LMLCT (16%)	LMLCT $\pi \rightarrow$ 4p(33% Cu)
	36953[c]	0.0318	1.578	α-MLCT (47%) β- Metal-based electronic transition (107 %)	MLCT (39%Cu)3d→π* Metal-based electronic transition (20% Cu) 3d+(12% Cu)3s+π → 4p (29% Cu)+π*

~45700	41823[d]	0.042	0.869	α-MLLCT (33%) β-MLLCT (60%)	MLLCT (26% Cu)3d+(14% Cu)3s+(13% Cu) 3p+π → π*
	41835[a]	0.0245	1.051	α-MLLCT (58%) β-MLLCT (76 %)	MLLCT (>26% Cu)3d+(13% Cu)3s → π*
	42185[c]	0.0426	0.873	α-MMLCT (54%) β-MLLCT (68 %)	MMLCT (41% Cu)3d→4p(21% Cu)+π* MLLCT (13% Cu) 3p+π → π*
	42190[a]	0.0629	1.548	α- Metal-based electronic transition (147%) β-MLLCT (31 %)	Metal-based electronic transition (14% Cu) 3d+π→4s (12% Cu)+π* MLLCT (17% Cu) 3d+π→π*
	42819[b]	0.1197	1.061	α- Metal-based electronic transition (95%) β-LMCT (15%)	Metal-based electronic transition (24% Cu)3d+(10% Cu) 3s+π→4p(35% Cu)+π* LMCT π→4s(36% Cu)
	43153[a]	0.0103	1.562	α-MLLCT (75%) β-MLLCT (46 %)	MLLCT (16% Cu) 3d+(12% Cu) 3p+π→ π*
	43961[d]	0.1537	0.992	α-MLMCT (165%) β-MLMCT (90%)	MLMCT (24% Cu)3d (14% Cu)3s+π → 4p(18% Cu)
	44152[a]	0.0702	1.723	α-MLLCT (67%) β- Metal-based electronic transition (56 %)	MLLCT (20%Cu)3d+π→π* Metal-based electronic transition (24%Cu)3d+π→4s(18% Cu)+π*

	44265[c]	0.1539	0.946	α- Metal-based electronic transition (210%) β- Metal-based electronic transition (125 %)	Metal-based electronic transition (>24% Cu)3d+(>12% Cu)3s+π → 4p (19% Cu)+π*
	44686[b]	0.0262	2.214	α- Metal-based electronic transition (162%) β-Ligand-based electronic transition (19 %)	Metal-based electronic transition (31% Cu)3d+(11% Cu)3s+π → 4p(35% Cu)+π* Ligand-based electronic transition π→π*
	44814[a]	0.0199	0.952	α-MLLCT (57%) β- Metal-based electronic transition (107 %)	MLLCT (19%Cu) 3d+(10%Cu) 3s+π→π* Metal-based electronic transition (25% Cu) 3d (10% Cu)3s+π→ 4s (15% Cu)+π*
	45407[d]	0.0661	2.236	α-MLLCT (47%) β- Metal-based electronic transition (59 %)	MLLCT (11% Cu)3p+π→π* Metal-based electronic transition (31% Cu) 3d (13% Cu)3s → 4p (21% Cu)
	45574[a]	0.046	0.952	α-LMLCT (62%) β-Ligand-based electronic transition (68 %)	LMLCT π → 4s (12% Cu)+π* Ligand-based electronic transition π→π*
	45585[b]	0.0197	1.461	α-LMLCT (20%) β-LMLCT (731 %)	LMLCT π → 4p(>33% Cu)+π*

	45850[c]	0.0544	2.284	α-MLLCT (65%) β- Metal-based electronic transition (68 %)	MLLCT (12% Cu)3p+π→π* Metal-based electronic transition (32% Cu)3d+(12% Cu)3s+π→ 4p (22% Cu)+π*
	46654[a]	0.0183	1.833	α-MLLCT (95%) β-MLLCT (46 %)	MLLCT (>11% Cu) 3p+π → π*
	46759[b]	0.0208	2.443	α- Metal-based electronic transition (51%) β- Metal-based electronic transition (74 %)	Metal-based electronic transition (>23% Cu)3d+(>12% Cu)3s+π → 4p (>34% Cu)+π*

[a] BVP86_C_2_staggered, [b] BVP86_C_{2v}, [c] PBE0_C_2_eclipsed, [d] TPSSh_C_2_eclipsed

* Only the most dominant transition is shown for each spin; weight is given in parenthesis. Assume, arbitrarily, that less than 60% metal character is more appropriately classed as an ML orbital rather than an M orbital.

6.7 Excited state calculations on [Cu(benzene)]$^{+/2+}$

To explore other possible contributions to the experimental spectra, excitation energies and oscillator strengths were also calculated for the [Cu(benzene)]$^{+/2+}$ complexes at the TDDFT-PBE0/6-311++G**[SDD] level of theory. These results are plotted as stick spectra on the experimental spectra in Figure 6.9 and Figure 6.10, tabulated in Table 6.5 and Table 6.6. From these data it would appear that there two electronic transitions ($f \geq 0.01$) from [Cu(benzene)]$^{2+}$ that are calculated to appear within the profile of the experimental spectrum; however, this ion has not been observed in these or other experiments that have investigated Cu^{2+}/benzene complexes. For [Cu(benzene)]$^{+}$ there are also two possible electronic transitions, but their energies and oscillator strengths fall outside the experimental profile.

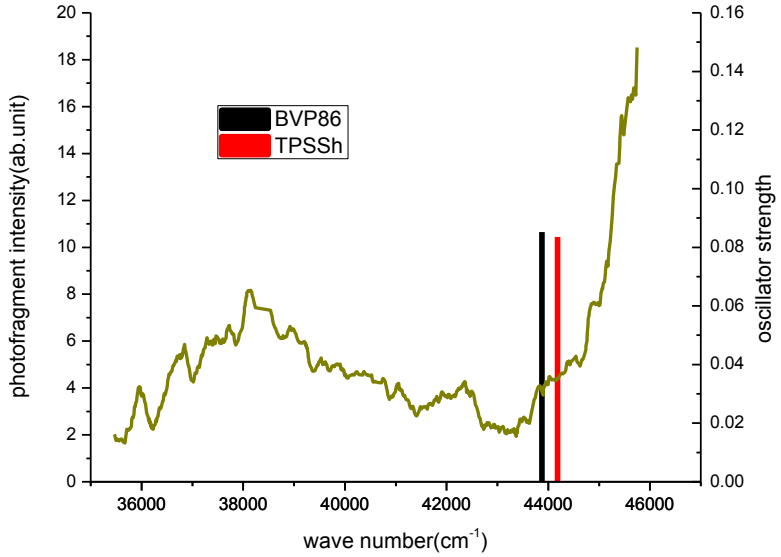

Figure 6.9 TDDFT of $[Cu(benzene)]^+$ using PBE0 functional, 6-311++G(d,p)[SDD] as basis sets, for BVP86 and TPSSh optimized structures overlaid by UV photofragmentation spectroscopy

Table 6.5 Summary of observed and calculated TDDFT electronic transitions and oscillator strengths (f ≥ 0.01 in the experimental range 35,000 – 47,000 cm^{-1}) of $[Cu(benzene)]^+$ using PBE0. The weight and character of the dominant configuration for each spin, and the % Cu character, is also provided.

Peak positions / cm^{-1}		f	NTO description*	Assignment*
Observed	Calculated			
~45700	43875[a]	0.0852	MLCT(48%) MLCT(47%)	MLCT 3d(>70% Cu)→π*
~45700	44183[b]	0.0835	MLLCT(50%) MLLCT(50%)	MLLCT 3d(59% Cu)+π→π*

[a] BVP86, [b]TPSSh

* Assume, arbitrarily, that less that 60% metal character is more appropriately classes as an ML orbital rather than an M orbital.

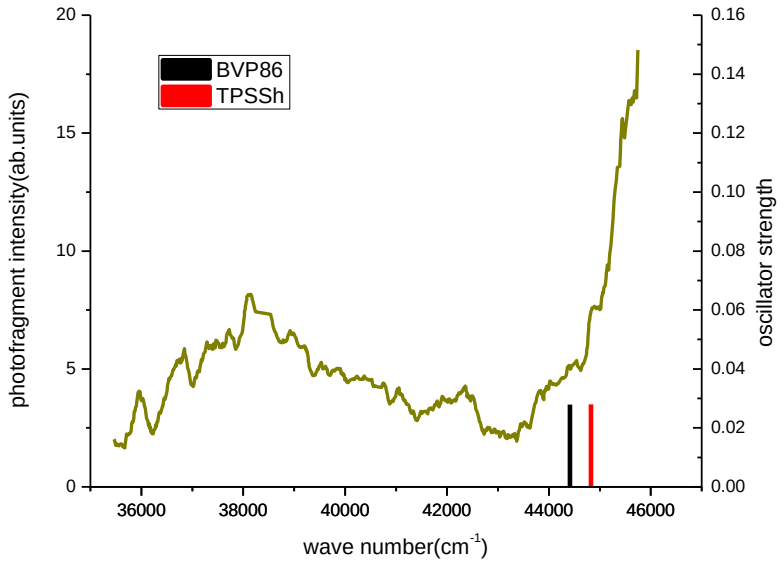

Figure 6.10 Calculated excitations of $[Cu(benzene)]^{2+}$ on TDDFT-PBE0/6-311++G(d,p)[SDD] level, for BVP86 and TPSSh optimized geometries overlaid by UV photofragmentation spectroscopy

Table 6.6 Summary of observed and calculated TDDFT electronic transitions and oscillator strengths (f ≥ 0.01 in the experimental range 35,000 – 47,000 cm-1) of $[Cu(benzene)]^{2+}$ using PBE0, along with the $\langle \hat{S}^2 \rangle$ value which should be 0.75 in the absence of spin contamination. The weight and character of the dominant configuration for each spin, and the % Cu character, is also provided.

Peak positions / cm^{-1}		f	$\langle \hat{S}^2 \rangle$	NTO description*	Assignment*
Observed	Calculated				
~45700	44415[a]	0.0279	1.272	α-MLLCT (93%) β-MLLCT (51 %)	MLLCT (12% Cu) 3d → π*
~45700	44827[b]	0.028	1.278	α-MLLCT (93%) β-MLLCT (51%)	MLLCT (12% Cu) 3d → π*

[a] BVP86, [b]TPSSh

* Only the most dominant transition is shown for each spin; weight is given in parenthesis. Assume, arbitrarily, that less that 60% metal character is more appropriately classes as a ML orbital rather than an M orbital.

From what has been discussed above, it can be found that the excitations arising from three conformers of $[Cu(benzene)_2]^{2+}$ calculated on TDDFT-PBE0/6-311++G(d,p)[SDD] level have a better agreement with the experimental UV spectra than TDDFT-CAM-B3LYP and TDDFT-TPSSh data. The calculated excitations in $[Cu(benzene)]^{+/2+}$ can match the large feature in the spectra. However, all of the calculated excitations in the open-shell complexes ($[Cu(benzene)_2]^{2+}$ and $[Cu(benzene)]^{2+}$) have significant spin contamination and hence there is uncertainty over their validity. All of these calculated excitations are plotted as stick spectra together with the UV spectra in Figure 6.11 to fully evaluate the spectra. From Figure 6.11, it can be seen that the TDDFT calculation data match the UV spectra amazingly well. The degree of the spin contamination is qualified by $\langle \hat{S}^2 \rangle$ values for selected excitations in the following section.

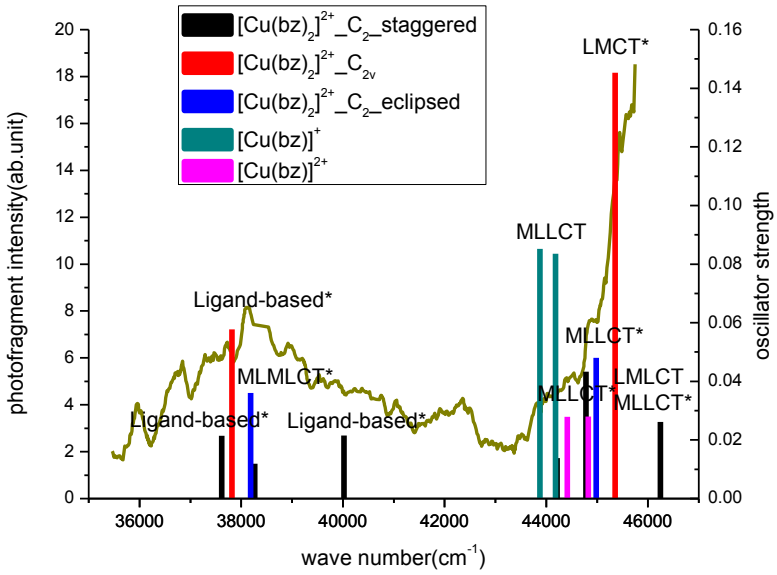

Figure 6.11 Experimental spectra overlaid with the TDDFT data on the PBE0/6-311++G(d,p)[SDD] level of dication $[Cu(benzene)_2]^{2+}$, based on BVP86 and TPSSh optimized geometries, for the C_2_staggered, C_{2v} and C_2_eclipsed conformers, and TDDFT data of $[Cu(benzene)]^{+/2+}$ on the same level of theory based on BVP86 and TPSSh optimized geometry. (The excitations are labelled in different colours so it's clear which peaks are from the dication and which are from the monocation) The dominant transitions in different conformers are labelled in their nature and with asterisk (*) if they are spin contaminated.

Together with the TDDFT-CAM-B3LYP and TDDFT-TPSSh data, the assignments, excited energies and oscillator strengths of the most intense electronic transitions for three conformers of $[Cu(benzene)_2]^{2+}$ optimized with BVP86, PBE0 and TPSSh functionals are summarized in Table 6.7. From this table, one can notice that, apart from the TDDFT-TPSSh/TPSSh data for the C_2 (eclipsed) conformer; assignments for the most dominant electronic transitions obtained with different methodologies are consistent. For individual conformers, it would appear that the different functions do not influence the nature of the electronic transitions involved (LMCT etc), but there can be shifts in excitation energy and oscillator strength.

Table 6.7 Comparison of the dominant transition for the two conformers of $[Pb(benzene)_2]^{2+}$. The notation TD-functional1/functional2 is used to indicate the functional used in the TD calculation and the geometry optimization, respectively. The 6-311++G(d,p) basis set with SDD on Pb was used in all cases.

Method	C_2 (staggered)			
	E / cm^{-1}	f	NTO description	Assignment
TD- CAM-B3LYP /BVP86	45852	0.0349	α- Ligand-based electronic transition (18%) β-MLLCT (97 %)	Ligand-based electronic transition $\pi \rightarrow \pi^*$ MLLCT (11% Cu) $3p+\pi \rightarrow \pi^*$

TD-PBE0/BVP86	44779	0.0433	α-MLLCT (26%) β-MLLCT (85 %)	MLLCT (12% Cu) 3d + (11% Cu) 3p + π → π*
TD-TPSSh/BVP86	44152	0.0702	α-MLLCT (67%) β- Metal-based electronic transition (56 %)	MLLCT (20%Cu)3d+π→π* Metal-based electronic transition (24%Cu)3d+π→4s(18% Cu)+π*
	C_{2v}			
TD- CAM-B3LYP /BVP86	46888	0.1173	α-LMCT (114%) β-L(LM)CT (45 %)	LMCT π → 4s (14% Cu) L(LM)CT π → 4p (36% Cu)+π*
TD-PBE0/BVP86	45356	0.1453	α-LMCT (16%) β-LMCT (30 %)	LMCT π → 4s (>22% Cu)
TD-TPSSh/BVP86	42819	0.1197	α- Metal-based electronic transition (95%) β-LMCT (15%)	Metal-based electronic transition (24% Cu)3d+(10% Cu) 3s+π→4p(35% Cu)+π* LMCT π→4s(36% Cu)
	C_2 (eclipsed)			
TD- CAM-B3LYP /TPSSh	46884	0.0478	α-MLLCT (22%) β-MLLCT (175 %)	MLLCT (18% Cu) 3d (12% Cu) 3s+(13% Cu) 3p +π → π*
TD-PBE0/TPSSh	44984	0.048	α-MLLCT (37%) β-MLLCT (131 %)	MLLCT (18% Cu) 3d + (13% Cu) 3s+(12% Cu) 3p+π → π*
TD-TPSSh/TPSSh	43961	0.1537	α-MLMCT (165%) β-MLMCT (90%)	MLMCT (24% Cu)3d (14% Cu)3s+π → 4p(18% Cu)

6.8 Photofragmentation mechanism

In addition to contributions from $[Cu(benzene)_2]^{2+}$, a complete analysis of the experimental spectra requires that possible contributions from $[Cu(benzene)]^{+/2+}$ also be taken into account. However, previous experiments,[5c] had suggested that

$[Cu(benzene)]^{2+}$ is not stable. There is not an obvious mechanism that accounts for the photofragments observed for $[Cu(benzene)_2]^{2+}$ since critical photofragments such as Cu^+ and $benzene^+$ are not observed. However, the dication complex decays with considerable excess energy as a result of charge transfer, which means that quite extensive fragmentation is possible. For the Cu/C_6H_6 system the first and second ionisation energies of copper are 7.88 eV and 20.29 eV, respectively; these numbers are to be compared with the first ionisation energy of benzene, which is 9.42 eV. Therefore, charge transfer from Cu^{2+} to give Cu^+ and $C_6H_6^+$ would release a considerable amount of energy, some of which could easily lead to extensive fragmentation of the molecular ion. In an earlier study of $[Pb(C_6H_6)_2]^{2+}$ the only fragment observed as a result of photoexcitation was $C_6H_6^+$. The absence of any metal-containing ion signal, e.g. Pb^+, was attributed to the possibility that a large release of kinetic energy to the fragments from Coulomb explosion could result in ions being ejected from the trap. For a heavy metal ion, collisions with the helium buffer gas would not be sufficient to quench the ion's momentum. In addition, this earlier experiment provided evidence that fragment ions generated by the rapid decay of a precursor ion (< 5 ns) could themselves subject to photofragmentation during the remainer of a photon pulse. Given the above considerations, the following are offered as possible photofragmentation mechanisms:

$$[Cu(benzene)_2]^{2+} + h\nu \rightarrow [Cu(benzene)]^{+} + benzene^{+}$$

$$[Cu(benzene)]^{+} + h\nu \rightarrow Cu + benzene^{+}$$

$$benzene^{+} + h\nu \rightarrow C_3H_3^{+} + C_3H_3$$

$$\rightarrow C_3H_4^{+} + C_3H_2$$

$$\rightarrow C_4H_4^{+} + C_2H_2 \quad (1)$$

$$[Cu(benzene)_2]^{2+} + h\nu \rightarrow [Cu(benzene)]^{2+} + benzene$$

$$[Cu(benzene)]^{2+} \rightarrow Cu^{+} + C_3H_3^{+} + C_3H_3$$

$$\rightarrow Cu^{+} + C_3H_4^{+} + C_3H_2$$

$$\rightarrow Cu^{+} + C_4H_4^{+} + C_2H_2 \qquad (2)$$

In mechanism (1) a benzene cation is produced by the photo-induced charge transfer of singly charged $[Cu(benzene)]^{+}$.[137f] The resultant benzene^{+} is then photodissociated to give the observed fragment ions: $C_3H_3^{+}$, $C_3H_4^{+}$ or $C_4H_4^{+}$.[144e, 144j] In mechanism (2) these same ions are generated as a result of charge transfer during the Coulomb fission of $[Cu(benzene)]^{2+}$, where a possible energy difference of up to10.87 eV would be sufficient to drive the appropriate reactions in $C_6H_6^{+}$. Based on results of laser induced fragmentation of benzene cation reported by other groups,[144b, 144g, 144i] both of the appearance potentials of $C_3H_3^{+}$ and $C_4H_4^{+}$ are very low, and $C_3H_4^{+}$ is easy to form.

6.8 Spin contamination in open-shell excited states

Overall, TDDFT theory appears to be capable of providing accurately matches to those regions of the experimental spectrum where UV transitions have been recorded for $[Cu(benzene)_2]^{2+}$. However, one topic that has not been addressed until now is that of spin contamination and the extent to which it influences the validity of excitations that have been calculated for the open-shell complexes $[Cu(benzene)_2]^{2+}$ and $[Cu(benzene)]^{2+}$. Given that the ability of a standard adiabatic TDDFT method to describe double-excitation characters is considered particularly important in a d^9 system with a doublet ground state, the results of the single-electron excitations described by the adiabatic TDDFT calculations are not considered to be sufficiently reliable or accurate to identify the discrete electronic transitions that appear in the spectrum. Therefore, even this qualitative approach can only be considered as a general analysis rather than a definite answer because of the high probability of

unphysical states and/or missing states in the calculated spectrum due to the absence of doubly excitations in this adiabatic TDDFT treatment.

The extent of spin contamination for each of the calculated excitations has been qualified by $<\hat{S}^2>$ values and for a doublet system this should have a value of 0.75. Assuming that quartet states ($\hat{S}^2$ = 3.75) constitute the primary source of contamination in these dications, i.e.

$$|Cu(benzene)^{2+}\rangle = C_D|doublet\rangle + C_Q|quartet\rangle$$

$$\langle \hat{S}^2_{calc} \rangle = 0.75|C_D|^2 + 3.75|C_Q|^2$$

The percentage of doublet character in the Kohn-Sham wave function for each of the open-shell excited states are calculated and listed in Table 6.8. From these results, it can be seen that all of the calculated excitations suffer from some degree of spin contamination ($\Delta\hat{S}^2 = <\hat{S}^2> - 0.75$). Many of those with high $\Delta\hat{S}^2$ values should be discarded; however, there are three transitions appearing at 37820, 44984 and 45364 cm^{-1} where $\Delta\hat{S}^2 \approx 0.3$. If it is assumed that the dominate contribution to spin contamination comes from the next highest spin-allowed component, then these excited states have approximately 90% doublet character, in which case these excitations are highly likely to occur, and as noted earlier, they fall within the profile of the experimental spectrum. Obviously, any transitions calculated for $[Cu(benzene)]^+$ are not subject to spin contamination.

Table 6.8 The excited state spin contamination in each of the $[Cu(benzene)_2]^{2+}$ and $[Cu(benzene)]^{2+}$ excited states calculated by TDDFT-PBE0/6-311++G(d,p)[SDD], assuming that all spin contamination comes from the next highest allowed spin component. The significantly spin contaminated entry is in bold.

Complex	E(cm^{-1})	$<\hat{S}^2>$	$\Delta<\hat{S}^2>$	Doublet character (%)	Spin contamination (%)
$[Cu(benzene)_2]^{2+}$	**37614**	**2.530**	**1.78**	**40. 7**	**59.3**
	37820	1.027	0.277	90.8	9.2

	38187	**1.814**	**1.064**	**64.5**	**35.5**
	38264	**2.155**	**1.405**	**53.2**	**46.8**
	38646	**1.806**	**1.056**	**64.8**	**35.2**
	40022	**1.725**	**0.975**	**67.5**	**32.5**
	44213	**1.185**	**0.435**	**85.5**	**14.5**
	44779	**1.243**	**0.493**	**83.6**	**16.4**
	44984	1.071	0.321	89.3	10.7
	45356	**1.725**	**0.975**	**67.5**	**32.5**
	45364	1.082	0.332	88.9	11.1
	46245	**1.725**	**0.975**	**67.5**	**32.5**
$[Cu(benzene)]^{2+}$	**44415**	**1.272**	**0.522**	**82.6**	**17.4**
	44827	**1.278**	**0.528**	**82.4**	**17.6**

Since there is no excitation which is absolutely trustful in this set of calculations, the theory cannot be considered as a perfect solution for this open-shell system yet. However, the three excitations with ~10% spin contaminations at 38720, 44984 and 45364 cm^{-1} which are listed in Table 6.8, accompanied with the excitations at 43875 and 44183 cm^{-1} in the closed-shell $[Cu(benzene)]^{+}$ still have reasonable agreement with the experimental spectra, even though the resolution of the spectrum is not so good that can identify the discrete features arising from different electronic transitions.

6.9 Conclusion

A UV photofragmentation spectrum has been recorded for the Cu(II) sandwich complex $[Cu(benzene)_2]^{2+}$ in the gas phase using a quadrupole ion trap mass spectrometer, and where $C_3H_3^+$, $C_3H_4^+$ and $C_4H_4^+$ have been identified as photofragments. Using DFT, stable structures with C_2 and C_{2v} symmetries have been optimised and TDDFT used to identify a range of electronic transitions in $[Cu(benzene)_2]^{2+}$ which involve electron displacement of the form $\pi \rightarrow 3d$, $3d \rightarrow \pi^*$, $\pi \rightarrow \pi^*$, and $3d+3s \rightarrow 4p$. When spin contamination is taken into consideration, there are at least three electronic transitions that can be assigned to the experimental spectrum.

The open-shell electronic configuration of Cu^{2+} (d^9) leads to ground states with multi-excitation character. The extent of spin contaminated for all electronic transitions is characterized by their $<\hat{S}^2>$ values. Almost all calculated electronic transitions suffer from significant degree of spin contamination. This problem arise when using the standard adiabatic implementations of TDDFT to describe open-shell complexes where multi-excitation character can dominate the excited states.[43] The single-excitation theory does make a quantitative assignment of the experimental data in this special case, however, the adiabatic TDDFT methodologies are not considered to be sufficiently reliable or accurate because of the high possibility of unphysical states and/or missing states due to the absence of doubly excitations in this adiabatic TDDFT calculation. In the future, either improve the resolution of the spectra to see discrete features arising from different transitions or refine the theory for the open-shell complex will be helpful to solve the problems that have been addressed in this work.

Chapter 7 Ultraviolet photofragmentation spectroscopy of calcium dication benzene complex in the gas phase combined with DFT/TDDFT calculations

7.1 Introduction

The metal cation-π interaction is crucial in controlling both the ionization fraction and the gas-phase depletion of the metallic elements within astrophysical environments such as dense interstellar clouds and star-forming regions.[149] It is also recognized as contributing significantly to protein [150] and DNA stability [150b, 151]. The interaction between a cation and graphite is important for the development of battery materials.[152] Both experimental and theoretical studies have been carried out on cation-π interactions, and have provided valuable insights into their nature.[153] Moreover, the electronic structure of d^0 metal cation-benzene complex has no d orbital which makes them unique starting points for a general understanding of structure, bonding, and reactivity of transition metal compounds.[154]

The UV-visible spectra of alkaline earth metal complexes are routinely recorded in the condensed phase either in solution or in the form of a matrix.[9, 69] However, difficulties experienced in studies of condensed phase where the preparation and/or instability of a given type of complex may impede any systematic survey of metal-ligand interactions.[9] When sufficient number densities formed, metal complexes can be investigated in the gas phase via photodissociation or photodepletion methods using either infrared multi-photon excitation to generate vibrational spectra[155] or single photon UV-visible excitation to create electronic spectra[29a]. A range of groups have already be successful to form and to record electronic spectra of metal-aromatic ligand complexes in the gas phase using electrospray[26, 40a, 41a, 156] and laser vaporization[137g, 157] technique. Singly charged alkaline metal complexes have been the main subjects of their study, where the isolated 4s valence electron can provide

convenient electronic transitions at accessible wavelengths.[38, 158] Pick-up technique is possible to prepare a wide range of complexes containing alkaline earth metals in charge states commonly observed in condensed phase chemistry.[10, 27c, 159] A typical example is the combined experimental and theoretical investigation of $[Ca(pyridine)_4]^{2+}$ and $[Ca(picoline)_4]^{2+}$ in the gas phase.[10] The wavelengths at which the complexes start to exhibit electronic transitions in UV and at which absorption maxima occur were both in good agreement with the theory. Given the importance of calcium in catalysis, biochemistry and materials science, spectroscopic studies in different ligand environments, which can provide an opportunity to explore the possibility of developing spectroscopic markers for the calcium cation, become very important.

In this chapter, the doubly charged calcium benzene complex is prepared, trapped in the gas phase and exposed to the UV laser radiation. Intensities of photofragments are plotted as a function of photon energies to construct the UV photofragmentation spectroscopy. The DFT and TDDFT calculations are performed on $[Ca(benzene)_2]^{2+}$, $[Ca(benzene)(H_2O)_4]^{2+}$, $[Ca(benzene)(H_2O)_2]^{2+}$ and $[Ca(benzene)]^{+/2+}$, respectively.

7.2 Photofragment mass spectra of calcium dication-benzene complex

Details of experimental techniques for ion formation, trapping, photodissociation, detection and data processing have been described in Chapter 2. An example of mass spectra that is recorded without laser radiation is reported in Figure 7.1. There is a peak at 94.7 amu that could correspond to either $[Ca(benzene)(H_2O)_4]^{2+}$ or $[Ca(benzene)_2]^{2+}$. The previous spectroscopic measurement of $[Ca(pyridine)_4]^{2+}$ under the same experimental condition indicate that the calcium dication species has considerable affinity to pick up water molecules from the background.[10] Therefore, the excited states of $[Ca(benzene)_2]^{2+}$ could relax their energy by fragmenting or promoting chemical reactions between trapped ions and water molecules. There is a peak at 77.5 amu that corresponds to either $[Ca(benzene)(H_2O)_2]^{2+}$ or $benzene^+$. The

other three peaks at 66.7, 80.7 and 54.2 amu could correspond to $C_5H_7^+$, $C_6H_9^+$ and $C_4H_6^+$, which possibly arise from the collision between the fragment trapped ions and helium in the ion trap. With laser radiation, an example of UV photofragment mass spectra that is recorded with photon energy of 38610 cm^{-1} is reported in Figure 7.2. From Figure 7.2, it can be noticed that the intensity of the peak at 94.7 amu decreases significantly while the intensity of the peak at 77.6 amu is increasing. Meanwhile, two photofragment peaks which are very sensitive to the laser radiation appear at 40.3 and 52.2 amu. The peak at 40.3 amu could correspond to either Ca^+ or $C_3H_4^+$ and the peak at 52.2 amu corresponds to $C_4H_4^+$. The intensity variations of the peaks at 66.7, 54.2 and 80.6 amu have very limited influence on the final UV spectra, so they are ignored in the overall fragment analysis.

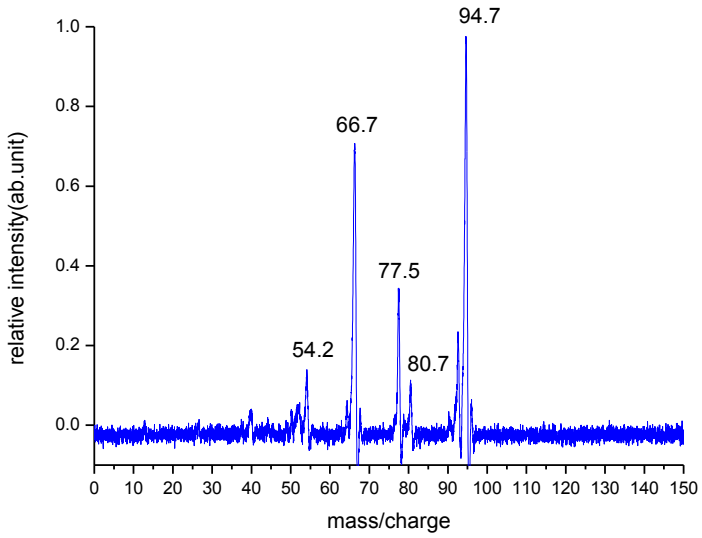

Figure 7.1 Mass spectrum of $[Ca(benzene)_2]^{2+}$.

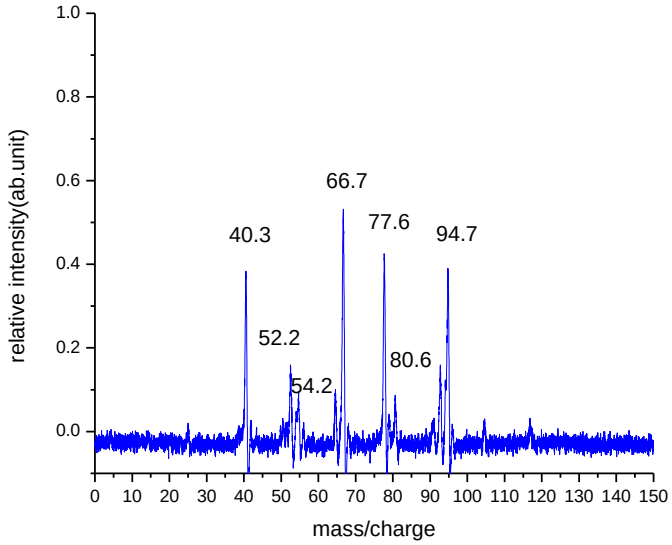

Figure 7.2 UV photofragment mass spectrum of calcium dication-benzene complex. (wave number=38610 cm^{-1})

To fully observe the response to the laser radiation during the scans, some typical examples of mass spectra that are recorded under the laser radiation with different wavelength are reported in Figure 7.3. From Figure 7.3(a), it can be noticed that the intensity of the peak at 94.7 amu decreases and the intensities of the peaks at 77.8, 52 and 40.2 amu increase significantly towards high frequencies. Therefore, overall photofragment intensity is calculated by sum of the intensities of the peaks at 77.8, 52 and 40.2 amu over itself plus the intensity of the parent ion peak at 94.7 amu. From Figure 7.3(b), an overlap of twelve mass spectra of calcium dication benzene complex essentially reflects its overall photodissociation behaviour in the ion trap and its response to laser radiation in each of the scans.

a

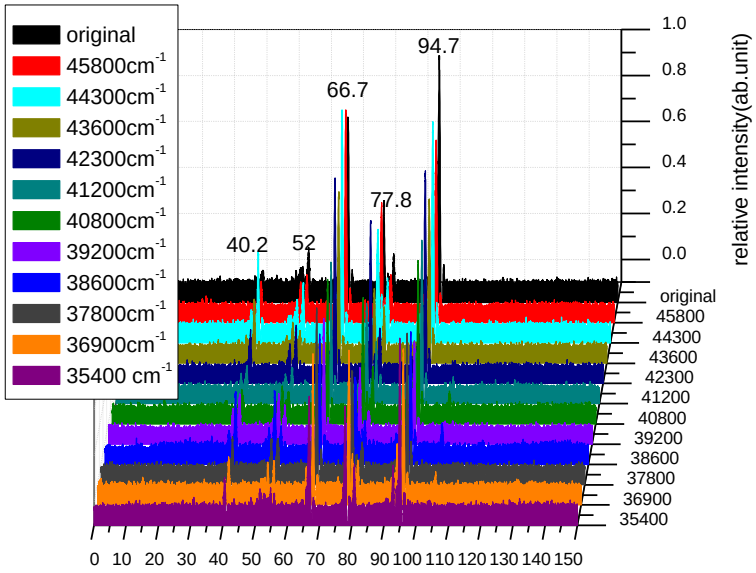

b

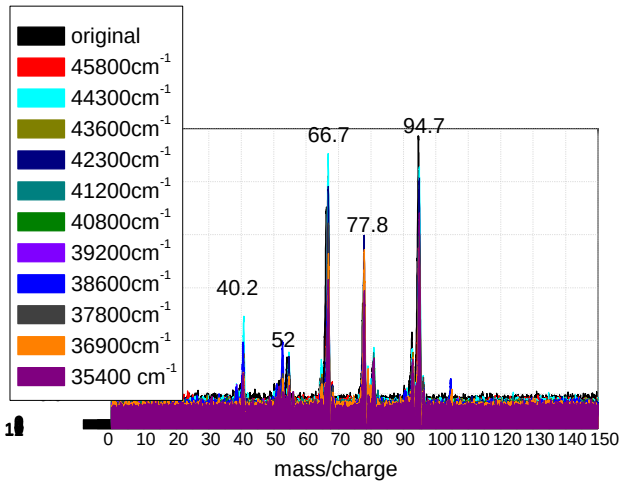

Figure 7.3 Three-dimensional photofragment mass spectrum: intensity *vs* m/e *vs* wave number, (a) comparison of twelve mass spectra examples (b) the overlap of twelve mass spectra.

7.3 UV photofragmentation spectroscopy of $[Ca(benzene)_2]^{2+}$

As described previously, the peaks at 40.2, 52 and 77.8 amu are considered as photofragment peaks. The peak at 94.7 amu is considered as parent ion peak. The overall intensity of photofragments over itself plus the intensity of parent ion leads to

the intensity of fracture fragment. The intensity of fracture fragment is normalised by laser power, then becomes normalized fragment intensity. The normalized fragment intensity is plotted against photon energy in wavenumber to construct the UV photofragmentation spectroscopy, which is reported in Figure 7.4. From Figure 7.4, it can be seen that there are two small features at around 37500 and 38200 cm^{-1}. Another resolved feature can be found at around 39800 cm^{-1}. A big feature builds up starting from 41000 cm^{-1} and extending beyond the upper limit of photon energy range.

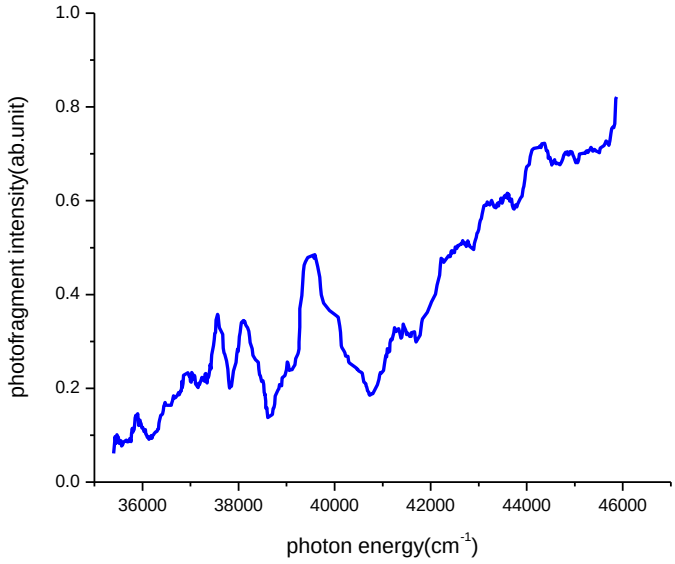

Figure 7.4 UV photofragmentation spectroscopy of calcium dication-benzene complex

7.4 Methodology of theoretical calculations

The structures of $[Ca(benzene)_2]^{2+}$, $[Ca(benzene)]^{+/2+}$ and $[Ca(benzene)(H_2O)_n]^{2+}$ (n=2 and 4) were calculated using DFT as implemented in Gaussian09. Geometry optimizations and frequency analysis were performed on BVP86[94, 121], PBE0[123] and TPSSh[122]/6-311++G(d,p) level. The frequency analysis was used to verify that the geometry was a real minimum without any imaginary frequency. Binding energies were determined from the difference between the total energy of $[Ca(benzene)_2]^{2+}$ and

the sum of the total energy of either $[Ca(benzene)]^+$ and $benzene^+$ or $[Ca(benzene)]^{2+}$ and a neutral benzene on the BVP86, PBE0 and TPSSh/6-311++G(d,p) level. Excitation energies and oscillator strengths of $[Ca(benzene)_2]^{2+}$, $[Ca(benzene)]^{+/2+}$ and $[Ca(benzene)(H_2O)_n]^{2+}$ (n=2, 4) were calculated using TDDFT for all of the optimized geometries. The SCF step of TDDFT was performed on CAM-B3LYP[125], PBE0[123] and TPSSh/6-311++G(d,p) level. The dominant transitions ($f \geq 0.01$) predicted by TDDFT that can be matched to features in the spectra were analyzed by calculating the natural transition orbitals (NTOs)[126] in order to identify the contribution each orbital makes to an electronic transition.

7.5 Calculated Structures and binding energies of $[Ca(benzene)_2]^{2+}$

There are two conformers of $[Ca(benzene)_2]^{2+}$ that are found minima without imaginary frequency using BVP86, PBE0 and TPSSh functional, 6-311++G(d,p) as basis set, which are C_2 (staggered) and C_{2v} (eclipse). The BVP86 optimized geometries for the both conformers are presented in Figure 7.6. In Figure 7.6, it can be seen that both of the structures are hemi-directed, where the rings of sandwich complex are not parallel. Instead, they had a centroid-Ca-centroid angle (angle in degrees from the center of one benzene ring to the metal to the center of the other benzene ring) of ~ 170° rather than 180°. This kind of 'non-VSEPR' (valence-shell electron-pair-repulsion)[160] bent structures has been found in several previous theoretical researches on neutral and singly/doubly charged calcium systems such as calcium dihalides[161], calcium dihydride[162], and $[Ca(L)_2]^{2+}$ (L=HF, H_2O, NH_3)[163]. The bent structures could be explained by core polarization and d orbital participation in σ bonding[154] or possibly by pseudo-Jahn-Teller effect[147]. The $[Ca(benzene)]^{2+}$ is essentially η^6 as expected with a C_{6v} symmetry, and the $[Ca(benzene)]^+$ is η^1 with an approximate C_s symmetry.

<a>C_{2v} (eclipsed)

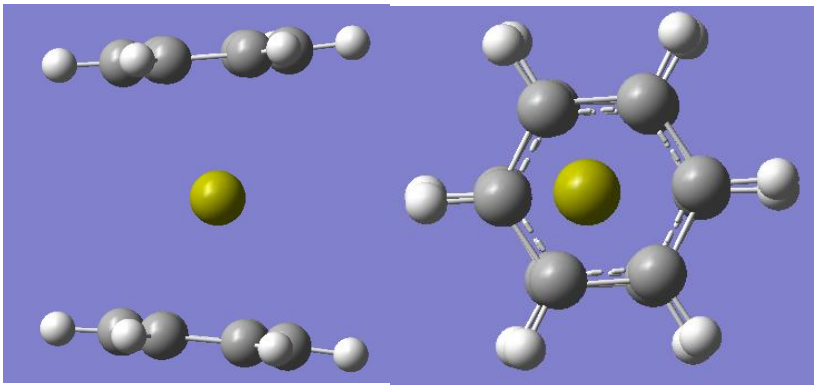

<b> C_2 (staggered)

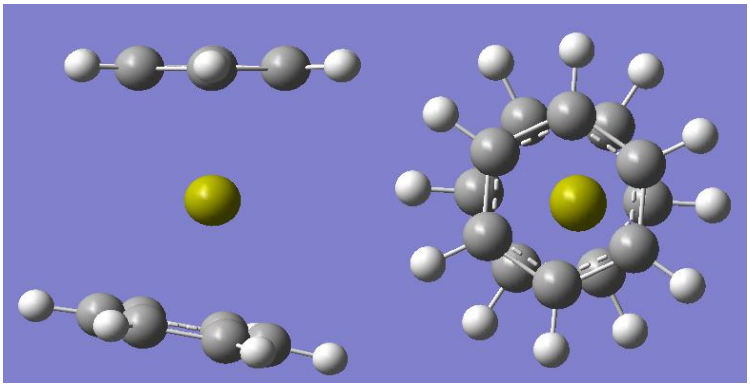

Figure 7.6 Geometries for C_2 and C_{2v} conformer of calcium dication-bis(benzene) complex, optimized using BVP86, 6-311++G(d,p) as basic sets, <a> C_{2v}, <b> C_2.

On the same level of theory (BVP86, PBE0 and TPSSh/6-311++G(d,p)), the $[Ca(benzene)(H_2O)_4]^{2+}$ was optimized within the C_2 point group, where the oxygen atoms were coordinated with the metal center. The structure of $[Ca(benzene)(H_2O)_2]^{2+}$ was optimized as C_1 geometry, which started from the structure generated by removing two water molecules from the optimized $[Ca(benzene)(H_2O)_4]^{2+}$ structure. Both of calcium dication-benzene-water structures found no imaginary mode in their

vibrational frequency analysis. The BVP86 optimized geometries are selected as an example and reported in Figure 7.7.

<a> $[Ca(benzene)(H_2O)_4]^{2+}$

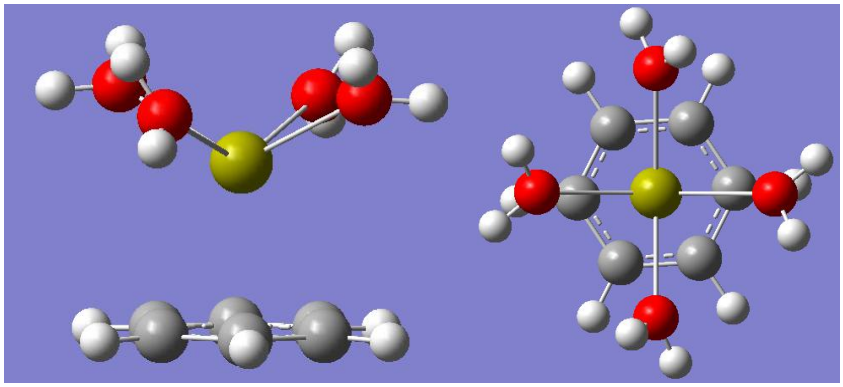

<b> $[Ca(benzene)(H_2O)_2]^{2+}$

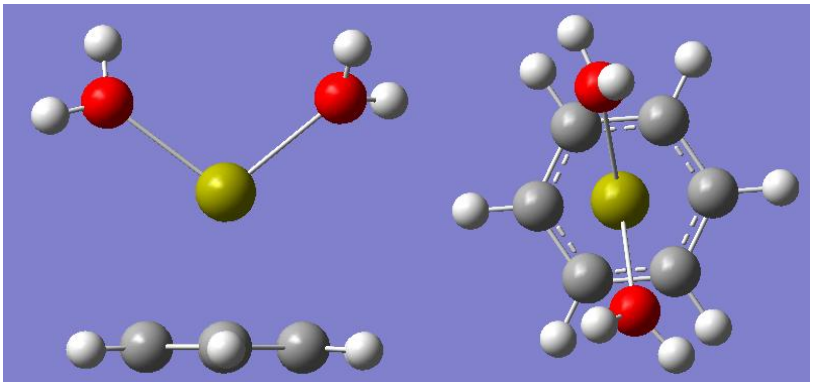

Figure 7.7 Geometries for $[Ca(benzene)(H_2O)_n]^{2+}$ (n=2 and 4) optimized using BVP86, 6-311++G(d,p) as basic sets, <a> $[Ca(benzene)(H_2O)_4]^{2+}$, <b> $[Ca(benzene)(H_2O)_2]^{2+}$.

The calculated binding energies for all optimized geometries of $[Ca(benzene)_2]^{2+}$, $[Ca(benzene)(H_2O)_4]^{2+}$ and $[Ca(benzene)(H_2O)_2]^{2+}$ are giving in Table 7.1. The binding energy of $[Ca(benzene)_2]^{2+}$ is defined as $[Ca(benzene)_2]^{2+} \rightarrow [Ca(benzene)]^{+} + benzene^{+}$ (charge transfer) and $[Ca(benzene)_2]^{2+} \rightarrow [Ca(benzene)]^{2+} +$ benzene (incremental neutral loss). The binding energy of $[Ca(benzene)(H_2O)_4]^{2+}$ is defined as

$[Ca(benzene)(H_2O)_4]^{2+} \rightarrow [Ca(benzene)(H_2O)_2]^{2+} + 2H_2O$ (neutral loss). The binding energy of $[Ca(benzene)(H_2O)_2]^{2+}$ is defined as $[Ca(benzene)(H_2O)_2]^{2+} \rightarrow [Ca(benzene)]^{2+} + 2H_2O$ (neutral loss). It is clear from this set of results that the calculated binding energies of staggered and eclipsed conformers for $[Ca(benzene)_2]^{2+}$ complex on the same level of theory are extremely close in energy (within a kJ/mol) so both of the conformers are accessible in experiment if this is the case. On the other hand, the sum of the calculated binding energies of $[Ca(benzene)(H_2O)_4]^{2+}$ and $[Ca(benzene)(H_2O)_2]^{2+}$ is much higher than the binding energy of $[Ca(benzene)_2]^{2+}$.

Table 7.1 Binding energies for all optimized structures of C_2 and C_{2v} conformers of calcium bis-benzene complex using BVP86 and TPSSh, 6-311++G(d,p) as basis set.

Reaction		Binding Energy (kJ/mol)		
	Geometries	BVP86	PBE0	TPSSh
$[Ca(benzene)_2]^{2+} + h\nu \rightarrow [Ca(benzene)]^{+} + benzene^{+}$	C_{2v}: Eclipsed	165.7	185.8	415.2
	C_2: Staggered	165.8	185.9	415.5
$[Ca(benzene)_2]^{2+} + h\nu \rightarrow [Ca(benzene)]^{2+} + benzene$	C_{2v}: Eclipsed	200	235.5	229.1
	C_2: Staggered	200.1	235.6	229.4
$[Ca(benzene)(H_2O)_4]^{2+} + h\nu \rightarrow [Ca(benzene)(H_2O)_2]^{2+} + 2H_2O$	C_2	215.6	235.4	224.6
$[Ca(benzene)(H_2O)_2]^{2+} + h\nu \rightarrow [Ca(benzene)]^{2+} + 2H_2O$	C_1	317.9	332.9	324.6

7.6 Excited state TDDFT calculations of $[Ca(benzene)]^{+/2+}$

As described in the photofragment mass spectra section, the trapped parent ion could be either one of the two possible calcium dication species or a mixture of both. It is quite difficult to identify the parent ion unequivocally by the photofragment mass spectra only. However, the assignment of calculated electronic transitions in $[Ca(benzene)]^{+/2+}$ could be helpful to fully evaluate the experimental spectra even if the parent ion is uncertain. Thus, the TDDFT calculations on transient intermediates

are performed as a start in this set of calculations. The calculated excitation energies and oscillator strengths are plotted as stick spectra alongside with the experimental spectrum in Figures 7.8-7.12. Assignment of dominant electronic transitions ($f \geq 0.01$) and nature of these electronic transitions are summarized in the Table 7.2-7.6. From Figure 7.8, the electronic transitions calculated on the CAM-B3LYP/6-311++G(d,p) level, based on BVP86 optimized geometries of $[Ca(benzene)]^+$ and $[Ca(benzene)]^{2+}$ have reasonable agreement with the experimental spectrum. An excitation in $[Ca(benzene)]^+$ involving a configuration mixing of metal-based and LMCT fits to the feature at around 37500 cm^{-1} very well. The other two mixing metal-based and LMCT electronic transitions in $[Ca(benzene)]^+$ which are slightly spin contaminated (S^2=0.775) are at 47712 and 47714 cm^{-1}, respectively. There are four LMCT transitions in $[Ca(benzene)]^{2+}$ at 43367, 43374, 45930 and 45932 cm^{-1}, respectively. They can be matched to the big feature which starts from ~41000 cm^{-1} and extends beyond upper limit of the photon energy range (namely, 'the large feature' or the feature at around 45870 cm^{-1}). There is no electronic transition can be assigned to the features at around 39800 and 38200 cm^{-1}.

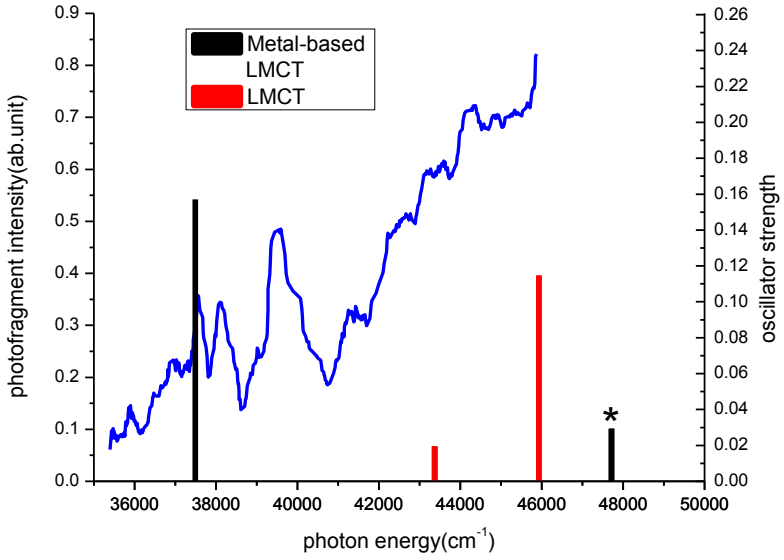

Figure 7.8 Results of TDDFT calculations of $[Ca(benzene)]^+$ and $[Ca(benzene)]^{2+}$ on the CAM-B3LYP/6-311++G** level for the BVP86/6-311++G** optimized geometries overlaid with UV

spectra. The dominant transitions are sorted in their natures and labelled with asterisk (*) if they are spin contaminated.

Table 7.2 Summary of observed and calculated electronic transitions, and oscillator strengths (f ≥ 0.01 in the range of 35,000 – 50,000 cm^{-1}) for the BVP86/6-311++G** optimized geometries of $[Ca(benzene)]^{+}$ and $[Ca(benzene)]^{2+}$ on the CAM-B3LYP/6-311++G** level, along with the $\langle \hat{S}^2 \rangle$ value. The weight and character of the dominant configurations for each spin, and the % Ca character, is also provided. Dominant transitions, theory and experiment, are shown in bold.

Observed	Calculated	f	$\langle \hat{S}^2 \rangle$	NTO descriptions*	Assignments*
37500	**37492[a]**	**0.1571**	**0.751**	**α- Metal-based electronic transition (200 %) β-LMCT (0.1 %)**	**Metal-based electronic transition 3s (91 % Ca)→ 4s (39 % Ca)+ 4p (30 % Ca) LMCT π → 3d (68 % Ca)**
45870	43367[b]	0.0195	0	LMCT(98%) LMCT(2%)	LMCT π → 4s+3d (>56% Ca)
	43374[b]	0.0195	0	LMCT(98%) LMCT(2%)	LMCT π → 4s+3d (>56% Ca)
	45930[b]	**0.1147**	**0**	**LMCT(52%) LMCT(48%)**	**LMCT π → 3d (67% Ca)**
	45932[b]	**0.1146**	**0**	**LMCT(52%) LMCT(48%)**	**LMCT π → 3d (67% Ca)**
	47712[a]	0.0293	0.776	α- Metal-based electronic transition (93%) β-LMCT (104 %)	Metal-based electronic transition 3s (92 % Ca)→ 4p (81 % Ca) LMCT π → 4s (87 % Ca)
	47714[a]	0.0294	0.776	α- Metal-based electronic transition (94%) β-LMCT (103 %)	Metal-based electronic transition 3s (92 % Ca)→ 4p (81 % Ca) LMCT π → 4s (87 % Ca)

[a]$[Ca(benzene)]^{+}$, [b]$[Ca(benzene)]^{2+}$

* Only the most dominant transition is shown for each spin; weight is given in parenthesis.

From Figure 7.9 and Table 7.3, it can be found that the excitation data on the same level of theory based on PBE0 optimized geometry is very similar as the TDDFT-CAM-B3LYP/BVP86 data, only with some slight shift in excitation energy and oscillator strength. The nature of the calculated electronic transitions does not change based on the two different geometries.

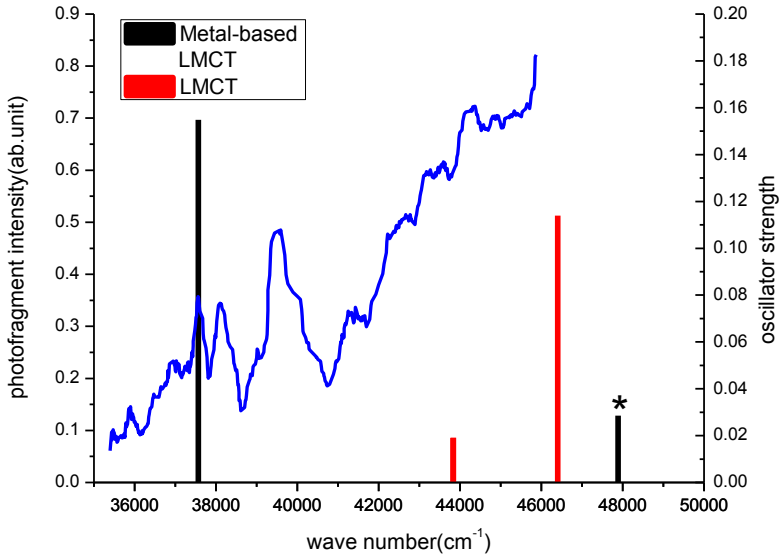

Figure 7.9 Results of TDDFT calculations of $[Ca(benzene)]^{+}$ and $[Ca(benzene)]^{2+}$ on the CAM-B3LYP/6-311++G** level for the PBE0/6-311++G** optimized geometries overlaid with UV spectra. The dominant transitions are sorted in their natures and labelled with asterisk (*) if they are spin contaminated.

Table 7.3 Summary of observed and calculated electronic transitions, and oscillator strengths (f ≥ 0.01 in the range of 35,000 – 50,000 cm^{-1}) for the PBE0/6-311++G** optimized geometries of $[Ca(benzene)]^{+}$ and $[Ca(benzene)]^{2+}$ on the CAM-B3LYP/6-311++G** level, along with the $\langle \hat{S}^2 \rangle$ value. The weight and character of the dominant configurations for each spin, and the % Ca character, is also provided. Dominant transitions, theory and experiment, are shown in bold.

Observed	Calculated	*f*	$<\hat{S}^2>$	NTO descriptions*	Assignments*
37500	**37567[a]**	**0.1548**	**0.751**	**α- Metal-based electronic transition (200%) β-LMCT(0.1%)**	**Metal-based electronic transition 3s(91% Ca)→4s(40% Ca)+4p(29% Ca) LMCT π→3d(68% Ca)**
45870	43831[b]	0.019	0	LMCT(98%) LMCT(2%)	LMCT π→4s(66% Ca)+3d(27% Ca)
	43834[b]	0.0191	0	LMCT(98%) LMCT(2%)	LMCT π→4s(66% Ca)+3d(27% Ca)
	46402[b]	**0.1139**	**0**	**LMCT(52%) LMCT(48%)**	**LMCT π→4s(31% Ca)+3d(68% Ca)**
	47886[a]	0.0285	0.775	α- Metal-based electronic transition (137%) β-LMCT(60%)	Metal-based electronic transition 3s(91% Ca)→4p(82% Ca) LMCT π→4s(85% Ca)

[a][Ca(benzene)]$^{+}$, [b][Ca(benzene)]$^{2+}$

* Only the most dominant transition is shown for each spin; weight is given in parenthesis.

From Figure 7.10 and Table 7.4, the distribution of electronic transitions calculated on the CAM-B3LYP/6-311++G(d,p) level based on TPSSh optimized geometry is very similar to the other two TDDFT-CAM-B3LYP data. There are two more mixing metal-based and LMCT electronic transitions in [Ca(benzene)]$^{+}$ can be found at 47810 and 47813 cm^{-1} with a slight spin contamination. In general, the TDDFT-CAM-B3LYP data of [Ca(benzene)]$^{+/2+}$ fits to the feature at around 37500 cm^{-1} and the large feature at around 45870 cm^{-1} in the spectra very well. Only the electronic transitions that appear at 47810 and 47813 cm^{-1} have a slight spin contamination. The nature of calculated excitations and the excitation energies are quit close only with a slight shift.

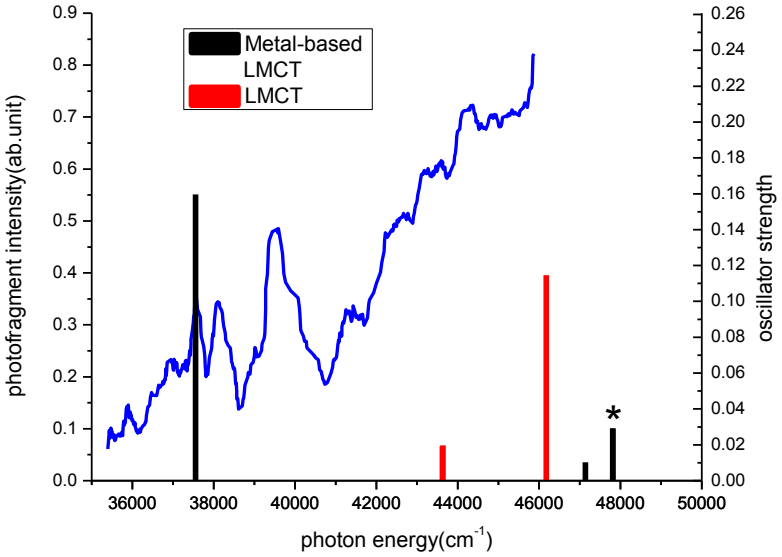

Figure 7.10 Results of TDDFT calculations of $[Ca(benzene)]^{+}$ and $[Ca(benzene)]^{2+}$ on the CAM-B3LYP/6-311++G** level for the TPSSh/6-311++G** optimized geometries overlaid with UV spectra. The dominant transitions are sorted in their natures and labelled with asterisk (*) if they are spin contaminated.

Table 7.4 Summary of observed and calculated electronic transitions, and oscillator strengths (f ≥ 0.01 in the range of 35,000 – 50,000 cm^{-1}) for the TPSSh/6-311++G** optimized geometries of $[Ca(benzene)]^{+}$ and $[Ca(benzene)]^{2+}$ on the CAM-B3LYP/6-311++G** level, along with the $\langle\hat{S}^2\rangle$ value. The weight and character of the dominant configurations for each spin, and the % Ca character, is also provided. Dominant transitions, theory and experiment, are shown in bold.

Observed	Calculated	f	$\langle\hat{S}^2\rangle$	NTO descriptions*	Assignments*
37500	**37554[a]**	**0.1596**	**0.75**	**α- Metal-based electronic transition (203%) β-LMCT(0.1%)**	**Metal-based electronic transition 3s(91% Ca)→4s(39% Ca)+4p(31% Ca) LMCT π→3d(68% Ca)**
45870	43622[b]	0.0194	0	LMCT(99%) LMCT(2%)	LMCT π → 4s+3d (>56% Ca)

	43637[b]	0.0196	0	LMCT(98%) LMCT(2%)	LMCT π → 4s+3d (>56% Ca)
	46176[b]	**0.1146**	**0**	**LMCT(52%)** **LMCT(48%)**	**LMCT** **π → 3d (67% Ca)**
	47141[a]	0.0102	0.75	α- Metal-based electronic transition (199%) β-LMCT(0.3%)	Metal-based electronic transition 3s(91% Ca)→4s(38% Ca)+4p(20% Ca) LMCT π→3d(92% Ca)
	47810[a]	0.0292	0.76	α- Metal-based electronic transition (155%) β-LMCT(42%)	Metal-based electronic transition 3s(91% Ca)→4p(83% Ca) LMCT π→4s(84% Ca)
	47813[a]	0.0291	0.76	α- Metal-based electronic transition (155%) β-LMCT(42%)	Metal-based electronic transition 3s(91% Ca)→4p(83% Ca) LMCT π→4s(84% Ca)

[a][Ca(benzene)]$^{+}$, [b][Ca(benzene)]$^{2+}$

* Only the most dominant transition is shown for each spin; weight is given in parenthesis. Assume, arbitrarily, that less that 60% metal character is more appropriately classes as a ML orbital rather than an M orbital.

The excitation energies and related oscillator strengths of [Ca(benzene)]$^{+}$ and [Ca(benzene)]$^{2+}$ have been calculated on the PBE0/6-311++G(d,p) level based on BVP86, PBE0 and TPSSh optimized geometries. Like the TDDFT-CAM-B3LYP data, the three TDDFT-PBE0 data looks very similar. There is no significant difference can be found in the nature of excitations and agreement between the calculation and spectra, but a slight shift in excitation energies and oscillator strengths. Therefore, the representative TDDFT-PBE0 data based on BVP86 optimized geometry is selected as a typical example and plotted as stick spectra alongside with the experimental UV spectra in Figure 7.11. Assignment of dominant

electronic transitions ($f \geq 0.01$) and nature of these electronic transitions are summarized in the Table 7.5. From Figure 7.11, the electronic transitions appear in the range of 41000-43000 cm^{-1}. There is no transitions can be found to match the features at around 37500, 38200 and 39500 cm^{-1}. The two mixing MLLCT and LMLCT transitions in $[Ca(benzene)]^{+}$ at 41790 and 42107 cm^{-1} can be matched to the large feature in the spectrum. It also needs to be noted that they are significantly spin contaminated. There are four LMCT transitions in the range of 42800-44800 cm^{-1} which have good agreement with the large feature at 45870 cm^{-1} in the spectrum.

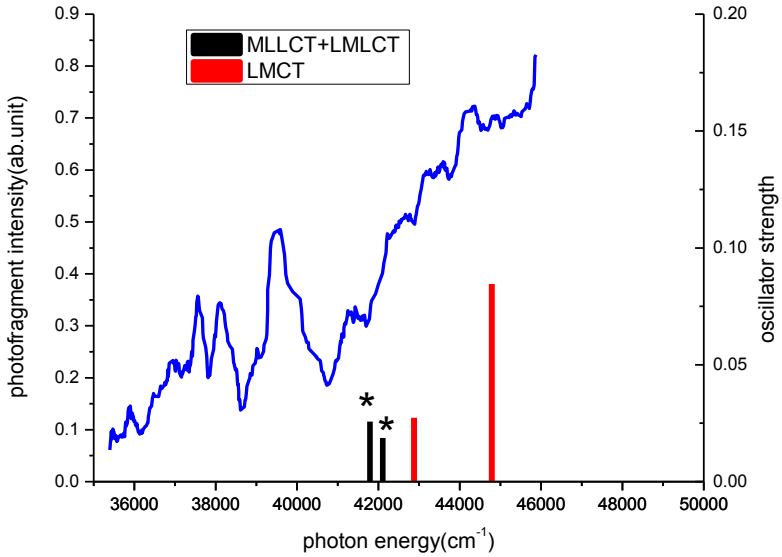

Figure 7.11 Results of TDDFT calculations of $[Ca(benzene)]^{+}$ and $[Ca(benzene)]^{2+}$ on the PBE0/6-311++G** level for the BVP86/6-311++G** optimized geometries overlaid with UV spectra. The dominant transitions are sorted in their natures and labelled with asterisk (*) if they are spin contaminated.

Table 7.5 Summary of observed and calculated electronic transitions, and oscillator strengths (*f* ≥ 0.01 in the range of 35,000 – 50,000 cm^{-1}) for the BVP86/6-311++G** optimized geometries of $[Ca(benzene)]^{+}$ and $[Ca(benzene)]^{2+}$ on the PBE0/6-311++G** level, along with the $<\hat{S}^2>$ value. The weight and character of the dominant configurations for each spin, and the % Ca character, is also provided. Dominant transitions, theory and experiment, are shown in bold.

Observed	Calculated	*f*	$<\hat{S}^2>$	NTO descriptions*	Assignments*
45870	41790[a]	0.0257	1.043	α-MLLCT (65%) β-LMLCT (99%)	MLLCT 3d (46 % Ca)+σ→ π* LMLCT π → 3d (15 % Ca)+π*
	42107[a]	0.0187	0.915	α-MLLCT (86%) β-LMLCT (75%)	MLLCT 3d (46 % Ca)+σ→ π* LMLCT π → 3d (15 % Ca)+π*
	42874[b]	0.0272	0	LMCT(96%) LMCT(4%)	LMCT π → 4s+3d (>32% Ca)
	42879[b]	0.0273	0	LMCT(96%) LMCT(4%)	LMCT π → 4s+3d (>32% Ca)
	44786[b]	**0.0845**	**0**	**LMCT(54%) LMCT(46%)**	**LMCT π → 3d (>70% Ca)**
	44788[b]	**0.0844**	**0**	**LMCT(54%) LMCT(46%)**	**LMCT π → 3d (>70% Ca)**

[a]$[Ca(benzene)]^{+}$, [b]$[Ca(benzene)]^{2+}$

* Only the most dominant transition is shown for each spin; weight is given in parenthesis. Assume, arbitrarily, that less that 60% metal character is more appropriately classed as a ML orbital rather than an M orbital.

Finally, the TDDFT calculations of $[Ca(benzene)]^{+/2+}$ have been performed on TPSSh/6-311++G(d,p) level based on BVP86, PBE0 and TPSSh optimized geometries. The TDDFT-TPSSh data based on BVP86 geometry is selected as a representative example to plotted as stick spectra alongside with the experimental UV spectrum in Figure 7.12. Assignment of dominant electronic transitions ($f \geq 0.01$) and nature of these electronic transitions are summarized in the Table 7.6. All of the

electronic transitions calculated in $[Ca(benzene)]^+$ can be matched to the large feature at 45870 cm^{-1} except for the intense excitation at 35161 cm^{-1}. Only one transition in $[Ca(benzene)]^+$ at 49709 cm^{-1} is spin contaminated ($<\hat{S}^2> = 0.82$) and has different nature (LMCT+LMLCT, last entry in Table 7.6). The calculated excitations in doubly charged species are mainly LMCT, which is as same as TDDFT-CAM-B3LYP and TDDFT-PBE0 data. They can be matched to the large feature at 45870 cm^{-1} in the spectrum.

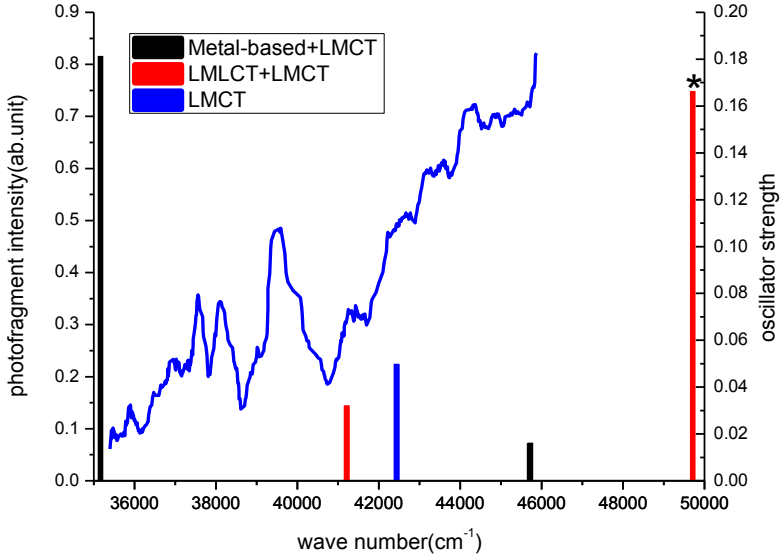

Figure 7.12 Results of TDDFT calculations of $[Ca(benzene)]^+$ and $[Ca(benzene)]^{2+}$ on the TPSSh/6-311++G** level for the BVP86/6-311++G** optimized geometries overlaid with UV spectra. The dominant transitions are sorted in their natures and labelled with asterisk (*) if they are spin contaminated.

Table 7.6 Summary of observed and calculated electronic transitions, and oscillator strengths (*f* ≥ 0.01 in the range of 35,000 – 50,000 cm^{-1}) for the BVP86/6-311++G** optimized geometries of $[Ca(benzene)]^{+}$ and $[Ca(benzene)]^{2+}$ on the TPSSh/6-311++G** level, along with the $\langle \hat{S}^2 \rangle$ value. The weight and character of the dominant configurations for each spin, and the % Ca character, is also provided. Dominant transitions, theory and experiment, are shown in bold.

Observed	Calculated	*f*	$\langle \hat{S}^2 \rangle$	NTO descriptions*	Assignments*
-	**35161[a]**	**0.1814**	**0.75**	**α- Metal-based electronic transition (200%) β-LMCT (0%)**	**Metal-based electronic transition 3s (90 % Ca) → 4p (48 % Ca)+4s (24 % Ca) LMCT π → 3d (62 % Ca)**
45870	41208[b]	0.0321	0	LMLCT (93%) LMCT (7%)	LMLCT π → 3d (44 % Ca)+4s (50% Ca) LMCT π→3d(76% Ca)
	41213[b]	0.0322	0	LMLCT (93%) LMCT (7%)	LMLCT π → 3d (44 % Ca)+4s (50% Ca) LMCT π→3d(76% Ca)
	42435[b]	0.05	0	LMCT(58%) LMCT(42%)	LMCT π→ 3d (>75 % Ca)
	42441[b]	0.0497	0	LMCT(58%) LMCT(42%)	LMCT π→ 3d (>75 % Ca)
	45705[a]	0.0161	0.75	α- Metal-based electronic transition (192%) β-LMCT(5%)	Metal-based electronic transition 3s(90% Ca)→4p(89% Ca) LMCT π→ 4s (82% Ca)
	45722[a]	0.0163	0.75	α- Metal-based electronic transition (193%) β-LMCT(5%)	Metal-based electronic transition 3s(90% Ca)→4p(89% Ca) LMCT π→ 4s (82% Ca)
	49709[a]	**0.1664**	**0.84**	**α-LMCT(59%) β-LMLCT(40%)**	**LMCT π→3d(73% Ca) LMLCT π→3d(43% Ca)+σ**

[a][Ca(benzene)]$^{+}$, [b][Ca(benzene)]$^{2+}$

* Only the most dominant transition is shown for each spin; weight is given in parenthesis. Assume, arbitrarily, that less that 60% metal character is more appropriately classes as a ML orbital rather than an M orbital.

From what has been discussed above, it can be found that the TDDFT-CAM-B3LYP data has the best agreement with the experimental UV spectra. The calculated mixing metal-based and LMCT transitions in [Ca(benzene)]$^{+}$ and LMCT ($\pi \rightarrow 3d$) transitions in [Ca(benzene)]$^{2+}$ can match the features at around 37500 and 45870 cm^{-1}, respectively. Excitations with the configuration of mixing metal-based and LMCT in [Ca(benzene)]$^{+}$ at around 47700 cm^{-1} are slightly spin contaminated. The nature of the dominant electronic transition is not affected by different geometry optimization functional but there are some slight difference in their excitation energies and oscillator strengths as expected. However, some spectral features cannot match to the calculated spectrum. For example, the feature at around 39500 cm^{-1} cannot be assigned by any calculated excitation.

7.7 Excited state TDDFT calculations of [Ca(benzene)$_2$]$^{2+}$

To identify the photofragmentation mechanism and bench mark theory in the systematic fashion, the excitation energies and oscillator strengths for both C_2 and C_{2v} conformer of [Ca(benzene)$_2$]$^{2+}$ are calculated on the same level of theory based on BVP86, PBE0 and TPSSh optimized geometries, respectively. The TDDFT-CAM-B3LYP data based on BVP86 geometry is selected as an example to plot as stick spectra overlaid with the experimental UV spectra in Figure 7.13. Assignment of dominant electronic transitions ($f \geq 0.01$) and nature of these electronic transitions are summarized in the Table 7.7. It can be seen that there is no electronic transition in [Ca(benzene)$_2$]$^{2+}$ falling in the range of laser wavelength that was applied in the experiment. The electronic transition with the lowest excitation energy in

$[Ca(benzene)_2]^{2+}$ appears at 48211 cm^{-1} (f = 0.012). The two mixing LMLCT and LMCT transitions at 48330 and 48473 cm^{-1}, and the LMCT transition at 48510 cm^{-1} are quite intense that can be matched to the large feature at 45870 cm^{-1} in the spectrum with a ~2000 cm^{-1} shift towards low energy. The other less intense transitions can be sorted to LMLCT, LMCT and mixing LMLCT and LMCT transition in their nature. The involved frontier orbitals are identified as π orbital in benzene molecule and 3d orbital in the calcium ion, which are consistent throughout different functional. The dominant LMCT electronic transitions are also found from the TDDFT calculations for copper and lead benzene complexes in the same range of photon energy. All of these electronic transitions are used to assign the large feature in the spectra that extended beyond the upper limit of the photon energy.

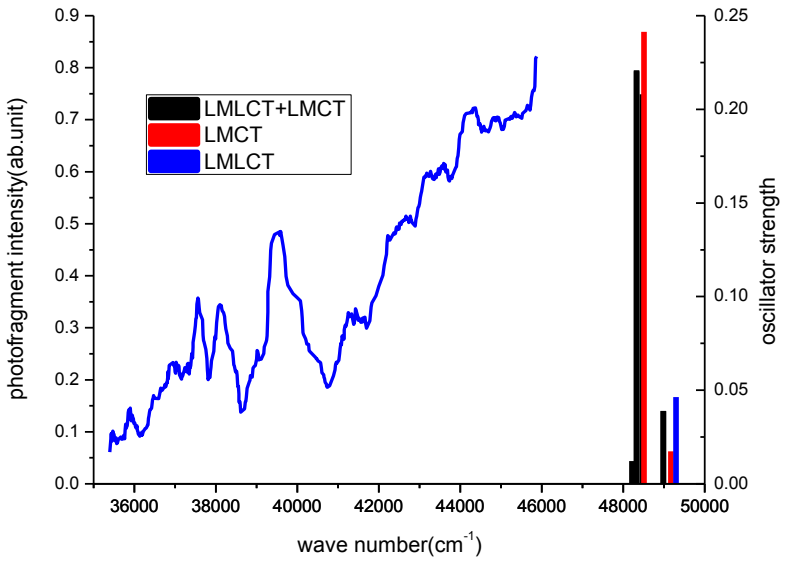

Figure 7.13 Calculated excitation energies and oscillator strengths of $[Ca(benzene)_2]^{2+}$ C_2 and C_{2v} conformers on the CAM-B3LYP/6-311++G** level based on BVP86/6-311++G** optimized geometry.

Table 7.7 Summary of observed and calculated electronic transitions, and oscillator strengths (*f* ≥ 0.01 in the range of 35000 – 50000 cm^{-1}) for the BVP86/6-311++G** optimized geometries of $[Ca(benzene)_2]^{2+}$ on the CAM-B3LYP/6-311++G** level. Dominant transitions, theory and experiment, are shown in bold.

Observed	Calculated	*f*	NTO descriptions*	Assignments*
45870	48211[b]	0.0122	LMLCT(60%) LMCT(39%)	LMLCT π→σ+3d(39% Ca) LMCT π→3d(42% Ca)
	48330[a]	**0.2204**	**LMLCT(51%)** **LMCT(49%)**	**LMLCT** **π→σ+3d(46% Ca)** **LMCT** **π→3d(45% Ca)**
	48473[b]	**0.2081**	**LMLCT(53%)** **LMCT(47%)**	**LMLCT** **π→σ+3d(46% Ca)** **LMCT** **π→3d(45% Ca)**
	48510[b]	**0.2414**	**LMCT(51%)** **LMCT(49%)**	**LMCT** **π→ 3d(45% Ca)**
	48983[a]	0.0389	LMLCT(98%) LMCT(1%)	LMLCT π→σ+3d(40% Ca) LMCT π→3d(46% Ca)
	48990[a]	0.0388	LMLCT(98%) LMCT(1%)	LMLCT π→σ+3d(40% Ca) LMCT π→3d(46% Ca)
	49169[b]	0.0173	LMCT(100%) LMCT(0.2%)	LMCT π→σ+3d(>39% Ca)
	49297[b]	0.0464	LMLCT(98%) LMLCT(2%)	LMLCT π→σ+3d(>39% Ca)

[a]$[Ca(benzene)_2]^{2+}$ C_{2v} conformer, [b]$[Ca(benzene)_2]^{2+}$ C_2 conformer.

* Assume, arbitrarily, that less that 60% metal character is more appropriately classes as a ML orbital rather than an M orbital.

The excited energies and oscillator strengths of most intense electronic transitions for the two conformers of $[Ca(benzene)_2]^{2+}$ and $[Ca(benzene)]^{2+}$ optimized by BVP86 and TPSSh functional, calculated using CAM-B3LYP, PBE0 and TPSSh functionals are

listed in Table 7.8. From this table, the excitation data, oscillator strengths, and assignment for the most dominant electronic transition obtained with different methodologies are consistent, except for the TD-CAM-B3LYP data of $[Ca(benzene)_2]^{2+}$ which has mixing LMLCT and LMCT configuration involved. In most of the results, the nature of the electronic transition is consistent throughout different functional but some slight difference on contribution from their frontier orbital as expected.

Table 7.8 Comparison of the dominant transition for the two conformers of $[Ca(benzene)_2]^{2+}$. The notation TD-functional1/functional2 is used to indicate the functional used in the TD calculation and the geometry optimization, respectively. The 6-311++G(d,p) basis set was used in all cases.

Method	$[Ca(benzene)_2]^{2+}$ C_{2v} (eclipsed)			
	E / cm^{-1}	f	NTO description	Assignment
TD- CAM-B3LYP /BVP86	48330.1	0.2209	LMLCT(51%) LMCT(49%)	LMLCT π→σ+3d(46% Ca) LMCT π→3d(45% Ca)
TD- CAM-B3LYP /TPSSh	48213.6	0.24	LMLCT (51%) LMCT (50 %)	LMLCT π→ 3d (>49 % Ca)+σ LMCT π→3d(50% Ca)
TD-PBE0/BVP86	44656.8 /44658.8	0.1169	LMCT(48%) LMCT(48%)	LMCT π → 3d (40% Ca)
TD-PBE0/TPSSh	44569.2	0.1131	LMCT(48%) LMCT(48%)	LMCT π → 3d (44% Ca)
TD-TPSSh/BVP86	41512.7	0.0682	LMCT(45%) LMCT(45%)	LMCT π → 3d (40% Ca)
TD-TPSSh/TPSSh	41368.4	0.0648	LMCT (46%) LMCT (45%)	LMCT π→3d(>44% Ca)
	$[Ca(benzene)_2]^{2+}$ C_2 (staggered)			
TD- CAM-B3LYP /BVP86	48510.7	0.2414	LMCT(51%) LMCT(49%)	LMCT π→ 3d(45% Ca)

TD- CAM-B3LYP /TPSSh	48213.6	0.2399	LMLCT (51%) LMCT (50 %)	LMLCT $\pi\rightarrow$ 3d (>49 % Ca)+σ LMCT $\pi\rightarrow$3d(50% Ca)
TD-PBE0/BVP86	44788.8	0.117	LMCT(49%) LMCT(46%)	LMCT $\pi\rightarrow$ 3d (>39 % Ca)
TD-PBE0/TPSSh	44571.2	0.1126	LMCT(48%) LMCT(48%)	LMCT $\pi \rightarrow$ 3d (44% Ca)
TD-TPSSh/BVP86	41621.5	0.0676	LMCT(46%) LMCT(43%)	LMCT $\pi \rightarrow$ 3d (40% Ca)
TD-TPSSh/TPSSh	41371.8	0.0648	LMCT(46%) LMCT(45%)	LMCT $\pi \rightarrow$ 3d (>44% Ca)
	$[Ca(benzene)]^{2+}$ C_{6v}			
TD-CAM-B3LYP/BVP86	45930.5/45932.6	0.1147	LMCT(52%) LMCT(48%)	LMCT $\pi \rightarrow$ 3d (67% Ca)
TD- CAM-B3LYP /TPSSh	46176.5	0.1146	LMCT(52%) LMCT(48%)	LMCT $\pi \rightarrow$ 3d (67% Ca)
TD-PBE0/BVP86	44786.8	0.0845	LMCT(54%) LMCT(46%)	LMCT $\pi \rightarrow$ 3d (>70% Ca)
TD-PBE0/TPSSh	45038.9	0.0847	LMCT(54%) LMCT(46%)	LMCT $\pi \rightarrow$ 3d (>70% Ca)
TD-TPSSh/BVP86	42435.8	0.05	LMCT(58%) LMCT(42%)	LMCT $\pi\rightarrow$ 3d (>75 % Ca)
TD-TPSSh/TPSSh	42687.6	0.0503	LMCT(57%) LMCT(43%)	LMCT $\pi \rightarrow$ 3d (>75% Ca)

7.8 Excited state TDDFT calculations of $[Ca(benzene)(H_2O)_n]^{2+}$ (n= 2, 4)

To investigate the excitations arising from calcium dication-benzene-water species, the TDDFT calculations of $[Ca(benzene)(H_2O)_{2/4}]^{2+}$ are performed. The excitation data and oscillator strength of $[Ca(benzene)(H_2O)_4]^{2+}$ and $[Ca(benzene)(H_2O)_2]^{2+}$ on

the CAM-B3LYP/6-311++G(d,p) level are plotted together with the experimental spectra in Figure 7.14 and 7.15.

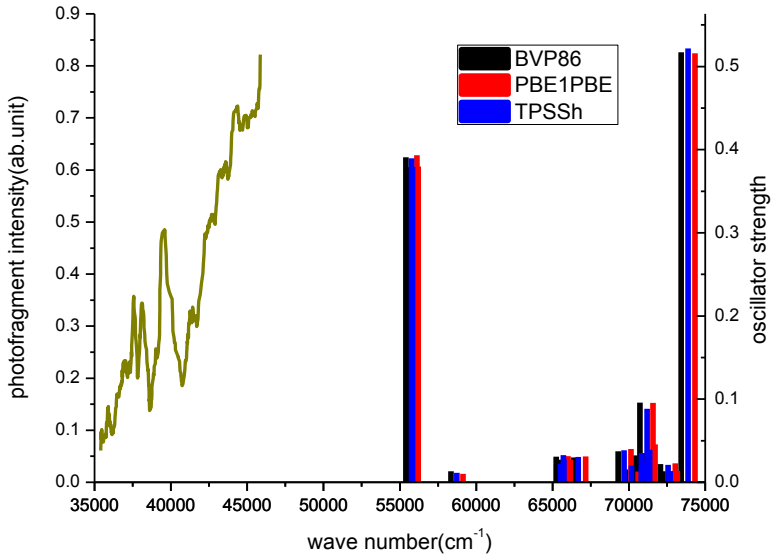

Figure 7.14 TDDFT calculations of $[Ca(benzene)(H_2O)_4]^{2+}$ on the CAM-B3LYP/6-311++G** level based on BVP86, PBE0 and TPSSh/6-311++G** optimized geometry.

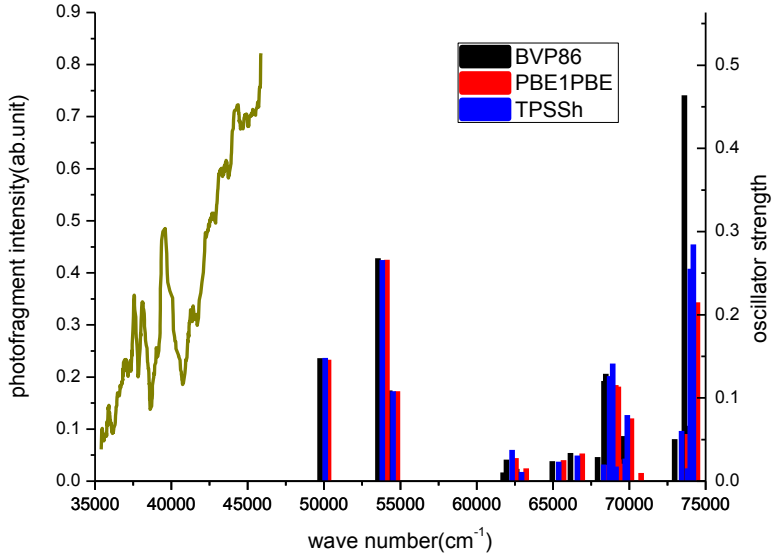

Figure 7.15 TDDFT calculations of $[Ca(benzene)(H_2O)_2]^{2+}$ on the CAM-B3LYP/6-311++G** level based on BVP86, PBE0 and TPSSh/6-311++G** optimized geometry.

From the two set of TDDFT data above, one may notice that there is no dominant calculated electronic transition that can be matched to the features in the spectra falling in the range of experimental range. It indicates that the contribution of $[Ca(benzene)(H_2O)_{2/4}]^{2+}$ species to the features in the experimental spectra cannot be supported by the TDDFT calculations on this level of theory. The calculated electronic transitions here could possibly be responsible for the features which appear far beyond the upper limit of the photon energy that this experiment covered. But without experimental evidence, there is no definite conclusion can be made. Therefore, due to the absence of the features that are beyond the experimental wavelength range, the experimental spectra cannot be used to bench mark the theory which is applied on calcium dication-benzene-water species in confidence.

7.9 Photofragmentation mechanism

From the calculations above, both $[Ca(benzene)]^{+/2+}$ and $[Ca(benzene)_2]^{2+}$ have been proved to have contribution to the UV spectrum. Along with this observation, the photofragment mass spectra display Ca^+(or $C_3H_4^+$), benzene$^+$ and $C_4H_4^+$. Two possible mechanisms that are capable of generating the product ions of interest are:

$$[Ca(benzene)_2]^{2+} + h\nu \rightarrow [Ca(benzene)\ ]^+ + benzene^+$$

$$[Ca(benzene)]^+ + h\nu \rightarrow Ca + benzene^+$$

$$benzene^+ + h\nu \rightarrow C_4H_4^+ + C_2H_2$$

$$\rightarrow C_3H_4^+ + C_3H_2 \qquad (1)$$

$$[Ca(benzene)_2]^{2+} + h\nu \rightarrow [Ca(benzene)]^{2+} + benzene$$

$$[Ca(benzene)]^{2+} \rightarrow Ca^+ + benzene^+$$

$$benzene^+ + h\nu \rightarrow C_3H_4^+ + C_3H_2$$

$$\rightarrow C_4H_4^+ + C_2H_2 \qquad (2)$$

For the sake of the first ionization energy of calcium and benzene (IE (Ca) = 6.11 eV, IE (Bz) = 9.24 eV)[35], Ca^+ should be produced rather than benzene$^+$ in the second step of mechanism 1. However, some experimental features can be matched to the calculated excitations in $[Ca(benzene)]^+$, which indicates this photofragment possibly presents in the photoexcitation cycle. Additional contributions to the photofragment spectrum could come from $[Ca(benzene)]^+$, if it fragmented from an electronic excited state that correlated with benzene$^+$ as a reaction fragment. This could happen by the photoexcitation of $[Ca(benzene)]^+$ followed by a charge transfer process between Ca^+ and neutral benzene. The resultant benzene$^+$ dissociates to $C_3H_4^+$ and $C_4H_4^+$ as mechanism 1. The other possibility is $[Ca(benzene)_2]^{2+}$ losing a neutral benzene followed by a charge transfer process where the $[Ca(benzene)]^{2+}$ dissociates to Ca^+ and benzene$^+$. The peak at 40.2 amu in the mass spectra can be identified as Ca^+ if this is the case. Subsequent photodissociation of benzene$^+$ could then produce $C_3H_4^+$, $C_4H_4^+$ as mechanism 2. Mechanism 2 provides the most obvious route to the appearance of benzene$^+$, and the match between calculated and experimental spectra provides evidence for the presence of $[Ca(benzene)]^{2+}$ ion. Therefore, the fragment benzene$^+$ observed from the mass spectra could be a charge transfer product of either $[Ca(benzene)_2]^{2+}$ or $[Ca(benzene)]^{+/2+}$.

On the other hand, the possible route for photodissociation of $[Ca(benzene)(H_2O)_4]^{2+}$ is as follow,

$$[Ca(benzene)(H_2O)_4]^{2+} + h\nu \rightarrow [Ca(benzene)(H_2O)_2]^{2+} + 2H_2O$$

$$[Ca(benzene)(H_2O)_2]^{2+} + h\nu \rightarrow [Ca(benzene)]^{2+} + 2H_2O$$

$$[Ca(benzene)]^{2+} \rightarrow Ca^+ + benzene^+$$

$$benzene^+ + h\nu \rightarrow C_3H_4^+ + C_3H_2$$

$$\rightarrow C_4H_4^+ + C_2H_2 \qquad (3)$$

In this case, the peaks at 77.8 and 40.2 amu could be considered as $[Ca(benzene)(H_2O)_2]^{2+}$ and Ca^+, respectively. It needs to be noted that there is no sufficient evidence can be found in the calculations to support that the $[Ca(benzene)(H_2O)_4]^{2+}$ and $[Ca(benzene)(H_2O)_2]^{2+}$ have contribution to the experimental spectra. Therefore the photofragmentation mechanism for the calcium dication-benzene-water species cannot be considered as a definite conclusion based on this experiment. Further experimental and theoretical investigations are required, if this complex is to be explained by theory with confidence in the future.

7.10 Conclusions

The UV photofragment spectra of calcium dication-benzene complex have been recorded. First, theory which is applied to the calculations of $[Ca(benzene)]^{+/2+}$ is bench marked by the experimental spectra. The TDDFT-CAM-B3LYP/BVP86 calculated excitations in $[Ca(benzene)]^+$ are in an excellent agreement with the experimental features at around 37500 cm^{-1} without spin contamination. Second, for the doubly charged species $[Ca(benzene)_2]^{2+}$ and $[Ca(benzene)]^{2+}$, the TDDFT calculations on the same level of theory have revealed that the calculated $\pi \rightarrow 3d$ LMCT transition can be used to assign the large experimental feature at ~45870 cm^{-1}. Last, TDDFT calculations on $[Ca(benzene)(H_2O)_n]^{2+}$ (n=2, 4) have been performed on the same level of theory. There is no dominant electronic transition can be found to match any feature in the experimental spectrum, which means this experiment is not sufficient to bench mark the theory when it is applied on $[Ca(benzene)(H_2O)_n]^{2+}$ species.

Overall, this combined theoretical and experimental investigation has provided some reasonable assignments for the spectra of Ca(II)-benzene complex. The theory indicates that the products of photoexcitation, namely $[Ca(benzene)]^+$ and $[Ca(benzene)]^{2+}$, play an important role in evaluating the spectra. It is also clear from

the theory that the excitation data and nature of involved frontier orbital in the doubly charged species are generally consistent throughout different functional (CAM-B3LYP, PBE0 and TPSSh), only with some shift in excitation energies and oscillator strengths. It must be noted that there are some features in the spectra such as the one at around 39500 cm^{-1} cannot be assigned by any calculated excitations.

Chapter 8 Conclusions and future investigations

8.1 General remarks

From the results reported in this thesis, the hybrid quadrupole ion trap instrument that built up by our group has been proved capable of forming the doubly charged metal dication-ligand sandwich complexes in the gas phase. The performance of the experimental apparatus is consistently stable throughout different metals. Its capability of producing structural spectra has allowed us to investigate a series of metal ions in their most common oxidation state that can be found in nature and develop the bench mark of the doubly charged metal-ligand complexes for the theory in a systemic fashion. In general, success of the gas-phase spectroscopic measurements using this technique has paved the way to make the calculated electronic transitions visible in the form of UV spectroscopic features, which is vital for the theory if it is to be applied on metal dication-ligand sandwich complexes with confidence in the future.

For the closed-shell systems, DFT methodologies such as BVP86, TPSSh/6-311++G(d,p) (SDD for the lead and copper atoms) are able to optimize bent geometries that the ML_2 sandwich species may adopt in the experiment which has been widely reported.[147-148, 154] The TDDFT methodologies can explain the charge transfer electronic transitions that might occur in the species during the experiment such as LMCT, ligand-based electronic transitions, which have a reasonable agreement with the experimental spectra. The nature of the calculated transitions in all doubly charged species and their involved orbitals are consistent throughout different functional only with some shift in excitation energies and oscillator strengths as expected.

However, in terms of open-shell systems, such as doubly charged copper-benzene sandwich complex and some other singly charged intermediates in the lead case, there

still are some hurdles to understand why the single-excitation theory can provide quantitative agreement between the experimental spectra and the calculated excitations with spin-contaminations. The degree of spin contamination of selected typical excitations are qualified by calculating the $<\hat{S}^2>$ values using the formula introduced by Ipatov[130]. It can be found that the analysis of involved orbital is insufficient to distinguish between physical and unphysical excitations in some cases. The calculation of $<\hat{S}^2>$ value needs to be added. Fortunately, most excited states in singly charged lead and calcium species preserve the expected value of $<\hat{S}^2>$, which can be trusted. However, almost all of calculated transitions in copper complex are significantly spin contaminated, which need to be removed or corrected in the future. To explain the open-shell system, the standard adiabatic theory needs to be refined, and to serve this goal, it is obvious that more state-resolved experimental spectra need to be produced in the future.

8.2 Lead dication-ligand complexes

The results of Pb(II) sandwich complexes shown that, when complexed with aromatic ligands, Pb^{2+} is capable of yielding structured UV spectra which exhibit discrete electronic transitions that include significant contributions from the metal ion. Two aromatic sandwich complexes, $[Pb(benzene)_2]^{2+}$ and $[Pb(toluene)_2]^{2+}$, have been prepared in the gas phase and their UV action spectra recorded from ions held and cooled in an ion trap. For the $[Pb(benzene)_2]^{2+}$, the largest feature in the spectra which is at around 45500 cm^{-1} is due to $\pi \rightarrow 6p$ LMCT transition. Whilst $[Pb(benzene)_2]^{2+}$ exhibits a spectrum with very little detail, that recorded for $[Pb(toluene)_2]^{2+}$ reveals a rich structure in the wavelength range 220 – 280 nm. All of the dominant spectral features arising from $[Pb(toluene)_2]^{2+}$ are attributed to LMCT transitions, although as the wavelength decrease, the $\pi \rightarrow \pi^*$ ligand-based electronic transitions via configuration mixing contribute to the spectra. Theory in the form of DFT shows that both types of complex take the form of hemi-directed structures, and that

$[Pb(toluene)_2]^{2+}$ can adopt three distinct conformers depending upon the relative positions of the two methyl groups. Further calculations, using adiabatic TDDFT to assign electronic transitions, provide evidence of individual $[Pb(toluene)_2]^{2+}$ conformers having been resolved in the experimental spectrum. Of relevance with regard to the development of methods for identifying Pb^{2+} as an environmental or biological pollutant, is the observation that there are distinct LMCT transitions in the UV that are sensitive to both the electronic properties of coordinating ligands (in this case benzene or toluene) and subtle changes in coordination geometry (conformers adopted by two toluene molecules) that accommodates Pb(II). The results also reveal that the addition of a methyl group makes the LMCT electronic transitions energetically more accessible, which leading to a significant difference in the nature of the UV spectrum.

8.3 Copper dication-bis(benzene) complex

From the result of copper-benzene complex, the doubly charged species has been found very unstable and sensitive to the UV laser radiation. Many photofragments of benzene instead of benzene cation, for example, $C_3H_3^+$, $C_3H_4^+$ and $C_4H_4^+$, have been observed in the photofragment mass spectra. The UV spectra produced broad feature instead of well-resolved discrete features in the Pb(II) spectra. There are two slipped structures and one bent structure have been found minima without imaginary mode that are optimized by BVP86, PBE0 and TPSSh functional, respectively. All of them have been found to have contributions to the two features in the spectra in the TDDFT data. For example, the TDDFT calculation for C_{2v} structure shows ligand-based electronic transitions and LMCT transitions, whereas the C_2_eclipsed structure shows MLMLCT and MLLCT transitions which can be matched to the features in the spectra. It indicates that the nature of excitations is sensitive to the coordination geometry that the complex may adopt. Unfortunately, the resolution of the spectra

cannot afford to identify the features that arising from the excitations in the different conformers.

In general, the calculated excitations in different conformers of $[Cu(benzene)_2]^{2+}$ have qualitative agreement with the features in the experimental spectrum. However, given that the ability of a standard adiabatic TDDFT method to describe double-excitation characters is considered particularly important in a d^9 system with an open-shell ground state, the results of the single-electron excitations described by the adiabatic TDDFT calculations are not considered to be sufficiently reliable or accurate to identify the discrete electronic transitions that appear in the spectrum. Therefore, even this qualitative approach cannot be considered as a definite solution here because of the high probability of unphysical states and/or missing states in our calculated spectrum due to the absence of doubly excitations in this adiabatic TDDFT treatment. These issues all demonstrate the inherent problems associated with treating a d^9 system with a single-excitation theory. It is also very interesting because the good match between theoretical and experimental data in this special case clearly addresses a fact that if theory is to be used to interpret the new state-resolved spectra emerging from experiments of the open-shell complexes with confidence in the future, it must be improved.

8.4 Calcium dication-benzene complex

From the results of calcium-benzene complex, the parent ion peak at 94.7 amu in the mass spectra is found to be difficult to identify, which could correspond to $[Ca(benzene)_2]^{2+}$ or $[Ca(benzene)(H_2O)_4]^{2+}$. The DFT and TDDFT calculations are performed based on these two possibilities. The theory suggests that the calculated excitations in $[Ca(benzene)_2]^{2+}$ and $[Ca(benzene)]^{+/2+}$ can be matched to the experimental spectra. The excitations in $[Ca(benzene)_2]^{2+}$ and $[Ca(benzene)]^{2+}$ calculated by TDDFT-CAM-B3LYP/BVP86 arise from π orbital of benzene and 3d

orbital of calcium. The excitations in $[Ca(benzene)]^+$ has a mixing configuration of metal-based and LMCT, which can be perfectly matched to the feature at around 37500 cm^{-1} without spin contamination. The TDDFT calculations of $[Ca(benzene)(H_2O)_4]^{2+}$ and $[Ca(benzene)(H_2O)_2]^{2+}$ are performed on the same level of theory. No calculated excitation can be found useful to assign any feature in the experimental spectra. These observations suggest that the TDDFT methodology can provide some reasonable agreement between calculated excitations and experimental features for calcium dication complex. But there are two features in the spectra at around 39800 and 38200 cm^{-1} that cannot be assigned which can be considered as an evidence that the theory need to be refined in the future.

8.5 Future investigations

The success of experimental techniques for trapping and photodissociating metal dication-ligand complexes has been demonstrated in this thesis and in some other papers.[10, 36, 42-43, 59, 155, 164] A combined experimental and theoretical investigation methodology has been established for doubly charged metal-ligand system in a systematic fashion. For the purpose of extending the database of spectroscopic bench mark, recording more UV spectra for metal dication-ligand complexes in this category will be the obvious goal in the future. In this line of research, the UV photofragmentation spectroscopy of $[Mn(picoline)_4]^{2+}$ has been recorded and reported in Figure 8.1. This set of results are absent in the main body of this thesis because of the difficulties in describing the open-shell systems using a standard adiabatic implementations of TDDFT. The lack of multi-electron excitations in TDDFT due to the adiabatic approximation has been highlighted in the combined theoretical and experimental research of $[Mn(pyridine)_4]^{2+}$.[43] The theoretical developments that go beyond the standard adiabatic approximation and consider the frequency dependence required for a non-adiabatic TDDFT approach might be helpful to solve these problems in the future.

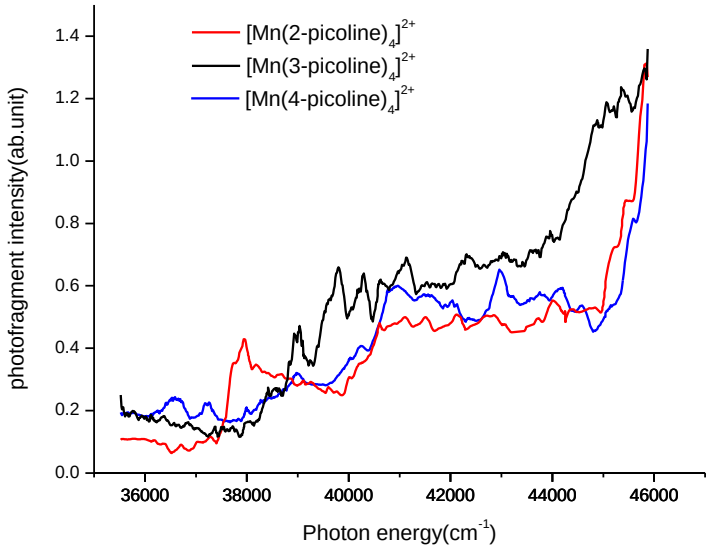

Figure 8.1 UV photofragmentation spectroscopy of $[Mn(4\text{-picoline})_4]^{2+}$, $[Mn(2\text{-picoline})_4]^{2+}$ and $[Mn(3\text{-picoline})_4]^{2+}$.

On the other hand, some DFT and TDDFT calculations for some other closed-shell complexes have already been performed using the methodologies that have been demonstrated in this thesis. For example, for the purpose of comparison with the lead benzene and toluene complexes, sandwich lead dication complexes with para-, orthro- and meta-xylene ligands were calculated using TDDFT (CAM-B3LYP, PBE0 and TPSSh, 6-311++G**[SDD] as basis set), based on their optimized geometries. The calcium toluene and other group two metal dication (Mg^{2+} and Sr^{2+}) complexes with benzene and toluene are also calculated on the same level of theory. The TDDFT-CAM-B3LYP/6-311++G(d,p)[SDD] data of lead dication-para-xylene complex is selected as an example to plot as stick spectra in Figure 8.2-8.3. The calculated excitation energies and oscillator strengths are summarized in Table 8.1. There are four structures that have minima without imaginary mode using BVP86 functional, 6-311++G(d,p)/SDD as basis set. From Figure 8.2, it can be seen that all of the conformers have some electronic transitions in the range of photon energy that is

accessible in the experiment. The density of the electronic transitions in lead-xylene complex is higher than lead-benzene in this wavelength range. Therefore, constructing a UV spectrum with discrete features, even conformation resolved features for this species will be very promising. From Figure 8.3 and Table 8.1, most of the dominant transitions are LMCT transition involving π orbital from xylene and 6p orbital from lead which is as similar as lead benzene and toluene complexes. This set of results will make a good comparison with the lead sandwich dication benzene and toluene complexes data in this thesis if the experimental spectra can be recorded in the future.

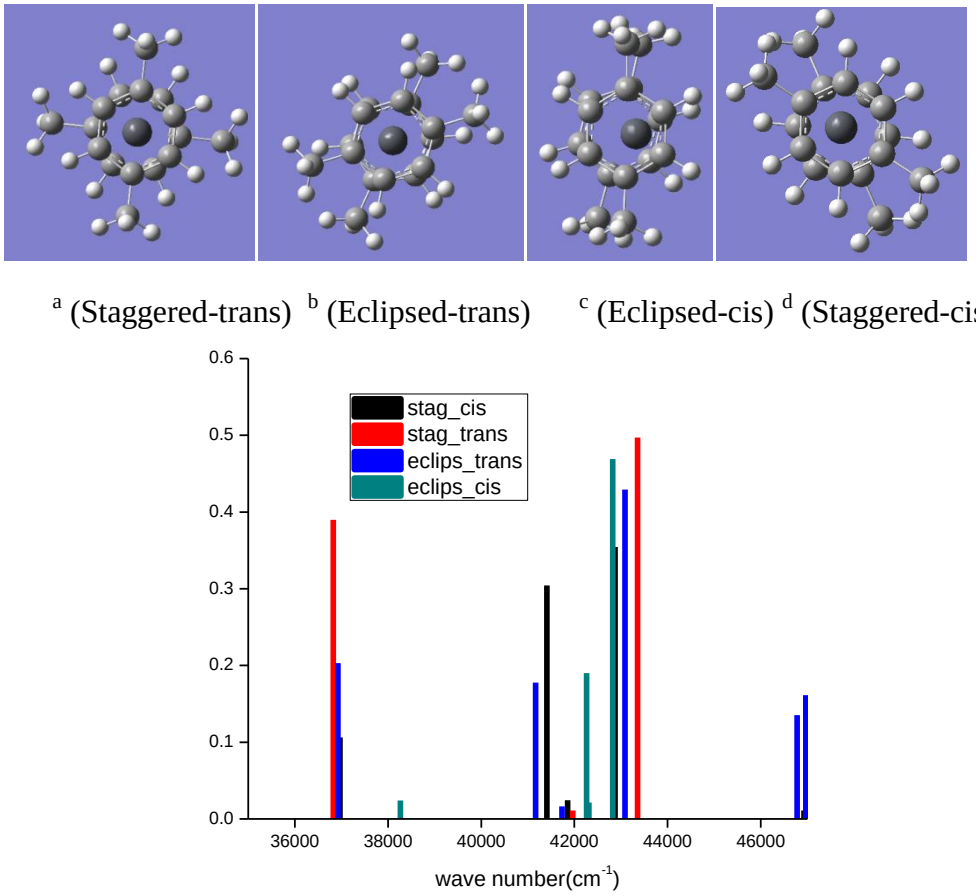

Figure 8.2 Calculated excitation energies and oscillator strengths of $[Pb(p\text{-xylene})_2]^{2+}$ using TDDFT-CAM-B3LYP/6-311++G(d,p)[SDD] for the BVP86 optimized geometry of all conformers. All of the optimized geometries are listed on the top of the spectrum (a. Staggered-trans, b. Eclipsed-trans, c. Eclipsed-cis, d. Staggered-cis).

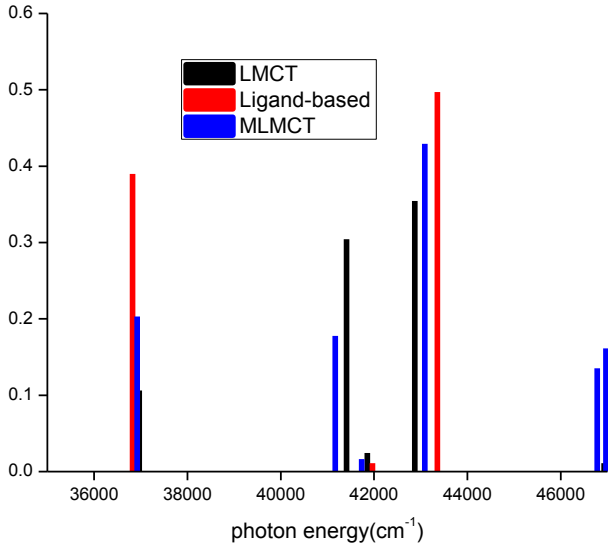

Figure 8.3 Calculated excitation energies and oscillator strengths of $[Pb(p\text{-xylene})_2]^{2+}$ using TDDFT-CAM-B3LYP/6-311++G(d,p)[SDD] for the BVP86 optimized geometry. The electronic transitions are sorted in their nature

Table 8.1 Summary of the calculated excitation energies and oscillator strengths ($f \geq 0.01$) of $[Pb(p\text{-xylene})_2]^{2+}$ on the CAM-B3LYP/6-311++G(d,p)[SDD] level for BVP86 optimized geometry. Dominant transitions are shown in bold. %contribution (weight) given in brackets

Excitation energies / cm^{-1}	Calculated Oscillator Strength	Nature NTO	Assignment
36826[a]	**0.3898**	**LMCT(50%) LMCT(50%)**	**LMCT π→6p(92%Pb)**
36924[b]	**0.203**	**LMCT(87%) LMCT(13%)**	**LMCT π→6p(>89%Pb)**
36967[d]	**0.1063**	**LMCT(94%) LMCT(6%)**	**LMCT π→6p(>87%Pb)**
38266[c]	0.0239	LMCT(99%) LMCT(1%)	LMCT π→6p(>64%Pb)
41169[b]	**0.1776**	**LMCT(51%) LMCT(48%)**	**LMCT π→6p(>92%Pb)**
41408[d]	**0.3042**	**LMCT(56%) LMCT(43%)**	**LMCT π→6p(>92%Pb)**

41733[b]	0.0164	Ligand-based electronic transition (52%) Ligand-based electronic transition (31%)	Ligand-based electronic transition π→π*
41855[d]	0.0245	Ligand-based electronic transition (51%) Ligand-based electronic transition (30%)	Ligand-based electronic transition π→π*
41967[a]	0.0109	Ligand-based electronic transition (51%) Ligand-based electronic transition (32%)	Ligand-based electronic transition σ*→π
42264[c]	**0.1902**	**MLMCT(67%) LMCT(31%)**	**MLMCT π→6p(92%Pb)**
42310[c]	0.0215	Ligand-based electronic transition (50%) Ligand-based electronic transition (31%)	Ligand-based electronic transition π→π*
42821[c]	**0.4691**	**LMCT(59%) LMCT(39%)**	**LMCT π→6p(92%Pb)**
42871[d]	**0.3545**	**LMCT(66%) LMCT(33%)**	**LMCT π→6p(>94%Pb)**
43087[b]	**0.4292**	**LMCT(59%) LMCT(39%)**	**LMCT π→6p(>95%Pb)**
43354[a]	**0.4971**	**LMCT(50%) LMCT(50%)**	**LMCT π→6p(95%Pb)**
46779[b]	**0.1352**	**Ligand-based electronic transition (52%) Ligand-based electronic transition (30%)**	**Ligand-based electronic transition π→π***
46929[b]	0.0111	LMCT(41%) LLCT(27%)	LMCT π→6p(102%Pb)
46968[d]	**0.1612**	**Ligand-based electronic transition (52%) Ligand-based electronic transition (29%)**	**Ligand-based electronic transition π→π***

[a] (stag_trans) [b] (eclips_trans) [c] (Eclips_cis) [d] (Stag_cis)

Note: only two greatest contributions are shown with the dominant transition listed first.

Bibliography

1. Purusottam jena, A. W. C. J., *nanoclusters: a bridge across disciplines, chapter 4: Cluster structures: bridging experiment and theory*. Elsevier: Amsterdam, 2010.
2. Stace, A. J.,*The Journal of Physical Chemistry A* **2002,** *106*, 7993-8005.
3. Stace, A.,*Science (Washington, DC, U. S.)* **2001,** *294*, 1292-1293.
4. Johnston, R. L., *Atomic and molecular clusters*. Taylor & Francis: London and New York, 2002.
5. (a) Akibo-Betts, G.; Barran, P. E.; Puskar, L.; Duncombe, B.; Cox, H.; Stace, A. J.,*J. Am. Chem. Soc.* **2002,** *124*, 9257-9264; (b) Cox, H.; Akibo-Betts, G.; Wright, R. R.; Walker, N. R.; Curtis, S.; Duncombe, B.; Stace, A. J.,*J. Am. Chem. Soc.* **2003,** *125*, 233-242; (c) Puskar, L.; Cox, H.; Goren, A.; Aitken, G. D. C.; Stace, A. J.,*Faraday Discuss.* **2003,** *124*, 259-273; (d) Cox, H.; Stace, A. J.,*J. Am. Chem. Soc.* **2004,** *126*, 3939-3947; (e) Puskar, L.; Barran, P. E.; Duncombe, B. J.; Chapman, D.; Stace, A. J.,*J. Phys. Chem. A* **2005,** *109*, 273-282; (f) Puskar, L.; Tomlins, K.; Duncombe, B.; Cox, H.; Stace, A. J.,*J. Am. Chem. Soc.* **2005,** *127*, 7559-7569.
6. Stephens W. E.,*Phys. Rev.* **1946,** *69*, 691.
7. W. C. Wiley, I. H. M.,*Review of Scientific Instruments* **1955,** *26*, 1150.
8. (a) Holm, R. H.; Kennepohl, P.; Solomon, E. I.,*Chem. Rev. (Washington, D. C.)* **1996,** *96*, 2239-2314; (b) Feraudi, G. J., *elements of inorganic photochemistry*. Wiley-Interscience Publication: New York, 1988.
9. Lever, A. B. P., Inorganic Electronic Spectroscopy. Elsevier: Amsterdam, The Netherlands, 1984.
10. Stewart, H.; Wu, G.; Ma, L.; Barclay, M.; Vieira, A. D.; King, A.; Cox, H.; Stace, A. J.,*J. Phys. Chem. A* **2011,** *115*, 6948-6960.
11. Kohler, M.; Leary, J. A.,*J. Am. Soc. Mass Spectrom.* **1997,** *8*, 1124-1133.
12. (a) Blades, A. T.; Jayaweera, P.; Ikonomou, M. G.; Kebarle, P.,*Int. J. Mass Spectrom. Ion Processes* **1990,** *102*, 251-67; (b) Spence, T. G.; Trotter, B. T.; Posey, L. A.,*J. Phys. Chem. A* **1998,** *102*, 7779-7786.
13. (a) Stace, A. J.; Walker, N. R.; Firth, S.,*J. Am. Chem. Soc.* **1997,** *119*, 10239-10240; (b) Walker, N. R.; Firth, S.; Stace, A. J.,*Chem. Phys. Lett.* **1998,** *292*, 125-132.
14. (a) Lustig, D. A.; Lubman, D. M.,*Review of Scientific Instruments* **1991,** *62*, 957-962; (b) Haefliger, O. P.; Zenobi, R.,*Review of Scientific Instruments* **1998,** *69*, 1828-1832.
15. (a) Cable, J. R.; Tubergen, M. J.; Levy, D. H.,*J. Am. Chem. Soc.* **1989,** *111*, 9032-9; (b) Pang, H. M.; Lubman, D. M.,*Anal. Chem.* **1989,** *61*, 777-9; (c) Li, L.; Hogg, A. M.; Wang, A. P. L.; Zhang, J. Y.; Nagra, D. S.,*Anal. Chem.* **1991,** *63*, 974-80.
16. Willey, K. F.; Yeh, C. S.; Robbins, D. L.; Duncan, M. A.,*J. Phys. Chem.* **1992,** *96*, 9106-11.
17. Plowright, R. J.; Ayles, V. L.; Watkins, M. J.; Gardner, A. M.; Wright, R. R.; Wright, T. G.; Breckenridge, W. H.,*J Chem Phys* **2007,** *127*, 204308.

18. (a) Jaeger, T. D.; Duncan, M. A.,*Int. J. Mass Spectrom.* **2005,** *241*, 165-171; (b) Jaeger, T. D.; Duncan, M. A.,*J. Phys. Chem. A* **2005,** *109*, 3311-3317; (c) Jaeger, J. B.; Pillai, E. D.; Jaeger, T. D.; Duncan, M. A.,*J. Phys. Chem. A* **2005,** *109*, 2801-2808; (d) Ayers, T. M.; Westlake, B. C.; Preda, D. V.; Scott, L. T.; Duncan, M. A.,*Organometallics* **2005,** *24*, 4573-4578; (e) Jaeger, T. D.; Pillai, E. D.; Duncan, M. A.,*J. Phys. Chem. A* **2004,** *108*, 6605-6610.
19. (a) Plowright, R. J.; Watkins, M. J.; Gardner, A. M.; Withers, C. D.; Wright, T. G.; Breckenridge, W. H.,*Phys Chem Chem Phys* **2009,** *11*, 1539-50; (b) Plowright, R. J.; Watkins, M. J.; Gardner, A. M.; Wright, T. G.; Breckenridge, W. H.; Wallimann, F.; Leutwyler, S.,*J Chem Phys* **2008,** *129*, 154315; (c) Wright, T. G.; Ellis, A. M.; Dyke, J. M.,*J. Chem. Phys.* **1993,** *98*, 2891-907; (d) Plowright, R. J.; Gardner, A. M.; Withers, C. D.; Wright, T. G.; Morse, M. D.; Breckenridge, W. H.,*J Phys Chem A* **2010,** *114*, 3103-13; (e) Hopkins, W. S.; Woodham, A. P.; Plowright, R. J.; Wright, T. G.; MacKenzie, S. R.,*J Chem Phys* **2011,** *134*, 094311.
20. Hopkins, W. S.; Hamilton, S. M.; MacKenzie, S. R.,*J. Chem. Phys.* **2009,** *130*, 144308/1-144308/8.
21. Keith-Roach, M. J.,*Anal. Chim. Acta* **2010,** *678*, 140-148.
22. (a) Choi, C. M.; Kim, H. J.; Lee, J. H.; Shin, W. J.; Yoon, T. O.; Kim, N. J.; Heo, J.,*J. Phys. Chem. A* **2009,** *113*, 8343-8350; (b) Yoon, T. O.; Choi, C. M.; Kim, H. J.; Kim, N. J.,*Bull. Korean Chem. Soc.* **2007,** *28*, 619-623.
23. Choi, C. M.; Lee, J. H.; Choi, Y. H.; Kim, H. J.; Kim, N. J.; Heo, J.,*J. Phys. Chem. A* **2010,** *114*, 11167-11174.
24. Choi, C. M.; Choi, D. H.; Heo, J.; Kim, N. J.; Kim, S. K.,*Angew Chem Int Ed Engl* **2012**.
25. (a) O'Brien, J. T.; Williams, E. R.,*J. Phys. Chem. A* **2008,** *112*, 5893-5901; (b) Bush, M. F.; Saykally, R. J.; Williams, E. R.,*ChemPhysChem* **2007,** *8*, 2245-53; (c) Cooper, T. E.; O'Brien, J. T.; Williams, E. R.; Armentrout, P. B.,*J. Phys. Chem. A* **2010,** *114*, 12646-12655.
26. (a) O'Brien, J. T.; Prell, J. S.; Steill, J. D.; Oomens, J.; Williams, E. R.,*J. Phys. Chem. A* **2008,** *112*, 10823-10830; (b) Dunbar, R. C.; Steill, J. D.; Polfer, N. C.; Oomens, J.,*J. Phys. Chem. A* **2009,** *113*, 845-851; (c) Dunbar, R. C.; Hopkinson, A. C.; Oomens, J.; Siu, C.-K.; Siu, K. W. M.; Steill, J. D.; Verkerk, U. H.; Zhao, J.,*J. Phys. Chem. B* **2009,** *113*, 10403-10408.
27. (a) Walker, N. R.; Wright, R. R.; Stace, A. J.; Woodward, C. A.,*Int. J. Mass Spectrom.* **1999,** *188*, 113-119; (b) Walker, N. R.; Wright, R. R.; Stace, A. J.,*J. Am. Chem. Soc.* **1999,** *121*, 4837-4844; (c) Walker, N.; Dobson, M. P.; Wright, R. R.; Barran, P. E.; Murrell, J. N.; Stace, A. J.,*J. Am. Chem. Soc.* **2000,** *122*, 11138-11145; (d) Wright, R. R.; Walker, N. R.; Firth, S.; Stace, A. J.,*J. Phys. Chem. A* **2001,** *105*, 54-64.
28. (a) Walker, N. R.; Wright, R. R.; Barran, P. E.; Murrell, J. N.; Stace, A. J.,*J. Am. Chem. Soc.* **2001,** *123*, 4223-4227; (b) Walker, N. R.; Wright, R. R.; Barran, P. E.; Cox, H.; Stace, A. J.,*J. Chem. Phys.* **2001,** *114*, 5562-5567.
29. (a) Puskar, L.; Barran, P. E.; Wright, R. R.; Kirkwood, D. A.; Stace, A. J.,*J. Chem. Phys.* **2000,** *112*, 7751-7754; (b) Puskar, L.; Stace, A. J.,*The Journal of Chemical Physics* **2001,** *114*, 6499-6501.
30. (a) Duncombe, B. J.; Ryden, J. O. S.; Puskar, L.; Cox, H.; Stace, A. J.,*J. Am. Soc. Mass Spectrom.* **2008,** *19*, 520-530; (b) Duncombe, B. J.; Duale, K.; Buchanan-Smith, A.; Stace, A. J.,*J. Phys. Chem. A* **2007,** *111*, 5158-5165; (c)

Duncombe, B. J.; Puskar, L.; Wu, B.; Stace, A. J.,*Can. J. Chem.* **2005,** *83*, 1994-2004.
31. Chen, X.; Wu, G.; Wu, B.; Duncombe, B. J.; Stace, A. J.,*J. Phys. Chem. B* **2008,** *112*, 15525-15528.
32. (a) McQuinn, K.; Hof, F.; McIndoe, J. S.; Chen, X.; Wu, G.; Stace, A. J.,*Chem. Commun. (Cambridge, U. K.)* **2009**, 4088-4090; (b) Chen, X.; Stace, A. J.,*Chem. Commun. (Cambridge, U. K.)* **2012,** *48*, 10292-10294.
33. Kebarle, P.,*Annu. Rev. Phys. Chem.* **1977,** *28*, 445-76.
34. cooks, R. G. B. J. H., Caprioli. R. M., Lester. G. R., *Metastable ions*. First ed. ed.; Elsevier: Amsterdam, 1973.
35. Stace, A. J.,*J. Phys. Chem. A* **2002,** *106*, 7993-8005.
36. Cox, H.; Stace, A. J.,*Int. Rev. Phys. Chem.* **2010,** *29*, 555-588.
37. Mizukami, S.; Okada, S.; Kimura, S.; Kikuchi, K.,*Inorg. Chem.* **2009,** *48*, 7630-7638.
38. Duncan, M. A.,*Annu. Rev. Phys. Chem.* **1997,** *48*, 69-93.
39. Keesee, R. G.; Castleman, A. W., Jr.,*J. Phys. Chem. Ref. Data* **1986,** *15*, 1011-71.
40. (a) Spence, T. G.; Trotter, B. T.; Burns, T. D.; Posey, L. A.,*J. Phys. Chem. A* **1998,** *102*, 6101-6106; (b) Spence, T. G.; Trotter, B. T.; Posey, L. A.,*J. Phys. Chem. A* **1998,** *102*, 7779-7786.
41. (a) Thompson, C. J.; Aguirre, F.; Husband, J.; Metz, R. B.,*J. Phys. Chem. A* **2000,** *104*, 9901-9905; (b) Thompson, C. J.; Faherty, K. P.; Stringer, K. L.; Metz, R. B.,*Phys Chem Chem Phys* **2005,** *7*, 814-8.
42. Wu, G.; Norris, C.; Stewart, H.; Cox, H.; Stace, A. J.,*Chem. Commun. (Cambridge, U. K.)* **2008**, 4153-4155.
43. Wu, G.; Stewart, H.; Lemon, F. D.; Cox, H.; Stace, A. J.,*Mol. Phys.* **2010,** *108*, 1199-1208.
44. March, R. E.,*Journal of Mass Spectrometry* **1997,** *32*, 351-369.
45. R. March, J. F. J. T., *Quadrupole Ion Trap Mass Spectroscopy*. Willy: 2005.
46. W. Paul, O. O., E. Fischer, , *Forschungsberichte des Wirtschaft und Verkehrministeriums Nordrhein Westfalen,*. Koln and Opladen: Westdeutscher Verlag, 1958; Vol. No. 415.
47. Fischer, E.,*Z. Phys.* **1959,** *156*, 1-26.
48. Rettinghaus, V. v. G.,*Z. Angew. Phys.* **1967,** *22*, 321-326.
49. D. C. Burnham, D. K.,*Bull. Am. Phys. Soc. Ser.* **1968,** *II*.
50. J. E. P Syka, W. J. F., Jr. Quadrupole Fourier transform mass spectrometer and method. 1988.
51. M. Nappi, V. F., M. Soni, R. G. Cooks,*Int. J. Mass Spectrom.* **1998,** *177*, 91-104.
52. (a) Dehmelt, H. G.,*Adv. At. Mol. Phys.* **1967,** *3*, 53-72; (b) Dehmelt, H. G.,*Adv. At. Mol. Phys.* **1969,** *5*, 109-154.
53. (a) P. H. Dawson, N. R. W.,*J. Vac. Sci. Technol.* **1968,** *5*, 11-18; (b) P. H. Dawson, N. R. W.,*J. Vac. Sci. Technol.* **1968,** *5*, 11-18.
54. Dawson, P. H.; Lambert, C.,*International Journal of Mass Spectrometry and Ion Physics* **1975,** *16*, 269-280.
55. W. Paul, H. S. Aparatus for separating charged particles of different specific charges. 1956.
56. Jonscher, K. R.; Yates, J. R., 3rd,*Anal Biochem* **1997,** *244*, 1-15.

57. Wuerker, R. F.; Shelton, H.; Langmuir, R. V.,*Journal of Applied Physics* **1959,** *30*, 342-349.
58. Nappi, M.; Weil, C.; Cleven, C. D.; Horn, L. A.; Wollnik, H.; Cooks, R. G.,*International Journal of Mass Spectrometry and Ion Processes* **1997,** *161*, 77-85.
59. Wu, G.; Chapman, D.; Stace, A. J.,*Int. J. Mass Spectrom.* **2007,** *262*, 211-219.
60. Bethe,*Ann. physik* **1929,** *3*, 133.
61. Van Vleck, J. H.,*Physical Review* **1932,** *41*, 208-215.
62. Figgis, B. N., *Introduction to ligand fields*. Interscience publishers a division of John Wiley & Sons: New York, London. Sydney, 1961.
63. Isci, H.; Mason, W. R.,*Inorg. Chem.* **1983,** *22*, 2266-72.
64. Nazeeruddin, M. K.; Zakeeruddin, S. M.; Kalyanasundaram, K.,*J. Phys. Chem.* **1993,** *97*, 9607-12.
65. Suzuki, M.; Nishida, Y.,*Inorg. Chim. Acta* **1980,** *44*, L9-L11.
66. Tennent, D. L.; McMillin, D. R.,*J. Am. Chem. Soc.* **1979,** *101*, 2307-11.
67. Spence, T. G.; Burns, T. D.; Guckenberger, G. B.; Posey, L. A.,*J. Phys. Chem. A* **1997,** *101*, 1081-1092.
68. Geoffroy, G. L.; Wrighton, M. S., *Organometallic Photochemistry*. Academic Press: 1979; p 352 pp.
69. Cotton, F. A., Wilkinson, G. , *Advanced Inorganic Chemistry*. Wiley: London, 1988.
70. (a) Kim, S. K.; Bernstein, E. R.,*J. Phys. Chem.* **1990,** *94*, 3531-9; (b) Yamazaki, I.; Baba, H.,*J. Chem. Phys.* **1977,** *66*, 5826-7.
71. Wu, G.; Chapman, D.; Stace, A. J.,*International Journal of Mass Spectrometry* **2007,** *262*, 211-219.
72. Guan, J.; Puskar, L.; Esplugas, R. O.; Cox, H.; Stace, A. J.,*J. Chem. Phys.* **2007,** *127*, 064311/1-064311/12.
73. Aitken, G. D. C.; Cox, H.; Stace, A. J.,*J. Phys. Chem. A* **2012,** *116*, 3035-3041.
74. Laboratories, C. R. vapor pressure curves for the more common elements (cont.). After Honig (Ref. 5:14).
75. Wolfgang Paul, H. S. Apparatus for separating charged particles of different specific charges. 1960.
76. Feistel, H.,*scientific American* **1973,** *228*, 15-23.
77. Wu, G.; Stace, A. J.,*Chemical Physics Letters* **2005,** *412*, 1-4.
78. LTD, Mullard, *Mullard Technical Handbook*. 1985.
79. Orazio, S., *Principles of Lasers*. 4th Edition ed.; Springer: 1998.
80. O. Svelto, D. C. H., *Principles of Lasers, .* New York, 1989.
81. Meyers, R. A., *Encyclopaedia of Lasers and Optical Technology Ed. .* New York, 1991.
82. GrÄFenstein, J.; Cremer, D.,*Molecular Physics* **2001,** *99*, 981-989.
83. Jensen, F., *Introduction to Computational chemistry*. second edition ed.; John Wiley & sons, Ltd: 2007.
84. Thomas, L. H.,*Mathematical Proceedings of the Cambridge Philosophical Society* **1927,** *23*, 542-548.
85. Dirac, P. A. M.,*Proc. Camb. Phil. Soc.* **1930,** *26*, 376.
86. Teller, E.,*Reviews of Modern Physics* **1962,** *34*, 627-631.
87. Kohn, P. H. a. W.,*Physical Review B* **1964,** *136*, B864.

88. (a) Kohn, W.,*Rev. Mod. Phys.* **1999,** *71*, 1253-1266; (b) Kohn, W.; Sham, L. J. *Self-consistent equations including exchange and correlation effects*; Univ. of California: 1965; p 21 pp.
89. Vosko, S. H.; Wilk, L.; Nusair, M.,*Canadian Journal of Physics* **1980,** *58*, 1200-1211.
90. Perdew, J. P.; Zunger, A.,*Physical Review B* **1981,** *23*, 5048-5079.
91. Perdew, J. P.; Wang, Y.,*Physical Review B* **1992,** *45*, 13244-13249.
92. Ceperley, D. M.; Alder, B. J.,*Physical Review Letters* **1980,** *45*, 566-569.
93. Becke, A. D.,*Physical Review A* **1988,** *38*, 3098-3100.
94. Perdew, J. P.,*Physical Review B* **1986,** *33*, 8822-8824.
95. (a) Lee, C.; Yang, W.; Parr, R. G.,*Physical Review B* **1988,** *37*, 785-789; (b) Miehlich, B.; Savin, A.; Stoll, H.; Preuss, H.,*Chemical Physics Letters* **1989,** *157*, 200-206.
96. (a) Perdew, J. P.; Chevary, J. A.; Vosko, S. H.; Jackson, K. A.; Pederson, M. R.; Singh, D. J.; Fiolhais, C.,*Physical Review B* **1992,** *46*, 6671-6687; (b) Perdew, J. P.; Chevary, J. A.; Vosko, S. H.; Jackson, K. A.; Pederson, M. R.; Singh, D. J.; Fiolhais, C.,*Physical Review B* **1993,** *48*, 4978-4978; (c) Perdew, J. P.; Burke, K.; Wang, Y.,*Physical Review B* **1996,** *54*, 16533-16539.
97. Becke, A. D.,*The Journal of Chemical Physics* **1996,** *104*, 1040-1046.
98. Tao, J.; Perdew, J. P.; Staroverov, V. N.; Scuseria, G. E.,*Physical Review Letters* **2003,** *91*, 146401.
99. (a) Nolan, M.; Watson, G. W.,*The Journal of Chemical Physics* **2006,** *125*, 144701-6; (b) Bally, T.; Sastry, G. N.,*The Journal of Physical Chemistry A* **1997,** *101*, 7923-7925; (c) Cramer, C. J.; Barrows, S. E.,*The Journal of Organic Chemistry* **1998,** *63*, 5523-5532; (d) Bra ̈da, B.; Hiberty, P. C.; Savin, A.,*The Journal of Physical Chemistry A* **1998,** *102*, 7872-7877; (e) Sodupe, M.; Bertran, J.; Rodr ́guez-Santiago, L.; Baerends, E. J.,*The Journal of Physical Chemistry A* **1998,** *103*, 166-170; (f) Poater, J.; Sol à, M.; Rimola, A.; Rodr ́guez-Santiago, L.; Sodupe, M.,*The Journal of Physical Chemistry A* **2004,** *108*, 6072-6078; (g) Lundberg, M.; Siegbahn, P. E. M.,*The Journal of Chemical Physics* **2005,** *122*, 224103-9; (h) Gibson, M. C.; Brand, S.; Clark, S. J.,*Physical Review B* **2006,** *73*, 125120.
100. Zhao, Y.; Truhlar, D. G.,*Journal of Chemical Theory and Computation* **2008,** *4*, 1849-1868.
101. (a) Perdew, J. P.; Ruzsinszky, A.; Constantin, L. A.; Sun, J.; Csonka, G. b. I.,*Journal of Chemical Theory and Computation* **2009,** *5*, 902-908; (b) Perdew, J. P.; Ruzsinszky, A.; Tao, J.; Staroverov, V. N.; Scuseria, G. E.; Csonka, G. I.,*The Journal of Chemical Physics* **2005,** *123*, 062201-9; (c) Becke, A. D.,*The Journal of Chemical Physics* **1998,** *109*, 2092-2098.
102. Perdew, J. P.; Burke, K.; Ernzerhof, M.,*Physical Review Letters* **1996,** *77*, 3865-3868.
103. Adamo, C.; Barone, V.,*The Journal of Chemical Physics* **1999,** *110*, 6158-6170.
104. Yanai, T.; Tew, D. P.; Handy, N. C.,*Chemical Physics Letters* **2004,** *393*, 51-57.
105. Runge, E.; Gross, E. K. U.,*Physical Review Letters* **1984,** *52*, 997-1000.
106. Gross, E. K. U.; Kohn, W.,*Physical Review Letters* **1985,** *55*, 2850-2852.
107. Martin, R. L.,*The Journal of Chemical Physics* **2003,** *118*, 4775-4777.

108. J. S. Casas, J. S., *Lead Chemistry, Analytical Aspects, Environmental Impact and Health Effects*. Elsevier: 2006.
109. Claudio, E. S.; Ter, H. M. A.; Forde, C. E.; Stern, C. L.; Zart, M. K.; Godwin, H. A.,*Inorg. Chem.* **2000,** *39*, 1391-1397.
110. (a) Arena, G.; Contino, A.; Longo, E.; Sciotto, D.; Spoto, G.,*Journal of the Chemical Society, Perkin Transactions 2* **2001,** *0*, 2287-2291; (b) Sanchiz, J.; Esparza, P.; Villagra, D.; Dom ínguez, S.; Mederos, A.; Brito, F.; Araujo, L.; S ánchez, A.; Arrieta, J. M.,*Inorganic Chemistry* **2002,** *41*, 6048-6055; (c) Zhang, Y.; Jiang, J.,*The Journal of Physical Chemistry A* **2009,** *113*, 12179-12186; (d) Lapouge, C.; Cornard, J. P.,*The Journal of Physical Chemistry A* **2005,** *109*, 6752-6761; (e) Cuenot, F.; Meyer, M.; Espinosa, E.; Guilard, R.,*Inorganic Chemistry* **2005,** *44*, 7895-7910; (f) B átka, D.; Farkas, E.,*Journal of Inorganic Biochemistry* **2006,** *100*, 27-35.
111. Lee, J. S.; Kumari, S.; Yang, D.-S.,*J. Phys. Chem. A* **2010,** *114*, 11277-11284.
112. Cai, X.; Zhang, Y.; Zhang, X.; Jiang, J.,*Journal of Molecular Structure: THEOCHEM* **2006,** *801*, 71-80.
113. Cuenot, F.; Meyer, M.; Espinosa, E.; Guilard, R.,*Inorg. Chem.* **2005,** *44*, 7895-7910.
114. Roudjane, M.; Kumari, S.; Yang, D.-S.,*J. Phys. Chem. A* **2012,** *116*, 839-845.
115. Kurikawa, T.; Takeda, H.; Hirano, M.; Judai, K.; Arita, T.; Nagao, S.; Nakajima, A.; Kaya, K.,*Organometallics* **1999,** *18*, 1430-1438.
116. (a) Xing, X.; Tian, Z.; Liu, H.; Tang, Z.,*J. Phys. Chem. A* **2003,** *107*, 8484-8491; (b) Liu, H.; Xing, X.; Sun, S.; Gao, Z.; Tang, Z.,*J. Phys. Chem. A* **2006,** *110*, 8688-8694.
117. (a) Lapouge, C.; Cornard, J. P.,*J. Phys. Chem. A* **2005,** *109*, 6752-6761; (b) Cornard, J. P.; Lapouge, C.; Dangleterre, L.; Allet-Bodelot, C.,*J. Phys. Chem. A* **2008,** *112*, 12475-12484; (c) Cornard, J. P.; Dangleterre, L.; Lapouge, C.,*J. Phys. Chem. A* **2005,** *109*, 10044-10051; (d) Cornard, J. P.; Lapouge, C.,*Chem. Phys. Lett.* **2007,** *438*, 41-46.
118. Jarzecki, A. A.,*Inorg. Chem. (Washington, DC, U. S.)* **2007,** *46*, 7509-7521.
119. (a) Zhang, Y.; Jiang, J.,*J. Phys. Chem. A* **2009,** *113*, 12179-12186; (b) Zhang, Y.; Zhang, X.; Liu, Z.; Bian, Y.; Jiang, J.,*J. Phys. Chem. A* **2005,** *109*, 6363-6370.
120. Becke, A. D.,*Phys. Rev. A: Gen. Phys.* **1988,** *38*, 3098-100.
121. Vosko, S. H.; Wilk, L.; Nusair, M.,*Can. J. Phys.* **1980,** *58*, 1200-11.
122. Tao, J.; Perdew, J. P.; Staroverov, V. N.; Scuseria, G. E.,*Phys. Rev. Lett.* **2003,** *91*, 146401/1-146401/4.
123. (a) Adamo, C.; Barone, V.,*J. Chem. Phys.* **1999,** *110*, 6158-6170; (b) Perdew, J. P.; Burke, K.; Ernzerhof, M.,*Phys. Rev. Lett.* **1996,** *77*, 3865-3868; (c) Perdew, J. P.; Burke, K.; Ernzerhof, M.,*Phys. Rev. Lett.* **1997,** *78*, 1396.
124. (a) http://www.theochem.uni-stuttgart.de; (b) Kuechle, W.; Dolg, M.; Stoll, H.; Preuss, H.,*Mol. Phys.* **1991,** *74*, 1245-63.
125. Yanai, T.; Tew, D. P.; Handy, N. C.,*Chem. Phys. Lett.* **2004,** *393*, 51-57.
126. Martin, R. L.,*J. Chem. Phys.* **2003,** *118*, 4775-4777.
127. (a) Davidovich, R. L.; Stavila, V.; Marinin, D. V.; Voit, E. I.; Whitmire, K. H.,*Coord. Chem. Rev.* **2009,** *253*, 1316-1352; (b) Kaupp, M.; Schleyer, P. v. R.,*J. Am. Chem. Soc.* **1993,** *115*, 1061-73; (c) Shimoni-Livny, L.; Glusker, J. P.; Bock, C. W.,*Inorg. Chem.* **1998,** *37*, 1853-1867.

128. Jiang, S.; Zhu, K.; Mao, Z.; Zhang, K.; Yang, S.; Yang, J.; Pei, J. Coal slime water treatment and recovery process and apparatus. CN102616903A, 2012.
129. (a) Maurice, D.; Head-Gordon, M.,*J. Phys. Chem.* **1996,** *100*, 6131-7; (b) Rinkevicius, Z.; Tunell, I.; Salek, P.; Vahtras, O.; Agren, H.,*The Journal of Chemical Physics* **2003,** *119*, 34-46.
130. Ipatov, A.; Cordova, F.; Doriol, L. J.; Casida, M. E.,*J. Mol. Struct.: THEOCHEM* **2009,** *914*, 60-73.
131. Lifu Ma, T. T., Joseph Koka, Helen J. Kimber, Hazel Cox, A. J. Stace,*J. Chem. Phys.* **2013,** *138*, 164301/1-164301/11.
132. Atkins, P.; Julio, P., *Atkins' Physical Chemistry, 7th Edition*. Oxford University Press: 2002; p 1149 pp.
133. Shriver, D. F.; Atkins, P. W.; Langford, C. H., *Inorganic Chemistry, Pt. 2. 2nd Ed*. Tokyo Kagaku Dozin Co., Ltd.: 1996; p 656 pp.
134. NIST chemistry webbook. Accessed 2012.
135. Dougherty, D. A.,*Science (Washington, D. C.)* **1996,** *271*, 163-8.
136. Muetterties, E. L.; Bleeke, J. R.; Wucherer, E. J.; Albright, T.,*Chem. Rev.* **1982,** *82*, 499-525.
137. (a) van, H. D.; von, H. G.; Meijer, G.; Maitre, P.; Duncan, M. A.,*J. Am. Chem. Soc.* **2002,** *124*, 1562-1563; (b) Jaeger, T. D.; Van, H. D.; Klippenstein, S. J.; Von, H. G.; Meijer, G.; Duncan, M. A.,*J. Am. Chem. Soc.* **2004,** *126*, 10981-10991; (c) Willey, K. F.; Cheng, P. Y.; Bishop, M. B.; Duncan, M. A.,*J. Am. Chem. Soc.* **1991,** *113*, 4721-8; (d) Hettich, R. L.; Jackson, T. C.; Stanko, E. M.; Freiser, B. S.,*J. Am. Chem. Soc.* **1986,** *108*, 5086-93; (e) Sohnlein, B. R.; Yang, D.-S.,*J. Chem. Phys.* **2006,** *124*, 134305/1-134305/8; (f) Ruan, C.; Yang, Z.; Rodgers, M. T.,*Phys. Chem. Chem. Phys.* **2007,** *9*, 5902-5918; (g) Meyer, F.; Khan, F. A.; Armentrout, P. B.,*J. Am. Chem. Soc.* **1995,** *117*, 9740-8.
138. Puskar, L.; Stace, A. J.,*Mol. Phys.* **2005,** *103*, 1829-1835.
139. Bauschlicher, C. W., Jr.; Partridge, H.; Langhoff, S. R.,*J. Phys. Chem.* **1992,** *96*, 3273-8.
140. (a) Wedderburn, K. M.; Bililign, S.; Levy, M.; Gdanitz, R. J.,*Chem. Phys.* **2006,** *326*, 600-604; (b) Kandalam, A. K.; Rao, B. K.; Jena, P.; Pandey, R.,*J. Chem. Phys.* **2004,** *120*, 10414-10422; (c) Pandey, R.; Rao, B. K.; Jena, P.; Blanco, M. A.,*J Am Chem Soc* **2001,** *123*, 3799-808; (d) Pandey, R.; Rao, B. K.; Jena, P.; Newsam, J. M.,*Chem. Phys. Lett.* **2000,** *321*, 142-150.
141. Di, B. S.; Lanza, G.; Fragala, I. L.; Marks, T. J.,*Organometallics* **1996,** *15*, 3985-3989.
142. (a) Deeth, R. J.; Paget, V. J.,*J. Chem. Soc., Dalton Trans.* **1997**, 537-546; (b) Davies, I. W.; Deeth, R. J.; Larsen, R. D.; Reider, P. J.,*Tetrahedron Lett.* **1999,** *40*, 1233-1236; (c) Bentz, A.; Comba, P.; Deeth, R. J.; Kerscher, M.; Seibold, B.; Wadepohl, H.,*Inorg. Chem.* **2008,** *47*, 9518-9527; (d) Burton, V. J.; Deeth, R. J.,*J. Chem. Soc., Chem. Commun.* **1995**, 573-4; (e) Deeth, R. J.,*J. Chem. Soc., Dalton Trans.* **2001**, 664-669; (f) Deeth, R. J.; Hearnshaw, L. J. A.,*Dalton Trans.* **2005**, 3638-3645; (g) Deeth, R. J.; Hitchman, M. A.,*Inorg. Chem.* **1986,** *25*, 1225-33; (h) Deeth, R. J.,*J. Chem. Soc., Dalton Trans.* **1993**, 1061-4.
143. Zhou, J.; Wang, W.-N.; Fan, K.-N.,*Chem. Phys. Lett.* **2006,** *424*, 247-251.
144. (a) Sedgwick, J. B.; Nelson, P. R.; Steiner, P. A.; Moran, T. F.,*Organic Mass Spectrometry* **1988,** *23*, 256-260; (b) Yokoyama, A.; Zhao, X.; Hintsa, E. J.;

Continetti, R. E.; Lee, Y. T.,*The Journal of Chemical Physics* **1990,** *92*, 4222-4233; (c) Eland, J. H. D.; Schulte, H.,*The Journal of Chemical Physics* **1975,** *62*, 3835-3836; (d) Andlauer, B.; Ottinger, C.,*The Journal of Chemical Physics* **1971,** *55*, 1471-1472; (e) Field, F. H.; Hamlet, P.; Libby, W. F.,*Journal of the American Chemical Society* **1967,** *89*, 6035-6038; (f) Smith, R. D.; DeCorpo, J. J.,*The Journal of Physical Chemistry* **1976,** *80*, 2904-2910; (g) Ausloos, P.,*Journal of the American Chemical Society* **1981,** *103*, 3931-3932; (h) Krailler, R. E.; Russell, D. H.; Jarrold, M. F.; Bowers, M. T.,*Journal of the American Chemical Society* **1985,** *107*, 2346-2354; (i) H. M. Boechat-Roberty, R. N., S. Pilling, A. F. Lago, G. G. B. de Souza,*Mon. Not. R. Astron. Soc.* **2005,** *000*, 1-8; (j) Newby, J. J.; Stearns, J. A.; Liu, C.-P.; Zwier, T. S.,*The Journal of Physical Chemistry A* **2007,** *111*, 10914-10927.

145. Duncan, M. A.,*Int. J. Mass Spectrom.* **2008,** *272*, 99-118.
146. Deeth, R. J.; Gerloch, M.,*Inorg. Chem.* **1984,** *23*, 3853-61.
147. Garcia-Fernandez, P.; Bersuker, I. B.; Boggs, J. E.,*J. Phys. Chem. A* **2007,** *111*, 10409-10415.
148. Craciun, S.; Donald, K. J.,*Inorg. Chem.* **2009,** *48*, 5810-5819.
149. (a) A. Klotz, P. M., P. Boissel, G. Serra, B. Chaudret, J. P. Daudey,*Astron. Astrophys* **1995,** *304*, 520; (b) Dunbar, R. C.; Petrie, S.,*Astrophys. J.* **2002,** *564*, 792-802.
150. (a) Minoux, H.; Chipot, C.,*J. Am. Chem. Soc.* **1999,** *121*, 10366-10372; (b) Wintjens, R.; Lievin, J.; Rooman, M.; Buisine, E.,*J. Mol. Biol.* **2000,** *302*, 395-410.
151. McFail-Isom, L.; Shui, X.; Williams, L. D.,*Biochemistry* **1998,** *37*, 17105-17111.
152. O., B. J., *Handbook of Battery Materials*. Wiley-VCH, Germany: Weinheim, 1999.
153. (a) Kim, K. S.; Tarakeshwar, P.; Lee, J. Y.,*Chem. Rev. (Washington, D. C.)* **2000,** *100*, 4145-4185; (b) Ma, J. C.; Dougherty, D. A.,*Chem. Rev. (Washington, D. C.)* **1997,** *97*, 1303-1324.
154. Kaupp, M.,*Angew. Chem., Int. Ed.* **2001,** *40*, 3534-3565.
155. Wu, G.; Guan, J.; Aitken, G. D. C.; Cox, H.; Stace, A. J.,*J. Chem. Phys.* **2006,** *124*, 201103/1-201103/4.
156. (a) Bush, M. F.; Oomens, J.; Saykally, R. J.; Williams, E. R.,*J. Am. Chem. Soc.* **2008,** *130*, 6463-6471; (b) Mino, W. K., Jr.; Szczepanski, J.; Pearson, W. L.; Powell, D. H.; Dunbar, R. C.; Eyler, J. R.; Polfer, N. C.,*Int. J. Mass Spectrom.* **2010,** *297*, 131-138; (c) Bush, M. F.; O'Brien, J. T.; Prell, J. S.; Wu, C.-C.; Saykally, R. J.; Williams, E. R.,*J. Am. Chem. Soc.* **2009,** *131*, 13270-13277; (d) Choi, C. M.; Lee, J. H.; Choi, Y. H.; Kim, H. J.; Kim, N. J.; Heo, J.,*J. Phys. Chem. A* **2010,** *114*, 11167-11174.
157. (a) Dougherty, D. A.,*Science (Washington, D. C.)* **1996,** *271*, 163-8; (b) Caldwell, J. W.; Kollman, P. A.,*J. Am. Chem. Soc.* **1995,** *117*, 4177-8; (c) Jacobson, D. B.; Freiser, B. S.,*J. Am. Chem. Soc.* **1984,** *106*, 3900-4; (d) Ranatunga, D. R. A.; Freiser, B. S.,*Chem. Phys. Lett.* **1995,** *233*, 319-23; (e) Dunbar, R. C.; Klippenstein, S. J.; Hrusak, J.; Stoeckigt, D.; Schwarz, H.,*J. Am. Chem. Soc.* **1996,** *118*, 5277-5283; (f) Ho, Y.-P.; Yang, Y.-C.; Klippenstein, S. J.; Dunbar, R. C.,*J. Phys. Chem. A* **1997,** *101*, 3338-3347; (g) Hoshino, K.; Kurikawa, T.; Takeda, H.; Nakajima, A.; Kaya, K.,*J. Phys. Chem.* **1995,** *99*, 3053-5; (h) Judai, K.; Hirano, M.; Kawamata, H.; Yabushita,

S.; Nakajima, A.; Kaya, K.,*Chem. Phys. Lett.* **1997,** *270*, 23-30; (i) Reddic, J. E.; Robinson, J. C.; Duncan, M. A.,*Chem. Phys. Lett.* **1997,** *279*, 203-208; (j) Nakajima, A.; Nagao, S.; Takeda, H.; Kurikawa, T.; Kaya, K.,*J. Chem. Phys.* **1997,** *107*, 6491-6494; (k) Weis, P.; Kemper, P. R.; Bowers, M. T.,*J. Phys. Chem. A* **1997,** *101*, 8207-8213; (l) Lin, C.-Y.; Chen, Q.; Chen, H.; Freiser, B. S.,*J. Phys. Chem. A* **1997,** *101*, 6023-6029.

158. Scott, A. C.; Buchanan, J. W.; Flynn, N. D.; Duncan, M. A.,*Int. J. Mass Spectrom.* **2008,** *269*, 55-61.

159. (a) Wu, B.; Duncombe, B. J.; Stace, A. J.,*J. Phys. Chem. A* **2008,** *112*, 2182-2191; (b) Wu, B.; Duncombe, B. J.; Stace, A. J.,*J. Phys. Chem. A* **2006,** *110*, 8423-8432; (c) Barran, P. E.; Walker, N. R.; Stace, A. J.,*J. Chem. Phys.* **2000,** *112*, 6173-6177; (d) Woodward, C. A.; Dobson, M. P.; Stace, A. J.,*J. Phys. Chem. A* **1997,** *101*, 2279-2287; (e) Stace, A. J.; Dobson, M. P.; Woodward, C. A.,*Chem. Phys. Lett.* **1997,** *267*, 171-174; (f) Woodward, C. A.; Dobson, M. P.; Stace, A. J.,*J. Phys. Chem.* **1996,** *100*, 5605-7.

160. R. J. Gillespie, I. H., *The VSEPR Model of Molecular Geometry*. Boston, 1991.

161. (a) Seijo, L.; Barandiaran, Z.; Huzinaga, S.,*J. Chem. Phys.* **1991,** *94*, 3762-73; (b) Kaupp, M.; Schleyer, P. v. R.; Stoll, H.; Preuss, H.,*J. Am. Chem. Soc.* **1991,** *113*, 6012-20; (c) Dyke, J. M.; Wright, T. G.,*Chem. Phys. Lett.* **1990,** *169*, 138-44.

162. (a) Kaupp, M.; Schleyer, P. v. R.; Stoll, H.; Preuss, H.,*J. Chem. Phys.* **1991,** *94*, 1360-6; (b) DeKock, R. L.; Peterson, M. A.; Timmer, L. K.; Baerends, E. J.; Vernooijs, P.,*Polyhedron* **1990,** *9*, 1919-34; (c) Von, S. L.; Schwerdtfeger, P.,*Chem. Phys. Lett.* **1990,** *170*, 555-60.

163. (a) Bauschlicher, C. W., Jr.; Sodupe, M.; Partridge, H.,*J. Chem. Phys.* **1992,** *96*, 4453-63; (b) Kaupp, M.; Schleyer, P. v. R.,*J. Phys. Chem.* **1992,** *96*, 7316-23; (c) Glendening, E. D.; Feller, D.,*J. Phys. Chem.* **1996,** *100*, 4790-7; (d) Han, Y.-K.; Jeong, H. Y.,*J. Phys. Chem.* **1996,** *100*, 18004-18005.

164. (a) Anthony J. Stace, H. C., Lifu Ma, Tsukiko Takashima, Helen Kimber, Joseph Koka,*Journal of American Chemical Society* **2013,** *in press*; (b) Cox, H.; Norris, C.; Wu, G.; Guan, J.; Hessey, S.; Stace, A. J.,*Dalton Trans.* **2011,** *40*, 11200-11210.

Publications

1. Lifu Ma, Joseph Koka, Helen J. Kimber, Hazel Cox, A. J. Stace, Conformation-resolved UV spectra of Pb(II) complexes. A gas phase study of the sandwich structures $[Pb(toluene)_2]^{2+}$ and $[Pb(benzene)_2]^{2+}$, J. Chem. Phys., 138, 164301/1-11.

2. Lifu Ma, Joseph Koka, Hazel Cox, A. J. Stace, A Gas Phase UV Spectrum of a Cu(II)-Bis(benzene) Sandwich Complex: Experiment and Theory, J. Chem. Phys., submitted.

3. Stewart, H.; Wu, G.; Ma, L.; Barclay, M.; Vieira, A. D.; King, A.; Cox, H.; Stace, A. J., Ultraviolet Photofragmentation Spectroscopy of Alkaline Earth Dication Complexes with Pyridine and 4-Picoline (4-Methyl pyridine). J. Phys. Chem. A 2011, 115, 6948-6960.